Quantitative Investigation of the Multicomponent Fuel Droplet Combustion Using High Speed Imaging and Digital Image Processing

A Thesis Submitted to the University of Sheffield for the Degree of Doctor Philosophy in the Faculty of Engineering

By

AHMAD MUNEEREL-DEEN FAIK

(M.Sc. 2006)

August 2017

Department of Mechanical Engineering

Dedication

To the woman who lived the dream and did not witness the achievement ...

My Mother (may Allah grant her His mercy)

To the man who supported and continues to support ...

My Father (may Allah bless him)

This is the result of the eagerness, diligence, and dedication which I learnt from both of you

Contents

Declaration

No portion of the work referred to in the thesis has been submitted in support of an application for another degree or qualification of this or any other university or institute of learning.

Publications

Journal Papers:

[1]. **Faik, A. M.**, Zhang, Y., 2014. Quantitative Spray Analysis of Diesel Fuel and its Emulsions Using Digital Image Processing. *EPJ Web of Conferences*. Vol. 92. EDP Sciences, 2015.

[2]. **Faik, A. M.**, Zhang, Y., Hanriot, S., 2016. Droplet Combustion Characteristics Of Biodiesel–Diesel Blends Using High Speed Backlit and Schlieren Imaging. *Heat Transfer Engineering*, Accepted.

[3]. **Faik, A. M.,** Ma, Z., Zheng, L., Zhang, Y., 2017. Quantitative Investigation of the Flame Characteristics throughout Droplet Combustion of the Diesel-in-water Emulsions. Under Preparation.

[4]. **Faik, A. M.**, Zhang, Y., 2017. Multicomponent Fuel Droplet Combustion Investigation Using Magnified High Speed Backlighting and Shadowgraph Imaging. Under Preparation.

Conference Presentations:

[1]. **Faik, A. M.**, Zhang, Y., 2014. Quantitative Spray Analysis of Diesel Fuel and its Emulsions Using Digital Image Processing. *International Conference on Experimental Fluid Mechanics (EFM 2014)*, Cesky Krumlov, Czech Republic, Oral Presentation.

[2]. **Faik, A. M.**, Zhang, Y., Hanriot, S., 2016. The Investigation Of Droplet Combustion Characteristics Of Biodiesel–Diesel Blends Using High Speed Camera. *12th International Conference on Heat Transfer, Fluid Mechanics, and Thermodynamics (HEFAT 2016)*, Malaga, Spain, Oral Presentation.

[3]. Zheng, L., **Faik, A. M.**, Zhang, Y., 2016. Flame Colour Analysis for the Droplet Combustion of Water-in-Diesel Emulsions. *12th International Conference on Heat Transfer, Fluid Mechanics, and Thermodynamics (HEFAT 2016)*, Malaga, Spain, Oral Presentation.

[4]. **Faik, A. M.**, Zhang, Y., 2017. High Speed Visualization of the Liquid-Phase Dynamics during the Combustion of Multicomponent Fuel Droplet. *8th European Combustion Meeting (ECM 2017)*, Dubrovnik, Croatia.

Acknowledgments

Abstract

The liquid-phase processes occurring during fuel droplet combustion are important in deciding the behaviour of the overall combustion process, especially, for the multicomponent fuel droplets. Hence, understanding these processes is essential for explaining the combustion of the multicomponent fuel droplet. However, the very fast combustion of the too small fuel droplet makes experimental investigation of these processes uneasily affordable.

In the present work, a high speed backlighting, and shadowgraph imaging and subsequent image processing leading to quantitative analysis of the multicomponent fuel droplet combustion including liquid-phase dynamics are performed. Two categories of multicomponent fuels – in which diesel is the base fuel – are prepared and utilized. The first category is biodiesel/diesel and bioethanol/diesel blends, while the second category is the water-in-diesel and diesel-in-water emulsions. The portion of the added components is set to 10%, 20%, and 30% of the total mixture volume for all the multicomponent fuel mixtures (blends and emulsions).

Specific optical setups are developed in-lab and used for tracking droplet combustion. The first setup is associated with the backlighting imaging with the resulting magnification of the droplet images being 30 times the real size. The second optical setup is used for Schlieren and shadowgraph imaging, with the resulting magnification being 10 times the real size for both techniques. Those magnifications made it possible to visualize the droplet interior at high imaging rates (250, 1000, 10000, and 40000 fps) so that tracking of the droplet liquid-phase processes is easily performed.

Using the aforementioned optical setups, spatial and temporal tracking of nucleation, bubble generation, internal circulation, puffing, microexplosion, and secondary atomization during the combustion of the isolated multicomponent fuel droplets are performed. This offered the privilege of full sequential tracking of droplet secondary atomization from initiation to sub-droplet generation.

Emulsion fuel droplet fragmentation has also been tracked and visualized using Schlieren imaging. The effect of water content of the emulsion on the intensity of the resulting droplet explosion wave has also been evaluated.

Spatial and temporal tracking of the sub-droplets generated by secondary atomization, and their subsequent combustion, in addition to their overall lifetimes have

also been performed. Accordingly, a comparison of the burning rate constant between the parent droplet and the resulting sub-droplets is carried out.

Specifically written and developed algorithms are used for image processing and feature extraction purposes. These algorithms are executed using Matlab. Using these algorithms, droplet projected area, perimeter, equivalent diameter, flame height and width, and sub-droplet generation rate have been temporally evaluated.

The high speed magnified imaging and subsequent image processing revealed that the rate of droplet secondary atomization is higher than those obtained by relatively low imaging rate. Additionally, it is shown that during a large portion of its entire lifetime, the droplet geometry has been affected by combustion significantly.

The combustion of two-interacting multicomponent fuel droplets at different spacing distances has also been investigated. The liquid-phase processes inside both droplets have been conceived. The effect of secondary atomization from one droplet on the other neighbouring droplet has also been studied.

The burning rate constants evaluated for the interacting fuel droplets are found to have the same trends as the isolated droplet combustion. However, the ratio of the droplet burning rate constant of the interactive droplet combustion to that of the isolated droplet combustion is higher than unity. The nucleation rate within the interacting fuel droplets is also found to be higher than that within the corresponding isolated fuel droplets.

List of Figures

11

13

15

16

17

List of Tables

Nomenclature

Symbol	Description
ΔD	Droplet size variation.
A	Area (mm^2).
B	Spalding transfer number.
Cp	Constant-pressure specific heat (kJ/kg.K)
D	Diameter (mm).
Đ	Mass diffusivity (m^2/s).
f	Focal length (mm)
H	Flame Height (mm)
$\dot{H}$	Rate of heat release (kJ/kg)
hc	Heat of combustion (kJ/kg)
h_{fg}	Latent heat of vaporization (kJ/kg)
K	Burning rate constant (mm^2/s).
k	Thermal conductivity (W/m.K)
m	Mass (kg)
$\dot{m}$	Mass burning rate (kg/s)
N	Engine rotational speed (rpm)
P	Perimeter (mm)
q	Heat per unit mass (kJ/kg)
r	Radius (mm)
t	Time (s)
T	Temperature (K)
W	Flame Width (mm)
x	Spacing distance (mm)
Y	Mass fraction

Greek Symbols

Symbol	Description
Δ	Difference
δ	Droplet deformation
η	Normalized burning rate ratio for interactive droplet combustion
λ	Thermal conductivity (W/m.K)
ρ	Density (kg/m^3)
υ	Stoichiometric Air/Fuel ratio

Subscripts

Symbol	Description
0	Initial
∞	Environment

eff	Effective
exp	Explosion
F	Fuel
f	Flame
g	Gas
i	Instantaneous
l	Liquid
maj	Major
min	Minor
O	Oxygen
s	Surface

Abbreviations

BD	Biodiesel-in-diesel blend
bsfc	Break specific fuel consumption
DW	Diesel-in-water emulsion
ED	Ethanol-in-diesel blend
F.F.	Free Fall
fps	Frames per second
HLB	Hydrophile-Lipophile Balance number
LDA	Laser Doppler Anemometry
LDV	Laser Doppler Velocimetry
LIF	Laser Induced Fluorescence
M.G.	Microgravity
N.G.	Normal Gravity
PDA	Phase Doppler Anemometry
PDI	Phase Doppler Interferometry
PLIF	Planar Laser Induced Fluorescence
RGB	Red, Green, Blue model for colour image representation
SiC	Silicon Carbide
TIFF	Tag Image File Format
WD	Water-in-diesel emulsion

Notes:

- Fuel terminology is listed in Appendix (A).

- Other symbols have been mentioned in their locations.

Chapter 1. Introduction

1.1 Motivations

Combustion has been identified and exploited since the early forms of human life. Fire has been used as a source of heat and light, it led to the expansion in digestive food variety, and helped to fabricate the metal tools used for hunting and farming [1]. Additionally, it has been assumed as one of the universe basic elements in addition to water, earth, and air [2]. However, the paradigm shift in combustion explanation occurred in the late eighteenth century, with Lavoisier's postulations on the role of oxygen in combustion and the invention of the safety lamp and premixed gas burner, in addition to the studies in flame propagation and detonation. These besides Semenov's theory in thermal ignition and chain reactions, and the works of Zeldovich, Damköhler, and Von Karman in the first half of the twentieth century, in addition to the contributions of many other researchers and scientific societies have helped in pushing combustion investigation many steps forward [3].

Presently, combustion plays an essential role in industry, transportation, energy production, and different aspects of life and civilization, and accounts for the highest portion of energy production around the world. Therefore, great efforts are conducted and being applied to investigate, develop, and then control the diverse combustion processes and systems with the associated phenomena. All these efforts are aspired by one objective that is to make energy production safer, cleaner, and more efficient.

Liquid hydrocarbon fuels contribute a great amount of this energy, due to the ease and flexibility of transporting and storing these fuels compared to the gaseous forms, in addition to their availability compared to the solid fuels. However, liquid fuels cannot be used in their bulky form. Therefore, in most of the applications the liquid fuel is mixed with the oxidizer and burned in the form of sprays of small size droplets. This form of combustion is relevant to a variety of systems including diesel, rocket, and gas turbine engines, in addition to the oil-fired boilers, furnaces, and process heaters. Hence, for developing these systems, a thorough understanding of the basic physical processes related to spray combustion is essential, not only for increasing energy production but also for controlling the fire hazard when handling the fuels, and reducing the combustion-generated pollution.

However, spray combustion is a complicated multidimensional aerothermochemical problem that involves different physical and chemical processes interacting simultaneously. These processes include – but not limited to – multicomponent two-phase flows, chemical reactions, heat and mass transfer, and phase change [4]. Thus, a detailed understanding of spray combustion requires a full comprehension of each of these processes along with the associated occurring phenomena. Though, this can only be performed by localizing the analysis within the spray instead of giving overall descriptions, i.e. microscopic rather than macroscopic investigation. This can be achieved by exploring an individual droplet as opposed to the complete spray, giving the fact that the spray is an ensemble of individual droplets that constitute the dispersed phase that is surrounded by a gaseous medium which represent the continuous phase.

Accordingly, droplet combustion has been the subject of a vast number of investigations both experimentally and theoretically in an effort to address the mentioned physical and chemical processes taking place during spray combustion [5]. However, there are still some gaps to be filled by further investigations. Droplet combustion of the multicomponent fuels is one of these areas that need further comprehension. The multicomponent fuel is defined in the present work as the mixture of two or more liquid fuels or fuel mixtures that are prepared prior to combustion. This include, fuel blends, emulsions, and all other mixtures resulting from the physical mixing rather than chemical reaction of the mixture constituents. In this context, the single-component fuel is meant to be the regular neat liquid fuel that is used in its original form without mixing with other components, such as regular diesel, gasoline, ethanol, and methanol.

Hence, the aim of the present work is to fill in some of these gaps. This would be achieved by implementing experiments on three different categories of droplet combustion, namely, multicomponent fuel droplet combustion, in-droplet dynamics, and the reciprocal interaction of two-neighbouring droplets during combustion. These aims and a summary of the overall motivations behind this work are shown in Figure 1-1.

Conversely, optical diagnosis is one of the mostly implemented techniques in combustion measurements both qualitatively and quantitatively. And it is receiving an increased interest due to a variety of advantages such as non-disturbing the flow field inside the measured system, quick and precise record of the instantaneous changes in the environment under study, and large data provided in comparison to other measurement techniques [6]. However, a single optical technique is limited in the number of parameters studied for every process. Therefore, in the present work three different imaging

techniques are used for studying droplet combustion, namely, the backlighting imaging, shadowgraphy, and Schlieren imaging. This resulted in covering as much as possible of the processes and phenomena associated to droplet combustion.
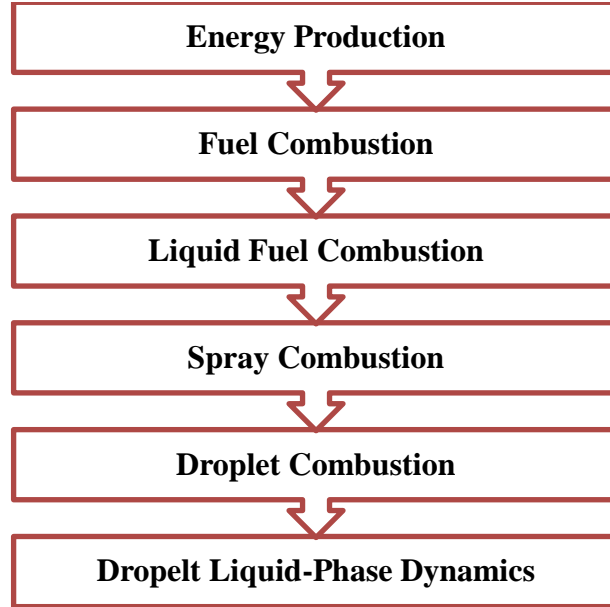
Figure 1-1: Motivation sequence of the present work.

In conclusion, the main motivation behind the present work is taking the current understanding of droplet combustion a step further by carrying out an in-focus experimental investigation of the liquid-phase dynamics during the combustion of the multicomponent fuel droplet using three different high speed imaging techniques.

1.2 Objectives

According to the aforementioned motivations, the main objective of the present work is the study of the multicomponent fuel droplet combustion using high speed imaging. This objective in turn, is subdivided into the following sub-objectives:

i. Performing a comprehensive review of the up-to-date research works in droplet combustion. The intension is to collect, classify, outline, and summarize all the possible available previous work dedicated to droplet combustion.

ii. Developing an optical setup (or setups) capable of tracking the different processes occurring within the liquid-phase of the droplet during combustion. Considering

initial droplet diameter, size variation, transparency, and the chaotic nature of combustion, in addition to the short time span of the overall process.

iii. Using the developed setups for studying the combustion of multicomponent fuel droplets with an emphasis to the droplet liquid-phase processes. These include nucleation and bubble dynamics, puffing and microexplosion, and sub-droplet generation by secondary atomization.

iv. Developing and validating appropriate algorithms for processing the images obtained by experimentation, and extracting the required droplet features with high precision and minimum uncertainty.

v. Testing different fuels and fuel mixtures and providing quantitative data for the droplet combustion characteristics of these fuels.

vi. Studying the effect of multi-droplet interaction on the droplet liquid-phase dynamics of the multicomponent fuel droplets during combustion.

vii. Providing quantitative data for the occurrence of puffing and microexplosion and secondary atomization rate during the combustion of multicomponent fuel droplets.

1.3 Thesis Outline

The thesis is divided into eight chapters arranged sequentially to outline the development of the work carried out starting from the motivations behind the work and ending with the main findings and conclusions. These chapters are as follows:

Chapter 1 contains the motivation and objectives of this work. The covered areas of droplet combustion and the used diagnosis techniques for each area are outlined as well. Afterwards, the work objectives are listed.

Chapter 2 presents a theoretical review of the problem starting from atomization and liquid fuel combustion, in addition to a basic description of droplet combustion and the classical "D^2-law" theory. The most used diagnostic techniques for droplet combustion investigation have also been reviewed.

Chapter 3 outlines the main experimental features of the work, including multicomponent fuel preparation, droplet generation, suspension, and ignition techniques. Then, the image processing methodology and algorithms are explained. Furthermore, data validation and error analysis for the experimental results and image processing algorithms have been depicted in the end of the chapter.

Chapter 4 demonstrates the experimental work carried out for evaluating the characteristic parameters in the combustion of an isolated multicomponent fuel droplet. These include the burning rate constant, droplet size evolution, and the flame stand-off ratio, in addition to the droplet shape variation throughout the entire droplet combustion time.

Chapter 5 focuses on the puffing and microexplosion processes leading to secondary atomization and sub-droplet emission from the isolated multicomponent fuel droplets during combustion.

Chapter 6 tracks the droplet liquid-phase including nucleation and bubble generation and growth inside the multicomponent fuel droplet during combustion.

Chapter 7 presents the combustion characteristics of two-interacting droplets of the multicomponent fuels using magnified high speed imaging.

Chapter 8 summarizes the overall findings of the present work, and proposes the probable future works for further investigations.

Additionally, five appendices are incorporated at the end of the thesis for elucidating the auxiliary data and methods used in the present work. These include fuel terminology, fuel properties, droplet diameter evaluation methods, published burning rates, and the Matlab code flowcharts.

Chapter 2. Literature Review

2.1 Introduction

Combustion as a process is an extremely fast exothermic reaction that releases energy in the form of heat and propagates through the surrounding environment in the form of flame [7]. Combustion is an integral of different physical and chemical processes that start by fuel-oxidizer mixing, proceed by ignition and flame propagation, and terminate by the production of various chemical substances as a result of fuel oxidation. The essential part of combustion is the flame, since it is the zone where fuel and oxidizer meet and react and it is the region of the highest temperature in combustion. Therefore, it has received and still receiving the greatest interest in scientific investigation. The flame is defined as a rapidly propagating, self-sustaining, reaction in a tiny space between the fuel and oxidizer. Flames are classified according to different categories depending on the type of reactants, flow condition, and other factors. The most famous flame classifications are based on:

- ***Combustible Mixture Formation***: flames are classified according to the fuel/oxidizer mixing into *Premixed Flames* and *Diffusion Flames*. Premixed flames take place when the fuel and oxidizer are well mixed prior to combustion, or the fuel-oxidizer mixing occurs ahead of the flame front as in the Bunsen burner. Whereas the diffusion flames occur when the fuel and oxidizer enter the combustion zone separately and react rapidly as they mix.
- ***Type of Flow***: flames are classified according to the reactants nature of flow into *Laminar Flames* when the flow is laminar, and *Turbulent Flames* for turbulent flows [8].

Examples of flame types and applications are shown in Table 2-1. Diffusion flames are preferred in the majority of industrial applications since it is safer to keep the fuel and oxidizer away from each other, in addition to the greater flexibility they provide in controlling combustion intensity and flame structure. Turbulence on the other hand is more preferred in combustion than laminar flow due to the resulting mixing enhancement by turbulence compared to laminar flow [9]. However, diffusion flames are sometimes superimposed on the premixed flames in some practical combustion systems involving the combustion of liquid fuels.

Table 2-1: Flame types with examples.

Flow/Flame	Premixed	Diffusion
Laminar	Bunsen Burner	Candle Flame
Turbulent	Spark Ignition Engine	Compression Ignition engine

On the other hand, combustion may be classified according to the physical state of the reactants. Where, the term *homogeneous combustion* is used for describing the combustion of fuel that is in the same physical state as the oxidizer, such as the Bunsen flame. Whereas the *heterogeneous combustion* describes the combustion when the fuel and oxidizer are initially in different physical phases, such as the combustion of coal particle in air [10]. Since the majority of combustion applications are based on burning the fuel in air; therefore, the heterogeneous combustion will take place basically in the combustion of liquid and solid fuels due to the multiphase nature of the combustion of these fuels. And, due to the same reason, heterogeneous combustion is more complicated than the homogeneous combustion. Therefore, further investigations are required for acquiring in-depth information and developing the understanding of the chemical and physical processes that take place throughout the heterogeneous combustion. Hence, the scope of the present work is the heterogeneous combustion of liquid fuels in air.

2.2 Liquid Fuel Combustion

A large portion of the global energy requirements comes from burning liquid hydrocarbons. This is due to the ease and flexibility of transporting and storing these fuels compared to the gaseous forms, in addition to their availability compared to the solid fuels.

Liquid fuel combustion may take different forms according to the type and quantity of liquid and the nature of combustion system. These forms are shown in Figure 2-1. Some of these forms take place in the form of accidental fires such as the *Pool Fire* and the *Spill Fire*. The former type occurs for the liquid fuels stored in open tanks, buds, and fuels accumulated in depressions in the ground. The term pool is usually used for describing liquids of free surface and considerable depth (more than 10mm). In the pool fire the depth of the liquid is important in deciding the burning rate and continuity of combustion. When the depth is high, the heat dissipation to the bottom of the liquid is of minimum effect on the burning rate. The spill fire on the other hand is assumed as special case of the pool fire

that occurs throughout the burning of a leaking liquid fuel on a non-blocked space. In such case, liquid spread continues, causing the area of the burning surface to increase until reaching dynamic equilibrium. Examples of such case are the leakage of liquid fuel from a pipe or a damaged vessel. The topography of the surface plays a key role in deciding whether the liquid will spread uniformly over the ground or flow in discrete channels.
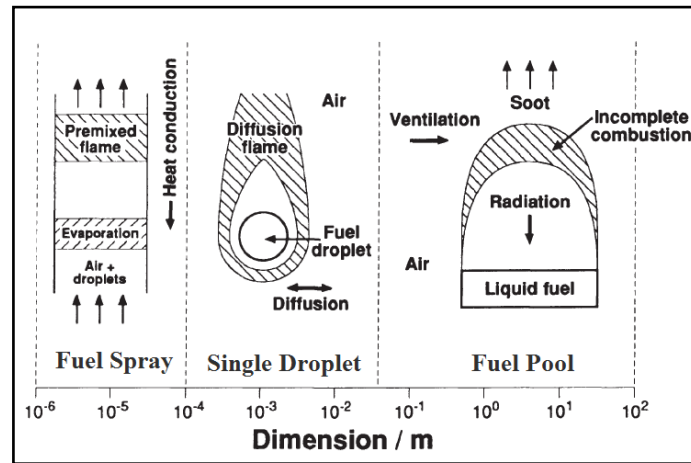
Figure 2-1: Different types of liquid fuel combustion at different sizes [1].

Liquid depth is affected by the properties of liquid itself and the nature of the surface where the flow is taking place. If the depth of the liquid is increased, the combustion will take the form of pool fire rather than spill fire [11]. Each of these configurations take the form of non-premixed or diffusion flame.

However, in the majority of applications liquid fuel combustion is planned and controlled. Though, in these applications, the essential property of the liquid fuels that may affect the nature of their combustion form is that the ignition point of the fuel-oxidizer mixture is usually higher than the evaporation point of the liquid fuel. Accordingly, combustion will occur mainly – if not only – in the gaseous phase. Hence, the fuel tendency for evaporation is called *volatility*. Liquid fuels are classified according to volatility into volatile and non-volatile fuels. Volatile fuels usually vaporize and mix with the oxidizer, and then burn in a premixed flame, such as gasoline combustion in the spark ignition engine. While, the non-volatile fuels are usually vaporized during combustion, leading to diffusion flame configuration. Example of this type of fuels is the diesel combustion in the compression ignition engine [12]. In the latter, the fuel is injected in the form of spray into a high pressure high temperature air so that the bulk of liquid fuel will disintegrate into smaller size droplets which will evaporate and burn locally. This form of

spray combustion involves different physical and chemical processes that interact simultaneously throughout the overall combustion process. This interaction makes it worthwhile to invest in the investigation and further analysis of such processes in an objective to comprehend the nature and mechanism of each of these processes. Therefore, liquid fuel spray combustion will be the scope of the rest of the present work.

2.2.1 Liquid Fuel Spray Combustion

Spray combustion earliest implementation was in the late nineteenth century for burning non-volatile liquid fuels. Certainly it remained the main technique of burning heavy fuel oils at present in spite of the use of fluidized bed combustors.

The burning liquid fuel spray is different from a premixed gaseous fuel; the former is being non uniform in composition. The liquid fuel exists in the form of discrete variable size droplets moving in random directions and variable velocities compared to the main stream. This form of non-uniformity in the combustible mixture leads to irregularities in flame propagation through the spray, which makes the combustion zone geometrically poorly defined [13]. Liquid fuel combustion consists mainly of four processes, namely: spray formation, fuel evaporation, combustible mixture formation, and mixture combustion [14,15]. The fuel spray is usually formed by injecting the fuel through a nozzle at very high pressure (up to 2000 bar) towards the combustion chamber (that is normally a hot environment). Once it leaves the nozzle, the liquid jet takes the form of a conical spray as shown in Figure 2-2.
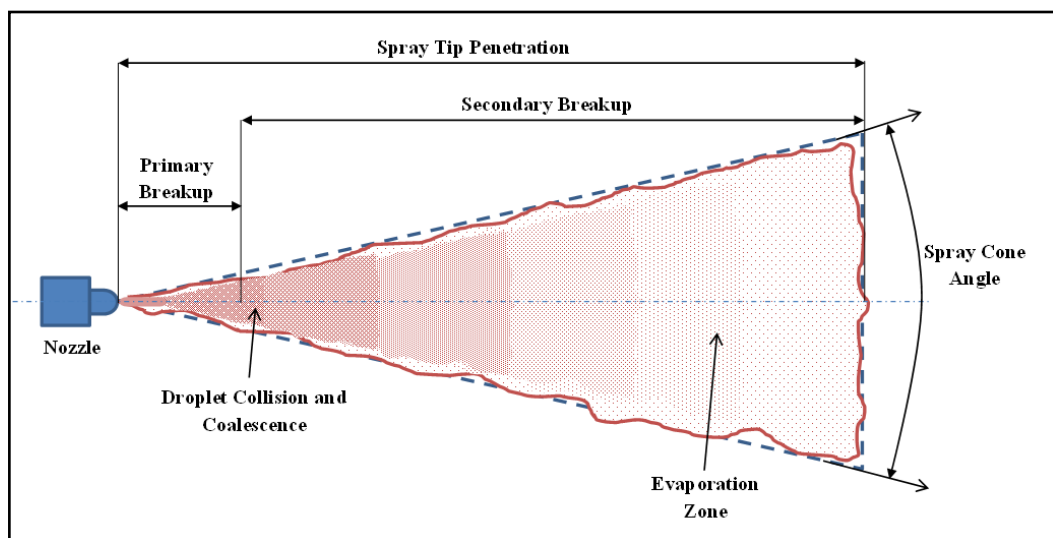
Figure 2-2: Spray formation and breakup (reproduced from [16]).

Turbulence inside the liquid stream causes its break up into a bundle of liquid threads that subsequently progress into a dense cloud of different size droplets that penetrate through the gas into the combustion zone, evaporate and mix with the oxidizer to initiate (and then maintain) combustion. Liquid break up and droplet formation is known as *atomization*. Atomization is important in combustion, since most of the combustion systems (such as the industrial furnaces and internal combustion engines) work on liquid fuels that cannot be used before being atomized. And it is essential in increasing the combustion efficiency in such systems because of the high liquid surface to mass ratio generated after atomization, which in turn leads to higher rates of evaporation and mixing, and then combustion [17].

2.2.2 Atomization and Droplet Formation

Atomization is defined as the conversion of liquid from its bulky form into a spray of droplets and other physical dispersions of small particles in a gaseous environment. This could take place due to the kinetic energy of the liquid being atomized, such as that carried out by the pressure atomizers, or by being in contact with high-velocity gaseous substance, in what is called the air-assist atomizers, or as a result of an external force, such as the flash boiling atomization, effervescent atomization, ultrasonic atomization, and electrostatic atomization [17].

Despite how the sheet is produced, its instability is increased by the surrounding aerodynamic disturbances, causing it to spread out from the nozzle with a decrease in its thickness and perforations that take place and develop toward each other creating threads and ligaments as shown in Figure 2-3. The collapse of these ligaments with each other leads to the formation of variable size droplets. This initial collapse of the spray into threads and ligaments, and then into droplets is called *primary break-up*. The size of the resulting droplets ranges from few microns to hundreds of microns [18], and is determined by the liquid sheet initial thickness, velocity gradient between the liquid and the surrounding gas, and liquid physical properties (mainly viscosity and surface tension) [17]. These droplets may undergo a subsequent break-up due to the aerodynamic forces resulted by the velocity gradient between the droplets and environment. This subsequent break-up is called *secondary atomization* [16].
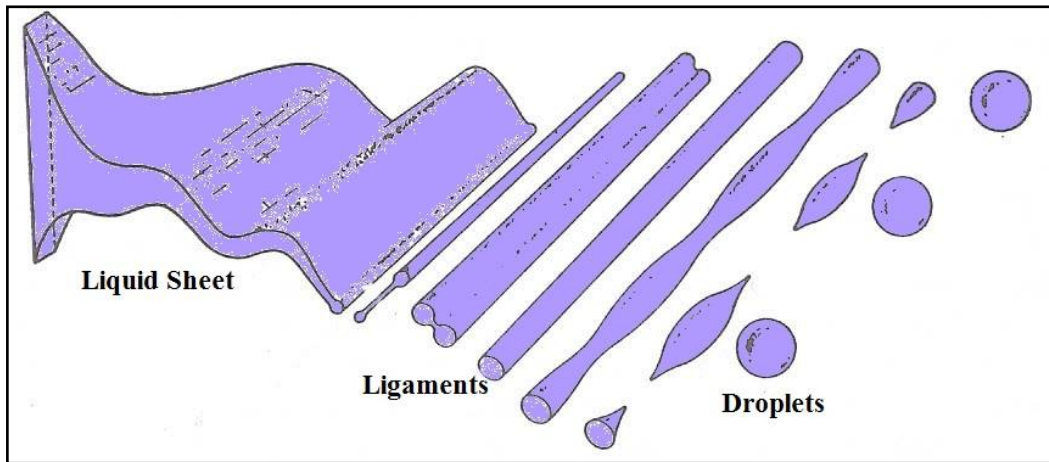
Figure 2-3: Idealized process of droplet formation from a liquid sheet [19].

Thence, it is found that droplet size variation has an effect on both spray and engine performance characteristics. Spray tip penetration distance and velocity are found to increase with increasing droplet size due to the longer evaporation time required [20,21]. Flame shape is affected by droplet size as well. Large droplets usually burn in a diffusion flame around the liquid phase, while a premixed gas flame appearance is noticed in the combustion of very small droplets, due to the complete evaporation of these droplets upstream of the flame front [22]. Furthermore, NOx formation is found to decrease by decreasing droplet size in the spray due to enhanced evaporation and the domination of premixed combustion mode compared to the diffusion combustion mode of the large size droplets [23].

Accordingly, it can be deduced how prominent are the droplet characteristics in defining the fuel spray and engine performance characteristics. Hence, a comprehensive understanding of the single constituent of the spray would be helpful for explaining the more general spray structure. This is due to the fact that the fuel spray is an integral of a large number of small size droplets. Therefore, the previously set scope of the work on liquid fuel combustion is further converged to single fuel droplet combustion.

2.3 Droplet Combustion

Studies of spray combustion are categorized into two major trends: the first is based on analysing the real combustion process, starting from single fuel droplet combustion or an idealized spray, while in the second trend; direct observations of spray combustion are made to investigate the different accompanying phenomena such as flame length,

31

radiation, flame oscillation and stability. Moreover, spray combustion could be studied theoretically using the information from a single fuel droplet in the turbulent gas diffusion combustion [24]. Therefore, droplet combustion investigation is essential for understanding spray combustion, since the spray prior to combustion turns into an integral of a large number of fine droplets.

First of all, it is important to differentiate between the different forms of droplet combustion. In fact, there are two forms of droplet combustion; the first is the *monopropellant* droplet combustion, where the fuel and oxidizer exist in a single substance, as it is seen in the combustion of hydrazine by nitromethane [25]. This form of droplet combustion has been the subject of a variety of research work, both experimental [26–28], and theoretical [29–33]. The second form is the *bipropellant* droplet combustion, which is by far more employed in practical applications that involve fuel droplet combustion in a surrounding oxidizing medium (usually air). The present work is conducted mainly on the second form of droplet combustion.

2.3.1 The Classical Theory of Droplet Combustion

The first experimental work carried out for investigating the combustion of an isolated fuel droplet belongs to Godsave in 1949 [34] and 1950 [35], and Kumagai and Isoda in 1950 [36]. Whereas, the first and simplest model designed for describing droplet evaporation and combustion – also known as the *classical theory* (or D^2-*law*) of droplet combustion – is carried out by Godsave [37] and Spalding [38] in 1953 [39]. The classical theory exemplifies the essential physics and gives an elementary speculation on droplet regression rate [4]. In this model, the fuel droplet is exposed to a stagnant oxidizing environment. This droplet evaporates at its surface, though the resulting vapour diffuses outward and reacts with the oxidizer – which is diffusing inward from the surroundings – in a non-premixed flame, as shown in Figure 2-4.

The fuel vapour and oxidizer consume each other in the flame zone in a stoichiometric reaction. The heat generated by the reaction conducts inward towards the droplet and outward towards the environment. The heat portion conducted towards the droplet will provide the required energy for persisting droplet evaporation and maintaining combustion until full consumption of the fuel droplet.
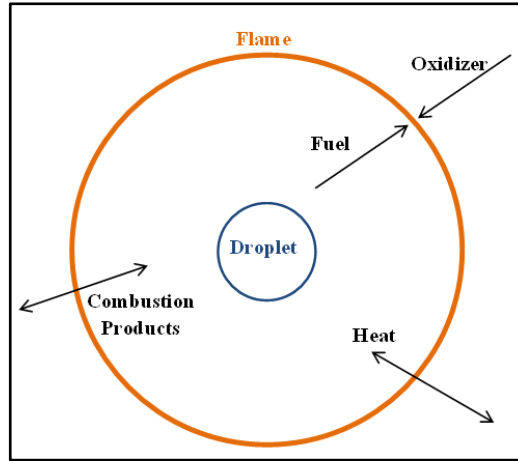
Figure 2-4: Combustion model of an isolated liquid droplet in an infinite oxidizing medium.

The resulting heat is transferred from the flame through conduction and radiation towards both the environment and the droplet surface [39]. Hence, the energy, fuel, and oxidizer conservation equations are taking the forms shown in equations 2-1, 2-2, and 2-3 respectively:

$$r^2 \rho v \frac{d(C_p T)}{dr} = \frac{d}{dr}\left[r^2 \frac{\lambda}{C_p} \frac{d(C_p T)}{dr}\right] - r^2 \dot{H} \qquad \ldots\ldots\ldots \qquad \textbf{(2-1)}$$

$$r^2 \rho v \frac{dm_F}{dr} = \frac{d}{dr}\left[r^2 D\rho \frac{dm_F}{dr}\right] - r^2 \dot{m}_F \qquad \ldots\ldots\ldots \qquad \textbf{(2-2)}$$

$$r^2 \rho v \frac{dm_O}{dr} = \frac{d}{dr}\left[r^2 D\rho \frac{dm_O}{dr}\right] - r^2 \dot{m}_O \qquad \ldots\ldots\ldots \qquad \textbf{(2-3)}$$

For solving the above equations, and developing the classical theory of droplet combustion, the following assumptions have been made:

i. Quasi-steady droplet combustion.

ii. Spherical symmetry. Therefore, convection and diffusion only take place radially, and, temperature and mass fractions of the fuel and oxidizer depend only on the radial position.

iii. Stoichiometric reaction between the fuel and oxidizer at the flame front. Hence, the rate of change of energy is determined by the rate of consumption of both reactants.

iv. The chemical kinetics are infinitely fast compared to diffusion, resulting in an infinitesimally thin flame interface between fuel and oxidizer.

v. The gas-phase heat capacity and transport properties are all constant.

vi. Gas-phase quasi-steadiness.

vii. Uniform and constant droplet temperature close to the saturation point, so that the heating up period is neglected.

viii. Both Soret and Dufour effects are neglected. This is to neglect the heat flux due to concentration difference and mass diffusion due to temperature gradient.

ix. Single-component fuel droplet with no internal flows in any dimension.

x. No soot formation, negligible radiation. To cancel out the effect of luminosity radiation in the conservation of energy term.

xi. Unity Lewis number. For combining the energy and mass conservation equations and eliminating the rate-dependent source terms.

Correspondingly, equations (2-1)-(2-3) are simplified and solved for evaluating the main characteristic parameters of droplet combustion as follows:

The mass burning rate of the burning droplet is evaluated as:

$$\dot{m}_F = \frac{4\pi k_g r_s}{c_{pg}} \ln[1 + B] \qquad \text{.........} \qquad \text{(2-4)}$$

Flame temperature is expressed in terms of droplet surface temperature, fuel properties, and stoichiometric fuel/air mixture as:

$$T_f = T_s + \frac{q_i + h_{fg}}{c_{pg}(1 + v)}[vB - 1] \qquad \text{.........} \qquad \text{(2-5)}$$

Flame radius, on the other hand, is expressed in terms of the droplet radius as shown in equation (2-6). This ratio is known as the flame stand-off ratio of droplet combustion.

$$\frac{r_f}{r_s} = \frac{\ln[1 + B]}{\ln\left[\frac{1+v}{v}\right]} \qquad \text{.........} \qquad \text{(2-6)}$$

Fuel mass fraction at the droplet surface has also been evaluated as:

$$Y_{F,s} = \frac{B - \left(1/v\right)}{B + 1} \qquad \text{.........} \qquad \text{(2-7)}$$

Where (B) is the Spalding transfer number, and it is defined as:

$$B = \frac{(\Delta h_c / \nu) c_{pg} (T_\infty - T_s)}{q_i + h_{fg}}$$ .... (2-8)

The burning rate constant of droplet combustion is also evaluated in terms of fuel properties and the transfer number as:

$$K = \frac{8k_g}{\rho_l c_{pg}} \ln[1 + B]$$ .... (2-9)

Where, it is actually a constant at the steady-state only, and it represents the slope of the droplet size variation with time. Hence, the general equation of the temporal droplet size variation is expressed as:

$$D^2(t) = D_0^2 - Kt$$ .... (2-10)

Equation (2-10) is known as the D^2-law of droplet combustion. From which, the overall droplet lifetime is determined by letting $D^2(t_d) = 0$;

$$t_d = \frac{D_0^2}{K}$$ .... (2-11)

As it is shown in the above listed equations, the formulation of the classical theory of droplet combustion facilitated the prediction of droplet burning rate, flame temperature and radius, and on-surface fuel concentration. However, those predictions represent the approximate (rather than real) values. This is due to the assumptions used for developing the theory which simplified the solution but accordingly, omitted the effect of some of the physical and chemical processes that take place in the combustion of real fuel droplets. The quasi-steadiness assumption for example, eliminates the time-dependent variables in the conservation equations, but, it excludes the transient processes at the same time, such as droplet heating, ignition, and flame extinction. The effect of droplet heating on the resulting combustion behaviour is investigated [40–45], and is shown to be significantly effective on the droplet lifetime and combustion behaviour [40–42]. The estimated droplet heating period is found to be about 10-20% of the total droplet lifetime [40,41]. Droplet

35

ignition delay time is also important in the real combustion systems, since it defines the portion of heterogeneous combustion and the rate of heat and mass transfer to and from the droplet [46]. The droplet ignition delay time is considerably variable and is affected by the type of fuel [47–49], droplet initial size [50,51] and initial temperature [51], and the environmental pressure and temperature [52,53].

The constant transport properties assumption causes uncertainty in the results due to the strong dependence of the thermophysical properties on both temperature and species concentration [54,55]. These uncertainties may reach about 20% of the experimentally evaluated characteristics [54]. Therefore, different theoretical models have been developed for investigating droplet combustion under variable transport properties [56–58].

On the other hand, experimental investigation of the droplet combustion under zero or microgravity conditions have revealed the formation of sootshell around the droplet for different types of fuels [59–64]. A sample image of this sootshell is shown in Figure 2-5. This finding practically neutralized the assumption of no soot formation that is used for developing the classical theory of droplet combustion.
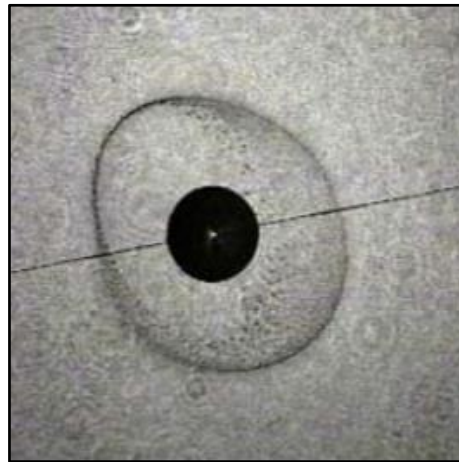
Figure 2-5: Shadowgraph image of the soot shell formation during the combustion of ethanol fuel droplet in microgravity [62] (with permission from the publisher).

Accordingly, the values predicted by the use of the classical theory of droplet combustion may be utilized for primary estimation purposes rather than precise calculations. However, the characteristic parameters set by the classical theory, such as the burning rate constant, flame stand-off ratio, and droplet lifetime became the key parameters to be evaluated throughout the majority of the research work conducted for

36

investigating droplet combustion both theoretically and experimentally. A review of the development of such research works is performed below.

2.3.2 Development of the Droplet Combustion Investigation

After the D^2-law formulation by Godsave and Spalding, and the preceding pioneering experiments of Godsave, and Kumagai and Isoda, droplet combustion investigation received an increased interest and experienced rapid development, especially with the evolution of both instrumentation and experimental techniques, on one hand, and the computers and computational methods on the other. Kumagai and Isoda [65] performed the first droplet combustion experiment under microgravity conditions. They aimed to prove the spherical symmetry assumptions of the classical theory by eliminating the effect of buoyancy and natural convection on the droplet burning rate. Due to the effect of buoyancy, the visible flame takes a more oval-like shape rather than the spherical shape assumed by the classical theory, as shown in Figure 2-6 for a diesel fuel droplet burning under both microgravity and normal gravity conditions.
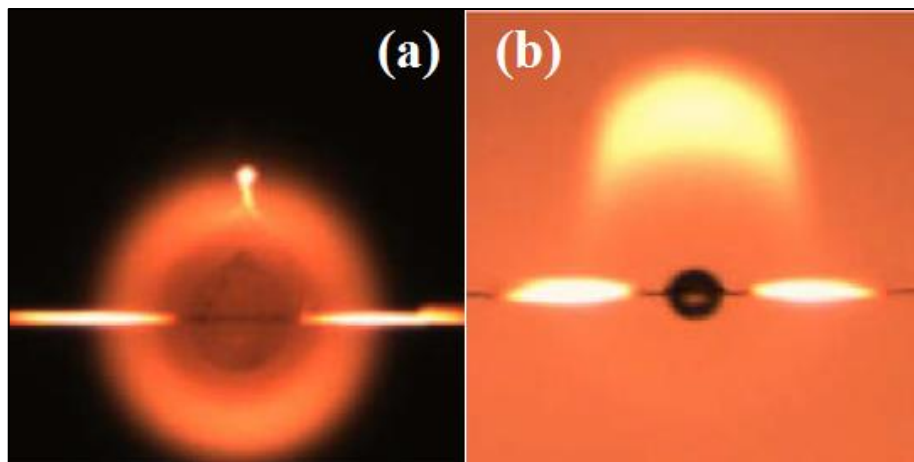
Figure 2-6: The shape of the flame surrounding a burning droplet as it appears under: (a) microgravity conditions, (b) normal gravity conditions [66] (with permission form the publisher).

Accordingly, Kumagai and Isoda have created the microgravity environment for their experiment by suspending the droplet inside a freely falling chamber and imaging the droplet – that is ignited inside the chamber – when the chamber passes a certain predefined point in its path as shown in Figure 2-7. Glass windows are added to the chamber to allow imaging the droplet during combustion.

37
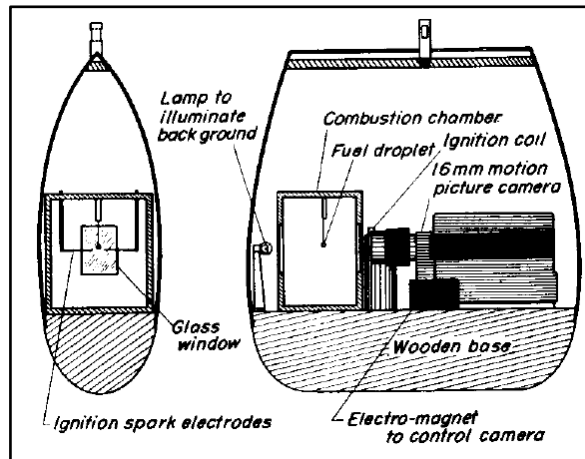
Figure 2-7: The falling chamber used by Kumagai and Isoda [67] (with permission from the publisher).

This experiment is then developed by Kumagai and his co-workers for eliminating the effect of the suspending fibre [68–70], and studying the effects of air flow [71], and initial droplet diameter [72] respectively on the droplet burning rate under microgravity conditions. The work of Kumagai and Isoda was the start of a new path in droplet combustion investigation that is carried out under zero/micro/low gravity conditions. Some are carried out according to the same principle of freely falling chamber. This is encouraged by the establishment of the drop tower facilities for performing gravity-related studies, such as the NASA zero-gravity and 2.2 second drop towers operated in the mid-sixties of the last century, and the MGLAB, ZARM, and NML drop towers in Japan, Germany, and China respectively.
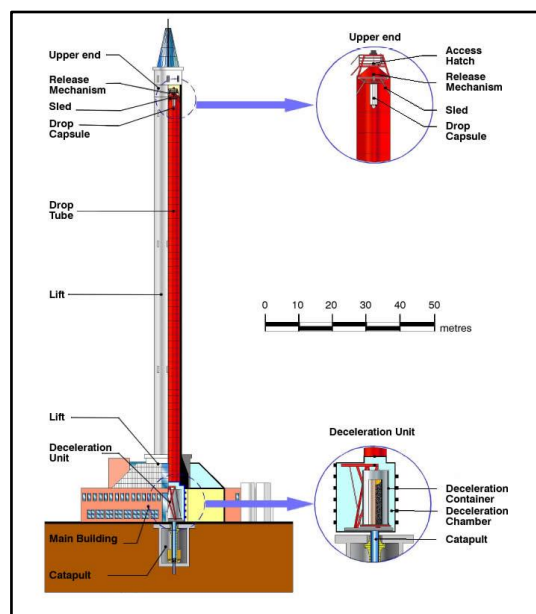
Figure 2-8: The 110m Height ZARM Drop Tower in Bremen, Germany [73].

38

The drop towers are air-evacuated, specially built structures either above the ground (towers), or underground (shafts) of heights around 100 m, in which microgravity experiments are carried out by free falling capsules inside these towers [73], as shown in Figure 2-8. These towers may generate a microgravity environment in the range of (10^{-5}-10^{-6} g). Diversity of droplet combustion research work has been carried out using these towers [49,59,62,74–77].

Another microgravity experiments are carried out using the parabolic flight technique [78–82]. The experiments are performed inside specially modified aircrafts which are used for reducing the gravity by flying through paths with a set of parabolic trajectories as shown in Figure 2-9. The microgravity generated using this technique is about (10^{-2} g) [73,78,79,81,82], which is lower than that obtained by the drop tower method. The third method for investigating droplet combustion under reduced gravity conditions is to perform the test in space. This is carried out on-board either the International Space Station ISS [77,83–87], or space shuttles with specifically assigned experimental testing missions, such as the space shuttle Columbia, in which a variety of experiments are carried out [88–92].
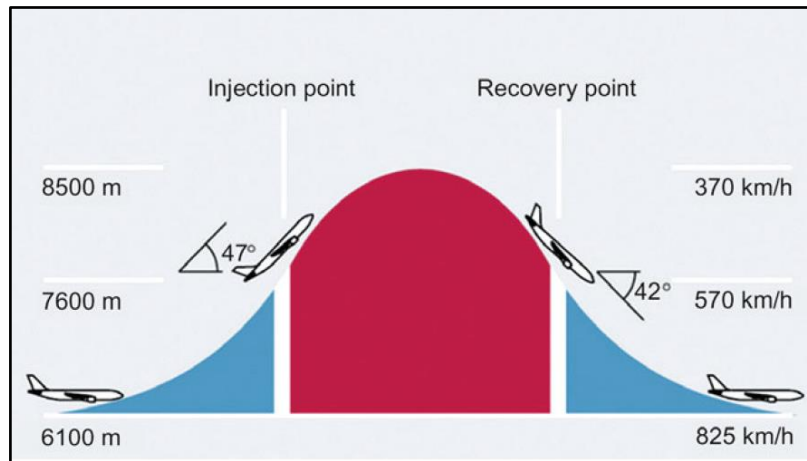
Figure 2-9: Parabolic Flight Profile of the Zero-Gravity Airbus A300 Aircraft of Novespace - France [73].

Likewise, droplet combustion investigation under normal gravity conditions has also been extensively performed, since the real fuel combustion usually takes place under normal – rather than reduced (or zero) – gravity environments. Despite the effects of buoyancy and natural convection associated with the normal gravity conditions, the experimental work performed under certain conditions has the privilege of flexibility and suitability for every type of measurement techniques. The size and weight limitations

associated with the falling chamber and drop tower techniques are not encountered in the normal gravity experiments. The cost effectiveness and ease of repeatability are other factors to be added for the advantages of the normal gravity experiments when compared to the microgravity experiments carried out in space and the parabolic flights. Therefore, in a 276 sample statistical survey of the published work on droplet combustion research for the period of time from the early 1950's to 2017, the portion of experimental research work carried out under normal gravity conditions is found to be higher than that of the corresponding work under reduced (or micro) gravity conditions as shown in Figure 2-10. Among these 276 experimental research papers, 63% are performed under normal gravity and the remaining 37% is carried out under reduced gravity conditions. A variety of research areas have been considered under normal gravity conditions, these include but not limited to droplet ignition [52,93,94], burning rate [95–97], microexplosion [98,99], and sooting behaviour [100], of different single-component [95,101–105] and multi-component [93,94,98,99] fuels, and under variable environmental conditions [52,96,97,102,106,107].
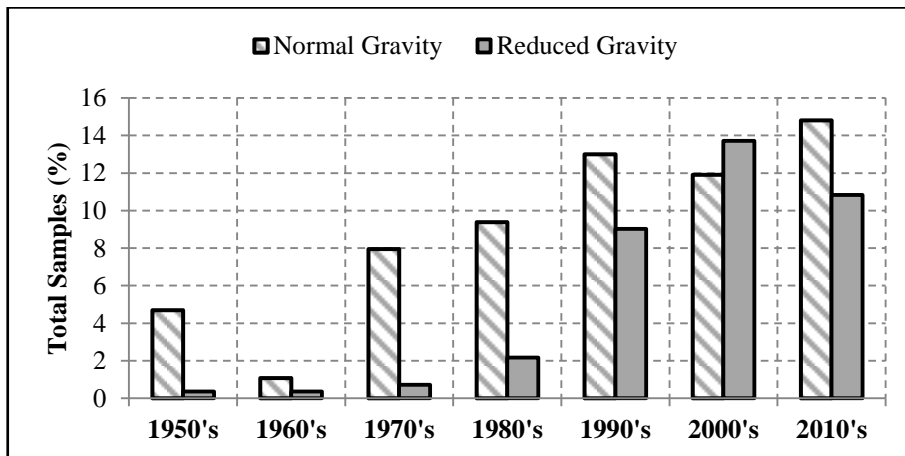
Figure 2-10: Comparison between the portion of research work on droplet combustion carried out under normal gravity and that carried out under reduced gravity conditions for the period 1949-2017.

Droplet combustion modelling, on the other hand, has encountered substantial developments since the earliest description and formulation of the D^2-law by Godsave and Spalding. New models have been – and are being – developed for more accurate description of the problem and precise evaluation of the corresponding parameters. These models commenced initially with the attempts to modify the D^2-law model. Initially, Goldsmith and Penner [108] modified Godsave's model by eliminating the unity Lewis number assumption, and using temperature dependent – rather than Godsave's constant –

specific heat and thermal conductivity. More generalized formulas for the transport properties are then set and used by Kassoy and Williams [54] for studying droplet combustion. Afterwards, different models are developed for studying droplet heating [40–45], ignition [43,53,109–113], extinction [109,110,114,115], and other aspects of droplet combustion.

However, droplet combustion investigation has not been limited to studying the combustion of isolated single-component fuel droplets. Instead, interacting droplet clusters and streams has also been investigated, in addition to the implementation of multicomponent fuels and fuel mixtures on an extensive number of droplet combustion studies. Despite the importance of the isolated, single-component fuel droplet combustion model in understanding the overall droplet combustion process and proving the classical theory of droplet combustion, but, the multicomponent fuel droplet and interacting multi-droplet combustion models are more realistic compared to the aforementioned model. Since, the majority of liquid fuels utilized in combustion applications are in fact mixtures of different components rather than a single component, and are burning in the form of sprays of a large number of droplets that are interacting together within the boundaries of the spray. Accordingly, further exploration of these two categories is believed to be helpful. Hence, detailed reviews of the multicomponent fuel droplet combustion and the combustion of interacting fuel droplets are outlined in sections (2.4) and (2.5) respectively.

2.4 Multicomponent Fuel Droplet Combustion

A large portion of fuels are utilized in the form of multicomponent fuels or fuel mixtures. These fuels are either initially produced in the multicomponent form (such as the diesel fuel), or prepared as multicomponent fuel mixtures prior to usage. These mixtures are either taking the form of blends (such as diesel and gasoline blending with alcohol), emulsions (as in the water-in-oil emulsions), or slurries (found in the coal/water mixtures).

Three main purposes are behind the use of fuel mixtures in combustion: the first is increasing the performance of the combustion system by the addition of higher heating value fuels. The second is reducing the harmful environmental impact of the conventional fuels. And the third is the depletion of the conventional liquid fuel resources. Hence, the components added to the conventional fuels are usually selected according to the above mentioned purposes, and have to fulfil the conditions of system performance, fuel

availability and sustainability, and better environmental impact. Accordingly, alcohols and biofuels are the most utilized fuels with the conventional liquid fuels in combustion applications, because of their evidenced soot and NOx reduction effects and relatively comparable combustion efficiency as those of the conventional liquid fuels.

In the multicomponent fuel mixtures, no chemical reaction will occur between the fuel constituents, and each constituent sustains its own physical and chemical properties. Therefore, the combustion of the resulting mixture is more complicated than the pure fuel combustion, because different components are burning simultaneously at the same point and instant of time. Hence, unlike the single component fuel droplet combustion – in which droplet evaporation is the rate controlling process – the multicomponent fuel droplet combustion encompasses the effect of droplet interior heat and mass transfer [116].

As a result, the multicomponent fuel droplet combustion is much more complicated compared to the single-component fuel droplet combustion. Firstly, the different constituents of the multicomponent fuel have different boiling points and different evaporation rates that leads to creating concentration gradients inside the droplet (in the liquid phase). Secondly, due to the boiling point gradient, a difference in volatility tendency is expected. Hence, the more volatile components tend to evaporate first until their concentrations are reduced, changing the concentration gradient inside the droplet. Lastly, the evaporation of the more volatile components reduces their concentrations but does not consume them completely. Thus, the remaining quantities of the highly volatile components tend to diffuse to the droplet surface due to their tendency of evaporation, and the less volatile components will tend to diffuse inward. This in turn, will create an internal circulation in the liquid phase, and will affect the evaporation rate of the droplet because of concentration difference on its surface along its lifetime [117]. Therefore, the main parameters that are affecting droplet combustion of the multicomponent fuels are: (i) the volatility and relative concentration of each of the constituents of the multicomponent fuel, (ii) the miscibility of these constituents, and (iii) the relative motion inside the droplet [4]. Each of these parameters has its direct effect on the resulting combustion behaviour of the multicomponent fuel. The volatility and concentration gradient of the constituents paly an essential rule in the circulation inside the droplet. The phase change characteristics within the liquid-phase of the droplet are controlled by the miscibility of these constituents on each other. Whereas, the relative motion inside the droplet will enhance evaporation on the droplet surface by assisting outward flow of the volatile components inside the droplet.

Accordingly, droplet combustion of the multicomponent fuels has been – and is being – investigated extensively both theoretically and experimentally for better understanding of the physical and chemical processes associated with this form of droplet combustion. Primarily, the multicomponent fuel droplet combustion investigation is carried out by Wood, Wise, and Inami [118] for evaluating the effect of changing fuel composition on the resulting burning rate of the fuel droplet. They have used heptane, trimethylpentane, and dibutyl ether all blended with butanol individually to form binary mixtures. From that time hitherto, the multicomponent fuel droplet combustion has been extensively investigated in an effort to comprehend its nature and understand the various associated processes. For instance, assuming uniform composition and temperature distributions within the droplet liquid-phase, Law [119] developed two theoretical models for describing the unsteady combustion of the multicomponent fuel droplet. However, the uniform composition distribution is unattainable in the real droplet combustion process.

On the other hand, Wang, Liu, and Law [116] characterized three distinct stages during the combustion of freely falling heptane/propanol, hexadecane/propanol, heptane/hexadecane, and propanol/water mixture droplets. These three stages are: the volatile component evaporation and consumption stage, the transition droplet heating stage, and the quasi-steady combustion stage. These stages have also been described by Niioka and co-workers [120,121] for fibre-supported heptane/hexadecane droplets burning in high pressure and high temperature environments respectively. And, described by Botero et al., [122] and Hoxie, Schoo, and Braden [99] during the combustion of freely falling diesel/ethanol and biodiesel/ethanol, and fibre-supported biodiesel/butanol blend droplets respectively. However, in certain cases these three stages are not distinctive, due to the relatively fast consumption rate of the volatile component, so that the combustion of the droplet will take the form of single-component fuels [59].

Additionally, different types of multicomponent fuel mixtures have been devoted for experimental studies. These include fuel blends that are either paraffin-based [59,98,116,120,123–127], diesel-based [99,102,122,128–132], and/or alcohol-based [116,129,133–136] mixtures; in addition to water-in-oil [125,129,137–143], oil-in-water [144–146], and alcohol/oil [124,147] emulsions; and liquid-solid mixtures [93,148–150] in which micro- and nano-particles are added to the liquid fuel for increasing its heating value and in turn enhancing its combustion efficiency.

Besides, different physical processes which are associated with the combustion of multicomponent fuel droplets have been the scope of a large portion of studies, such as the

puffing and microexplosion leading to droplet secondary atomization. These processes are initiating and occurring in the liquid-phase of the fuel droplet either in the surface or deep within the droplet internals, and are directly affecting the overall droplet combustion behaviour. Accordingly, further exploration of these processes is essential for more in depth understanding of the multicomponent droplet combustion. Hence, a review of the origins, physics, consequences, and the research work associated with these processes is outlined below.

2.4.1 Droplet Puffing, Secondary Atomization, and Microexplosion

Droplet microexplosion is defined as the prompt fragmentation of the multicomponent droplet as a result of nucleation and explosive boiling of the less boiling point component(s) [98,151]. If this fragmentation is less intensive and limited to part of the droplet, it is usually called as puffing. Though, Tsue et. al. [139] and Watanbe et al., [152], gave a more specific definition for droplet puffing, that is the process of vapour jet liberation form the surface of the multicomponent fuel droplet. This vapour jet is usually filled with finely small sub-droplets of the dispersed phase. The continuous phase may also detaches from the droplet surface in the form of ligaments or small size droplets as a consequence of an intensive puffing incident [153]. This detachment of ligaments and small droplets is called secondary atomization. Therefore, the secondary atomization is defined as the processes of droplet disintegration into smaller size droplets. This disintegration results when the dynamic forces acting on the droplet are higher than the restoration force of the droplet [154].

Puffing and microexplosion are direct results of the nucleation and bubble generation within the multicomponent fuel droplets. The occurrence of these processes during the multicomponent fuel droplet combustion is firstly described by Dryer and co-workers [123–125,155] who gave a general name for these processes that is the *disruptive burning* of the multicomponent fuel droplets. The same phenomenon has been distinguished by Avedisian and co-workers [64,126,147] for n-heptane based binary fuel mixtures including emulsions. Hoxie, Schoo, and Braden [99], Botero et al., [122], and Segawa et al., [145] have also described the occurrence of disruptive burning during the combustion of soybean oil/butanol, diesel/ethanol/biodiesel blends and n-hexadecane/water emulsion droplets respectively. Lasheras, Fernandez-Pello, and Dryer [124] studied the disruptive burning of

the ethanol/n-paraffin and n-propanol/n-paraffin binary solutions under atmospheric pressure. They found that droplet disruption results from the homogeneous bubble nucleation, expansion, and explosion inside the droplet. Recently, Avulapati et. al., [131] have studied the puffing and microexplosion occurrence during the droplet combustion of diesel/ethanol, diesel/biodiesel, and ethanol/biodiesel blends, in addition to a diesel-biodiesel-ethanol micro-emulsion. Whereas Zhang et al., [156] have investigated the puffing occurrence during the heating and evaporation of biodiesel/butanol fuel droplets. Numerical modelling on the other hand has also been performed for more detailed understanding of these phenomena. Watanabe et. al., [157] have developed a numerical model of emulsion fuel spray combustion with an emphasis on the puffing occurrence. Shinjo and co-workers have performed extensive numerical investigations on the dynamics of puffing and microexplosion during the evaporation of single fuel droplet [151], and a group of fuel droplets[158], in addition to the combustion of single and multiple fuel droplets [159]. They have made a detailed description of the initiation and development of puffing and partial microexplosion as shown in Figure 2-11. They have found also that the puffing intensity is a function of the size and depth of the bursting bubble.
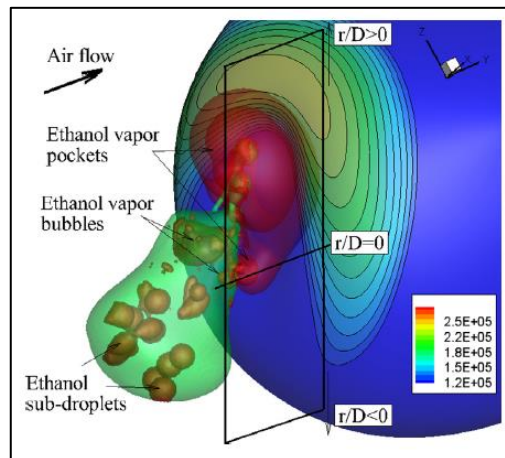
Figure 2-11: Puffing from an ethanol-in-decane emulsion droplet [159].

Watanabe and co-workers on the other hand, have conducted a series of experimental studies dedicated for characterizing the secondary atomization from emulsified fuels in the form of spray [160–162] and single-isolated droplet [160,163,164]. They have used shadowgraph imaging for tracking the secondary atomization occurrence from an evaporating water-in-n-decane emulsion spray and found the same puffing behaviour for the single droplet of 1 mm diameter and the spray of 50 µm average droplet size [161].

Furthermore, it is reported that droplet complete microexplosion occurs in a time interval less than 200 µs [4], and that this time scale is longer than the time scale available for the real spray combustion [151,161], therefore, this phenomenon has not much been the scope of experimental investigations. However, the total combustion time (in ms) inside a 4-stroke engine can be evaluated as a function of the rotational speed according to equation (2-12) [165]:

$$t = \frac{60 * 1000}{\left(N/2\right)}$$ .... **(2-12)**

The evaluated combustion time values for a range of engine rotation speeds are listed in Table 2-2. These time values are sufficiently enough for the real spray droplets to undergo heating, phase separation, and complete microexplosion, even at low possibilities. Therefore, further investigation of droplet microexplosion is required for comprehending the current understanding of this phenomenon.

Table 2-2: The total combustion time with respect to the rotational speed for a 4-stroke engine.

Engine Speed (rpm)	Total Combustion Time (ms)
1000	120
2000	60
3000	40
4000	30
5000	24
6000	20

In conclusion, a substantial number of studies have been conducted to explain the physics of puffing, secondary atomization, and microexplosion. As a result, the effects of these processes on the combustion efficiency by enhancing fuel evaporation and fuel/air mixing are well addressed. Additionally, the effect of nucleation and bubble growth in the droplet liquid-phase on the initiation and development of these processes is also established. Nonetheless, further comprehension of the physics of these processes including initiation and development is required. This can be executed by conducting a

magnified experimental visualization and tracking of the droplet liquid-phase for obtaining in-depth quantitative and qualitative description of these processes and the corresponding mechanisms.

2.4.2 Nucleation and Bubble Generation

Nucleation is defined as the appearance of the first forms of the new phase when a thermodynamic system undergoes phase change [166]. It is shown in the formation of bubbles in a boiling liquid, and ice crystals in the solidification of water. For boiling liquids, nucleation takes place due to the metastability of the liquid compared to its vapour. Liquid metastability results either from liquid superheating above its boiling point or expansion below the saturated pressure (the so called cavitation). Hence, the nucleation occurs due to the tendency of the liquid to retrieve equilibrium [167]. This form of nucleation arises within the bulk of the liquid and is known as the *Homogeneous Nucleation*. If the nucleation takes place at the liquid interface regions rather than the bulk, it is termed as the *Heterogeneous Nucleation* [168].

Despite its type and occurrence location, the most important parameter in nucleation is the nucleation limit – also known as the superheat limit – of the liquid. The nucleation limit in boiling is defined as the maximum temperature before the critical point at which the liquid maintains its phase without experiencing any phase change. The energy released from the vaporizing liquid at the nucleation limit is sometimes sufficient to create the so called *vapour explosion*. This explosion takes place as a result of either the thermal detonation waves resulting from energy release or due to the excessive bubble growth rate compared to the liquid response [169]. Hence, in the case of multicomponent fuel droplet combustion, the interior of the droplet is heated by convection and radiation from the surrounding flame and hot gases. Due to boiling point difference between the different components of the multicomponent fuel, the lower boiling point components become superheated. When the droplet temperature approaches the nucleation limit of that component, bubble nucleation takes place within the droplet liquid-phase leading to vapour bubble formation [168]. These bubbles move towards the droplet surface due to the density difference, and then burst outside the droplet by pressure difference across the bubble as shown in Figure 2-12.
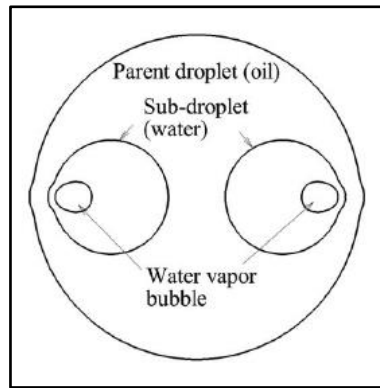
Figure 2-12: Schematic representation of the vapour bubble formation inside an evaporating water-in-oil droplet [151].

Bubble nucleation occurrence inside the multicomponent fuel droplets is important since it leads to enhancing liquid fuel evaporation and fuel air mixing, and in turn improving the combustion efficiency. The occurrence of nucleation within the burning droplet has been reported by Lasheras et. al., [123,124] during the combustion of binary n-paraffin mixtures. They have detected droplet size increase during droplet combustion and attributed it to the bubble formation. Chung and Kim [170] have also attributed the water sub-droplets increase within a water-in-dodecane emulsion droplet evaporating on a hot surface to the formation of water bubbles. They have detected the water sub-droplet increase by comparing droplet microscope images before and after heating. Wang, Liu, and Law [116] have also conceived bubble nucleation inside freely falling, burning, multicomponent fuel droplets, and evaluated the bubble growth rate and the bubble to droplet size ratio. Tsue et. al., [171] have imputed the microexplosion occurrence to the formation of water vapour bubbles inside the burning droplets of n-dodecane-in-water and n-tetradecane-in-water emulsions. Wang et. al., [172] have spotted heterogeneous nucleation occurrence as a result of trapped air bubbles inside the collision-merging methanol/alkane droplets. These air bubbles serve as nucleation sites inside the droplet. A more comprehensive theoretical description of the nucleation and bubble formation within emulsion fuel droplets is given by Shinjo et. al., [151,158,159]. They have shown that droplet puffing is the result of bubble growth inside the droplet as shown in Figure 2-13. Bubble burst at the droplet surface has also been described, and the effect of initial locations of the boiling bubble and the dispersed phase sub-droplet on the bubble burst intensity has also been evaluated.
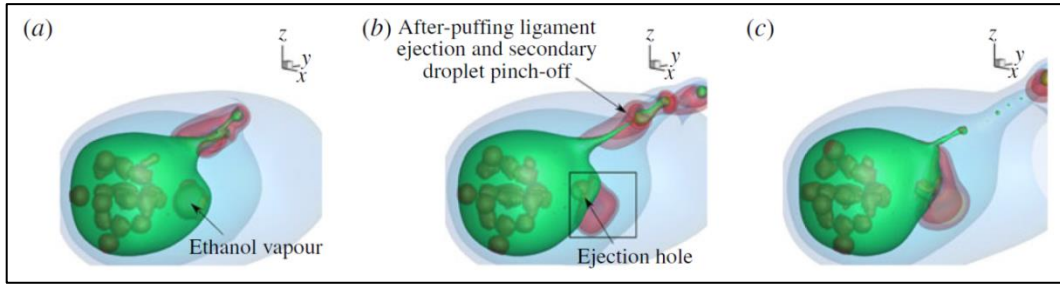
Figure 2-13: Theoretical simulation of the vapour bubble movement inside an evaporating ethanol-in-decane droplet [158].

From the above, it can be inferred that in almost all the studies, bubble nucleation has been reported and deduced with respect to droplet size increase. However, except the numerical simulation work performed by Shinjo et al., bubble nucleation initiation, growth, and its subsequent dynamics inside the burning multicomponent fuel droplet has not been well investigated. In particular, magnified experimental investigation of the droplet liquid-phase dedicated for studying bubble nucleation is not available. Therefore, part of the present work is devoted for conducting such experimental investigation for different multicomponent fuel droplets.

2.5 The Combustion of Interacting Fuel Droplets

The classical D^2-law of droplet combustion assumes isolated droplet combustion for neglecting the effect of interaction between the droplet and its neighbouring droplets. This assumption, in particular, is useful for simplifying the model but it is imprecise for real spray combustion applications. In the typical spray situations, there is a strong mutual interaction between the droplets in a specific neighbourhood and among the overall spray volume. This interaction is intensely affecting the ambient environment surrounding the droplets, and in turn affects the evaporation and burning rates of each individual droplet [117]. Hence, considering this interaction in the study of droplet combustion for spray applications is indispensable.

For investigation and problem characterization purposes, the multi-droplet interactive combustion is classified into three levels. The first level is termed as the *droplet array,* and involves the interaction of a few number of droplets within a specific space. In the second level of interaction, the number of droplets is higher, and is called the *droplet group*, whereas, the third level of interaction accounts for the entire spray [173]. In these

levels, the number of droplets and the spacing between them are the main effective parameters.
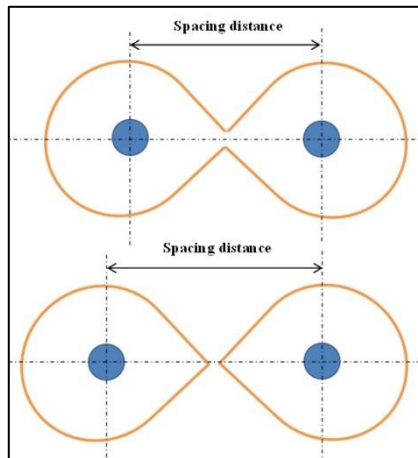
Figure 2-14: The effect of spacing between two-neighbouring droplets [173] (with permission from the publisher).

Droplet spacing is the distance between the centres of two adjacent droplets as shown in Figure 2-14. This spacing is crucial in deciding the shape and behaviour of droplet combustion. Where, there is a critical droplet spacing below which the adjacent droplets are burning in one envelope flame, whereas for higher values of the spacing distance each droplet will has its own surrounding flame as shown in Figure 2-14. The droplet spacing distance is usually normalized by and expressed in terms of the droplet diameter, for example, it is found that the ratio of the critical droplet spacing to the diameter of n-heptane droplets is about 17 [117].

The effect of droplet spacing on the combustion behaviour of the interacting fuel droplets has been widely investigated. It is found that increasing the droplet spacing will decrease the ignition delay time [174,175] and increase the flame spread [176] of the interacting droplets. The droplet burning rate on the other hand, is found to decrease by increasing the droplet spacing [134,177,178], however, it is claimed by Struk et al., [107] that this effect is relatively less significant. Accordingly, and in order to quantify more knowledge on its effect on the combustion of interacting fuel droplets, a relatively wide range of the droplet spacing distance has been tested and presented in literature. Table 2-3 shows the mostly used values of the normalized droplet spacing distance with the corresponding number of burning droplets as published in the literature.

Table 2-3: Selected published work showing the range of droplet spacing with the number of droplets.

Work performed by	No. of Droplets	Normalized Spacing Distance
Okai et al., [134,178,179]	2	2-6
Struk et al., [107]	2	5-20
Nomura and co-workers [176,180]	10	2-12.75
Kataoka et al., [181]	13	4-35
Segawa et al., [81,175]	49	3-16

As shown by the table, a variety of droplet numbers and normalized spacing distances are studied. However, the investigation on multiple droplets interaction is only devoted for the above mentioned parameters, while the effect of the mutual interaction between these neighbouring droplets has not been well addressed. Therefore, a magnified investigation of multiple droplets undergoing combustion is carried out in the present work as part of the understanding of the droplet dynamics during combustion.

2.6 Droplet Combustion Diagnostics

Even with the development in computation and numerical simulation, experimental investigation remains essential for understanding and explaining the effective parameters and related phenomena associated with the burning droplet along its overall lifetime.

Form the first experiments performed by Godsave in the early 1950's [37] to the present day, experimental investigation of the droplet combustion has been mainly carried out using optical diagnostic methods. This is because of the short combustion time available for experimentation, which requires a relatively fast response method for tracking the process. This is mainly offered by the optical methods compared to other non-optical techniques. Additionally, with the short droplet combustion time, it is impossible to track and explore the different processes associated with combustion. Instead, experimental data saving, and gradual tracking of the processes should be carried out for detailed investigation. Again, this is offered by the optical diagnostic methods, where the visual samples of the droplet combustion tests are saved in different forms (images, films or any other forms) for later investigation. All these, in addition to the non-intrusiveness and full reflection of the testing field led to the optical diagnostic methods are being the mostly implemented techniques for droplet combustion investigations.

However, some fine thermocouples are used in a number of experimental investigations for droplet temperature [143,149] and the surrounding gas temperature [99,182,183] measurements. Nonetheless, compared to the optical measuring techniques, these thermocouples suffer from the same drawbacks of the non-optical methods formerly mentioned [184]. This is especially when high sampling rates are required. Hence, the emphasis in the present work is on the fast, non-intrusive, optical diagnostic techniques. Further descriptions of the types and characteristics of these techniques are shown below.

2.6.1 Shadowgraphy

Shadowgraphy gives the main features of a subject without large modifications in illumination. This is because of the use of point-light source [185], and the projection of parallel light on the object under study and collecting the resulting shadow on a viewing screen [186]. The light spreading from the point source is collected by a lens that transfers it into a parallel light rays passing through the test object towards the second lens, and then to the viewing screen (or camera) as shown in Figure 2-15(a).
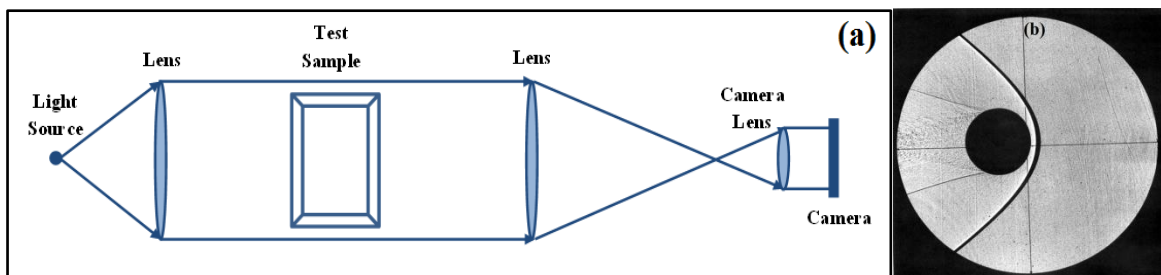
Figure 2-15: (a) Parallel light shadowgraph setup, (b) sample shadowgram of a spherical particle moving in stagnant air (reproduced from [185]).

This type of setup is termed as the *parallel setup*. If the two lenses are replaced by two concave mirrors, the resulting setup will take the z-like shape and termed as the *z-setup*, as shown in Figure 2-16(c). The light rays passing through the test object refract and deviate away from the original path. This deviation is displayed on the viewing screen as shown in Figure 2-16(c).

The shadowgraph imaging is invented by Robert Hooke in the seventeenth century [186], but its first scientific implementation for flow visualization is carried out by Vincenz Dvorak in the late nineteenth century [185,186]. He focused sunlight onto a 1 mm aperture and projected the diverging light onto a white wall in his darkened lab. Hence, the

refracted light rays appeared in the form of shadows on the white wall [186]. Dvorak then used this imaging method for describing different phenomena such as the convection from a warm hand and mixing in air and water.

Since then, shadowgraph imaging has been used extensively for studying different aspects of flow including fluid dynamics [187–190], heat transfer [191–193], and combustion [194–196]. Droplet combustion likewise, has been the scope of several experimental studies in which shadowgraphy is the principal visualizing technique. Kobayasi [197] used shadowgraph imaging for tracking and imaging both evaporation and combustion of 0.7-1.7 mm diameter droplets suspended inside a high temperature furnace. With the aid of the images obtained using this method, he was able to evaluate the burning rate of different single-component and multi-component fuels. Faeth et al., [198] used shadowgraphy at 100 fps imaging rate for studying the combustion of isolated decane droplets suspended inside a high pressure chamber. Tanabe et al., [199] utilized shadowgraphy at 250 fps with a laser light source for visualizing soot formation during the combustion of n-decane fuel droplet in a standing sound wave. A sample of the obtained images is shown in Figure 2-5. Some other experimental investigations of droplet evaporation [200] and combustion [143,201] have been carried out using shadowgraph imaging for tracking droplet size evolution.

2.6.2 Schlieren

Schlieren imaging is usually used for visualizing the flows with variable density gradients [202]. It is one of the most frequently used methods for visualization in aerodynamics and thermodynamics, because it combines both simplicity and high resolution [185]. Similar to shadowgraphy, the Schlieren imaging is based on utilizing a point-light source, and passing a parallel light rays through the test field. Besides, in the Schlieren method, a knife edge is ordinarily placed between the second lens (or mirror) and the viewing screen as shown in Figure 2-16. This knife edge is located at the focal length of the second lens (or mirror) and used for cutting off part of the illumination light and decreasing its intensity. This technique is developed by August Toepler in the second half of the nineteenth century for visualizing the flow within the compressible fluids. Although the first implementation of the knife edge in optical studies belongs to Leon Foucault in the same period [185,186,202].
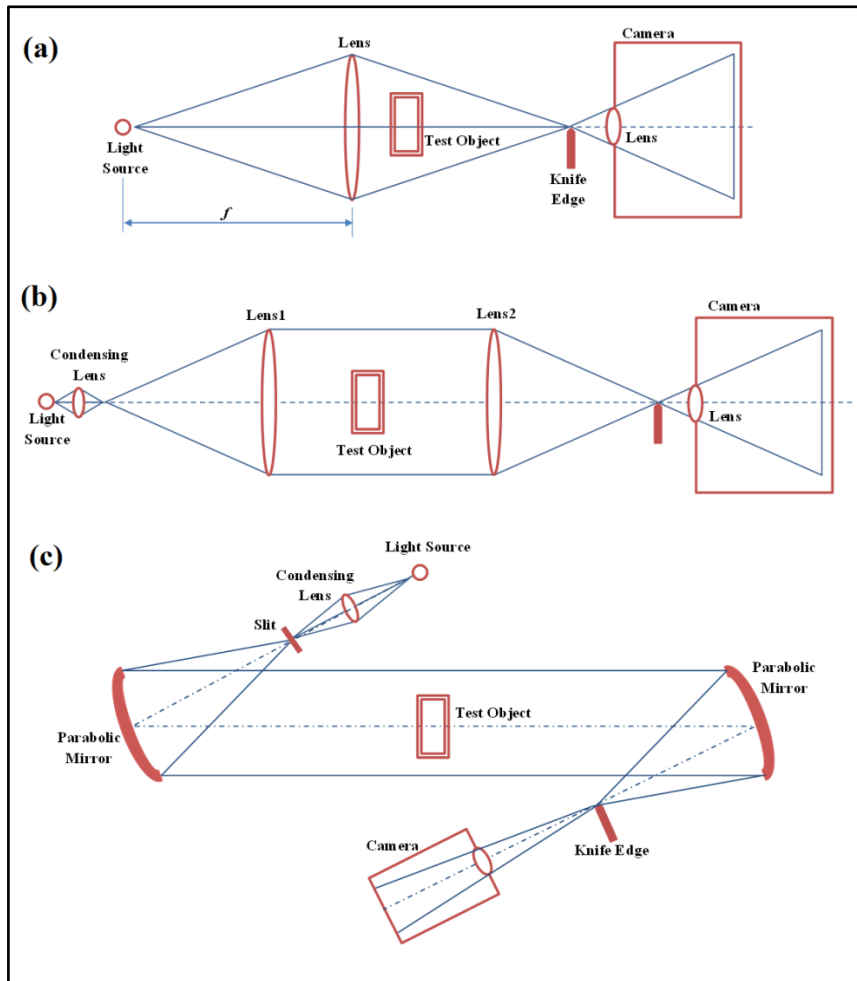
Figure 2-16: Schematic layout of three different Schlieren arrangements: (a) Single-lens, (b) Dual-lens, (c) Z-type two-mirror Schlieren (reproduced from [186]).

There are different types of Schlieren imaging according to the type, quantity, and arrangement of the optical components. These types include the *single-field-lens* Schlieren shown in Figure 2-16(a). In this arrangement a large diameter high quality lens is required for providing the adequate sharpness. Due to the use of a single lens, the illumination light is transferred passing the test object in the converging form rather than the parallel rays, which is disadvantageous in some applications [186]. This type is then modified to the *dual-field-lens* Schlieren shown in Figure 2-16(b). This type is the mostly used setup for Schlieren experiments due to its simplicity. It overcomes the light problem associated with the first type by providing parallel light rays through the test object. Additionally, a condensing lens is usually placed after the light source for increasing light effectiveness [186]. When the two lenses in the dual-field-lens Schlieren are replaced by two mirrors, the system will take the form shown in Figure 2-16(c), that is the *z-type two-mirror Schlieren*. Any type of mirrors can be used in this setup; however the concave mirrors are mostly

utilized. Despite its popularity in flow visualization experimental research, careful setup considerations are required for this type. Such as the minimum distance between the two mirrors that should be twice the focal length (*f*) for providing the proper size for the test object, and the optimum off-axis angle, for eliminating any optical aberration [186]. In addition to these types, more Schlieren arrangements are available in literature, such as the single-mirror coincident Schlieren, single-mirror off-axis Schlieren, and multiple pass mirror system [186].

Schlieren imaging is one of the first methods used and continued to be used for droplet combustion investigation. Kumagai and Isoda [65] carried out the first published experimental work on spherical droplet combustion under microgravity conditions created by the use of a falling chamber. They implemented the dual-field-lens Schlieren for tracking the combustion of n-heptane and ethanol fuel droplets. A spark light is used for illumination during the experiments. When the falling chamber reaches its optical axis, the spark light is activated by a photo-relay action. They have reported that the Schlieren method used was insufficient for tracking flame boundaries during droplet combustion; direct imaging is used in accordance for that purpose. This is in controversy with what is reported by Krier and Wronkiewicz [203] who used the same dual-field-lens Schlieren setup for studying the combustion of n-heptane and n-pentane fuel droplets. They reported the reason for using Schlieren imaging is the insufficient flame luminosity that makes it irrelevant for direct self-illuminated imaging, and invisible compared to the relatively high intensity illumination for backlighting imaging. Ogami et al., [204] used the z-type two mirror Schlieren for investigating 1-butanol droplet combustion under oscilatory flow, high pressure, microgravity conditions. A set of sample Schlieren images of their work is presented in Figure 2-17.
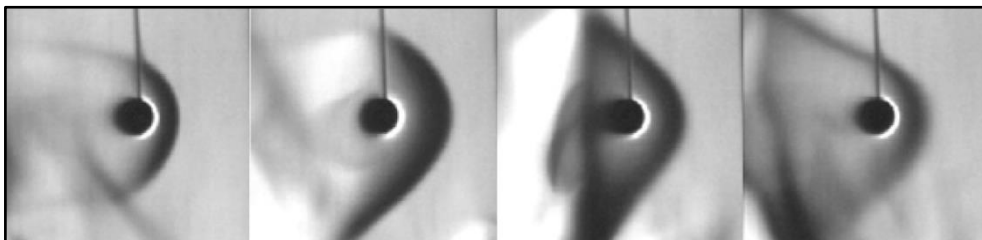
Figure 2-17: Sample Schlieren images of droplet combustion [204] (with permission from the publisher).

Illumination is executed by a xenon lamp, and camera framing rate is varied through the range of 250-1000 fps. This optical setup is the same as that used by Reichenbach et al.,

[205] – with carbon arc lamp as the light source – for studying droplet ignition and flame propagation within a linear n-octane droplet array in normal gravity. Camera framing rate is set to 200 and 400 fps. Okajima and Kumagai [69] used the single-mirror off-axis Schlieren illuminated by a mercury vapour lamp for visualizing the hot gas region during the combustion of ethanol, benzene, and n-heptane fuel droplets under zero-gravity conditions. Camera framing rate is set to 21 fps.

2.6.3 Laser-Based Techniques

The invention of laser in the sixth decade of the twentieth century led to the start of a new era in flow visualization and measurement. This is represented by the development of novel methods that are based on either light scattering, such as the Mie scattering and Raman spectroscopy, or laser-induced-fluorescence. In the majority of these systems, the laser beam is transmitted through the flow field in the form of a thin light sheet. This light sheet is either directly scattered by the particles or molecules in the flow, or absorbed by molecules which will fluoresce in accordance [206]. In both cases, the camera – that is usually placed perpendicular to the light sheet propagation plane – will capture the cross-sectional view of the flow field, from which both quantitative and qualitative investigations of the flow field characteristics can be performed. Nevertheless, the type of visualization method plays an essential role in deciding the type of information acquired from the flow field. Hence, in the next paragraphs, a brief explanation of the mostly utilised laser-based techniques with their working principles is carried out.

Laser Induced Fluorescence:

The Laser Induced Fluorescence (LIF) earliest implementation was in 1982. But, regardless of this relatively short history, the LIF techniques are now among the widely used tools for flow measurements [207]. The principle of flow measurement using LIF techniques is based on the fluorescence from atoms, molecules, or seeding particles when excited by the action of laser. The natural fluorescence of these atoms, molecules, and particles is originally weak, and it is enhanced by the energy of the laser. The intensity of this fluorescence depends on the number of the excited atoms, molecules, or particles at each testing condition. Hence, this intensity variation is the bases of the measurement using LIF methods, and is used mainly for measuring species concentration and field

temperature of the flow. However, with some specific arrangements of the system, it can be used for estimating the velocity and pressure distributions [207].

The LIF methods have been used for studying droplet combustion. Castanet, Lebouché, and Lemoine [208] used the two-colour LIF method for evaluating the temporal variation of droplet temperature with time during the combustion of monodisperse ethanol droplet stream. Pfeil et al., [209] used the *Planar Laser Induced Fluorescence* (PLIF) method for studying the effect of blending ethanol with ammonia borane on the droplet combustion of the resulting fuel mixture. The term PLIF is usually used for describing the LIF technique that is based on atoms and molecules excitation rather than seeding particles excitation [206]. Pfeil et al., used a 283.2 nm wavelength laser for exciting the OH radicals, so the method they used is termed as the OH-PLIF method. Beck, Koch, and Bauer [210] on the other hand, have used the CH-PLIF method, in which a 390.3 nm wavelength laser is used for exciting the CH radicals during the combustion of n-heptane fuel spray. Whereas, Burkert et al., [211] used a 353.373 nm wavelength laser for exciting the formaldehyde radicals in the Formaldehyde-LIF during the combustion of single gas-to-liquid diesel droplet. Additionally, the LIF method has been utilized for evaluating the temperature variation during droplet evaporation rather than combustion [212–214].

Laser Doppler and Phase Doppler Techniques:

The first invention of the laser Doppler systems was in the sixth decade of the twentieth century directly after laser invention, whereas, its first implementation for flow measurements was twenty years later. The phase Doppler systems, on the other hand, are first developed and used in the mid-nineties of the same century. Once they have been used, both techniques received increased attention, high reputation, and in accordance, continuous development among other measurement techniques. This is due to the relatively high accuracy, spatial and temporal resolution, and sensitivity to directional change [215]. The laser Doppler measurement principle is based on the Mie scattering effect. Hence, the flow is seeded by particles having flow ability, so that their movement is a reflection of the flow motion [216]. The light scattered from these particles – also known as the tracer particles – is used for measuring the velocity of the flow. This technique is therefore referred to as the *Laser Doppler Velocimetry* (LDV), or the *Laser Doppler Anemometry* (LDA). A monochromatic laser is usually used as a light source in the LDV systems. The laser beam first splits into two beams using a beam splitter as shown in Figure 2-18. The interference of these two beams crossing in the test volume creates a fringe pattern on the

phot detector. The velocity information of the moving tracer particles is obtained from the scattered field as a result of the Doppler effect [215].
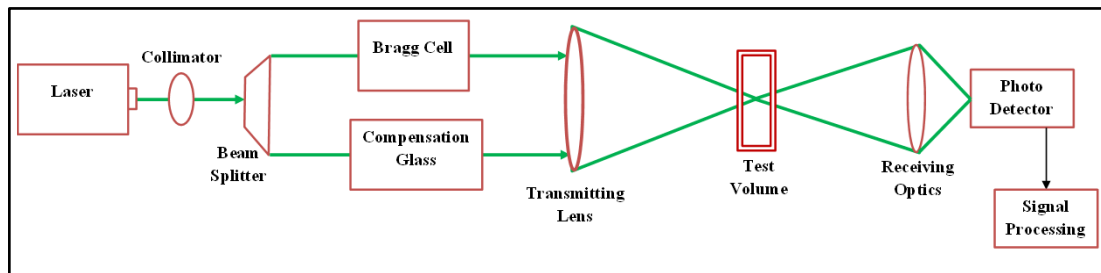
Figure 2-18: Schematic drawing of the dual-beam LDV system [215].

The phase Doppler measurement technique, on the other hand, is based on analysing the frequency shift of the light scattered from the tracer particles for evaluating the flow velocity. Hence, it is referred to as the *Phase Doppler Anemometry* (PDA). These particles are moving through the interference of at least two laser beams as shown in Figure 2-19, therefore, this method is sometimes referred to as the *Phase Doppler Interferometry* (PDI) [217]. The PDA technique is also used for evaluating the size of the particles within the flow, such as droplets, bubbles, and solid particles. This is carried out using the scattered light coming from two different directions. This light has a phase difference that is proportional to the size of those particles to be measured [217].
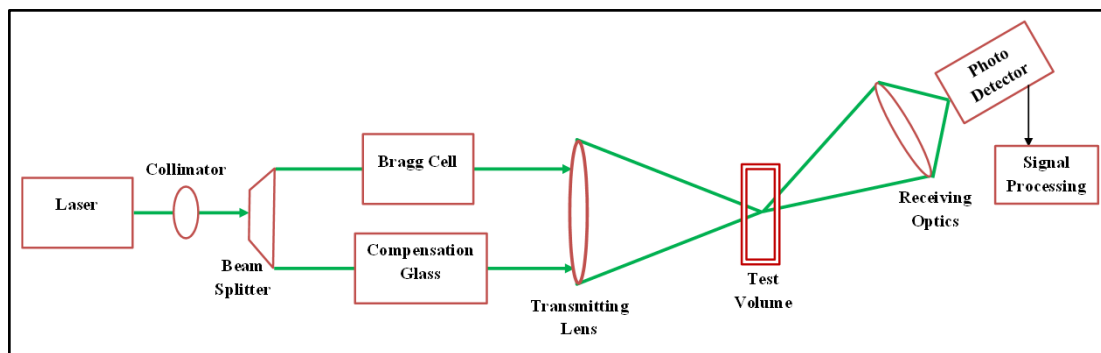
Figure 2-19: Schematic drawing of the dual-beam PDA system [215].

Accordingly, both the laser Doppler and phase Doppler techniques have been utilized in the droplet combustion studies. Kawazoe, Ohsawa, and Fujikake [218] used the dual-beam LDA system for evaluating droplet size and velocity of light oil fuel sprays burning inside two different types mini burners. A 5W argon ion laser (514.5 nm wavelength) with 10.01° cross-beam angle has been used for measurements. The covered cross sectional area

of the test volume is (1150 μm x 100 μm). Birouk and co-workers [219,220] utilized the LDA method for characterizing the turbulence intensity around isolated fuel droplets undergoing combustion. Standard pressure conditions are used in the first work, whereas high pressure conditions are applied in the second. They found that the turbulence around the burning droplet has a negligible effect on droplet burning rate under atmospheric pressure, however, this effect is found to increase under elevated pressure conditions. Sankar et al., [221] used the PDI system for measuring droplet size and velocity. They have implemented the PDI system as a part of an integrated diagnostic system including rainbow thermometer and point-diffraction interferometer for studying the combustion of an isolated n-heptane droplet in free fall. Castanet, Lebouché, and Lemoine [208] used the PDA method for evaluating the temporal variation of droplet size with respect to time during the combustion of monodisperse ethanol droplet stream.

Particle Velocimetry Techniques:

As the name manifests, the particle velocimetry methods are used for evaluating the velocity of the flow field. The working principle of these methods is based on seeding the flow to be visualized with tracer particles as show in Figure 2-20.
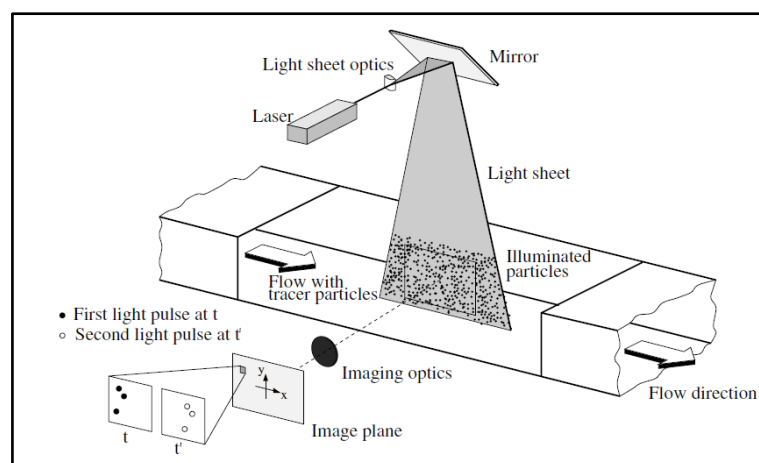
Figure 2-20: PIV setup for flow visualization in a wind tunnel [222].

These particles are illuminated by a laser sheet rather than laser beam for increasing the cross-sectional area of the flow field. The movement of these particles is tracked and recorded using an orthogonally (relative to the laser sheet) placed camera [222]. At least two successful images of the tracer particles at different instants of time are required for evaluating the velocity vectors of those particles [223].

The term particle velocimetry comprises different measurement techniques that share the same described working principle. However, the two main particle velocimetry techniques are the particle image velocimetry (PIV) and particle tracking velocimetry (PTV). The key difference between these two methods is the image-density number of the tracer particles. That is the number of particles in a test area representing the intersection of the laser sheet and a circle of diameter equivalent to that of a test area in the image projected into the fluid [224]. The image density number (N_I) is evaluated according to equation (2-13) as:

$$N_I = \frac{\pi}{4} C \Delta Z_0 \left(\frac{d_I}{M}\right)^2 \qquad \qquad \text{.........} \qquad \textbf{(2-13)}$$

where C is the average concentration of the tracer particles per unit volume, ΔZ_0 is the laser sheet thickness, d_I is the diameter of the test area, and M is the image magnification co-efficient. Hence, the particle velocimetry technique is characterized according to the image density number as follows [224]:

$N_I \ll 1$ →   Low density particles   →   PTV Method

$N_I \gg 1$ →   High density particles   →   PIV Method

The particle velocimetry techniques have been used for studying droplet combustion. Birouk and Toth [220] used the PIV technique for evaluating the turbulent integral length scale during the combustion of n-heptane and n-decane fuel droplets in a high pressure environment. Roth et al., [225] utilized the PIV method for evaluating droplet velocity during the combustion of upward flowing monodisperse droplet stream. Whereas, Nomura et al., [226] relied on the PTV method for evaluating droplet velocity during the combustion of partially pre-vaporized droplet stream. In addition, the PIV has also been used in the droplet evaporation studies [227–229].

2.6.4 Optical Interferometry

The wavelength of the visible light is relatively small; hence, any small alterations in the optical path will lead to measurable variations in the intensity of an interference pattern. Accordingly, highly accurate measurements are performed using the optical interferometry [230]. The first implementation of optical interferometry in the flow

measurement investigation was carried out by Ernst Mach in the late nineteenth century [185]. Interferometry is characterized by the formation of sufficiently visible interference fringes on the test section. This is due to the matching between the path lengths of the interfering light beams, so that the resulting difference in the path length is less than the coherence length [202]. The working principle of interferometry is based on the response to the change in the speed of light when passing different media. The interferometers respond directly to the refractive index of the media. The light passing through different fluids of various refractive indices will experience speed change and, in turn, phase shift. This phase shift is detected by the interferometers [202].

Different types of interferometers have been utilized in flow measurements, such as the Rayleigh interferometer, the Mach-Zeldovich interferometer, the Sagnac interferometer, and the Michelson interferometer [230]. The latter has been used by Moriue et al., [47] for studying the single droplet combustion of n-decane when diluted by 1-Methylnaphthalene and 1,2,4-trimethylbenzene. Using this method, they were able to detect the occurrence of cold-flame during ignition besides the hot-flame. The same interferometer is used by Tanabe et al., [82] for detecting the occurrence of cool-flame during the ignition of an isolated n-decane droplet. The schematic drawing of the working principle of the Michelson interferometer is shown in Figure 2-21.
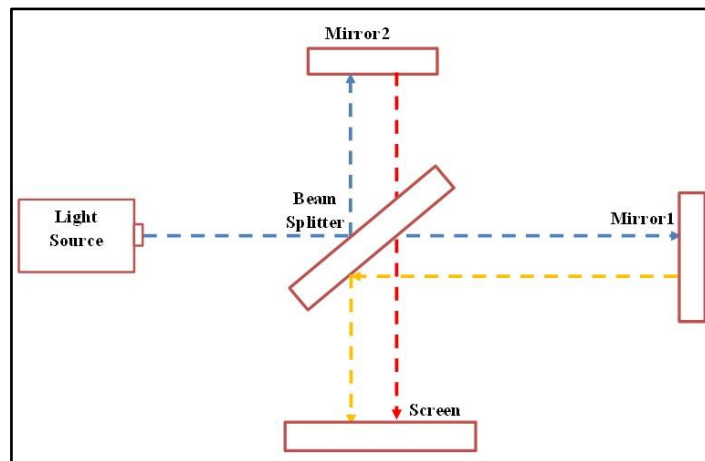
Figure 2-21: Michelson interferometer [230].

In this interferometer, a beam splitter is used for splitting the light emitted from the light source, and then combining the light reflected back from the mirrors as shown in Figure 2-21. Additionally, Sankar et al., [221] have used the point-diffraction interferometry (PDI) for evaluating the gas-phase temperature distribution during the

combustion of freely falling n-heptane droplets. As mentioned in section (2.6.3), Sankar et al., have used an integrated, laser-based, diagnostic system for complete investigation of the combustion of freely falling fuel droplets. The point-diffraction interferometer is a part of this system.

2.6.5 Self-Illuminated Direct Imaging

Direct imaging is one of the widely used imaging methods in droplet combustion. In this method the light emitted from the sooty flame surrounding the droplet is used for illumination. Hence, no external light source is required for droplet and flame illumination. Therefore, self-illuminated direct imaging is usually implemented for flame tracking purposes such as the work conducted by Mikami and co-workers for studying flame spread [231–233], and that performed by Marchese et. al., [74,234] for studying the emission of different radicals, and the flame intensity variation analysis used by Ambekar et. al. [26] for studying the droplet combustion of isopropyl nitrate blends as shown in Figure 2-22. As the figure shows, flame intensity is varying with the fuel mixture composition; therefore, it has been used for comparison between the different fuel mixtures.
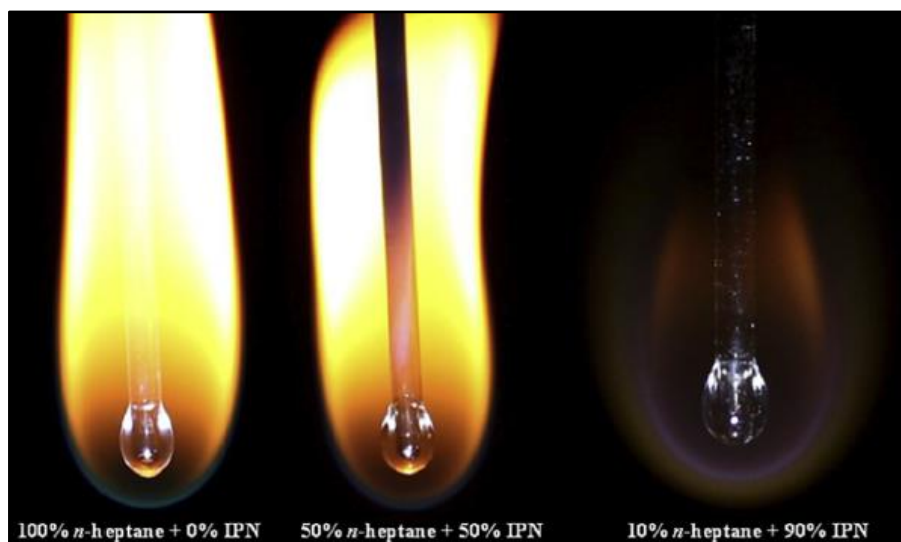
Figure 2-22: The burning droplet and the surrounding luminous flame tracking using self-illuminated direct imaging [26] (with permission from the publisher).

Furthermore, this imaging method is also used when the work is carried out in a limited space, so that no enough room for lighting source is available in the testing section. Therefore, the self-illumination provides the proper lighting required for imaging and

process tracking. Examples of that are the droplet combustion experiments inside a heated furnace conducted by Hoxie, Schoo, and Braden [99], and the micro-tube droplet combustion experiments carried out by Yao et. al., [235].

2.6.6 Backlighting Imaging

Backlighting (or backlit) imaging has been used extensively for tracking droplet size evolution during combustion. It is pursued by placing the droplet between the lighting source and imaging system as shown in Figure 2-23.
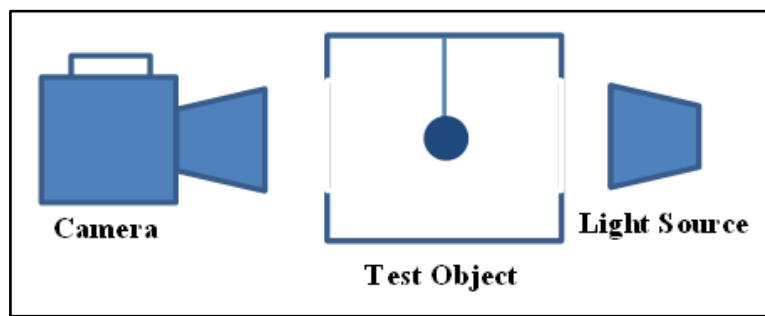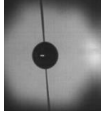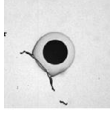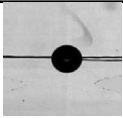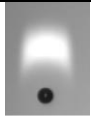
Figure 2-23: Schematic of the backlighting imaging arrangement.

This makes the droplet boundaries look sharp and ensures that they are easily distinguished, increasing the opportunities of tracking droplet lifetime and its size evolution rate more accurately. As a result, backlighting imaging has been implemented in the vast majority of droplet combustion experimental studies.

In view of that, it is aimed to find the backlighting imaging setup that provides the mostly proper magnification for the intended work. Therefore, samples of experimental studies with their representative images, in addition to the spatial resolution and the maximum obtained magnifications are shown in Table 2-4. The spatial resolution of the image is the ratio of the physical length to image pixels. The studies listed in Table 2-4 are selected because they include sufficient descriptions of the optical imaging setup characteristics. As the table demonstrates, the maximum obtained zoom is 10x of the original size despite the small spatial resolution values. These magnification rates are sufficient for precisely tracking the droplet surface boundaries, but not much helpful for droplet interior tracking.

Table 2-4: Samples of the spatial resolution and magnification ranges for droplet combustion shown in literature.

No.	Authors	Image Resolution	Spatial Resolution	Magnification	Sample Image
		(pixel*pixel)	µm/pixel	(X)	
1	Nomura et. al. [180]	1280*1024	6-10	10	
2	Liu et. al., [236]	580*580	32	---	
3	Wu and Yang [237]	800*600	22	4	
4	Han et. al., [132]	1024*1024	5.3	10	
Note: All the images in this table are used with permissions from the corresponding publishers.					

The only adequate magnification for droplet liquid-phase visualization was performed by Miglani, Basu, and Kumar [153] with 3.9 µm/pixel spatial resolution. They have used a microscopic lens attached to the high speed camera for studying the droplet combustion of a water/ethanol droplet blended with nanostructured ceria particles. A sample of the images obtained by them is shown in Figure 2-24.
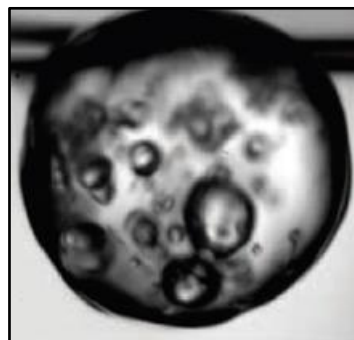
Figure 2-24: Sample of the images obtained by [153] (with permission from the publisher).

Ultimately, a variety of optical diagnostic techniques have been used for droplet combustion investigations. Each of which has its own features that makes it suitable for a specific function. Hence, for the formerly set objectives of magnified investigation of the

droplet liquid-phase dynamics, the most proper technique is found to be the backlighting imaging. However, some optical arrangements have to be performed for obtaining the maximum possible zoom for proper visualization of the droplet interior. Additionally, since secondary atomization involves sub-droplets emission away from the parent droplet, shadowgraph imaging is utilized for tracking secondary atomization from the droplet surface, also with proper magnification. Thus both backlighting and shadowgraphy are implemented for droplet combustion investigation in the present work.

2.7 Summary

In the previous discussions, a detailed description of the droplet combustion problem has been carried out. From which, a route map for the development of the current work's objectives has been outlined. These objectives are drawn from the motivations set in Chapter One. The importance of single droplet combustion in the study of the overall spray combustion is revealed. Then, a general review of the droplet combustion research development is facilitated. This review is converged to the combustion of multicomponent and interacting fuel droplets. These two categories are believed to be more realistic and close to the real spray combustion than the isolated single-component droplet combustion. Hence, investing in experimental research on those categories is substantial. Accordingly, the rest of the present work is dedicated to experimental investigation of the combustion of isolated and interacting multicomponent fuel droplets. An emphasis is placed on the droplet liquid-phase processes that occur during combustion. These include nucleation, bubble generation and dynamics, puffing and micro-explosion, secondary atomization and sub-droplet combustion.

Studying the liquid phase processes of the burning droplet requires a highly magnified visualization technique with very short response time for proper tracking of the different processes occurring at very short time spans. Consequently, a review is performed on the main diagnostic techniques utilized for droplet combustion investigation. With the aid of this review, high speed backlighting imaging found to be the most appropriate technique for tracking the liquid-phase processes of the burning droplet. With proper optical setup, and in conjunction with the high speed imaging, sharp, magnified, illuminated images of the droplet boundaries and interior will be acquired. Shadowgraph imaging, on the other hand, is found to be suitable for tracking the sub-droplets emitted by

secondary atomization, because it offers the option of magnified shadow images of the object with larger view field compared to the backlighting imaging technique. Therefore, both techniques are utilized in the present work with the aid of high speed camera for studying the combustion of multicomponent fuel droplet.

In the following chapters, detailed explanations of the experimental work carried out and the main findings with their interpretations and significance to droplet combustion and in turn, to the practical combustion systems will be presented. These are preceded by the experimental considerations and image processing methods which are explained in Chapter Three.

Chapter 3. Experimental Considerations, Image Processing, and Validations

3.1 Introduction

The present work is an investigation of the internal and external droplet dynamics during the combustion of multicomponent fuels. This investigation has been carried out experimentally with high speed imaging being the main technique for tracking droplet physics throughout its overall lifetime. Yet, there are some measures and processes applied before, during, and after the experimental work which should be outlined. Hence, this chapter is devoted for depicting these processes. The first of these processes is the multicomponent fuel preparation that is described in section (3.2). While the methods used for droplet generation, suspension, and ignition as well as the optical setups are clarified in section (3.3). Procedures and algorithms used for image processing owing to feature extraction are demonstrated in section (3.4), whereas section (3.5) shows the calibration for the true size calculations. Finally, a summary of the chapter is shown in section (3.6).

3.2 The Fuels under Investigation

Diesel fuel is of great importance in energy production by combustion. However, the major problem with diesel is the pollutant emissions during its oxidation, particularly CO and NOx emissions. This, in addition to the other problems associated with the fossil fuels such as depletion, price fluctuation, and increased energy demands, all together are playing a crucial rule in the future of diesel fuel utilization in energy production. Hence, a variety of solutions are explored and being explored for tackling – or mitigating the effect of – these problems. Blending the diesel with oxygenated fuels is one of the solutions used for decreasing CO emissions. Alcohols are the most famous oxygenated fuels that have been added to diesel in the internal combustion engines [238–243]. Alcohols are produced by vegetable and fruit fermentation which makes them renewable resources. However, the high latent heat of vaporization and low cetane number makes alcohols not sufficient for replacing the diesel completely [244]. This in addition to the harmful environmental and biological effects of alcohol presented in the formation of the photochemical smog and

high volatility of the alcohols [242]. Hence, blending diesel with alcohols offers the optimal solution rather than complete replacement.

Biodiesels on the other hand are presently the most widely attractive fuels for this objective due to various advantages; such as higher biodegradation, reduced toxicity, safe storage, and enhanced lubricity compared to the ordinary diesel fuels [245]. In fact, they are being increasingly utilized in gas turbine engines [246–248] in addition to the compression ignition engines [249–251]. Biodiesels are derived from animal fats or vegetable oils and are usually blended with diesel in different proportions and used without substantial engine modifications. This is due to the complete miscibility of biodiesel on diesel fuels [245]. However, compared to conventional diesel fuels, biodiesel has a higher viscosity that results in poor atomization characteristics [156,245], and higher NOx emission due to the increase in combustion efficiency and adiabatic flame temperature by the presence of oxygen in biodiesel [249,252]. Therefore, biodiesel addition to diesel in the form of blends is practically advocated than complete replacement.

Additionally, emulsifying the diesel by water has been used in an objective to decrease the NOx formation [253–257]. Water addition decreases the overall combustion temperature, which in turn reduces N_2 oxidation and NOx formation.

Accordingly, ethanol, biodiesel, and water have been selected to be added to diesel fuel for producing the multicomponent fuels in the present work. In addition to the above reasons of using these three additives, the difference in diesel miscibility of these liquids is considered. Biodiesel is completely miscible in diesel as stated above. Ethanol is partially miscible in diesel [240], that's why it is used in the form of blend and emulsion [244]. And water is immiscible in diesel. Hence, the effect of additive miscibility on diesel will also be considered in the present work. Therefore, the fuels utilized in the present work are:

- **Single Component (Neat) Fuels:**

These are the base fuels of the multicomponent fuels. Three single fuels have been used in the present work. These fuels are:

  - *Diesel*: it is the base fuel in the present work. The type of diesel used in the experimental work is the regular *Shell Diesel Fuel*.

  - *Biodiesel*: it is a B-100 *Petrobras* biodiesel. It is produced from both tallow and soy with a composition of 40% and 60% by volume respectively.

  - *Bioethanol*: it is a *Biofuel-500 Gardeco* plant-based ethanol produced by industrial distillation.

- **Multicomponent Fuels:**

- *Emulsions*: two types of emulsions have been prepared in-lab and used for studying droplet combustion. These emulsions are *Water-in-Diesel* and *Diesel-in-Water* emulsions. Further discussions on the emulsification process and concentration proportions are outlined in section (3.2.1).

- *Blends*: two types of blends have been prepared and implemented for experimentation. These are the *Biodiesel/Diesel*, and *Bioethanol/Diesel* blends. The blending process and proportions of constituents are further clarified in section (3.2.2).

3.2.1 Diesel Fuel Emulsification

The *emulsification* is the process of blending two (or more) immiscible liquids, with the aid of an emulsifier (or surfactant agent) [258]. For water-in-diesel emulsions, the water is added to the diesel so that the former is the dispersed phase and the latter is the continuous phase [151]. This is exactly the opposite in the case of diesel-in-water emulsions, where diesel is the dispersed phase and water is the continuous phase [258]. An illustration of the structure of the two emulsion types is shown in Figure 3-1.
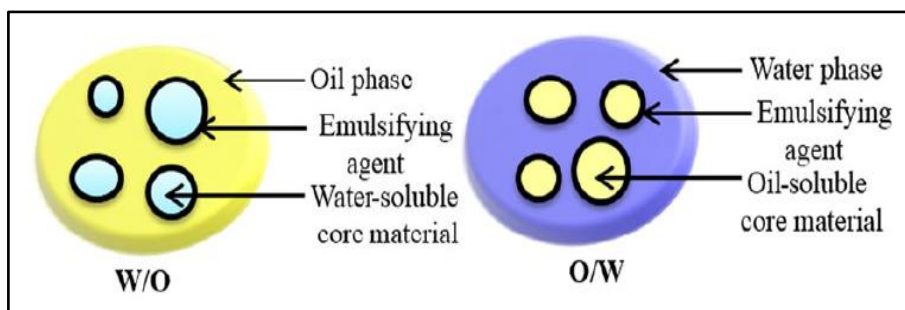
Figure 3-1: The difference between the water-in-oil and oil-in-water emulsions [259] (with permission from the publisher).

These two types of emulsions have been prepared and tested in the present work. The reason behind using them is to investigate the effect of emulsion type – in addition to the concentrations – on the behaviour of the droplet during combustion. Since, the ratio of the densities of both the dispersed phase and the continuous phase is found to influence the rate of nucleation within the emulsions [260]. This in turn, will have an effect on the droplet combustion behaviour. For that reason, further investigation on this point is

supposed to be worthy. The preparations of these emulsions in addition to the criterion followed for emulsifier selection are all discussed below.

3.2.1.A Emulsifier Selection

Since emulsions are mixtures of two (or more) insoluble liquids, they are thermodynamically unstable. This instability comes from higher free energy of the mixture by surface energy compared to other mixtures. Therefore, droplet coalescence inside the emulsion will occur so as to minimize the surface area while maximizing the volume. This in turn leads to phase separation within the emulsion. Consequently, producing a long-lasting emulsion requires a third agent that accumulates at the interface between the two liquids forming the emulsion; this agent is the *emulsifier (or surfactant)*. The rule of the emulsifier is to form protective, elastic, and relatively strong film layer that can withstand droplet collision and prevent phase separation. However, the type of emulsifier is an essential parameter in defining the type of emulsion. Hydrophilic emulsifiers prompt the formation of oil-in-water emulsions, while water-in-oil emulsions are mostly produced by the use of lipophilic emulsifiers [261]. This is known as *Bancroft's Rule* which states that "*the phase in which the surfactant is more soluble is the continuous phase*" [262]. This solubility inclination is characterized by the Hydrophile-Lipophile Balance (HLB) number. The HLB number is developed by Griffin as the balance of the size and strength of both the hydrophilic and lipophilic groups within the emulsifier molecules [263]. Hence, each emulsifying agent has its own HLB number which is in the range of 0 to 20, and this number defines whether the emulsifier is oil-soluble or water-soluble as shown in Table 3-1.

Table 3-1: HLB ranges and applications [261].

$0 \leq HLB \leq 9$	oil-soluble emulsifiers	for producing water-in-oil emulsions
$11 \leq HLB \leq 20$	water-soluble emulsifiers	for producing oil-in-water emulsions
$HLB = 10$	hydrophilically-lipophilically balanced emulsifier	

Consequently, in the present work two emulsifiers have been selected for emulsion preparation. The first is the Polysorbate 80 (HLB = 15) for making the diesel-in-water

emulsions, and the other is the Sorbitan Mono Oleate (also known as Span 80) (HLB = 4.3) for making the water-in-diesel emulsions.

3.2.1.B Emulsion Preparation

In principle, emulsification is the process of mixing two (or more) liquids that are originally immiscible. Thus, the main task in the emulsification process is to finely disperse one of the liquids into the other. Therefore, the majority of practical emulsification techniques depend on the dispersion method and the application of mechanical energy to the system. When the disperse phase is exposed to a high velocity gradient, the droplets within will break up into smaller sub-droplets.

The water-in-diesel and diesel-in-water emulsions have been prepared in the lab prior to the combustion experiments. The method followed and described by Califano, Calabria, and Massoli [143] and Jackson and Avedisian [147] has been used for preparation. For each of the emulsions, the emulsifier is added to the continuous phase (diesel in the case of water-in-diesel emulsions, and water in the case of diesel-in-water emulsions) with a quantity less than 1% of the mixture volume. The emulsifier and the continuous phase are then stirred for ensuring solubility. The required quantity of the dispersed phase (water in the case of water-in-diesel emulsions, and diesel in the case of diesel-in-water emulsions) is then added gradually to the mixture. A 20000 rpm electric hand blender has been used for mixing the liquids for more than five minutes until a homogeneous milky white liquid is produced. The interpretation of emulsion colours is shown in Table 3-2. From the table, it is implied that the obtained emulsions are the coarse macro-emulsions with 3-100 μm disperse phase particles.

Table 3-2: Size range and appearance of emulsions [261].

Disperse Phase Particle Size (μm)	Emulsion	Appearance
0.001-0.003	Molecular Solution	Transparent
0.003-0.01	Micellar Solution	Transparent
0.01-0.1	Micro-Emulsion	Translucent
0.1-3	Fine Macro-Emulsion	Blue-White
3-100	Coarse Macro-Emulsion	Milky White

Water content in both emulsions has been fixed to 10%, 20%, and 30% of the total emulsion volume, and the remaining part is diesel. Figure 3-2 shows the samples prepared

in the lab prior to experiment. However, diesel-in-water emulsion of 40% water content has also been prepared, and many trials for igniting the droplet have been carried out, but without any success.

Finally, it is worthy to mention that for every new test, a new emulsion sample is prepared and tested. Hence, these samples are kept in small containers, and during the testing period no visible changes have been observed.
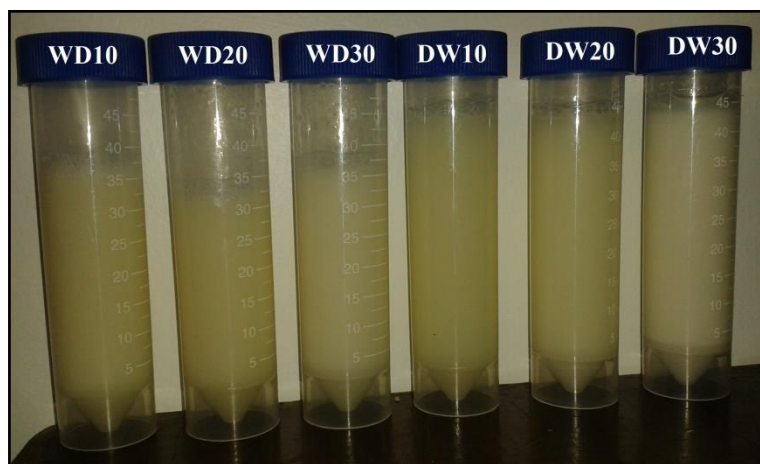
Figure 3-2: Prepared samples of water-in-diesel and diesel-in-water emulsions of 10%, 20%, and 30% water concentration.

3.2.2 Diesel Fuel Blending

Fuel blending is defined as the process of adding hydrocarbon fuels, additives, and/or other compounds to the base fuel in the form of mixing at different proportions to produce a final fuel of specific performance characteristics [264]. In the present work, *Biodiesel-in-Diesel* and *Bioethanol-in-Diesel Blends* have been prepared in-lab. For each blend, three blending proportions are used, in which diesel accounts for (90%, 80%, and 70%) of the total mixture volume, and the added fuel accounts for the remaining (10%, 20%, and 30%) respectively. These proportions are selected in accordance to those corresponding values of diesel emulsions. This ensures relatively comparable results.

Concisely, fifteen different liquid fuels have been utilized in the experiments of the present work. Three of them are single-component fuels, and the rest are multicomponent ones. A complete list of these fuels is shown in Figure 3-3, and their abbreviations and physical properties are shown in Appendices (A) and (B) respectively.
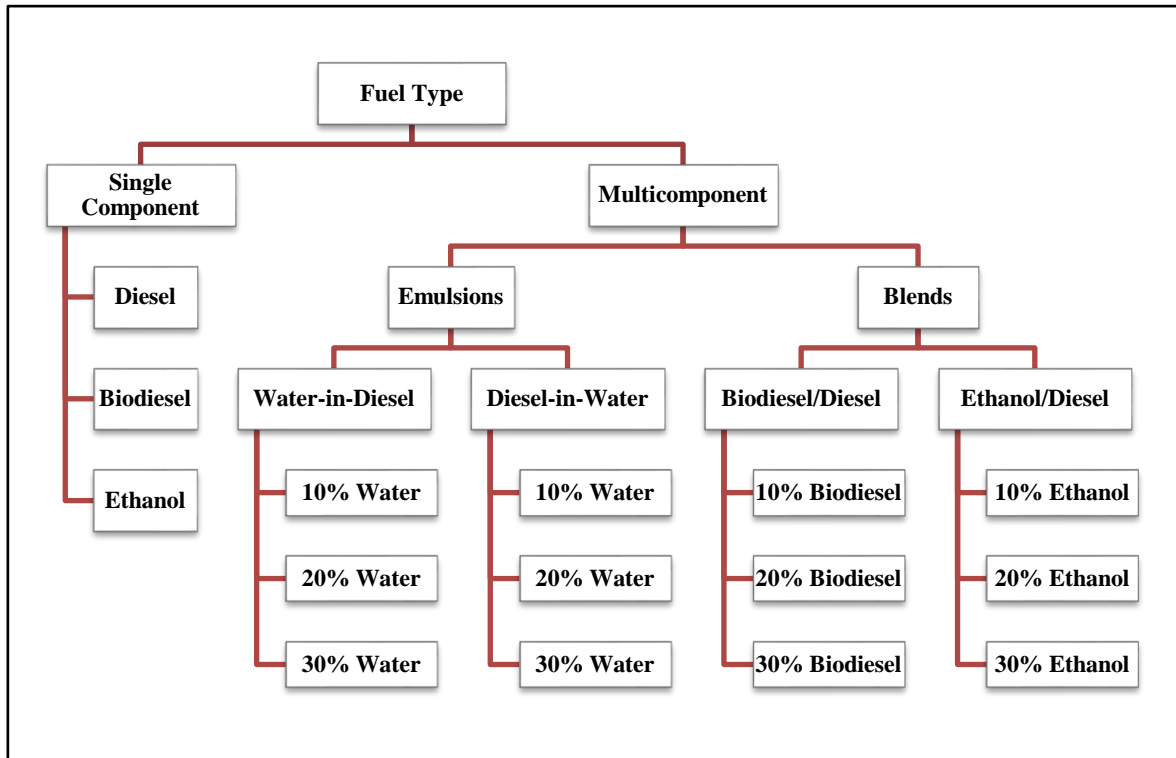
Figure 3-3: A chart of the fuels utilized in the present work.

3.3 Experimental Characterizations

The experimental work carried out during the course of the present work will be described in detail in the forthcoming chapters. Nevertheless, a brief characterization of the key instruments and processes implemented in experiments is found to be important. These include droplet generation and suspension, droplet ignition, and the optical setups for each test.

3.3.1 Droplet Generation, Suspension, and Ignition

Three major techniques are usually used for single droplet combustion investigations [265]. These techniques are shown in Figure 3-4.

In the first technique (Figure 3-4(A)), the fuel is introduced through a porous spherical structure to create a thin layer of fuel that is consumed during combustion. This technique has been used by [266–272] for studying flame structure throughout droplet combustion of different fuels.

Figure 3-4(C) shows the third technique in which the droplet is set to fall freely during combustion. This technique is used for studying the combustion of very small droplets analogous to the real size droplets as it is shown in [116,122,129,269,273–276].
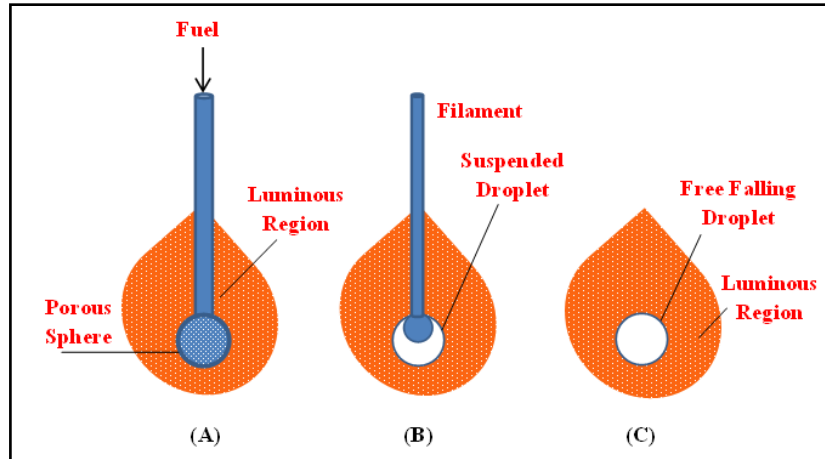
Figure 3-4: Laboratory fuel droplet generation and combustion in an oxidizing atmosphere: (a) porous sphere method, (b) suspended droplet method, and (c) falling droplet method (reproduced from [265]).

Figure 3-4(B) shows the second technique, that is droplet suspension on a thin filament. This technique is the most used among all methods, since it offers a relatively fixed droplet position for easier and more precise lifetime and burning tracking. Additionally, studying multi-droplet combustion in the form of an array is conceivable using this method. The filament may take the form of a single fibre [84,86,277,278] or a mesh of two-cross-shaped fibres [64,232,279,280], and it may be in different sizes ranging from (12 μm) to (250 μm).

For the present work, droplet suspension method is implemented for fixing the droplet. Because, studying the droplet liquid-phase dynamics requires the droplet to be fixed in a certain position so that it will be at the camera view field during its whole burning time without any fluctuation or outsized movement. This is ensured by droplet suspension. For the same reason, the droplet is required to be large in size for easier tracking of the internal processes that occur during combustion. Accordingly, increasing droplet size makes it difficult (if not possible) to use very thin filament (<50 μm) for suspending the droplet. This is proven by trials and evidenced by comparison with Liu et al., [281] who have used 14 μm fibre mesh for droplets with diameters less than 1 mm and 80 μm fibre mesh for droplets with diameters larger than 1 mm. Therefore, higher size filaments are required, with the need to keep this within the minimum possible limit.

Hence, a 100 µm diameter fibre is found to be proper for suspending the droplet in the present work.

On the other hand, careful selection of the filament material has also been considered. It is obvious that any material to be suitable for droplet suspension during combustion should have a melting point higher than the flame temperature (i.e. > 2000K in average). Silicon carbide (SiC) fibre (whose melting temperature is around twice the flame temperature) is found to be suitable for droplet suspension, especially with the fact that its effect on droplet burning rate is reported to be negligibly small for larger droplet diameters [281,282].
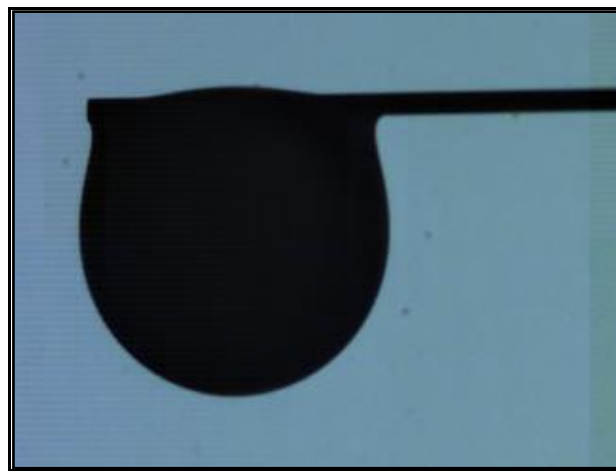
Figure 3-5: Droplet suspension using a single (100 µm) monofilament SiC fibre.

Consequently, the SiC fibre has been implemented for droplet suspension in the present work. It has been used in the form of a single monofilament of (100 µm) diameter. This fibre consists of 95 µm silicon carbide enforced by a 5 µm Tungsten core to increase its strength. Hence, this offered the privilege of suspending the droplet without being bent as shown in Figure 3-5.

Figure 3-6: Micro-fine syringe with hypodermic needle for droplet generation.

Droplet generation on the other hand, is performed using a micro-fine syringe with hypodermic (0.33 mm) diameter and (12.7 mm) length needle as shown in Figure 3-6. A relatively constant amount of fuel volume is injected every time for generating and suspending the droplet on the SiC fibre.

The initial diameters of all the droplets generated and adopted in experiments are evaluated using image processing and shown in Figure 3-7. As the figure shows, 302 sample droplets have been generated and used in experiments. 84% of these droplets are of initial diameter in the range of 1-1.4 mm, while the remaining 16% counts for the droplets that are outside this range ($0.8<D_0<1$ and $1.4<D_0<1.6$ mm respectively). The average diameter of all the droplets is evaluated to be 1.207 mm with a standard deviation of 0.269. Therefore, a relatively high repeatability is obtained using the micro-fine syringe for droplet generation. Although, this is a relatively large droplet size compared to the real size in practical applications. But, it is essential for visualizing and tracking the liquid-phase processes.

(a)   **(b)**
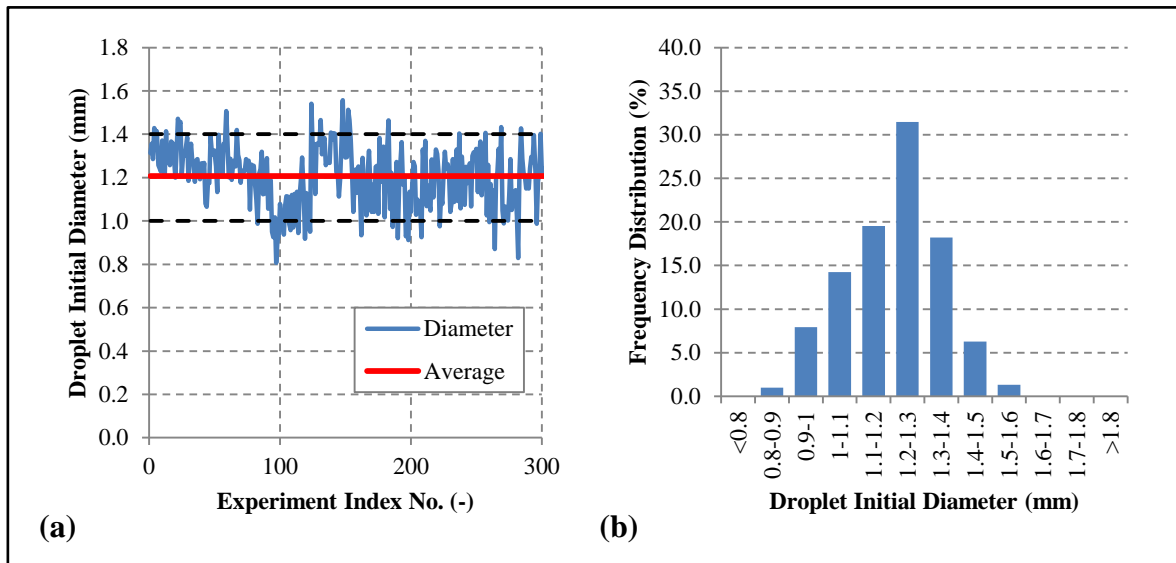
Figure 3-7: (a) The initial diameter of all the droplets adopted in experiments, (b) the frequency distribution of these diameters.

Additionally, it is worthy to point out that the use of droplets with relatively large sizes is prevalent in the experimental investigations of literature of droplet combustion. Figure 3-8 presents some representative samples of the large size droplets (above the real droplet size range) with respect to the publication year of the work. Despite the extensive

number of work carried out on large size droplets, only the largest size samples are selected for each year, since the figure is made for demonstration purposes only.
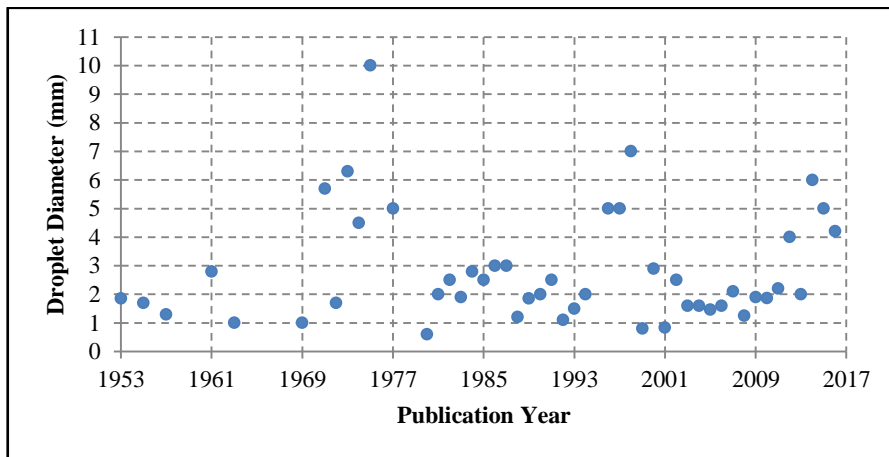
Figure 3-8: Representative samples of the large droplet initial size diameter range implemented in the literature of experimental droplet combustion.

As it is shown by the figure, the large size droplets are used in the past and being continually used in present for droplet combustion investigations. Since, it is easier to generate and investigate a larger droplet compared to the real size one. For that reason, the droplets generated and investigated in the present work are larger than the real droplet size.

However, as it will be shown in the next chapters, all the studied characteristic parameters are normalized with respect to the initial droplet diameter. This is to ensure a minimum effect of the droplet size variation on the studied parameters.

Eventually, droplet ignition has been carried out using the hot wire ignition method. Hot wire ignition is widely used for igniting the droplet in experimental work, for example those carried out by [99,150,180,283]. In the present work, two hot wire techniques have been attempted. The first is using the SiC fibre as a hot wire. This is carried out by heating the fibre on the side far from the droplet suspension location as shown in Figure 3-9. After the droplet is suspended, a butane flame is placed below the fibre 5 mm away from the droplet. This point is selected to keep the effect of the butane flame on droplet combustion to minimum. This includes preventing any form of interference between the butane flame and the flame surrounding the burning droplet. The heat generated in the zone above the flame is transferred quickly by conduction to the part suspending the droplet. This is due to the relatively high thermal conductivity of the SiC fibre. The butane flame is then removed after the droplet is ignited. The resulting ignition delay time using this method is estimated

to be in the range of 150 ms. This comprises the time period from placing the flame under the fibre to the first appearance of the visible flame around the droplet.
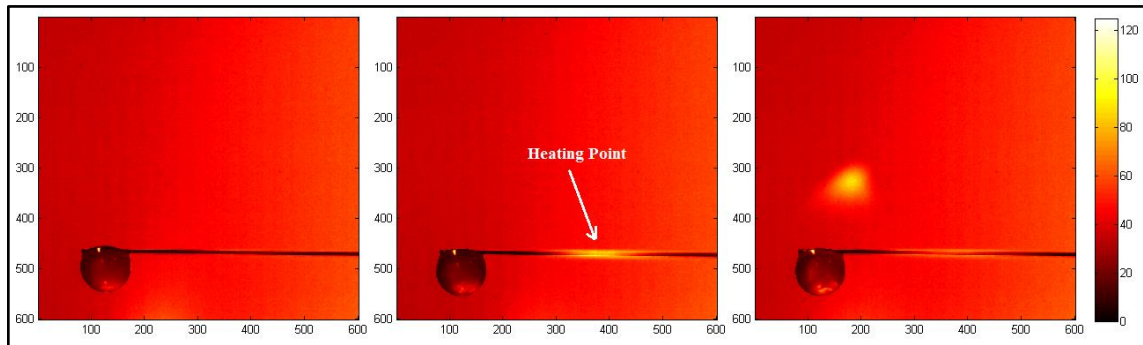
Figure 3-9: Droplet ignition by side heating of the SiC fibre. The legend in the figure represents the pixel intensity distribution.

The second hot wire ignition method applied in the present work consists of using an electrically heated kanthal wire coil as shown in Figure 3-10. The kanthal wire coil is first heated using a 28.5 W electric power supplied by 3.96 V DC power supply. The wire is then set below the droplet at a distance of 1.5 mm from the SiC fibre. It is then removed quickly after the droplet is ignited. The ignition delay time using this method is estimated to be about 50 ms, which is one-third that of the SiC fibre side heating.

Both methods are found to produce a reliable and repeatable droplet ignition for all the tested fuel droplets. The droplet initial diameter, for both ignition methods, is evaluated at the first image preceding the appearance of the visible flame around the droplet.
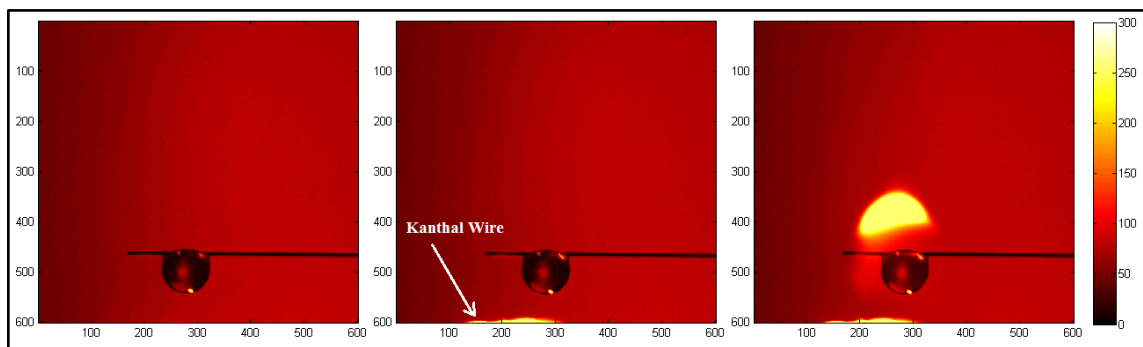
Figure 3-10: Droplet ignition using an electrically heated kanthal wire coil. The legend in the figure represents the pixel intensity distribution.

3.3.2 Optical Setups

Every measuring technique has its own capabilities and limitations that make it appropriate for a certain task rather than others. Therefore, a careful selection of the technique is essential for the outcomes required from the investigation. In the present work, the physical processes associated with droplet combustion of the multi-component fuel are investigated using high speed imaging. However, these processes are dissimilar to each other; some take place inside the droplet such as nucleation and cavitation, while others occur on the droplet surface like secondary atomization. Some of the processes are macroscopic such as droplet shape and size change during its lifetime, whereas some are relatively microscopic and require magnification for proper tracking such as the bubble growth and movement. Therefore, using a single imaging technique is not appropriate for studying these phenomena simultaneously. Thus, two imaging techniques have been employed sequentially in the present work for studying droplet combustion at different focusing levels. The techniques are the backlighting and shadowgraph imaging techniques which are presented below with a description of their major optical components whereas the full experimental setups and their descriptions are presented in the corresponding chapters.

3.3.2.A Backlighting Imaging

Backlighting imaging has been employed in the present work for obtaining sharp edges of the droplet boundaries in addition to focused imaging of the droplet internal dynamics. The major components of the optical setup for backlit imaging are shown in Figure 3-11. A 55mm Macro Extension Tube Set (a) is mounted between the high speed camera and the Nikon AF Micro NIKKOR 60mm f/2.8D Lens (b) for achieving the required magnification. An LED illuminator (d) is used for generating the backlight needed for imaging. In order to decrease the light intensity, a translucent white light diffuser (c) is mounted between the light source and droplet. Two types of LED illuminators have been used in experiments. The first is a 6-Volt, 72-LED domestic illuminator that is used for droplet size tracking at low framing rates. Whereas the second is an IDT 19-LED, 48-Volt, 200 Watt, high intensity illuminator which has been used for high frame rate imaging that requires intensive lighting.

Figure 3-11: Components of the optical setup used for backlit imaging of the droplet combustion: (a) Extension tube, (b) Lens, (c) Light diffuser, (d) Light source.

Using this optical setup, 20x and 30x magnification rates are achieved successfully. Hence, the ability of tracking the various dynamic processes inside the droplet throughout its overall lifetime is enhanced.

3.3.2.B Shadowgraph Imaging

Shadowgraph imaging has been implemented in the present work for tracking the puffing, microexplosion, and secondary atomization and sub-droplet emission during the combustion of the multicomponent fuel droplets. The optical components used for building the shadowgraph optical setup are shown in Figure 3-12.
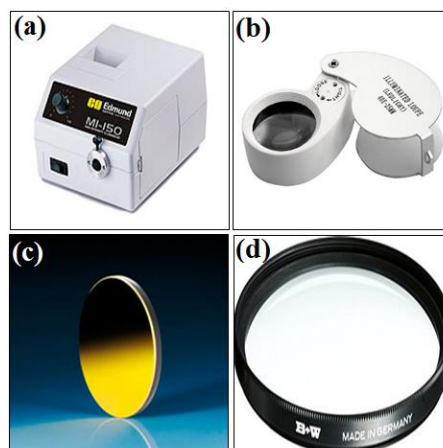
Figure 3-12: Components of the optical setup used for Shadowgraph imaging of the droplet combustion: (a) Light Source, (b) Magnifying Lens, (c) Concave Mirror, (d) Close-up Lens.

In this setup, light intensity is increased by mounting a Trixes 40x 25mm loupe eye magnifier lens (b) in front of the 150W halogen, Dolan-Jenner MI-150 fibre optic high intensity illuminator (a) that is used as the light source. Light is then reflected by two (75 mm diameter, 7 mm thick, 750 mm focal length) concave spherical mirrors (c) into a Hoya 49 mm Close-up lens (d) before which the droplet is mounted. This optical setup for shadowgraph imaging resulted in a (10x) magnification rate. Again, this has given the possibility of tracking puffing and secondary atomization and droplet size variation using shadowgraph imaging. The 10x, 20x, and 30x magnification rates have been schematically presented in Figure 3-13 to demonstrate the degree of amplification in the droplet recorded size compared to the real size.
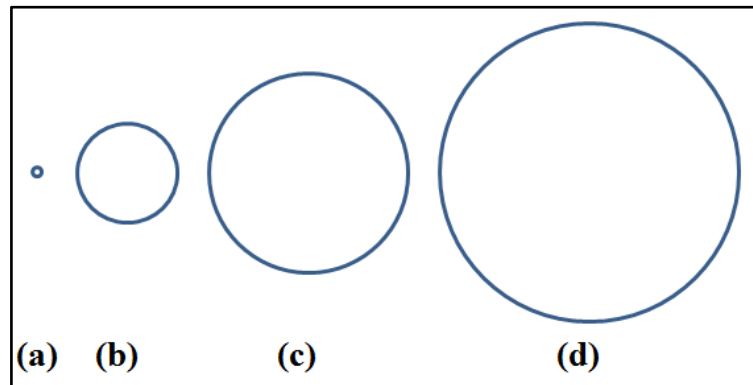
Figure 3-13: Schematic comparison between (a) the droplet real size, and the resulting magnifications by the optical setups: (b) 10x, (c) 20x, and (d) 30x magnification.

The 2 mm diameter spherical particle in Figure 3-13(a) is magnified into 20 mm, 40mm, and 60 mm diameter particles in Figure 3-13(b) to (d) to replicate the 10x, 20x, and 30x magnification rates respectively. From this figure, it can be inferred how helpful are those magnifications for tracking droplet boundaries and interior using high speed imaging.

Figure 3-14: The Photron FASTCAM SA4 Camera.

Eventually, the described techniques have been executed consecutively using a single Photron FASTCAM SA4 High Speed Colour Camera shown in Figure 3-14. The ultra-sensitive sensor of the camera increases the chance of obtaining highly clear images in low-light conditions. Camera imaging conditions have been varied according to each test, and are listed in Table 3-3 with the resulting magnification rate and spatial resolution. The acquired images are stored in the (TIFF) file format for further enhancement and analysis using specially built and developed Matlab algorithms. The processing structure and procedures are described in the next section.

Table 3-3: Camera settings with the resulting magnification rate and spatial resolution for each technique.

Imaging Technique	Frame Rate (fps)	Exposure Time (μs)	Image Resolution (pixel)	Area Covered (mm^2)	Spatial Resolution (μm/pixel)	Magnification Rate (X)
Backlighting	250	4000	1024 x 1024	17x17	16.6	10
	250	4000	384 x 288	3.84x2.88	10	20
Shadowgraph	10000	100	384 x 288	9.6x7.2	25	10
Backlighting	40000	25	320 x 240	3.2x2.4	10	30

3.4 Image Processing for Feature Extraction

Image acquisition is the final process in experimental work, and at the same time it is the first process in image processing. Image processing is essential for performing the full analysis, since the image is not an objective in its own, rather it is the information contained within the image that represent the objective, i.e. turning images into data. Therefore, after acquisition, a series of processes are performed sequentially on the images to extract the required features. These processes are carried out according to the sequence shown in Figure 3-15. Once read, the image is cropped into a specific size decided by the nature of analysis, whether it is droplet or flame analysis, for single droplet or two-droplet combustion. Later on, the cropped image went on the processing steps characterized by enhancement, morphological operations, segmentation, and feature extraction. A detailed explanation of each of these processes is shown below.
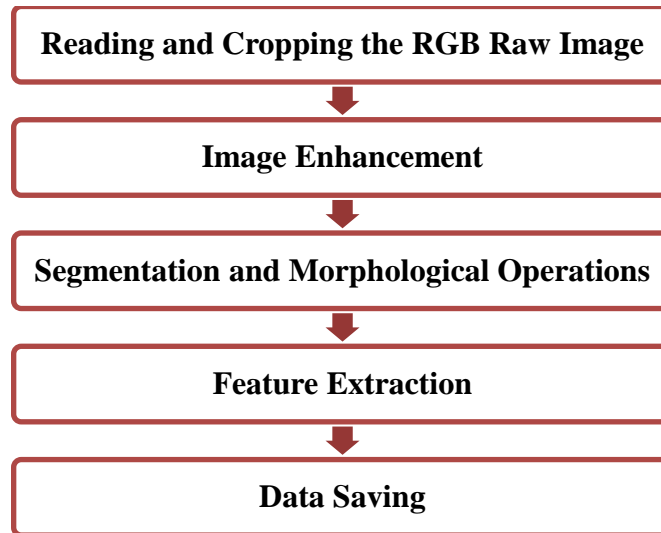
Figure 3-15: Flowchart of the image processing sequence in the present work.

3.4.1 Image Enhancement

Image enhancement is the process of image manipulation for obtaining an image that is more suitable for particular applications than the original one [284]. This manipulation is carried out by improving image contrast and object sharpness for efficient computer-aided analysis. However, image enhancement criteria are poorly defined, and are often subjective, because it depends on the application context rather than a standard objective [285]. Hence, image enhancement in the present work is carried out first by transforming the image from an RGB format into a grayscale format as shown in Figure 3-16(a and b).
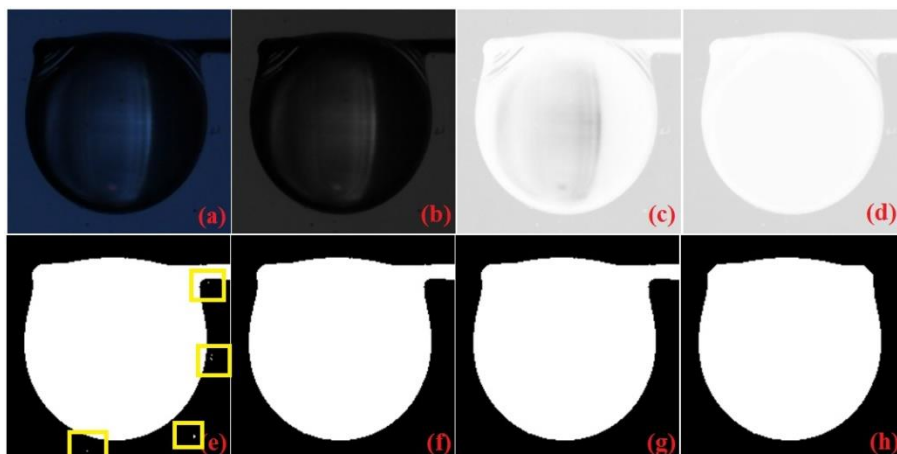
Figure 3-16: Sequence of image processing to isolate the droplet from its surroundings; (a) the original image, (b) grayscale image, (c) complementation, (d) holes filling (first), (e) thresholdeding, (f) noise removal by filtering, (g) holes filling (second), (h) final imge of the isolated droplet**.**

Then, image complementation is applied in the case of droplet analysis rather than flame analysis, because droplets are shown to be relatively dark in both backlit and shadowgraph imaging techniques. This is due to the droplet being between the light source and camera. Whereas, the flame is luminous by its own and its light intensity is higher than that of the light source, therefore it does not have the dark appearance of the droplet. An example of droplet image complementation is shown in Figure 3-16(c). Thereafter, image enhancement is preceded by working all the gaps that take place in the image due to light intensity difference. This is carried out by holes filling as shown in Figure 3-16(d and g).

To this point, the selected image enhancement processes fulfilled the objective of improving object sharpness and image contrast as it is demonstrated by Figure 3-16(a-d). Subsequently, segmentation and morphological operations are carried out as shown in section (3.4.2).

3.4.2 Segmentation and Morphological Operations

Segmentation in image processing is the process of subdividing the image into specific regions or objects of certain significance to the intended application [284]. Therefore, it is essential for describing the image and classifying its objects prior to feature extraction. Various methods are used for image segmentation depending on the objectives of image analysis and the required features [285]. Nonetheless, these methods are assorted under two major categories according to the approach of segmentation. The first category is boundary-based segmentation, in which the boundaries around the regions in the image are formed according the discontinuities in the image. The second category is region-based segmentation, where the similarity between image regions is the bases for segmentation. Thresholding is an example of the latter category [284,285], and it has been utilized for segmentation in the present work. Thresholding according to intensity is the process of differentiating between the pixels contained in an image. The pixels with values more than a certain threshold are assumed to be "foreground" and set white, while those less than the threshold are assumed as "background" and set black [285]. The effect of thresholding on the resulting image can be depicted by comparing the images shown in Figure 3-16(d and e) that are droplet images before and after thresholding respectively.

However, even with thresholding there are still some parts of the image that contain unfavourable noise that should be removed before going on analysis. Increasing the

threshold value will not solve the problem; in fact it may get it worse, because it may cut parts of the objects of interest. Therefore, finding another tool for finalizing the task is obligatory. This is done by the use of morphological operations.

The morphological operators in image processing serve as a tool to modify or extract the image components towards better representation of the shape and structure of the objects within the image [284,285]. There is a wide range of morphological operators such as erosion, dilation, and skeletonization, and a lot more that are useful in binary image in addition to grayscale image analysis. The use of morphological operations in image processing includes – but not limited to – filtering, segmentation, edge detection, noise removal, object counting, and feature recognition [285]. Hence, these operations have been implemented in the present work in two steps; the pre-processing and post-processing steps. In the pre-processing step, morphological operations are performed in the form of noise removal by filtering (Figure 3-16(f)) and erosion followed by dilation using the MATLAB function *imopen* (Figure 3-16(g)). While in the post-processing step, feature extraction is carried out mostly by morphological operations as it is further explained in section (3.4.4).

To this stage, the image is enhanced and modified to the form that is appropriate for efficient feature extraction. But, an evaluation of the effect of image processing on the shape and size of the objects in the image is essential. This is carried out by testing the similarity between the original raw image acquired by the optical system and that obtained by image processing. Accordingly, the degree of certainty and the amount of error margins can be estimated. All these validation approaches have been explained in section (3.4.3).

3.4.3 Validation and Error Estimation

As mentioned earlier, it is essential to ensure that the effect of image processing operations on the shapes and sizes of the elements within the processed image are always kept to minimum. Since, the processed image is the source of the data that will be used later for the intended analysis. Therefore, error analysis is performed for the digital image processing part of the present work and the uncertainty is estimated.

The error between the original image and processed image is firstly expressed in terms of *discrepancy,* and then uncertainty. The discrepancy is defined as the difference between two magnitudes of the same quantity [286]. Discrepancy testing is carried out

both visually and mathematically. Figure 3-17 shows a comparison between original images and those corresponding processed images. In row (a) of the figure are five original images of diesel fuel droplet combustion at different time intervals, while those corresponding processed images are shown in row (b), whereas row (c) shows the matching between the outer boundaries of the images in row (b) with the grayscale forms of the images in row (a).
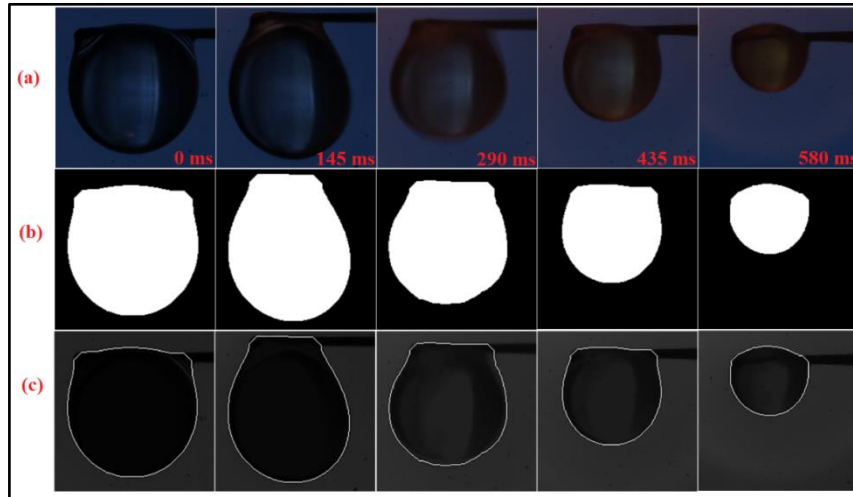
Figure 3-17: Comparison between the original image and the resulting processed image of diesel fuel droplet at different time periods; (a) original images, (b) processed images, (c) matching the boundary of the processed images with the grayscale form of the original image.

From the figure it can be seen that the processed images are almost exactly matching the original images regardless of droplet size or shape. Even at the worse cases of image blur such as that shown for the time (290 ms), the processed image is almost typically simulating the original one. This is highly favourable because sometimes the droplet movement takes it out of camera focusing point, especially for the multicomponent droplets. However, this droplet movement did not decrease the probability of obtaining relatively sharp images appropriate for precise feature extraction.

In addition to the visual matching between images shown in Figure 3-17, mathematical analysis is carried out to evaluate the exact discrepancy between images. This analysis is carried out according to the measured droplet major and minor diameters as the droplet is not fully circular.

Figure 3-18 shows a sample of the comparison between the measured major and minor diameters of the droplet shown in original image (a) and its corresponding processed image (b). The selected images are for the first case in Figure 3-17, which is for (0 ms)

droplet lifetime. This comparison has been applied for many images at different cases. The maximum evaluated discrepancy for both the major and minor diameters is found to be 1 pixel. This is in the cases of image blur like the one shown in Figure 3-17. This corresponds to 10 μm of real droplet size.
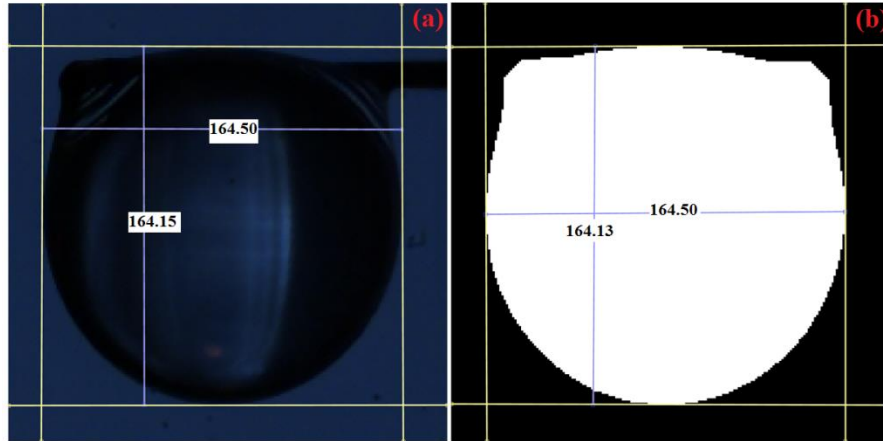
Figure 3-18: Comparison of the droplet major and minor diameters on (a) the original image, and (b) the same image after processing.

However, the average discrepancy is found to be 0.6 and 0.3 pixel which corresponds to 6 and 3 μm for the major and minor diameters respectively. Hence, the uncertainty is evaluated according to equation (3-1):

$$Uncertainty = ABS \left(\frac{X_{Org} - X_{Prc}}{X_{Org}} \right) \qquad \text{........} \qquad \textbf{(3-1)}$$

And the average uncertainty it found to be 0.3%.

From all the above, it can be inferred that the digital image processing operations utilized in the present work result in a highly accurate extraction of the objects within the image without deteriorating neither the shape nor the size of these objects. This ensures confidence in the subsequent data extracted from those images.

3.4.4 Feature Extraction

Feature extraction is the last step in the processing of images. The aim of this step is to convert the images into quantitative data that can be analysed, explained, and presented in the proper form. Feature extraction is also based on the morphological operations,

because these are the processes that deal with parameters like object shape, size, and quantity. Therefore, feature extraction in the present work is performed using various morphological operators, such as edge detection for flame size estimation, object counting for evaluating the rate of secondary atomization from a burning droplet, and area, perimeter, and centroid estimation for droplet size evolution and fluctuation monitoring respectively.

It is worthy to emphasise here that droplet size is expressed in its diameter, and there are different methods described in literature for evaluating this diameter from the images of the droplet. Some are using the equivalent diameter of the elliptical shape [287], and volume [142,183,288], and some are evaluating the diameter from the droplet projected area as an equivalent to sphere of the same diameter [77,84,197]. The last technique is implemented for droplet size evaluation in the present work. The selection criterion of this method is shown in Appendix (C).

Once the quantitative data is extracted from the images, they are saved in excel files for further analysis. Though, the extracted data is based on the image coordinates rather than the real coordinates. Therefore, it is required to convert these data into their corresponding real coordinates. This is done by calibrating the images using a known size object, and is shown in section (3.5).

3.5 Object True Size Calculation

The calibration in general is defined as the process of quantifying a relationship between the input and output data of a measuring system [289]. In order to attain the real dimensions of the investigated objects, object size calibration is carried out for defining the magnitude of magnification resulted by the optical setup. This has been performed with the aid of the SiC fibre whose real diameter is specified and permanently fixed.

Figure 3-19 shows the SiC fibre images for both backlighting imaging (a) and shadowgraph imaging (b). Since the real size of the fibre is known, then the real size of any object in the image can be evaluated in accordance to that of the fibre as shown in equation (3-2)

$$X_R = 100 * 10^{-3} \frac{X_{im}}{X_F} \qquad \text{........} \qquad \textbf{(3-2)}$$

Where:

X_R = the real value of the object (mm).

X_{im} = the corresponding value in the image (pixel).

X_F = the size of the SiC fibre in the image (pixel), and the $(100*10^{-3})$ is the real diameter of the fibre in mm.
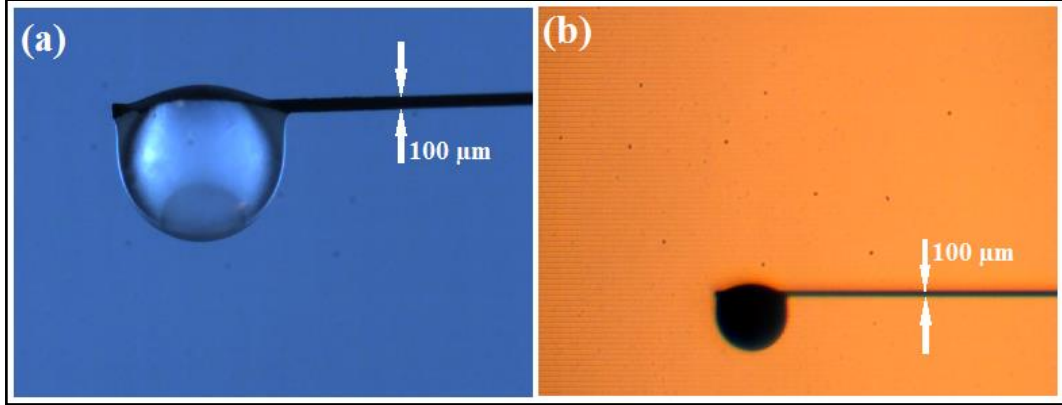
Figure 3-19: Camera calibration using the SiC fibre: (a) Backlighting imaging, (b) Shadowgraph imaging.

Accordingly, the real droplet diameter and flame height and width are all evaluated using equation (3-2). The real size of the area covered by the imaging system has also been evaluated according to the image size. The results are shown in Table 3-4 for all the image resolution values used in the present work.

Table 3-4: The area covered by the optical setup as evaluated by image size.

Image Resolution (pixel)	Corresponding Area (mm^2)
320 x 240	3.2 x 2.4
384 x 288	3.84 x 2.88
768 x 512	7.68 x 5.12
1024 x 1024	25.6 x 25.6

3.6 Summary

In the present chapter, some of the processes carried out prior to (and after) the experimental work have been presented and discussed. These include, fuel mixture preparation, droplet generation, suspension, and ignition, the optical setups, and image processing. The reason behind presenting these processes in this chapter is that these processes take place with every experimental test performed in the present work. Thus,

combining these processes in one chapter and referring to them whenever required is more practical than discussing them in every chapter.

Now, with the above processes explained in the present chapter, and the theoretical basis discussed in Chapter Two, describing the experimental work performed in the next chapters turn out to be less challenging. Though, the new task to be fulfilled is the validation of the experimental results and findings. This is executed particularly in Chapter Four.

Chapter 4. Size and Shape Characteristics of the Burning Isolated Multicomponent Fuel Droplet

4.1 Introduction

Droplet burning rate and size evolution throughout its overall lifetime are the most frequently studied parameters by the majority of droplet combustion research works. This is due to the impact of these two parameters on the performance of the corresponding practical combustion systems. Therefore, this chapter is devoted for exploring those parameters in addition to droplet size fluctuation with respect to the total combustion time. Droplet size analysis is performed to emphasize the difference in stability between the single-component fuel droplet combustion and multicomponent fuel droplet combustion on one hand, and between the different multicomponent fuel mixtures on the other. The analysis are carried out for diesel, biodiesel, and ethanol as the base fuels, in addition to the multicomponent fuels formed by biodiesel/diesel and ethanol/diesel blends in addition to water-in-diesel and diesel-in-water emulsions at different proportions.

For validation purposes, a comparison between the evaluated burning rates of diesel, biodiesel, and ethanol droplets and those corresponding values from another experimental works reported in literature has been performed first. Therefore, the burning rate is the first parameter presented for all the tested fuels. Then, droplet size evolution behaviours are presented with an emphasis on size fluctuation and its frequency to highlight the degree of instability resulted from combining two fuels. Finally, flame width and height are presented for all the fuels.

4.2 Experimental Setup

The schematic diagram of the experimental setup is shown in Figure 4-1. The droplet is suspended on the single monofilament SiC fibre described in Chapter Three. This fibre is attached to the sliding arm of a lab stand for easier control of the droplet position in accordance to the camera. Backlighting imaging with the optical setup described in section

(3.3.2.A) has been used for tracking droplet combustion throughout this experiment. This technique offers the benefits of sharply visualizing the boundaries of both the droplet and the corresponding flame. These boundaries are then used for tracking and calculating droplet size evolution and flame size variation in response to droplet combustion advancement.
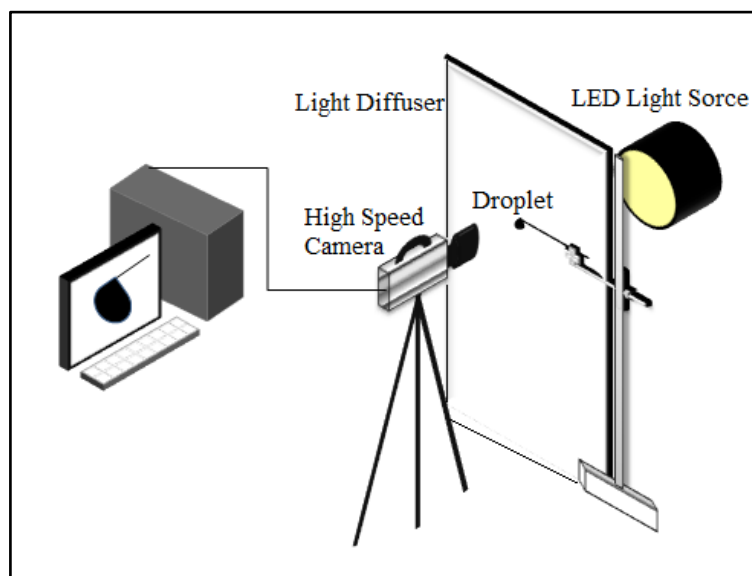
Figure 4-1: Experimental setup of the droplet combustion with backlighting imaging.

The high speed camera is set in front of the droplet, whereas the light source is installed behind the droplet as shown in the figure. The 6-Volt, 72-LED illuminator is used for providing the light required for illumination. The translucent white light diffuser is installed between the droplet and the light source for lower light intensity, and more uniform light distribution behind the droplet. Two camera settings are used in the tests. The first is used for droplet size change tracking, where the camera is set to 250 fps framing rate, 4 ms exposure time, and 384x288 pixels image resolution. The area covered by the camera was 3.84x2.88 mm^2, giving a spatial resolution of 10 µm/pixel for each image. The magnification rate achieved using this setup is 30 times the physical size. Therefore, a detailed investigation of the instantaneous droplet size and shape change during its overall lifetime is performed. The second setup is used for tracking flame characteristics, so the image resolution is set to 1024x1024 pixels, giving a spatial resolution of 16.6 µm/pixel, a covered area of 17x17 mm^2, and a 10x magnification rate. Camera framing rate and exposure time on the other hand, are fixed to the same values of the first setting. The investigated fuels are water-in-diesel and diesel-in-water emulsions, biodiesel/diesel and

ethanol/diesel blends, in addition to the neat diesel, biodiesel, and ethanol as single-component base fuels. The multicomponent fuel mixtures have been prepared in-lab prior to experiments according to the procedures described in section (3.2). The tests have been performed many times for each fuel, and three successful tests are selected and saved for processing in each case for each setup. The images have been stored in the (TIFF) format and processed according to specifically written Matlab algorithms following the processing procedures described in Chapter Three. The flowcharts of those algorithms are shown in Appendix (E). The obtained parameters are further discussed in section (4.3) below.

4.3 Results and Discussion

Figure 4-2 shows a representative sample of the obtained images for the combustion of WD20 fuel droplet (fuel terminology is listed in Appendix (A)). Such images have been processed for extracting the required characteristic parameters of droplet combustion.
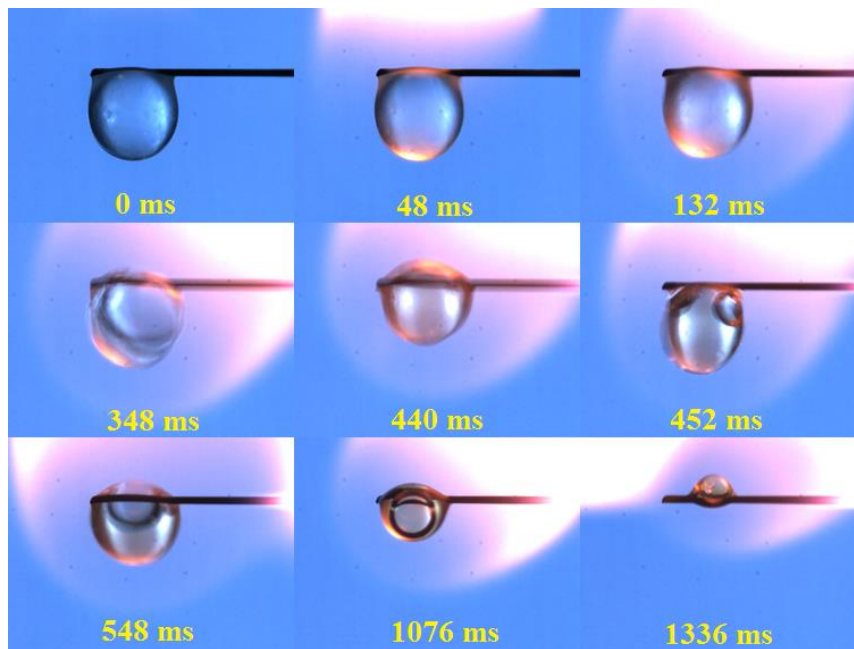
Figure 4-2: Temporal images of a burning WD20 fuel droplet.

As mentioned earlier, the aim of this chapter is to explore in details the droplet burning rate, size evolution, and shape change in addition to the flame characteristics of the multicomponent fuel droplets compared to those corresponding single-component fuel droplets. This exploration is carried out using the data extracted by processing the images

obtained from experiments. Droplet projected area, perimeter, major and minor diameters, and centroid are the extracted data from the processed images. These parameters are used for evaluating droplet size (expressed in its diameter), position, aspect ratio, sphericity, and roundness. The disparity in these parameters between the droplets of the tested fuels is discussed in the next section, before which, a validation of the experimental results is discussed.

4.3.1 Validation by Burning Rate Comparison

According to equation (2-11), droplet burning rate is the ratio between the initial droplet diameter squared and its total lifetime. Droplet lifetime is the interval of time between droplet ignition and flame extinction. Therefore, once the droplet initial diameter is extracted and its lifetime is determined, its burning rate can be easily evaluated.

On the other hand, the burning rate is reported extensively in the published literature for different fuel droplets. Hence, it can be used for validating the experimental results by comparison with the corresponding values from other published work. Especially, if it is known that the effect of droplet size change is compromised by the change in its lifetime. Thus, the burning rate can be used for comparison without any reluctance of droplet size variation between the present work and the published work. Accordingly, a full comparison is drawn for the combustion of diesel, biodiesel, and ethanol droplets and it is shown in Appendix (D). A summarised version of the table is shown in Figure 4-3. These fuels have been selected particularly because they are single-component so that the effect of fuel preparation method on the results is neglected. In addition to the availability of the burning rate data of these fuels in literature compared to the multicomponent fuels.

In general, Figure 4-3 illustrates that the burning rates published in literature are varied within a relatively wide range for each fuel, and that the estimated values in the present work are within these ranges. However, the present results show a certain similarity with a specific set of the published data. Hence, a detailed examination of the figure and the corresponding values in Appendix (D) reveals that the burning rate value is affected by the conditions under which the test is performed. Three different test conditions are reported for droplet combustion; suspended droplet combustion under microgravity conditions, suspended droplet combustion under normal gravity conditions, and combustion of freely falling droplets.

94
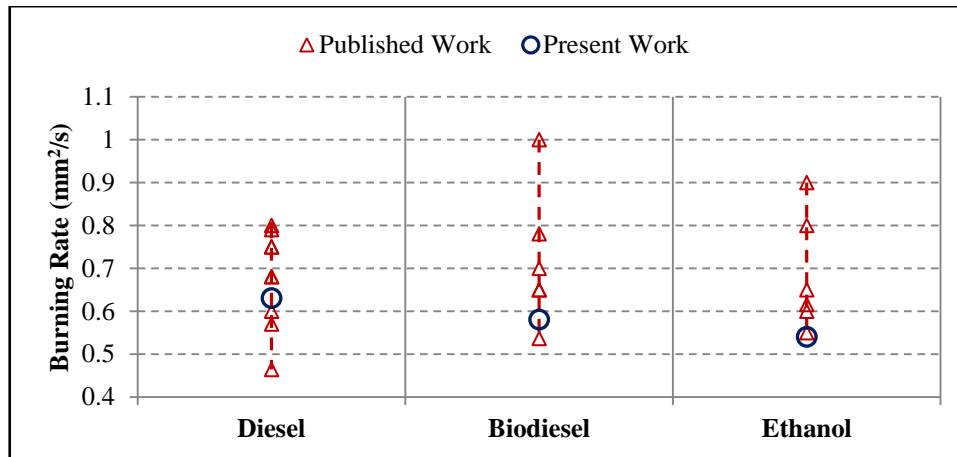
Figure 4-3: Burning rate comparison for diesel, biodiesel, and ethanol droplets respectively of the present work and those corresponding values published in literature.

The burning rate values of the present work show a quite close similarity with the majority of the published microgravity works [66,70,128,130,290] for the three fuels. This similarity is tested by evaluating the discrepancy between both values. The discrepancy is defined as the absolute of the net difference between two values of the same quantity [286]. If this discrepancy is less (or slightly higher) than the standard deviation of the data to be tested, then a high degree of confidence is reached [286]. The standard deviation of diesel, biodiesel, and ethanol are reported in Appendix (D) and are 0.04, 0.09, and 0.06 respectively. Whereas the discrepancies between the evaluated burning rates of these fuels and those corresponding values reported for microgravity testing conditions are found to be 0.03-0.06 for diesel, 0.03-0.08 for biodiesel, and 0.02-0.08 for ethanol. Thus, a high degree of confidence is built on the obtained burning rates for the three fuels. This, in turn is reflected on the overall experimental work carried out.

Furthermore, as it is shown in the Figure 4-3 and Appendix (D), the burning rate constant of the ethanol is too close to the minimum published values which are belonging to the burning rate constants at the microgravity conditions. This is attributed to the pure nature of the ethanol, where it is usually available in the form of single-component neat substance, and is utilized in all experimental work in this form. Diesel and biodiesel on the other hand, are available in different proportions and different structures according to the suppliers and different standards around the world. Hence, the burning rate constants of these two fuels are slightly dispersed compared to ethanol.

One more point to be revealed, that is the reason behind the relative dissimilarity between the current results and those corresponding published results under normal gravity

conditions despite that the current work is performed under normal gravity. This is explained by the effect of droplet suspension method. The size and mesh arrangement of the suspension fibre have in fact a certain effect on the droplet burning rate. This effect is clearly noticeable when comparing the burning rates of the same testing conditions but different suspension material or mesh in Appendix (D). For that reason, the effect of SiC fibre mesh arrangement on droplet burning rate has been investigated in the present work using diesel, biodiesel, and ethanol as the burning fuels. A cross-shaped (100 μm) SiC fibre mesh is used for suspending the droplet rather than the single-filament (100 μm) SiC fibre. The burning rates are then evaluated for the three fuels, and the comparison with those of the single filament fibre is shown in Figure 4-4.
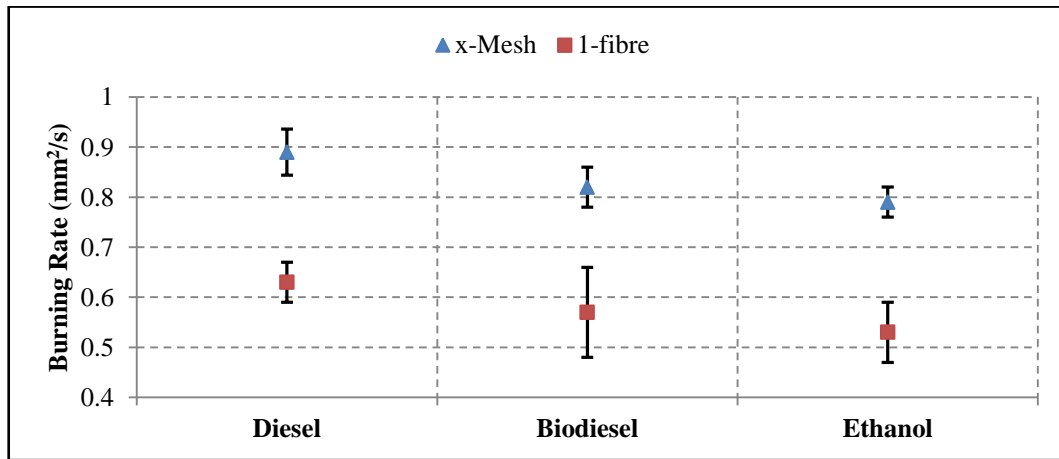
Figure 4-4: The effect of SiC fibre mesh arrangement on the burning rate of diesel, biodiesel, and ethanol droplets.

As it is shown in the figure, the droplet burning rates of diesel, biodiesel, and ethanol are all increased with the new fibre arrangement despite the net size of the fibre is the same. This suggests that a single filament fibre has less effect on droplet combustion than the cross-shaped mesh. Although it is reported that the thermal asymmetries resulted from the cross-shaped mesh are less than those from the single-filament fibres [281]. The reduction in droplet burning rate for diesel, biodiesel, and ethanol when using single filament fibre compared to the cross-shaped one of the same size is found to be 29%, 30%, and 33% respectively. However, a closer look to the burning rates of the cross-shaped fibre support experiments show that their values are almost similar to those corresponding burning rate values under normal gravity conditions in Appendix (D), especially those reported by Pan et. al., [66] for biodiesel, and Bartle et. al., [291] for ethanol. This in turn

confirms the similarity of the present experimental work with the equivalent published work using both single filament fibre and cross-shaped fibre mesh. Thereby, the analysis of droplet burning rate and the other parameters is continued in the forthcoming sections. Moreover, the values shown in Figure 4-4 represent the average values of ten samples for each fuel, with the error bars in the figure representing the standard deviation of these values. Except the biodiesel in single-fibre experiments, the standard deviation of all the cases is around 0.05 which is about 5% of the burning rate values. This in turn, suggests a good repeatability of the results.

4.3.2 Burning Rate of the Multicomponent Fuel Droplets

Once the droplet combustion experimental procedures and burning rate estimation method have been validated, continuing data analysis and presentation is viable at the moment. The burning rate of the multicomponent fuel droplets has been evaluated according to the same principle of the single-component fuel droplets shown in equation (2-11). That is by dividing the initial droplet diameter squared by the total droplet lifetime evaluated from ignition to flame extinction. Therefore, only the droplets proceeded successfully to the end are considered for evaluating droplet burning rate. That is because, in some of the multicomponent fuel droplets, especially for the water-in-diesel and diesel-in-water emulsions, the droplets go on explosion and do not proceed for complete combustion. However, in the case of diesel-in-water emulsions, for all mixture compositions, no single droplet survived to the end for complete evaporation and combustion, despite the amount of experimental tests carried out. All the droplets went on microexplosion rather than complete combustion. Accordingly, the slope of the droplet size evolution curve with time has been evaluated and assumed as the burning rate for this fuel mixture. This assumption is valid according to equation (2-10) in which the burning rate constant is the slope of the equation relating droplet size evolution with burning time. Additionally, this method of evaluating the burning rate has been implemented by other published works for evaluating the burning rate for emulsion droplets, such as that of Wang et al., [129].

Figure 4-5 shows the evaluated droplet burning rates of the multicomponent fuels with respect to the volume fraction of the component added to diesel. The figure is split into two parts to highlight the difference in behaviour between the emulsions and blends.
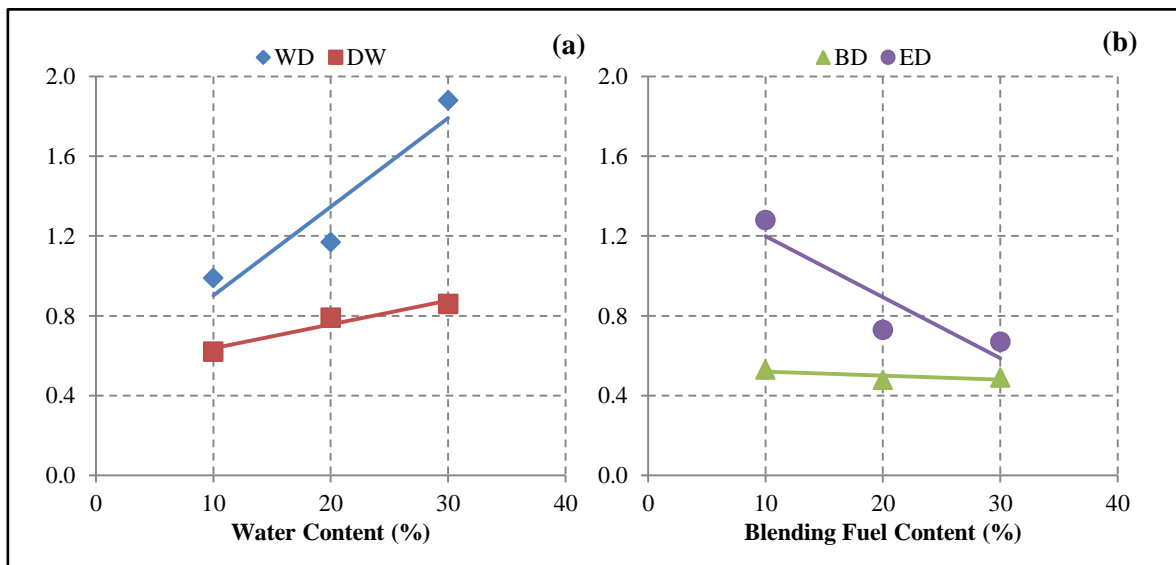
Figure 4-5: Droplet burning rate (mm^2/s) of the multicomponent fuels with respect to the amount of: (a) water content for the water-in-diesel and diesel-in-water emulsions, (b) blending agent for the biodiesel- and ethanol-blended diesel fuel droplets.

Figure 4-5(a) shows the burning rates of the water-in-diesel (WD) and diesel-in-water (DW) emulsions at 10%, 20%, and 30% volume fraction of water. Both types of emulsions show an increase in the burning rate with increasing water content in the emulsion, with the higher rates shown for the WD emulsions. This is attributed to the increase in puffing and secondary atomization from the emulsion droplets, which in turn, raises the disintegration of the droplet leading to the increases in its burning rate. This is in agreement with the results of both Wang et al., [129] for water-in-diesel emulsion, and Kim and Baek [292] for water-in-*n*-decane emulsion, but, at the same time it is in contrast with the burning rate values estimated by Jackson and Avedisian [147] for water-in-*n*-heptane emulsion. Thus, it may be inferred that the type of base fuel has an effect on the combustion behaviour of the emulsion, especially, its boiling point. The boiling points of diesel, n-decane, and n-heptane fuels are >170ºC [293], 174.1ºC, and 98.4ºC [294] respectively. The boiling point of n-heptane is lower than that of water; whereas, diesel and n-decane both have boiling temperatures higher than that of water. Therefore, the case of water-in-n-heptane emulsion is completely different from those of water-in-diesel and water-in-n-decane emulsions. In the latter emulsions, water is the component that undergoes superheat nucleation. Whereas in the former emulsion, both components have almost the same boiling point with that of n-heptane is slightly less than the boiling point of water. Hence, both components are likely to undergo evaporation at the same rate

without the occurrence of superheat nucleation. This probably is the reason behind the difference in burning rate behaviour.

Figure 4-5(b) shows the burning rate values of the biodiesel-blended diesel (BD) and ethanol-blended diesel (ED) for 10%, 20%, and 30% of the blending fuel. The figure shows that increasing the concentrations of ethanol and biodiesel in the mixture will lead to a steep – in the ED blends – and a slight – in the BD blends – decrease in the droplet burning rate. This is expected in light of the burning rate values of the single-component fuels (diesel, biodiesel, and ethanol) shown in Figure 4-3 and Figure 4-4 respectively. Since, the burning rates of both biodiesel and ethanol are less than that of diesel. Consequently, adding these fuels to diesel will result in decreasing the burning rate of the mixture. Again, this is in agreement with the published work on diesel burning rate values when blended with biodiesel and ethanol respectively [122].

According to Figure 4-5, the burning rates of the diesel-based multicomponent fuel droplets are variable both in behaviour and magnitude in response to several parameters, such as the concentration of the added substance, and boiling point difference between the diesel and the added constituent. This variation in burning rate ranges from 0.49 mm^2/s for BD30 to 1.88 mm^2/s for WD30. Then, the effect of this relatively broad range of burning rate on the consumption of the base fuel (diesel) is evaluated.

Figure 4-6 shows the effect of (a) water and (b) blends concentrations on diesel fuel consumption of the multicomponent fuel droplets. Diesel fuel consumption is normalized with respect to the burning rate of the neat diesel. As shown in Figure 4-6(a), emulsifying diesel by water results in increased diesel fuel consumption due to increasing the burning rate of the emulsion. This increase in diesel fuel consumption is shown to be less for the diesel-in-water emulsions; in fact it is negligibly small for the three concentrations. For the diesel blends shown in Figure 4-6(b), increasing the blending fuel results in decreasing diesel fuel consumption. This decrease may reach up to 70% and 50% of the neat diesel burning rate for ED30 and BD30 respectively. All that implies that blending diesel by either biodiesel or ethanol has a better impact on diesel fuel economy than water emulsification. This in turn will have an effect on the break specific fuel consumption of the engine fuelled with such fuels. The break specific fuel consumption (bsfc) of the engine is defined as the ratio of fuel consumption rate to the break power of the engine [165]. This means that the break specific fuel consumption is proportional to the fuel consumption rate.

99
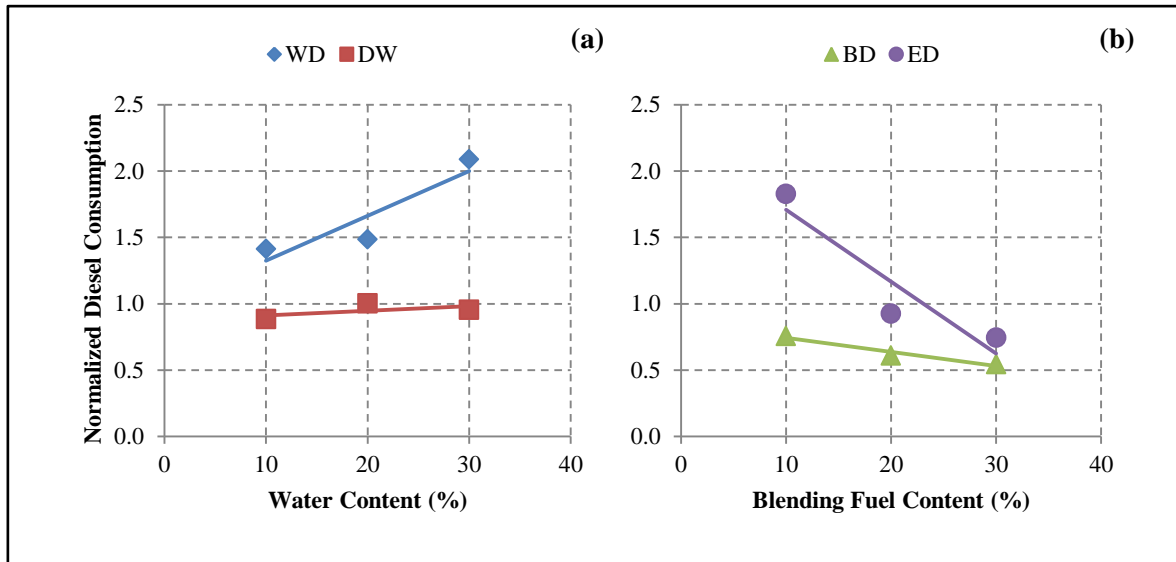
Figure 4-6: Normalized diesel consumption with respect to the amount of: (a) water content for the water-in-diesel and diesel-in-water emulsions, (b) blending agent for the biodiesel- and ethanol-blended diesel fuel droplets.

Hence, Figure 4-6 suggests that the break specific fuel consumption of the engine will increase when fuelled with the emulsified diesel and decrease when fuelled with ethanol-blended or biodiesel-blended diesel. This is in agreement with the published work on engine performance for diesel-water emulsions [253,255,295,296], but in contrast with that for diesel blends [238–240,249,297]. However, the above suggestion accounts only for one parameter of the brake specific fuel consumption that is the fuel consumption rate and disregards the other effective parameter that is the brake power. The brake power may vary by varying fuel type according to the heating value of the fuel. Hence, the above suggestion only gives an indication of the effect of changing fuel composition on the consumption rate rather than power output.

Once, the burning rate constant of the different multicomponent fuel droplets has been evaluated, it is time now for comparing the second important macroscopic parameter, that is the droplet size evolution with time. This is executed in the next section.

4.3.3 Droplet Size Evolution

Figure 4-7 shows the droplet size evolution with time for all the fuels tested in the present work. These include diesel, biodiesel, and ethanol as single-component fuels, in addition to biodiesel-blended diesel, ethanol-blended diesel, water-in-diesel emulsions, and diesel-in-water emulsions as multicomponent fuels. The multicomponent fuels are of 10%, 20%, and

30% volume fraction of the added component. Droplet size evolution is expressed in terms of its diameter squared. It has been tracked and estimated using droplet images during combustion. Droplet size is normalized by the droplet initial diameter squared to eliminate the effect of initial droplet size variation on the comparison between fuels. Instantaneous combustion time has also been normalized by the total droplet lifetime so that the effect of combustion time difference between the fuels is eliminated. Hence, an assessment of droplet combustion behaviour for all the tested fuels became appropriately conceivable by unifying the time domain. As mentioned in Chapter Three and Appendix (C), droplet diameter is estimated using the equivalent diameter of the droplet projected area from its sequential images for all the tested fuels. All the fuels listed in Figure 4-7 are of droplets that went through complete combustion, i.e. from the initial size to a size equal to zero. Except one case which is the diesel-in-water emulsion of all volume fractions, where the droplets experience explosion before complete evaporation despite the large number of trials carried out for investigating this case. Therefore, the final size of this case is not the complete combustion size; rather it is the explosion size. The first row of Figure 4-7 shows the size evolution of the single-component fuels; diesel, biodiesel, and ethanol respectively.

Generally, the combustion of these single-component fuels is smooth compared to the chaotic combustion of the multicomponent fuels. Additionally, the size variation of the three fuels relatively obeys the D^2-law of droplet combustion, especially after the first 20% of the droplet lifetime. A linear slope is obtained for the three fuels that is compatible with what is predicted by the D^2-law analysis. Whereas, in the first 20% portion of the droplet lifetime, droplet size is either equal to or relatively higher than its initial value. This is due firstly, to the combustion of the already existing fuel vapour that is generated by droplet vaporization prior to combustion, and secondly, to the heating of the initially cold droplet [40]. Therefore, droplet heating rather than evaporation is the dominant process in the early stages of combustion, and in turn, relatively constant droplet size behaviour is shown in the size evolution curve of the single-component fuels in Figure 4-7.

The second row of Figure 4-7 shows the size evolution of the biodiesel-blended diesel (BD) of 10%, 20%, and 30% biodiesel volume fractions respectively. Firstly, it can be inferred that the BD blends are burning relatively smoothly compared to the other multicomponent fuels as a result of the miscibility of diesel and biodiesel in each other leading to a relatively homogeneous mixture. Secondly, the early stage constant droplet size shown for the single-component fuels is also occurring with the BD fuel droplets.
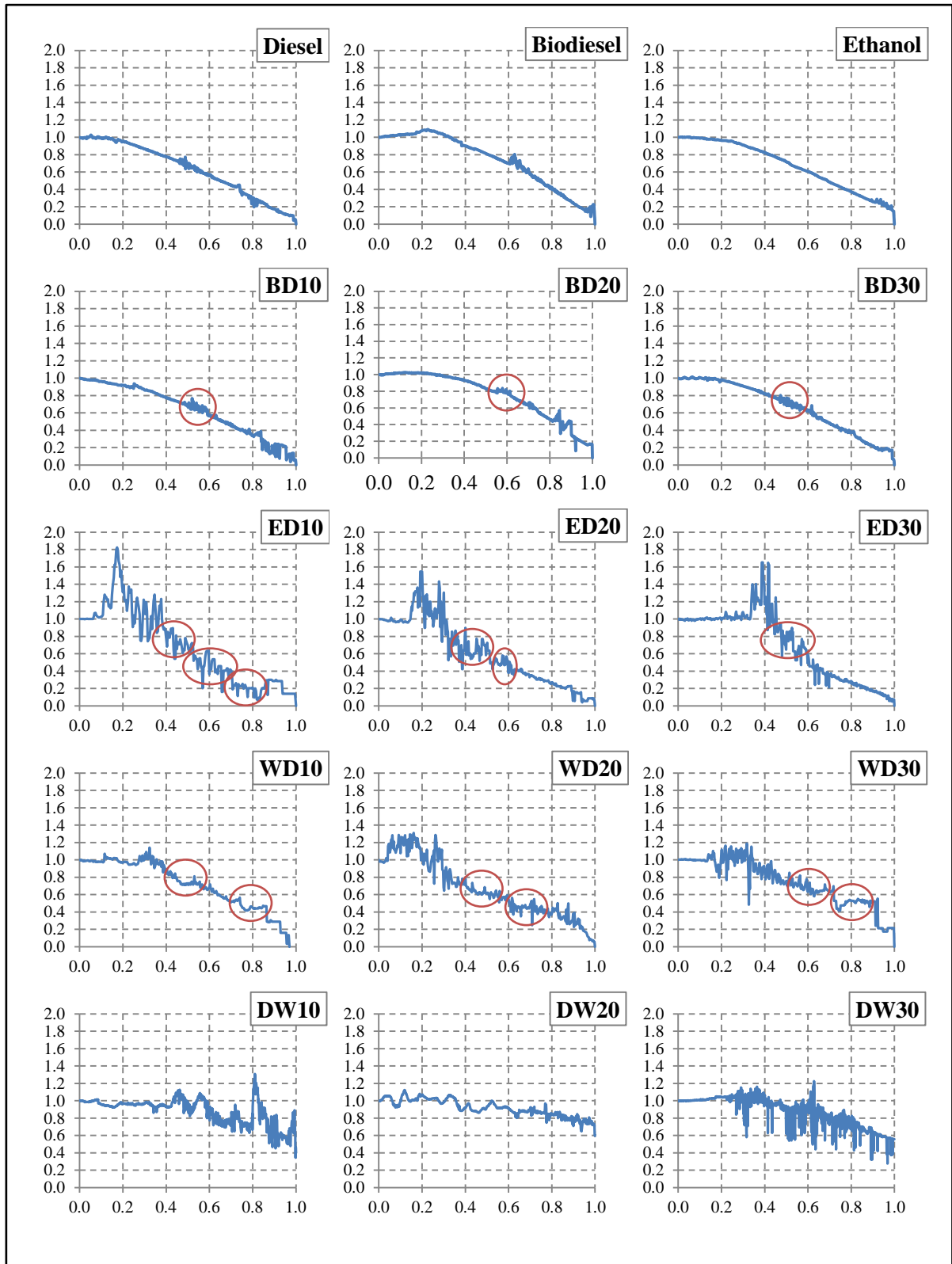
Figure 4-7: Droplet size evolution with respect to time for: the single-component fuels (1st row), biodiesel/diesel blends (2nd row), ethanol/diesel blends (3rd row), water-in-diesel emulsions (4th row), and diesel-in-water emulsions (5th row). The y-axis is the normalized droplet size $(D/D_0)^2$, and the x-axis is the normalized droplet lifetime (t/t_{total}).

Moreover, as shown in the regions highlighted by the circles in the second row of Figure 4-7, for a short time period within the interval bounded by the 50% and 60% portions of the droplet lifetime, a slightly constant droplet size pattern is noticed for the blends compared to diesel and biodiesel. This is referred to the heating and evaporation of the less volatile component in the multicomponent mixtures [116]. These components last to the end inside the droplet, and then start to boil and evaporate causing the droplet size to increase due to increased internal pressure by vapour generation [124]. In the present work, biodiesel is the less volatile component [298]. Hence, diesel will evaporate first leaving the biodiesel to accumulate in the centre of the droplet. This will result in a form of nucleation and phase separation between diesel and biodiesel as shown in Figure 4-8. After a certain time, the concentrations of the mixture will change due to diesel depletion and biodiesel accumulation resulting in a new mixture of high biodiesel concentration. Therefore, biodiesel will move towards the droplet surface due to concentration gradient. Though, at the droplet surface, biodiesel will evaporate at a temperature higher than that of diesel. This will result in increasing the droplet surface temperature, and accordingly increasing the temperature inside the droplet.
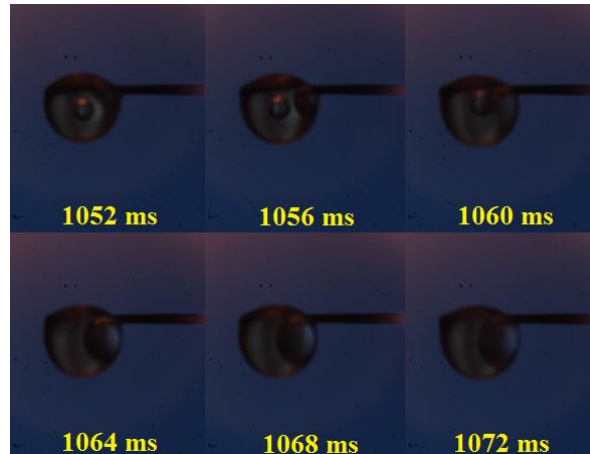
Figure 4-8: Bubble nucleation inside a burning BD10 fuel droplet (D_0=1.3 mm).

Consequently, the remaining diesel that is trapped inside that droplet will start boiling and generate bubbles that are growing and causing droplet expansion. This expansion is shown to occur in the second half of its lifetime and for the diesel and blends rather than biodiesel. For diesel, the expansion is less intensive compared to the biodiesel/diesel blends, and it may be related to the constituents of diesel. Since the diesel

fuel is a mixture of different components that have different volatilities, making the diesel droplet to behave similarly like the multicomponent fuel droplets [13].

The third row of Figure 4-7 shows the size evolution of the ethanol-blended diesel (ED) of 10%, 20%, and 30% ethanol volume fractions respectively. As the figure illustrates, the ED blends show the most chaotic behaviour among all the studied fuels. This is attributed to the partial miscibility of ethanol in diesel as stated previously. Hence, compared to the mixtures produced by blending diesel with biodiesel – which are completely miscible in each other – and the emulsions generated by mixing water with diesel – with the aid of the emulsifying agents – blending diesel with ethanol results in highly metastable mixtures. So, the relatively random droplet combustion behaviour of these blends is attributed to their metastable nature which leads to increased nucleation rate as shown in Figure 4-9. This is in agreement with the findings of Avulapati et. al., [131] for blending diesel with 10%, 25% and 50% ethanol by volume. Furthermore, in the ED blends ethanol is the more volatile component and diesel is the less volatile one, with a relatively large boiling point difference between them (in the order of 100). Hence, the superheat boiling described for the BD blends is expected to occur in the ED fuel droplets with diesel being the component experiencing superheat boiling. The constant droplet size regions shown in the BD blends have also been noticed for the ED blends and bounded by the red circles in Figure 4-7.
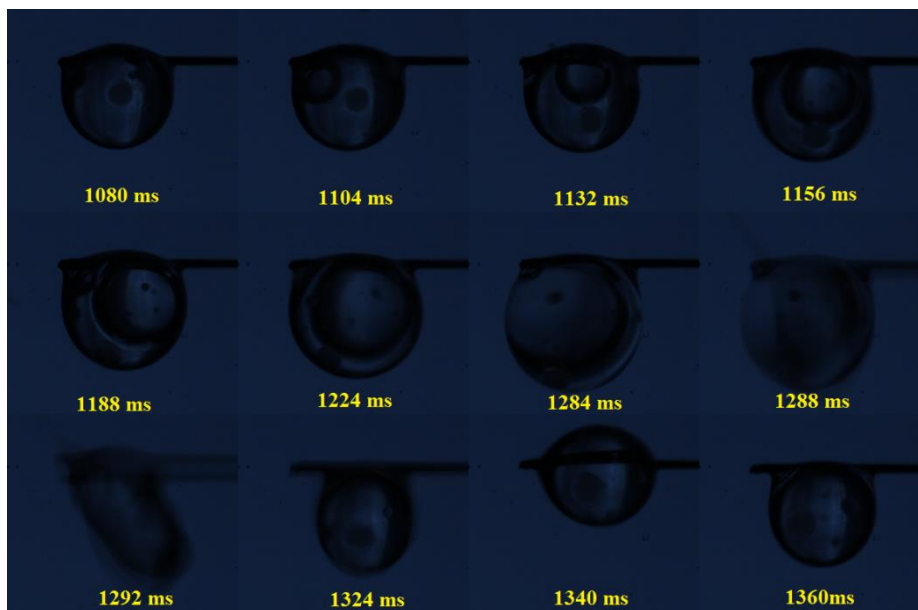
Figure 4-9: Size increase and instability due to bubble growth and puffing within a burning ED10 fuel droplet (D_0=1.23 mm).

The final two rows of Figure 4-7 show the size evolution of the water-in-diesel (WD) and diesel-in-water (DW) emulsions of 10%, 20%, and 30% water volume fractions respectively. As mentioned earlier, droplet fragmentation was the dominant behaviour during the combustion of the DW droplets. Accordingly, the droplets did not undergo complete combustion for the all water concentrations studied. The same combustion behaviour of the ED blends is shown to happen during the combustion of the emulsion droplets with less instability. This is due to the effect of the emulsifying agents used for preparing the emulsions. These agents act as mixture stabilizers that prevent phase separation within the emulsified fuel as discussed in Chapter Three.
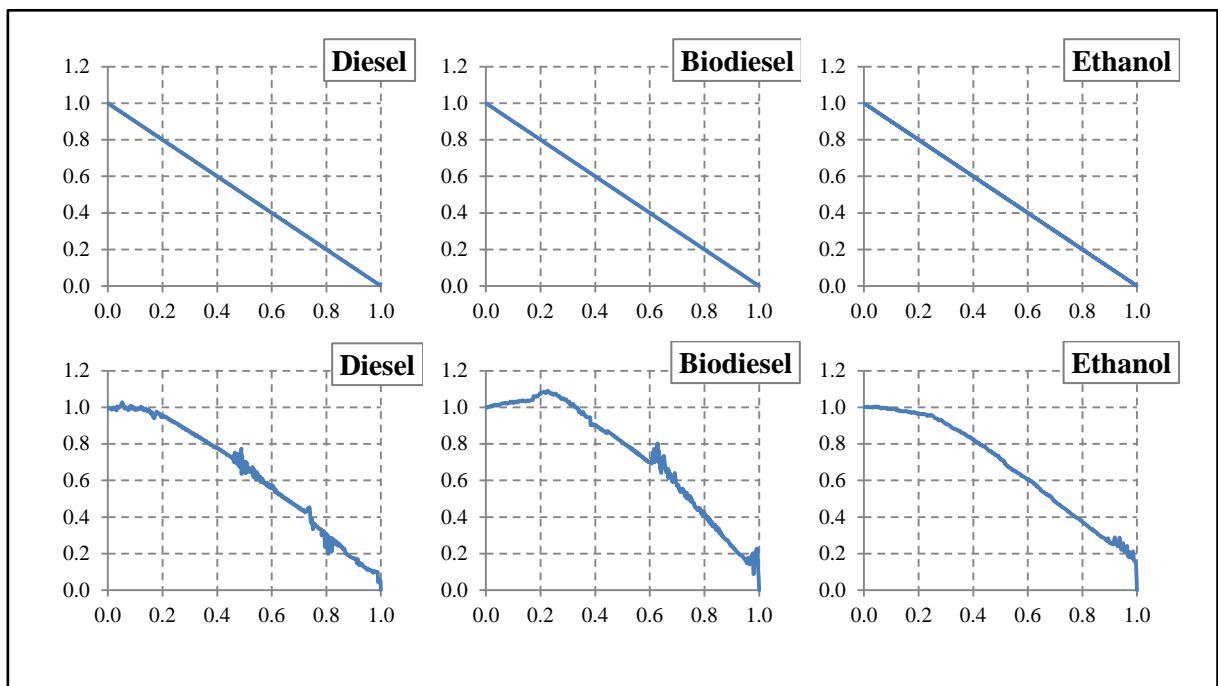
Figure 4-10: Comparison between the predicted droplet size evolutions using the D^2-law (upper row) and those evaluated from experimental results (lower row) for diesel, biodiesel, and ethanol. The y-axis is $((D/D_0)^2)$, and the x-axis is (t/t_{total})

Furthermore, in order to compare the difference between the theoretical prediction and experimental calculations, the droplet size evolutions of the three single-component fuels have been evaluated using the D^2-law equations described in Chapter Two. These evolutions have been drawn with those corresponding evolutions from experimentation in Figure 4-10. These three fuels have been selected because the D2-law is only valid for single-component fuels rather than the multicomponent fuels as it is shown in the assumptions used for developing the D^2-model in Chapter Two. Hence, as Figure 4-10

shows, the droplet size evolution predicted by the D^2-law equations (upper row of the figure) have excluded the first 20% heating period and its effect on droplet size increase shown in the corresponding experimental data. Additionally, the droplet size fluctuations in the midterm of its lifetime described previously did not appear in the corresponding theoretical graphs. Thirdly, the slopes of the curves – which represent the burning rate constant as discussed above – in the case of the theoretical evolutions are steeper than those corresponding experimental curve slopes for all the fuels, suggesting a higher burning rate prediction in the case of theory compared to experiment. All these points imply that the D^2-law model gives a good description of the overall droplet size behaviour, but its prediction of the detailed events is relatively unsuccessful. This in addition to the predicted burning rate constants are higher than those evaluated in experiments, in fact they are around twice the calculated values.

Generally, the multicomponent fuel droplets show higher droplet size fluctuations compared to the single-component fuel droplets. The intensity of these fluctuations is uneven among the multicomponent fuel droplets because of the effect of components miscibility in each other and the resulting mixture stability as explained above. Therefore, the intensity of size fluctuation of all the fuels under investigation has been evaluated and further explained in the next section.

4.3.4 Droplet Size Fluctuation

Droplet size fluctuation is used for evaluating the stability of the multicomponent fuel mixture during combustion. This stability reflects the interaction between the different constituents of the mixture, and the resulting subsequent processes such as nucleation, puffing, and secondary atomization. Therefore, in their investigation of the puffing characteristics from biodiesel/butanol droplets, Zhang et. al., [156] used droplet degree of deformation for detecting and characterizing puffing. They have defined the degree of deformation as the ratio between droplet actual perimeter and the equivalent perimeter that is evaluated using the droplet equivalent diameter obtained from the droplet projected area. This parameter is helpful in tracking puffing and secondary atomization due to the resulting change in the shape of the droplet in response to sub-droplet ejection from its surface. But, for cases as that shown in Figure 4-9 (images corresponding to 1224 ms and 1284 ms combustion time) where droplet size is increasing and its circular shape is not

changing, the degree of deformation is not effectively applicable. For that reason, droplet size fluctuation – the size increase in particular – has been chosen to illustrate the stability of the fuel mixtures under investigation.

Figure 4-11 shows the temporal size fluctuation of the burning BD10, ED10, WD10, and DW10 fuel droplets respectively compared to that of the neat diesel droplet. Droplet size fluctuation (ΔD) has been evaluated according to equation (4-1):

$$\Delta D = \frac{(D_{i+1} - D_i)}{D_0}$$ **………** **(4-1)**

This fluctuation has been normalized by the initial droplet diameter for minimizing the effect of droplet initial size variation on the results, and for the relevance and practicality offered by the non-dimensional quantities compared to their corresponding dimensional ones.

Figure 4-11 shows representative samples of each type of the fuel mixtures – biodiesel/diesel blends, ethanol/diesel blends, water-in-diesel emulsions, and diesel-in-water emulsions – in addition to a sample from the neat diesel fuel droplet tests. The figure shows that the intensity of size fluctuation is higher at the second half of the droplet lifetime for all the presented fuels. This intensity is occasionally high compared to the droplet initial diameter, as shown in the case of ED10 fuel droplet. The size fluctuation in this case is around 30% of the initial droplet diameter. Therefore, further exploration in these fluctuations is thought to be merited. However, due to the random nature of droplet size fluctuation, presenting it in the form of Figure 4-11 for every fuel is not practically worthy. Therefore, a broader statistical analysis is performed among three samples for each fuel and the maximum limit of the average values for every fuel has been evaluated.

Figure 4-12 shows the average droplet size fluctuations of all the fuels under investigation. These fuels are divided into three categories; (a) the single-component fuels (biodiesel, diesel, and ethanol), (b) the WD and DW emulsions, and (c) the BD and ED blends. The presented values are for the sum of the average values and standard deviation for each case in order to illustrate the maximum possible size increase rate. As it is shown in the figure, the multicomponent fuels have higher size fluctuations compared to the single-component fuels.
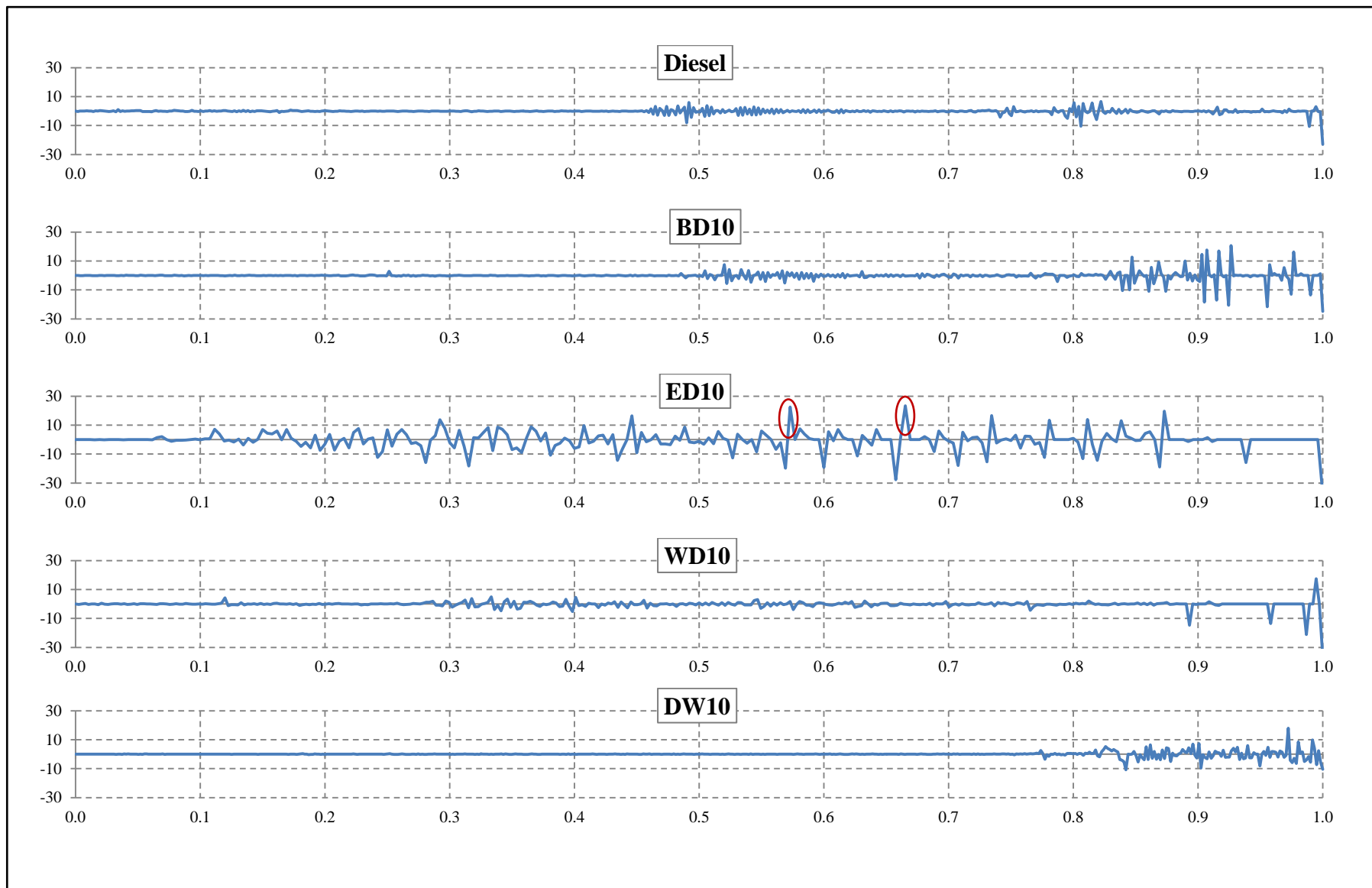
Figure 4-11: Temporal size fluctuation of diesel, BD10, ED10, WD10, and DW10 fuel droplets undergoing combustion. The x-axis the (t/t$_{total}$), and the y-axis is the droplet size variation normalized by the initial droplet diameter.

The larger average size fluctuation occurs during the combustion of ethanol/diesel blends that is about 7% of the instantaneous droplet diameter and 4% of the initial diameter in maximum in the case of ED10, and the rest of the mixtures are below these values.
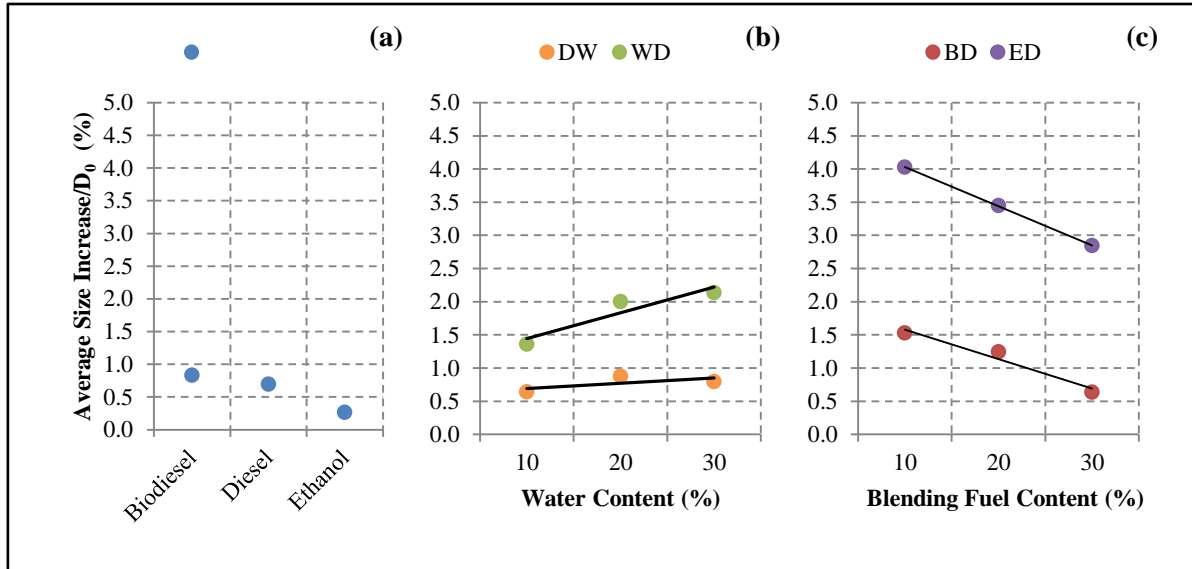
Figure 4-12: Average droplet size increase rate normalized with respect to droplet initial diameter for the: (a) single-component fuel droplets, (b) diesel/water and water/diesel emulsion droplets, and (c) biodiesel/diesel and ethanol/diesel blend droplets.

Furthermore, the BD and ED blends initially, have higher fluctuations than the corresponding emulsions of the same diesel concentration, as in the case of 10% additive mixture fuels. Increasing the additive concentration in the ED and BD blends then decreases the fluctuations in the droplet size. This is exactly the opposite in the case of emulsion droplets, where the fluctuation is increased by increasing the concentration of water in the emulsion. This can be explained by looking at the maximum droplet size increase in Figure 4-13, and the size increase time portion in Figure 4-14.

Figure 4-13 shows the higher value of droplet size with respect to its initial diameter. This value is the average of three samples for each fuel. The same three categories used in Figure 4-12 have been used for presenting the maximum values, except the BD data that has been moved to Figure 4-13(b) to show the similarity in behaviour. Second order polynomial curve fitting is used for connecting the points for each of the multicomponent fuels in Figure 4-13(b and c).
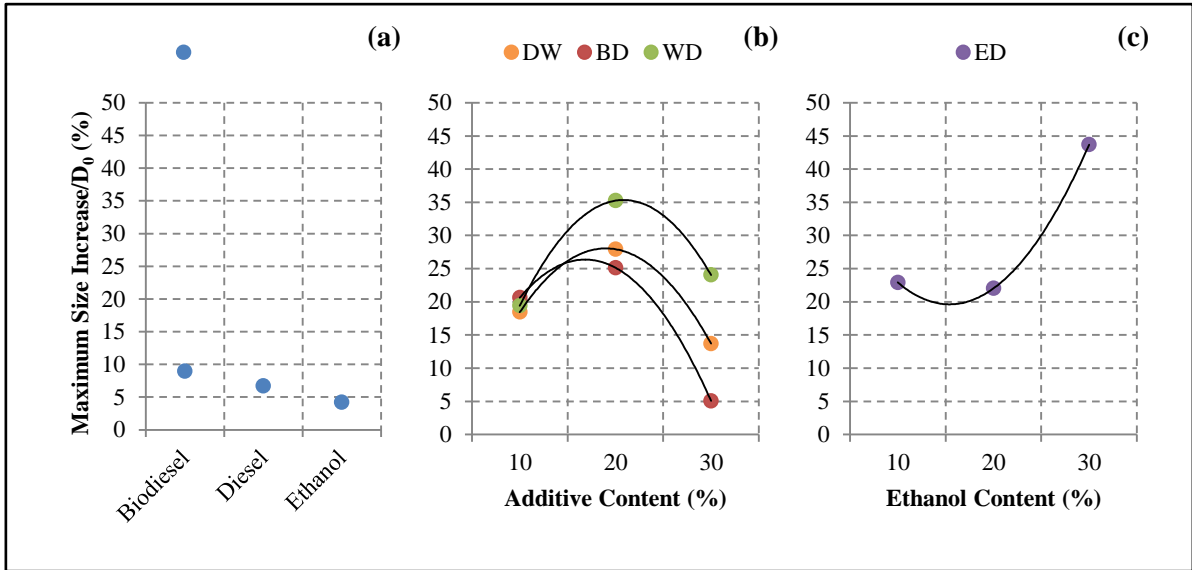
Figure 4-13: Maximum droplet size increase normalized with respect to droplet initial diameter for the: (a) single-component fuel droplets, (b) diesel/water, water/diesel and biodiesel/diesel droplets, and (c) ethanol/diesel droplets.

Figure 4-14 on the other hand, represents the portion of time with respect to the overall droplet lifetime where droplet size increase is occurring rather than size decrease.
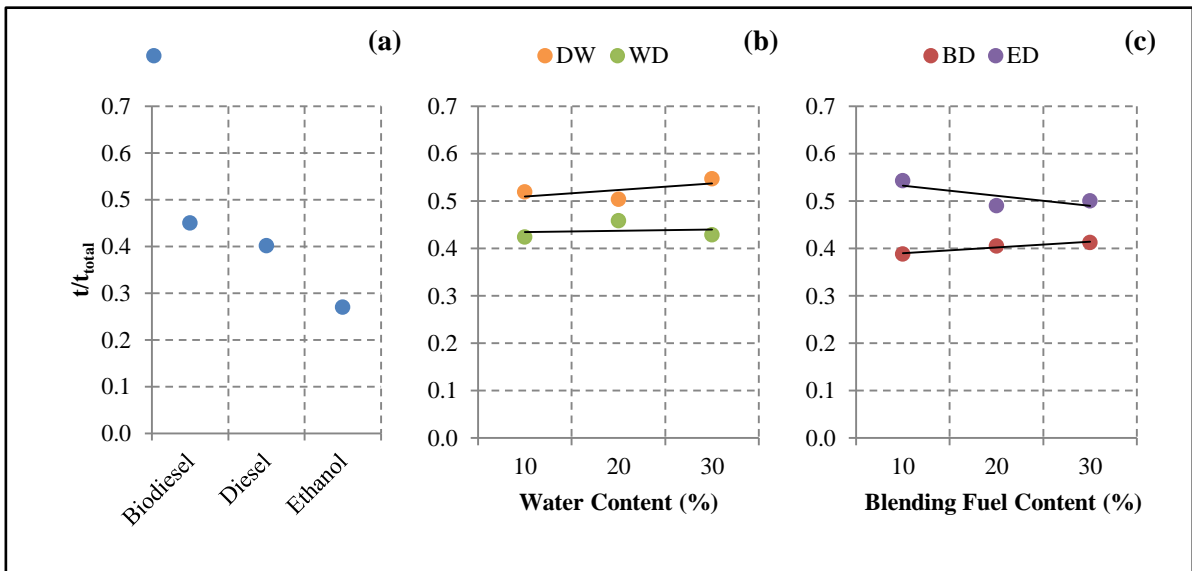
Figure 4-14: Average droplet size increase time with respect to the total droplet lifetime for the: (a) single-component fuel droplets, (b) diesel/water and water/diesel emulsion droplets, and (c) biodiesel/diesel and ethanol/diesel blend droplets.

From the figure, it can be seen that for all the fuels except neat ethanol, the size increase occurrence time is almost the same and it accounts for about 40-50% of the

110

droplet lifetime. This implies that in a large portion – almost half – of its lifetime, the burning multicomponent fuel droplet experiences size fluctuation leading to an increase in its diameter. This fluctuation is basically attributed to the stability of the multicomponent fuel mixture resulting from the miscibility of its components in each other. This is practically interpreted by the nucleation and bubble generation within the liquid-phase of the burning fuel droplet, and the subsequent puffing and secondary atomization.

Altogether, figures (4-11), (4-12), and (4-13) give a broader description for the stability of the multicomponent fuel droplets during combustion. Since, Figure 4-12 gives the average fluctuation rate among the overall droplet lifetime, Figure 4-13 gives the maximum size increase, and Figure 4-14 gives the time portion of that increase with respect to the droplet lifetime.

Hence, recalling the final finding of Figure 4-12 regarding the effect of additive concentration on the variation of average size increase. This effect can be explained in light of the three figures. Firstly, for the emulsions, increasing the water content in the emulsion increases the chance for superheat boiling of water and the resulting nucleation and bubble generation. This in turn, is reflected on the size increase rate and its occurrence time which both are increased for the WD and DW types of emulsions as shown in Figure 4-12(b) and Figure 4-14(b) respectively. Secondly, for the biodiesel/diesel blends, increasing the biodiesel content in the blend resulted in decreasing the average increase rate from 1.5% to 0.6% of the droplet initial diameter, and increasing the occurrence time span from 38% to 42% of the total droplet lifetime as shown in Figure 4-12(c) and Figure 4-14(c) respectively. In other words, the instability in the biodiesel/diesel fuel blend is reflected in the fluctuation time rather than fluctuation intensity. This could be attributed to the sequential combustion of diesel and biodiesel in the blend and the slightly low burning rate of the blends as shown in Figure 4-5. Thirdly, for the ethanol/diesel blends, the fluctuation size increase rate is decreased from 4% to 2.8% of the droplet initial diameter, and the occurrence time also decreased from 55% to 50% of the total droplet lifetime when the concentration of ethanol in the blend is increased from 10% to 30% as shown in Figure 4-12(c) and Figure 4-14(c) respectively. However, as shown in Figure 4-13(c), the maximum size increase is augmented from 23% to 44% by increasing the ethanol concentration in the blend from 10% to 30%. This implies that the mixture instability in the case of the ethanol/diesel blends is reflected in the form of smaller number of large scale fluctuations occurring in a shorter period of time. An example of

these large scale fluctuations is shown in the spikes bounded by the red circles in Figure 4-11.

Finally, despite its representation with respect to initial droplet diameter, the droplet size fluctuation could be instantaneously effective compared to the droplet instantaneous diameter, especially for smaller droplet diameters. Therefore, in order to quantify its significance, the maximum droplet size fluctuation rate is evaluated and normalized by the instantaneous droplet diameter for all the fuels under investigation and plotted in Figure 4-15. As it is shown in the figure, compared to droplet instantaneous diameter, the fluctuation rate is relatively high, and in some cases such as the ED blends, the fluctuation in the size is equivalent to – or even larger than – the droplet diameter. This is especially occurs in the end of the droplet lifetime where droplet diameter is relatively small. Additionally, it can be seen that in the case of DW emulsions, the fluctuations are too small compared to the corresponding WD emulsions and BD and ED blends. This is because the DW fuel droplets did not maintain combustion to the end of the droplet lifetime, rather droplet fragmentation takes place when droplet size still relatively large. Hence, the resulting $\Delta D/D_i$ ratio is high compared to the corresponding multicomponent fuel mixtures that are successfully burning towards the complete evaporation of the fuel droplet.
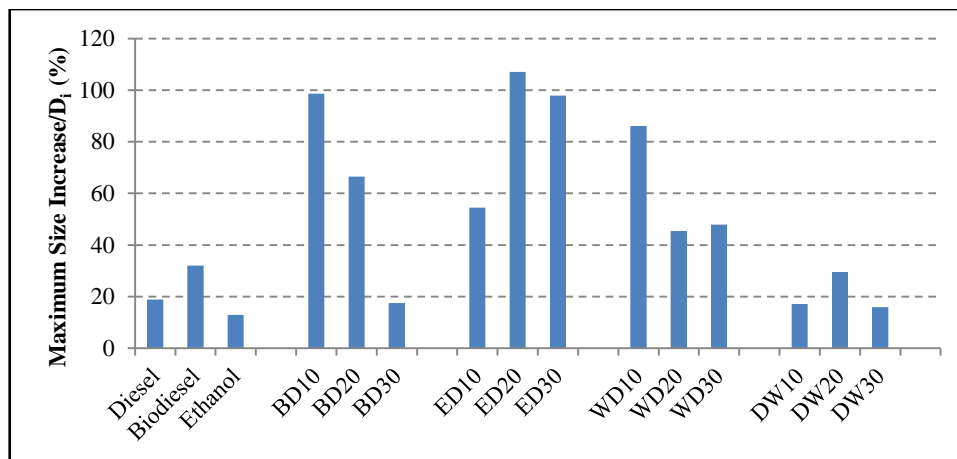
Figure 4-15: Maximum droplet size increase rate normalized with respect to droplet instantaneous diameter for the fuels under investigation.

4.3.5 Flame Characteristics

Figure 4-16 shows sample images of the luminous flame surrounding a WD10 fuel droplet. The first image represents the droplet just before ignition initiation, therefore it is

assigned time (t = 0 ms). The images at times 380 ms and 484 ms show the flame propagation, while the image at time 676 ms demonstrates the maximum dimensions of the flame. The influence of droplet puffing on the shape and appearance of the luminous flame is shown in the images of times 756 ms and 1504 ms. Flame shrinkage and extinction due to complete droplet evaporation and fuel consumption is shown in the images of time periods 1588 ms and 1616 ms respectively.

As shown by the images in Figure 4-16, flame boundaries are well defined and easily distinguished from both the droplet and surrounding environment, giving the opportunity to track and extract flame size variation during the overall combustion time. Additionally, as shown by the images, the effect of forced convection has been eliminated by working in a relatively quiescent environment. However, the natural convection and buoyancy could not be avoided because the experiments are performed under normal gravity conditions.
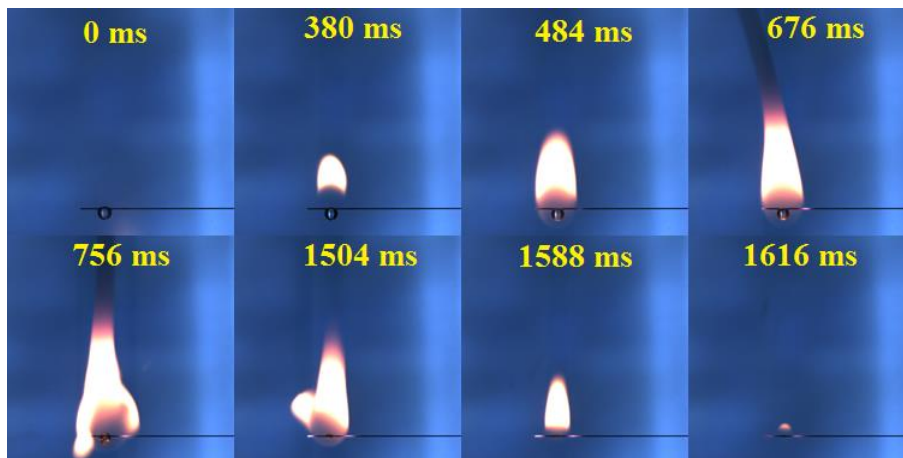
Figure 4-16: Sample images of the luminous flame surrounding a WD10 fuel droplet.

The flame tests have been carried out for all the fuels under investigation, including the single-component fuels – except neat ethanol – and the multicomponent fuel mixtures comprising the blends and emulsions. Ethanol has no luminous flame; therefore it has been excluded from the flame characteristic analysis. Three experimental tests have been performed for every fuel for assuring repeatability. The images obtained from these tests have been processed using the same sequence followed for the droplet image processing described in Chapter Three. The flowchart of flame image analysis is shown in Appendix (E). From the test images, flame height and width variation with time are evaluated. These parameters are normalized with droplet initial diameter for the same reasons mentioned

earlier regarding the elimination of droplet size variation effect on the obtained results, and the applicability of the non-dimensional quantities compared to the dimensional ones.

Figure 4-17 shows the temporal variation of the luminous flame height (H/D_0) and width (W/D_0) with time for the neat diesel and biodiesel fuel droplets. Both the flame height and width have been normalized according to the droplet initial diameter for each fuel. Time as well has been normalized in accordance to the total time required for complete combustion of the droplet, in order to study flame behaviour for all the fuels across the same portion of time. The flame height is assumed to start from the SiC fibre; hence the small portion of droplet size above the fibre has been neglected. From the figure it can be seen that diesel droplet has the highest flame ($H/D_0 \leq 11$) while biodiesel has the lowest ($H/D_0 < 7$). This is attributed to the sooting tendency of the fuels, where biodiesel has a lower sooting tendency compared to diesel that is classified as a sooting fuel. This supports the previous findings of the effect of biodiesel on decreasing soot generation when added to diesel [66,122,128]. This in fact is the idea behind blending diesel with biodiesel.
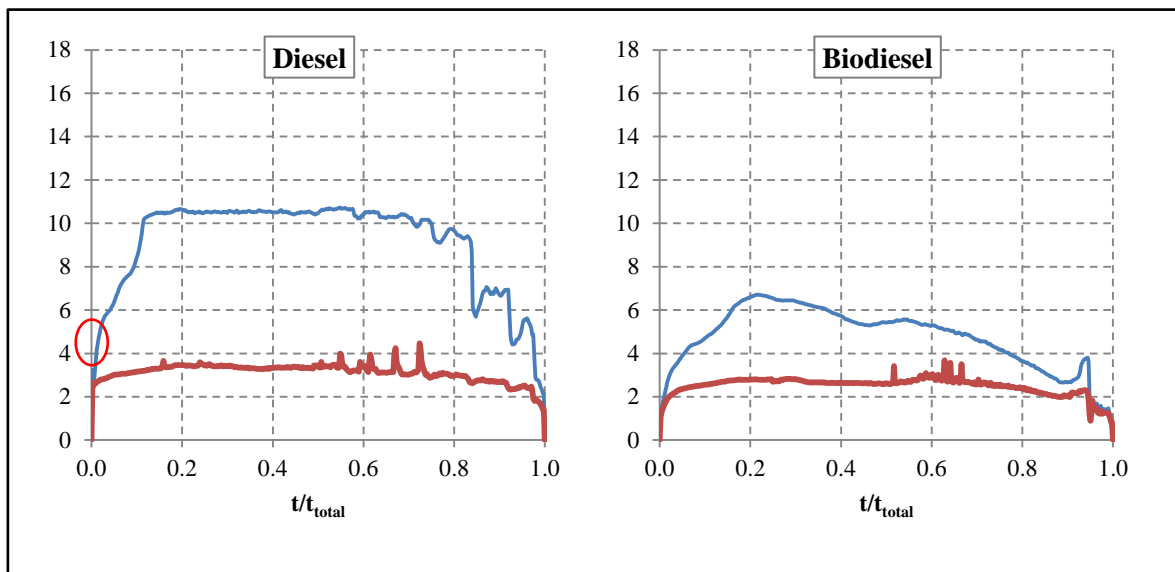
Figure 4-17: Temporal variation of the normalized flame height (blue) and normalized flame width (red) with time for neat diesel and neat biodiesel fuel droplets.

Furthermore, as shown in the flame height (blue) lines of Figure 4-17, there are three distinctive stages in the combustion of the fuel droplet. The first stage is shown in the early 20% of the droplet lifetime, where ignition and flame initiation takes place, followed by flame propagation. The second stage is for the next 60% of droplet lifetime, where steady

burning of fuel takes place, and flame size is relatively constant. And the third stage is the last 20% of the droplet lifetime, where the flame starts to shrink height wise while its width remains almost the same until the final stages of combustion. These stages are shown to occur during the combustion of both the neat diesel and neat biodiesel.

In addition, it is noticed that at the early 10% of the overall droplet combustion time, the diesel droplet experiences dramatic increase in flame height, as shown in the spike bounded by the red circle in Figure 4-17. This luminous flame height increase is further illustrated in Figure 4-18.
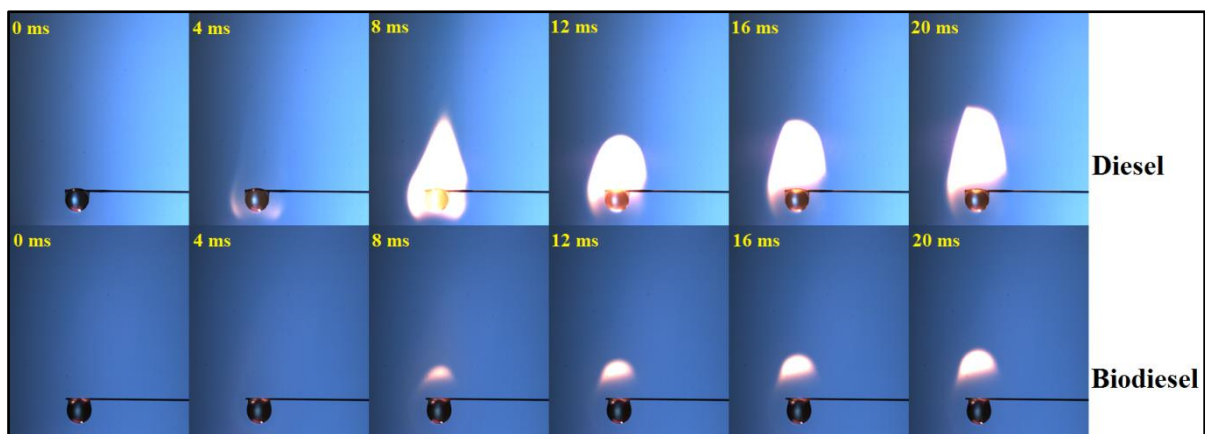
Figure 4-18: Flame increase during the early ignition stage for diesel and biodiesel fuel droplets.

For the diesel droplet, the first image is the droplet just before ignition initiation, that's why it is assigned time (t = 0 ms). In the second image – at 4 ms – the first appearance of the luminous flame takes place. This flame is a faint blue in colour implying a premixed combustion mode rather than the regular diffusion combustion of the liquid fuel droplets [13]. This flame is then followed by the sudden increase in the yellow luminous flame shown in the image of time 8 ms. Thereafter, the flame decreases slightly, and grow again, as shown in the image of time 12 ms and the subsequent images. This increase in flame height is therefore, attributed to the combustion of the diesel vapour that is generated during droplet heating prior to ignition. After the vapour is consumed by combustion, flame height decreases to a certain level that is defined by the rate of diesel fuel evaporation from the droplet surface and the tendency of this fuel to generate soot during combustion. However, this sudden increase in flame height has not been seen for the flame surrounding biodiesel droplets. As shown in Figure 4-18, the biodiesel flame grows gradually without any sudden increase in its dimensions. Additionally, the faint blue flame region in image 4 ms of the biodiesel fuel is barely recognized. This could be

attributed to the flash point of biodiesel that is much higher than that of diesel. This means that biodiesel needs a higher temperature for evaporation and ignition, in addition to the aforementioned low sooting tendency of biodiesel.

Figure 4-19 shows the temporal variation of the normalized luminous flame height (H/D_0) and width (W/D_0) with time for the biodiesel/diesel blends (first row), ethanol/diesel blends (second row), water-in-diesel emulsions (third row), and diesel-in-water emulsions (fourth row), all of 10%, 20%, and 30% additive agent volume fraction in the fuel mixture. From the figure it can be seen that the biodiesel/diesel blends have the most stable flames among all the studied fuel mixtures. This is due to the relatively stable droplet combustion of these blends compared to the other mixtures as shown in the previous sections. Besides, compared to the flame surrounding the neat diesel fuel droplet, the flames of all the diesel-based multicomponent fuels are lower in height and similar in width. Accordingly, lower sooting tendency of the multicomponent fuels is suggested. This is in agreement with the published data for biodiesel/diesel blends [66,299], ethanol/diesel blends [300], and water/diesel emulsions [137,168]. In addition, the three combustion stages shown during the combustion of the single-component fuels, are also recognisable for the multicomponent fuels, especially for the BD and ED blends. However, for the WD and DW emulsions, the third stage is shifting to the final 10% of the droplet lifetime. This is because the emulsion droplets usually suffer from higher rates of puffing leading to the droplet dose not burn steadily to the end of its lifetime – especially in the case of the DW emulsions – therefore, the third stage in the case of emulsions usually starts when the droplet is either partially or completely fragmented resulting in the rapid decrease of flame height in accordance.

Furthermore, the sudden increase in flame height observed during the combustion of the neat diesel droplet has also been observed during the early stages of droplet combustion of the ethanol/diesel blends and water-in-diesel emulsions as shown by the red bounding circles in Figure 4-19. Though, in the case of biodiesel/diesel blends, the sudden increase in flame height is barely recognized to occur during the combustion of the BD10, and its intensity is slightly decreasing with the increase of biodiesel concentration in the blend. This is clearly illustrated in Figure 4-20, especially by comparing the images of time 8 ms for all the blends.
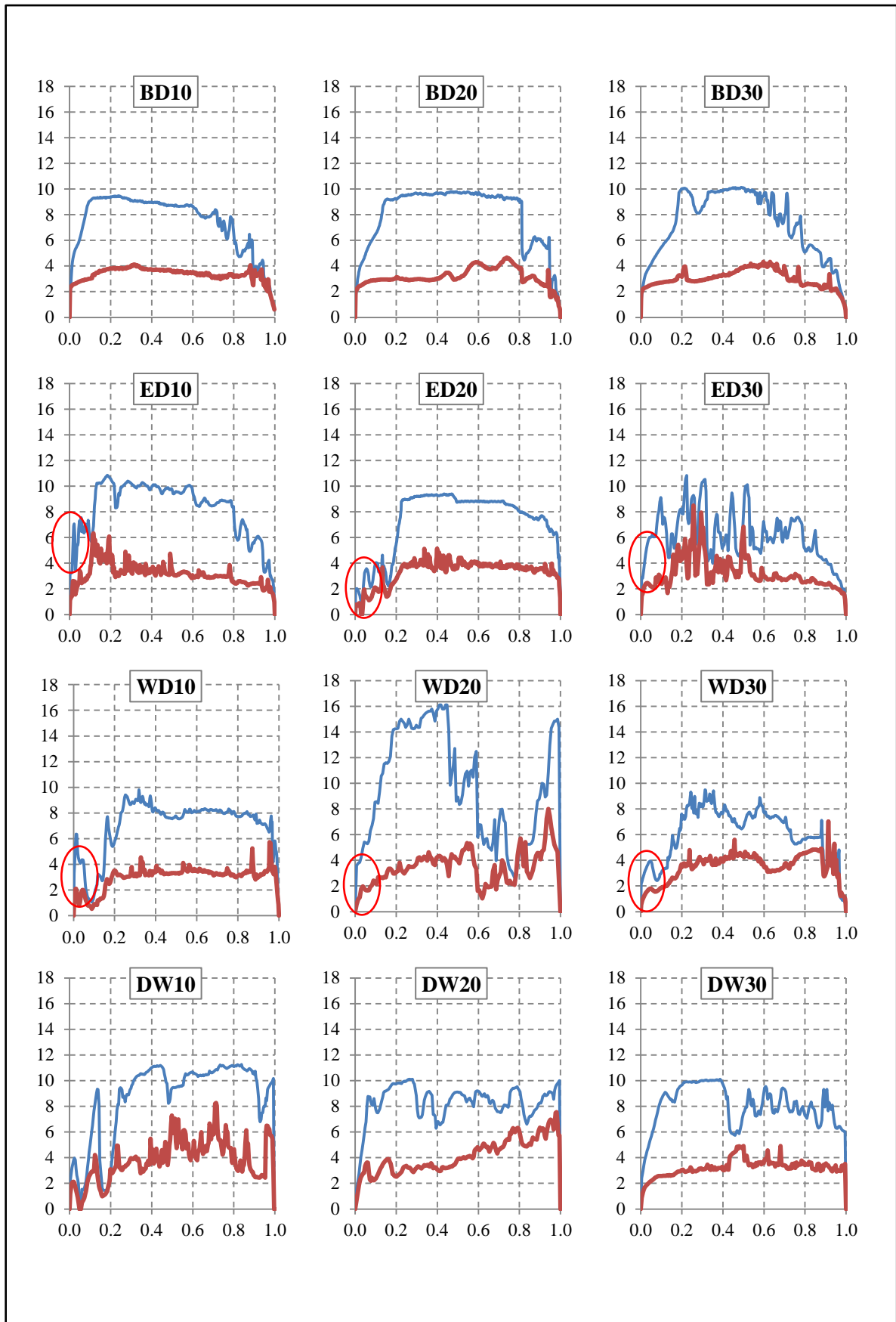
Figure 4-19: Temporal variation of the normalized flame height (blue) and normalized flame width (red) with time for the multicomponent fuel droplets.

117
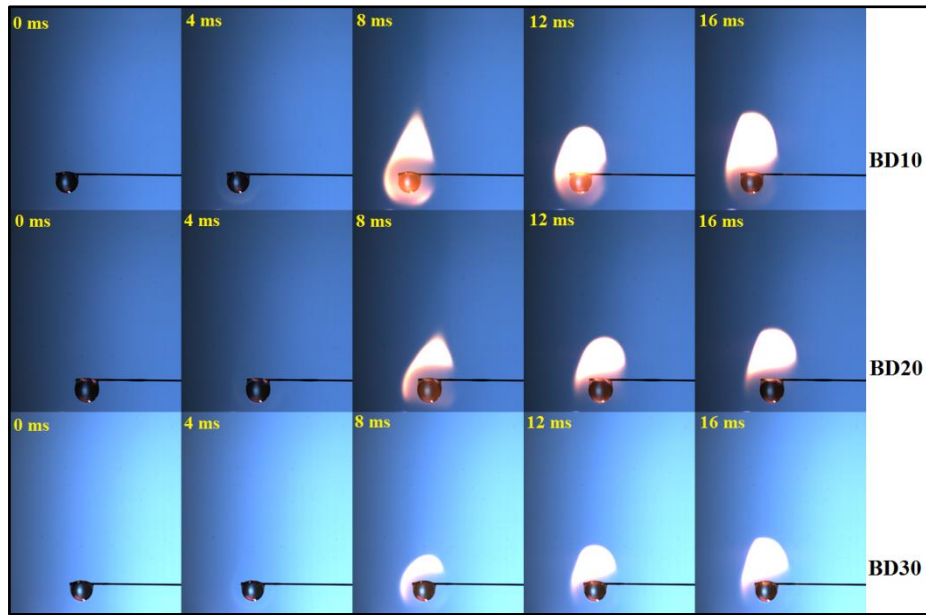
Figure 4-20: Ignition and flame initiation of the biodiesel/diesel blend droplets.

Contrariwise, flames surrounding the emulsion droplets have experienced sudden decrease in the size – both height and width – midterm the droplet lifetime as shown in the WD20 flame in Figure 4-19. This reduction in the luminous flame size is ascribed to the instantaneous blow-off of the flame due to water vapour emission from the droplet by puffing. This water vapour blows the soot – that gives the flame its luminosity – away from the droplet so that the luminous flame height appears to be reduced. This flame blow-off during droplet combustion has also been visualized and described by Teodorczyk and Wojcicki [275] for droplet combustion under forced convection, Yao et. al., [235] for droplet combustion in micro-tube, and Xu et. al., [130] during the combustion of biodiesel/diesel blends. Once the effect of the vapour jet is retracted, soot accumulation upstream resumes, and the flame retrieve its size as shown in Figure 4-21.
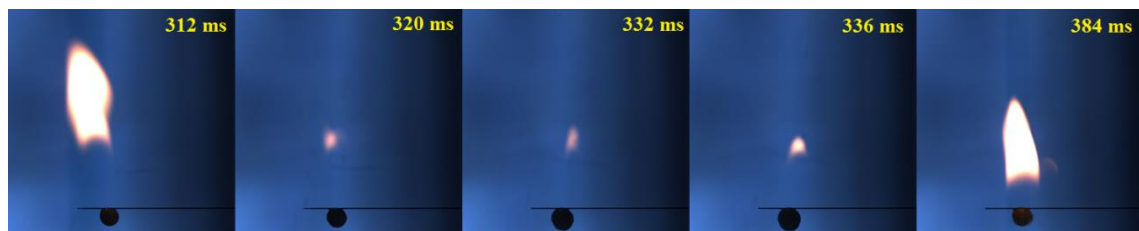
Figure 4-21: Flame size reduction during the combustion of WD20 emulsion fuel droplet.

Moreover, the puffing and secondary atomization has an effect on the shape and size of the flame surrounding the burning droplet. Size wise, this effect appears in the spikes

shown on the flame width (red) lines in Figure 4-19, whereas the effect of these processes on the shape of the flame is shown in Figure 4-22. As shown in the figure, the shape of the flame surrounding the droplet is highly affected by the puffing, leading to relatively considerable fluctuations in the size – especially the width – of the flame.

Figure 4-22: The effect of puffing on the shape of the flame surrounding the burning multicomponent fuel droplets.

The intensity of puffing and its effect on flame shape ranges between the relatively moderate puffing – such as the case of biodiesel/diesel blends – and the chaotic puffing shown in the ethanol/diesel blends. Some of these spikes in the flame width lines of Figure 4-19 are very intensive implying and reflecting a highly intensive puffing or microexplosion. An example of these spikes is the case of ED30 fuel droplet. As explained in the previous sections, the ED blend droplets show off a high degree of instability during combustion due to the metastable structure of the blend. So, the flame size of the ED30 fuel droplet shown in Figure 4-19 reflects this instability. Some sample images of the combustion of this droplet are shown in Figure 4-23.

Figure 4-23: The effect of droplet microexplosion on the shape of the flame surrounding an ED10 fuel droplet.

Finally, since flame width is almost constant and is not affected by buoyancy, it might be considered as the flame diameter. Especially, when compared with flame results under zero gravity conditions, it shows a good similarity in shape and magnitude [301]. Accordingly, with the aid of droplet diameter variation and using the flame width as its diameter, the flame stand-off ratio can be evaluated as the ratio of the flame width to the droplet instantaneous diameter. Figure 4-24 shows the temporal variation of flame stand-off ratio with time for neat diesel and neat biodiesel fuel droplets. The lines terminate when the droplet completely evaporates, while the time represents the full time span from the appearance of the luminous flame around the droplet to the complete flame extinction. As the figure shows, the flame stand-off ratio of both diesel and biodiesel are increasing with time. This is contrary to the D^2-lw predictions shown in equation (2-6) which estimates the flame stand-off ratio as a ratio of a constant quantity (the Spalding transfer number) to another constant quantity (the stoichiometric fuel/air ratio), leading to the stand-off ratio being constant despite the droplet size variation. However, the variable flame stand-off ratio is reported by the majority of experimental work conducted on droplet combustion such as [76,116,236], and is in agreement with the fuel accumulation principles [116]. It can be shown from the figure also that the stand-off ratio of the biodiesel fuel droplet is slightly higher than that of the diesel, which in turn results in the burning rate of the biodiesel is expected to be less than that of the diesel fuel droplet [150]. This is in agreement with the findings of Figure 4-3 that shows a lower burning rate of the biodiesel droplet compared to the diesel droplet.
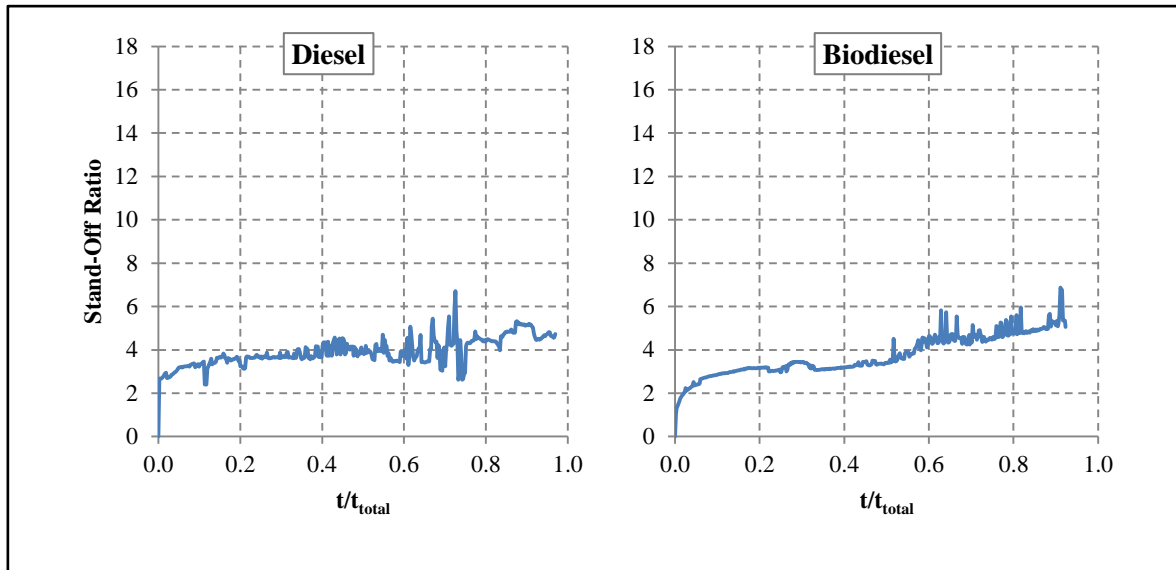
Figure 4-24: Flame stand-off ratio for neat diesel and neat biodiesel droplets.

Figure 4-25 shows the flame stand-off ratio variation with respect to the normalized time for the multicomponent fuel droplets. The first row is for the biodiesel/diesel blends, the second row is for the ethanol/diesel blends, while the third row is for the water-in-diesel emulsions, and the fourth row is for the diesel-in-water emulsions, all of 10%, 20%, and 30% volumetric concentrations of the added substance. The flame stand-off ratio of the multicomponent fuels is shown to be similar to those of diesel and biodiesel both in behaviour and magnitude. However, the fluctuations in the ratio are relatively higher, due to the quite unstable combustion of the multicomponent fuel droplet compared to that of the single-component fuel droplet. Additionally, some steep declines are noticed in the case of the water-in-diesel emulsions and ethanol/diesel blends as shown by the regions bounded by the red circles in Figure 4-25. These declines are due to the flame blow-off effect discussed formerly. Due to this effect, the flame shrinks in width and move away above the droplet as a result of the vapour jet release by puffing, this blow-off terminates and the flame refrain its regular shape and dimensions when the effect of the vapour jet is vanished.
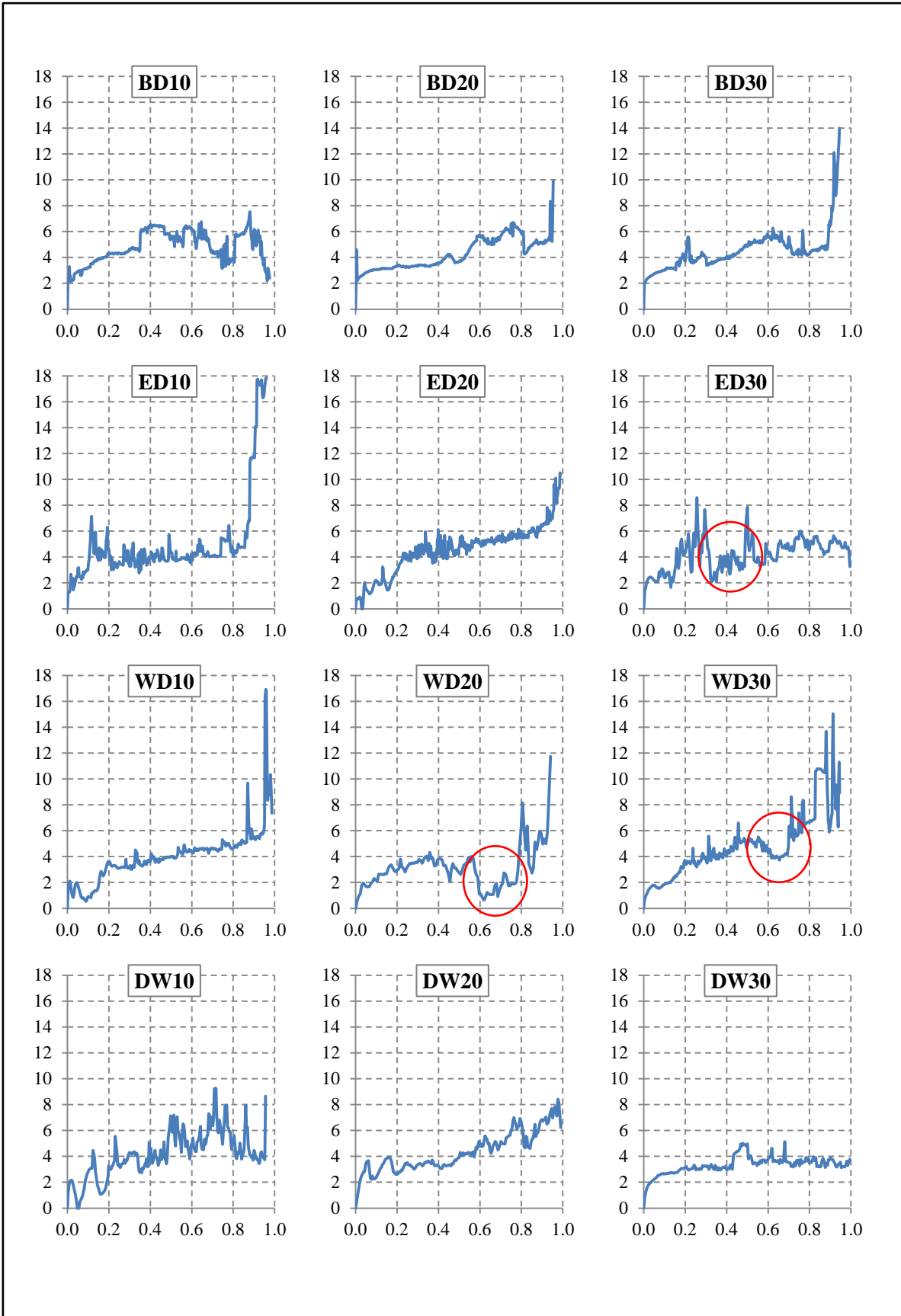
Figure 4-25: Flame stand-off ratio for biodiesel/diesel blend (1st row), ethanol/diesel blends (2nd row), water-in-diesel emulsions (3rd row), and diesel-in-water emulsions (4th row).

122

4.4 Summary

In the present chapter, a detailed analysis of the droplet macroscopic characteristics during combustion is performed. The main objective of this chapter was to validate the results of the present work and evaluate the main features of the droplet combustion for providing quantitative data to the fuels under investigation.

Isolated droplet experiments are carried out for investigating the combustion of the biodiesel/diesel blends, ethanol/diesel blends, water-in-diesel emulsions, and diesel-in-water emulsions in addition to the three single-component fuels, namely diesel, biodiesel, and ethanol.

In the start of the analysis, results validation is performed by comparing the calculated burning rate constants of the three neat fuels with the corresponding values in the published research works. Thereafter, the main characteristic parameters of droplet combustion are presented for all the fuels under investigation. These included the burning rate, droplet size evolution and fluctuation, and flame size.

The next chapters will concentrate on studying the liquid-phase processes occurring during the combustion of the multicomponent fuel droplets. This study is divided into three parts; the first part is the puffing, microexplosion, and secondary atomization during the combustion of the multicomponent fuel droplets. The second part is the nucleation and bubble generation during the combustion of multicomponent fuel droplets. And the third part is the interactive two-droplet combustion of the multicomponent fuels. Hence, in the next chapter, the first part of the liquid-phase analysis is performed.

Chapter 5. Puffing, Sub-Droplets Dynamics, and Micro-Explosion during the Combustion of Multicomponent Fuel Droplet

5.1 Introduction

The combustion of multicomponent fuel droplet is characterized by the occurrence of puffing, secondary atomization leading to sub-droplets generation, and sometimes microexplosion during the overall droplet lifetime. The initiation, development, and effect of these processes on the multicomponent fuel droplet combustion need to be further comprehended. Considering the microscopic size of the fuel droplets within the real spray, studying these processes during spray combustion is quite challenging. Alternatively, these processes can only be extensively investigated using an isolated fuel droplet undergoing combustion. Magnified visualization of the droplet surface and the surrounding environment during combustion will provide more in depth details about the occurrence of puffing and microexplosion, and in turn sub-droplet generation due to secondary atomization of the parent droplet. Although, these processes have been described in the isolated droplet combustion studies as shown in Chapter Two. This description is based on the consequent behaviour of the droplet combustion in response to the action of these processes. However, a detailed experimental investigation of the droplet liquid phase during combustion has not been reported.

Additionally, it is evidenced that some of these processes occur in a very short time interval, such as the microexplosion that is stated to occur in less than 200 μs [4], suggesting that the imaging rate should be higher than 5000 frames per second for the proper tracking of the phenomenon. Therefore, high speed imaging is found to be necessary for studying these physical processes.

Furthermore, in order to track the sub-droplets emitted from the parent droplet it is required to cover a large area around the droplet. This in turn will affect the magnification rate of droplet size image. Hence, in order to attain both droplet size magnification and sub-droplet tracking at the same time, magnified shadowgraph imaging is more preferred in this case than backlighting imaging. This is because the former ensures larger field of

view of the same droplet size compared to the latter, although, the magnification rate provided by backlighting is higher.

Consequently, magnified high speed shadowgraph imaging is implemented in the present chapter for the investigation of isolated multicomponent fuel droplets undergoing combustion. The same shadowgraph imaging setup is then modified into Schlieren imaging setup for tracking the explosion wave resulting from droplet microexplosion. This explosion wave is causing pressure perturbations in the air surrounding the droplet; these perturbations are detected by Schlieren rather than shadowgraphy as shown in Chapter Two. Hence, the wave resulting from droplet microexplosion is used for measuring the explosion intensity of the different fuel droplets.

Finally, in the rest of the chapter, the experimental work is described, followed by the main findings and their discussions. The discussions are started with droplet puffing of the different fuels, then secondary atomization is covered – as a consequence of puffing – with emphasis on the sub-droplet burning, and lastly droplet microexplosion is discussed.

5.2 Experimental Setup

Figure 5-1 shows the general imaging setup for both Schlieren and shadowgraphy. The only difference between the two imaging techniques is the knife edge shown in Figure 5-1 that is removed in the case of shadowgraphy and kept in the case of Schlieren. The Z-type Schlieren and shadowgraph arrangement has been used in the experiments because of the parallel light rays – passing the droplet – that provide better interpretation of the flow field [186]. These light rays are presented by the red lines in Figure 5-1.

The droplet on the other hand, is suspended on the single monofilament SiC fibre as specified in the last chapter. The light coming from the halogen light source is focused and magnified by the 45x condensing lens before reaching the first mirror, and focused again by the 3x condensing lens after passing the second mirror. The high speed camera is set to 10000 fps framing rate, 100 μs exposure time, and 384x288 pixels image resolution. The area covered by the camera was 9.6x7.2 mm^2, giving a spatial resolution of 40 μm/pixel for each image. The magnification rate achieved using this setup is 10 times the physical size without any on-screen magnification. Therefore, a detailed investigation of the instantaneous puffing and secondary atomization, and the consequent droplet shape variation during the overall combustion period is achieved.
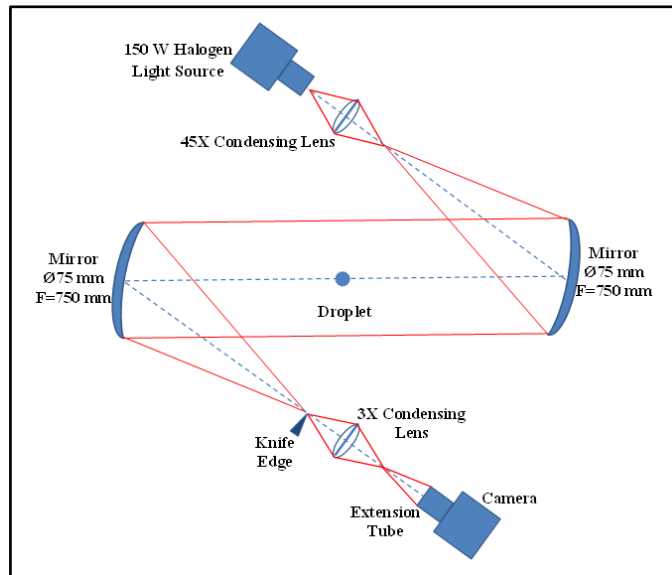
Figure 5-1: Schematic of the z-type Schlieren imaging setup.

The investigated fuels are biodiesel/diesel blends, ethanol/diesel blends, water-in-diesel emulsions, and diesel-in-water emulsions of 10%, 20%, and 30% volume content of the additive to diesel, in addition to the neat diesel, biodiesel, and ethanol as the base single-component fuels. The multicomponent fuel mixtures are prepared in the lab prior to experiments and according to the methods described in Chapter Three. The images have been stored in the (TIFF) format and processed using specially written Matlab algorithms. The flowcharts of these algorithms are shown in Appendix (E).

5.3 Results and Discussion

Figure 5-2 shows two sample images for the droplet using shadowgraphy. The figure shows how the start of combustion is easily recognized by the appearance of the sooty flame. This flame appearance has been used for deciding the start of droplet lifetime and combustion initiation.

Though, as the name of the chapter implies, and as explained in the introduction, the three main characteristic parameters investigated in the present chapter are: droplet puffing, sub-droplet dynamics, and droplet micro-explosion. These parameters are discussed according to the sequence of occurrence with respect to the overall droplet lifetime, starting with droplet puffing and ending with micro-explosion, but first, the puffing behaviour in the single-component fuel droplets is highlighted.
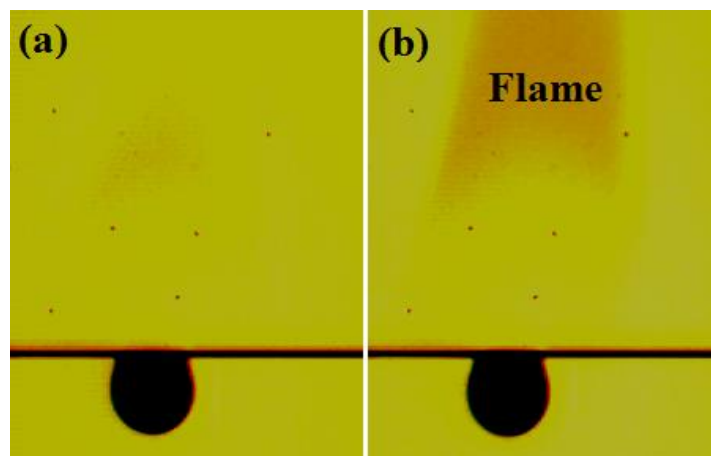
Figure 5-2: Two shadowgraph images of the same droplet (a) before combustion, (b) during combustion, distinguished by the appearance of the flame.

Additionally, it is worthy to emphasise here that the majority of images implemented in the current chapter are numbered from time (t = 0) which represents the start of the event or process described by the images. This believed to be beneficial in giving a better description of the complete real time required by the process discussed in the images. However, some images are numbered with respect to the overall droplet combustion time, since it is believed that describing these images and the corresponding processes with respect to the droplet lifetime is more beneficial than the above described numbering method.

5.3.1 Single-Component Droplets

Generally, the single-component fuel droplets did not experience puffing and secondary atomization occurrences during their lifetimes. However, some odd puffing incidents took place at the end of both neat biodiesel and neat diesel droplets as shown in Figure 5-3 and Figure 5-4 respectively. These puffing events are attributed to the heterogeneous nucleation inside the diesel and biodiesel droplets. This heterogeneous nucleation could be initiated by many reasons, such as trapped gas pockets and unexpected contaminating particles on the SiC fibre section covered by the droplet [123,155], or the effect of the fibre itself. However, the effect of the fibre itself is excluded because this puffing incident did not occur with the neat ethanol droplets. Therefore, the particles or gas pocket effect is more likely to be the reason behind this puffing rather than the SiC fibre.

This is supported by the fact that this puff is the only one occurred in the case of neat biodiesel.
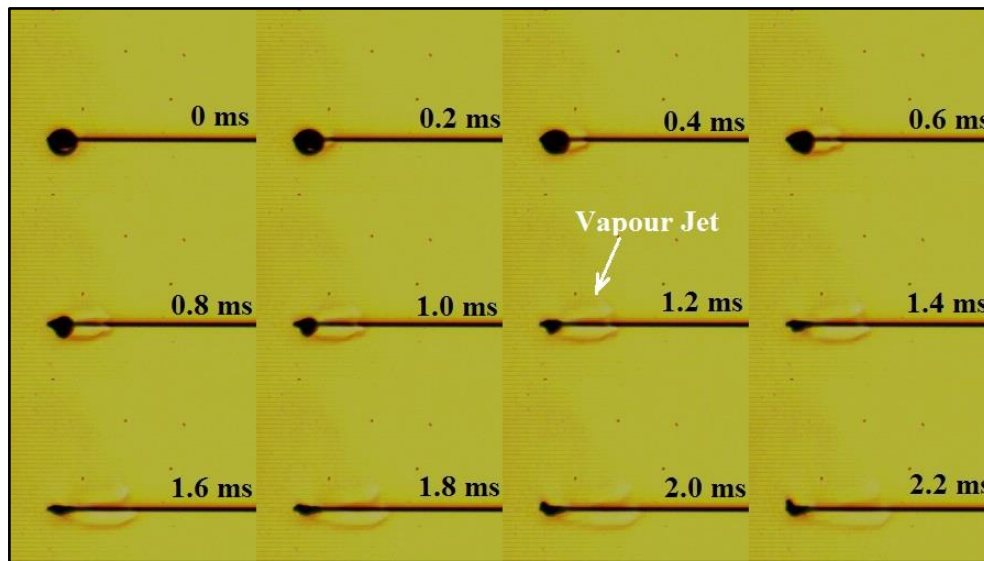
Figure 5-3: Biodiesel droplet puffing sequence at the end of its lifetime (the time starts from puffing initiation).

Although, a slightly higher number of puffs have occurred during the combustion of the neat diesel droplets compared to the corresponding neat biodiesel droplets, which can be linked to the fact that the neat diesel is not a pure substance, rather it is a mixture of different hydrocarbon fuels and additives [13]. Each of these additives has its own boiling point, even if they are comparable to each other. Therefore, puffing occurrence within the diesel droplet is reasonably higher than that of the biodiesel droplet. Figure 5-3 also illustrates the effectiveness of the shadowgraph imaging in tracking the vapour jets emerging from the droplet in the form of puffs. The boundaries of the jets are clearly distinguishable from other objects in the image including the droplet. However, the images shown in the figure are enhanced by 30% brightness reduction for proper visualization.

Figure 5-4 on the other hand, shows the diesel droplet recoiling after puffing occurrence. This recoiling is a result of the interaction between the droplet liquid surface tension (that is pulling the liquid towards the droplet centre) and the reaction force generated by the vapour jet ejection (which is pushing the liquid downwards). Therefore, the diesel droplet is rotating clockwise starting from the right hand side of the image to the left hand side. This movement leads to the gradual disappearance of the bump shown in images 0 ms to 1.6 ms that is initiated originally due to the vapour jet ejection by puffing. And, because the liquids are naturally incompressible, the inward movement of the bump

from the right produced a new bulge in the droplet surface on the left as shown in images 3.2 ms to 6.4 ms, which in turn is pulled inwards by the liquid surface tension. This action and reaction continues until the droplet retains its original circular shape that it has before puffing. The overall time required by the droplet to retain its shape was about 12 ms as shown in Figure 5-4.
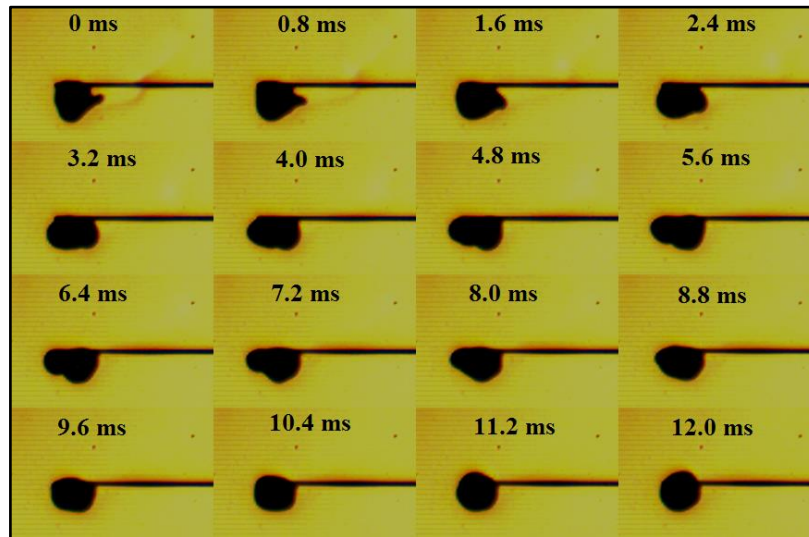
Figure 5-4: Diesel droplet recoiling sequence after puffing (the time starts at the end of puffing).

Furthermore, as it is mentioned above, the neat ethanol droplet did not experience any vapour ejection during its overall lifetime. Instead, it suffered from very small size sub-droplet ejections on the connection point with the SiC fibre as shown in Figure 5-5.
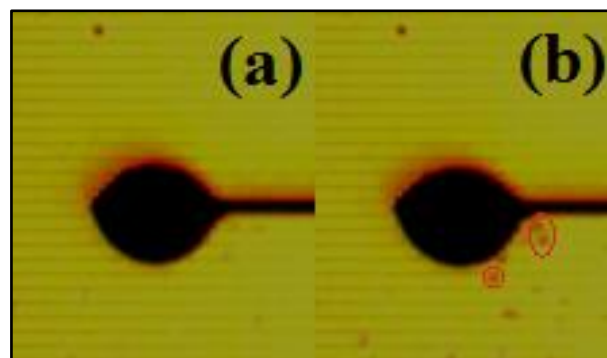
Figure 5-5: Sub-droplets emitted from a neat ethanol droplet.

These sub-droplet ejections are noticed to occur for diesel and biodiesel droplets, and are taking place only on the fibre side (right hand side of the image) rather than the free side (left side of the image). As discussed in Chapter Three and Chapter Four, the effect of

the fibre on the overall droplet burning rate is negligibly small, especially for the large size droplets [281,282]. So, this small effect is appearing on the contact between the droplet and the fibre, since the fibre temperature at that point is relatively higher than that of the droplet surface, causing higher droplet heating and evaporation rates at that point compared to the other regions of the droplet surface. Local boiling of the droplet surface at that point may also take place. This is because the droplet surface is already slightly below the boiling point of the fuel [267], so with the local heat gain from the fibre at that point, the droplet may experience local film boiling or the Leidenfrost effect. This is in agreement with the micro-convection and vortex-like soot flow in the droplet-fibre connection zone described by Liu et. al., [281]. However, these micron-size sub-droplets are very tiny in size compared to the parent droplet, and occurring at a relatively low rate compared to the overall fuel droplet lifetime, therefore, it is believed that the effect of these sub-droplets, and in a broader sense, the effect of the fibre on the overall droplet combustion is negligibly small.

With the puffing behaviour of the neat fuels being clarified and discussed, it is time now to continue the discussions with the puffing occurrence within the multicomponent fuel droplets.

5.3.2 Multicomponent Fuel Droplet Puffing Dynamics

Generally, the droplets of all the multicomponent fuel mixtures studied in the present work have experienced puffing and secondary atomization. The puffing incidents are shown to occur over the entire droplet lifetime. The number and intensity of these puffs are variable for each type of the multicomponent fuel mixtures. The biodiesel/diesel blends have shown the least number of puffs compared to the other mixtures that were relatively comparable to each other. Furthermore, some of the water-in-diesel and diesel-in-water emulsion droplets have suffered microexplosion before undergoing complete evaporation as it is discussed in Chapter Four. This in turn, have resulted in the emulsion droplets experiencing high number of puffs along a short period of time, resulting in higher puffing rates compared to the droplet of the biodiesel/diesel and ethanol/diesel blends. Additionally, despite the type of fuel mixture, almost all the droplets shared the same sequence of events before and during puffing. These events are shown in Figure 5-6 for puffing from an ED20 fuel droplet.
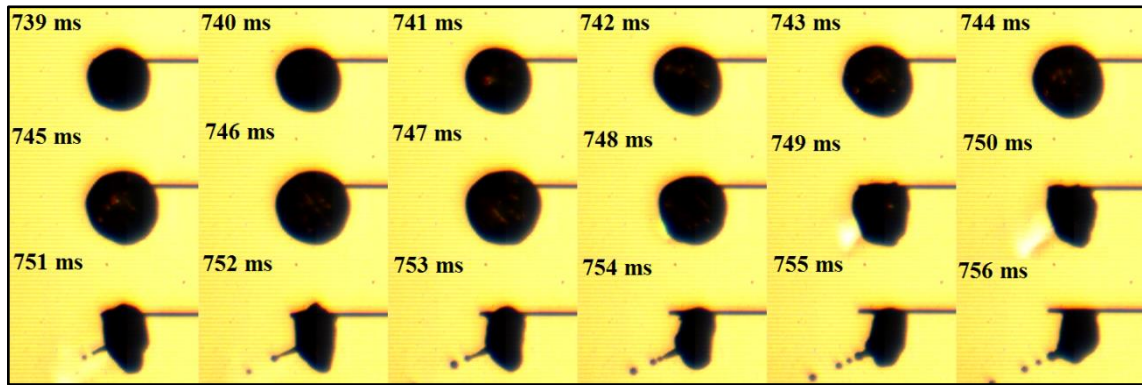
Figure 5-6: Temporal sequence of an ED20 droplet size change before and during puffing.

The first sign of puffing occurrence is the droplet size increase as shown in the images corresponding to time periods 741 ms to 747 ms in Figure 5-6 compared to time periods 739 ms and 740 ms. This increase in diameter is evaluated to be from 1.5 mm on 739 ms to 1.8 mm on 747 ms, which means about 20% of the droplet instantaneous diameter. This droplet size increase is attributed to the bubble growth inside the droplet prior to puffing [125,130]. This bubble continues pushing the thin layer of the droplet surface outwards from inside until the moment when the droplet surface cannot withstand this force, so the droplet raptures locally and the vapour contained in the bubble emerges outside in the form of a jet as shown by the white spray emerging from the droplet in Figure 5-6 images 748 ms to 750 ms respectively. The release of the vapour from the droplet causes sudden size reduction and shape deformation of the burning droplet as shown in images 749 ms to 756 ms compared to images 741 ms to 747 ms. To this point, vapour ejection by puffing is complete. However, different processes will take place within the droplet subsequent to the puffing incident according to the puffing strength [158]. If the puff is weak, the droplet will retain its original shape and size after a short period of recoiling as happened to the diesel droplet shown in Figure 5-4. But, if the puff is strong, ligament detachment from the droplet surface leading to sub-droplet generation will take place as shown in images 751 ms to 756 ms in Figure 5-6 for the ED20 fuel droplet, and Figure 5-7 for the WD10 fuel droplet. In the former, the puffing occurrence gave rise to four sub-droplets that are ejected from the droplet subsequently, whereas in the latter, many sub-droplets are generated and emitted away from the droplet as a result of a strong puff.

The mechanism by which ligament detachment takes place will be further discussed in Chapter Six. But, it should be emphasised here that prior to sub-droplet ejection, the parent droplet is found to encounter a certain shape change that may be linked to the

131

strength of the puff and in turn, to the size of the bubble triggering that puff. An example of this shape variation is shown in Figure 5-7 (image 0.8 ms and the followings). As shown in these images, droplet necking takes place on the droplet/fibre contact region, this necking occurred just after the vapour release. This implies that this necking is a result of the vacuum created on the droplet section near its surface due to vapour release by puffing. To fill up this vacuum and to compensate for the released vapour, droplet edges moved inwards creating this neck. This necking and inward movement may enhance sub-droplet evolution from the parent droplet by the impact of the oppositely moving droplet edges in one hand, and the decrease in sub-droplet ejection area and the resulting increase in the ejection velocity in the other hand. The effect of this necking can be shown by the relatively large number of sub-droplets emerged from the parent droplet during the same puffing incident.
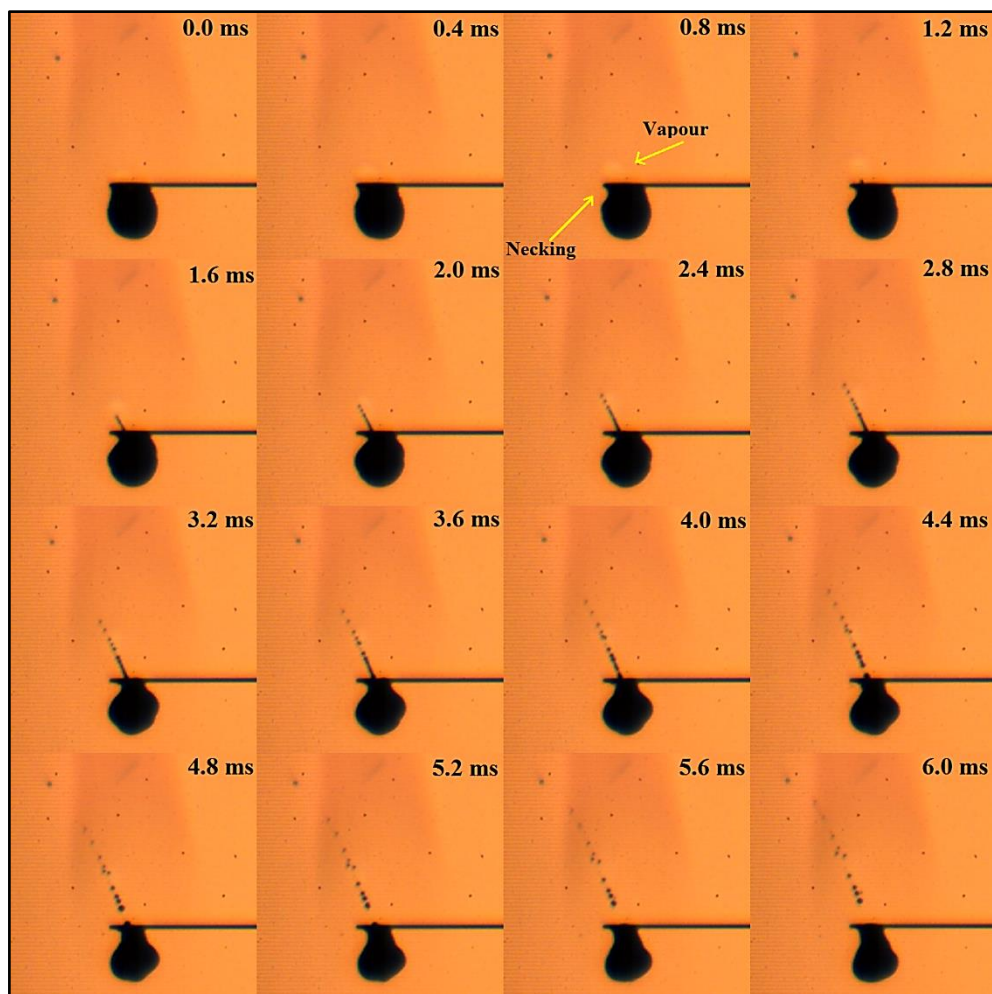
Figure 5-7: WD10 droplet necking prior to puffing and the resulted multiple sub-droplets subsequent an intense puffing incident.

Figure 5-8 gives another example on the effect of the fast motion of the droplet on the generation and ejection of the sub-droplets subsequent to puffing. The figure shows the temporal sequence of vapour puffing from a BD10 fuel droplet during combustion, leading to sub-droplet ejection as a result of the droplet recoiling by the thrust force of the puff. The emerging vapour downwards caused the droplet to move upwards in a reaction to the sudden thrust force of the vapour as shown by the images corresponding to times 0.6 ms and 0.9 ms compared to images 0.0 ms and 0.3 ms. Due to its suspension on the SiC fibre, the droplet upward motion turned into rotation about the fibre, which in turn increased its effect on the droplet surface. Therefore, this upward droplet movement exceeded the liquid surface tension force and resulted in a local disruption of the droplet surface leading to ligament detachment and sub-droplet generation as shown by image 1.2 ms and the following images. Additionally, images a and b in Figure 5-8 show the droplet size increase – although slightly – before puffing. This droplet size increase is attributed to the bubble growth inside the droplet as discussed previously.
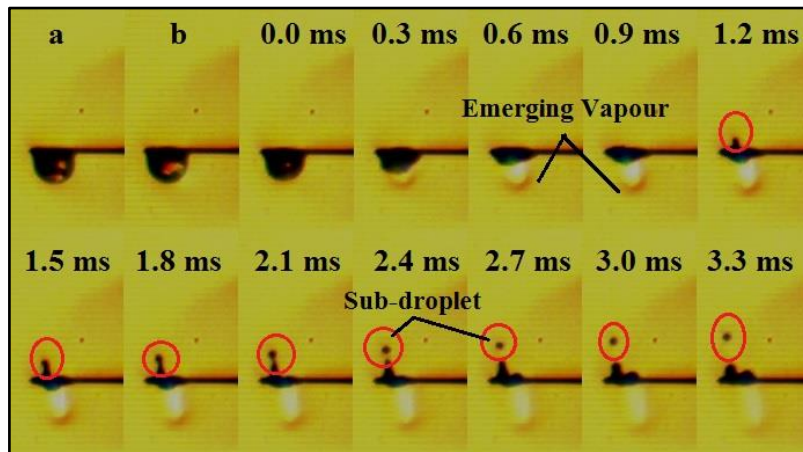
Figure 5-8: BD10 droplet secondary atomization upwards as a reaction to the puffing occurrence downwards (time is set from the start of puffing).

Moreover, the flame blow-off phenomenon presented and discussed in Chapter Four has been clearly revealed using shadowgraphy. Figure 5-9 shows the temporal sequence of flame blow-off during the combustion of a DW10 fuel droplet. Firstly, the flame is close to the droplet as shown in Figure 5-9 (images 361.6 ms to 362.2 ms), then, due to the effect of the vapour jet released by puffing from the droplet surface, the visible flame (or soot) segment that is the nearest to the droplet moves away from the droplet creating a gap with the latter as shown in images 362.6 ms to 366.2 ms. The height of this gap depends on the

intensity and penetration of the vapour jet, and it has been evaluated for the case shown in Figure 5-9 and found to be 2.5 mm from the position of the fibre. This gap decreased again and soot accumulation resumed once the effect of the vapour is vanished as shown in images 368.0 ms to 369.8 ms. This visible flame blow-off phenomenon has been found to occur during the combustion of the water-in-diesel and diesel-in-water emulsion droplets rather than the biodiesel/diesel and ethanol/diesel blends. This suggests that the intensity of the puffs resulting from the emulsion droplets is higher than those of the corresponding blend droplets.
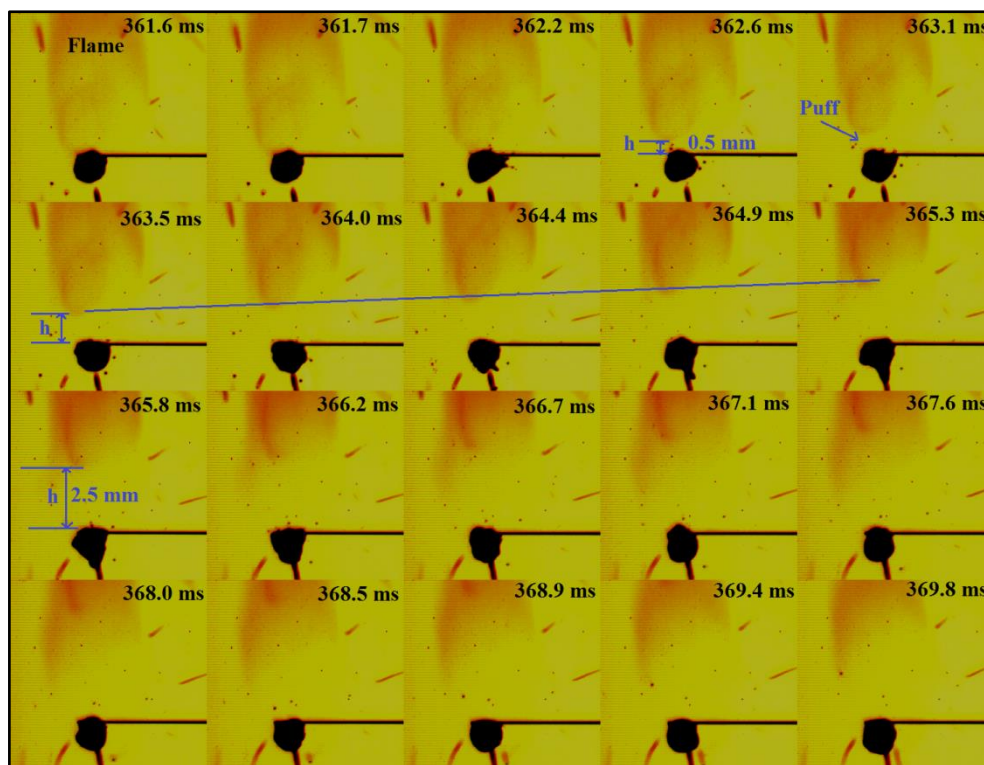
Figure 5-9: Flame blow-off subsequent to vapour jet puffing from a DW10 droplet.

Furthermore, the maximum penetration of the vapour jet is found to be variable, and is a function of the size of the growing bubble within the droplet [153]. This penetration is expressed in terms of the droplet instantaneous radius prior to puffing, and is found to range from a fraction of the droplet radius, as shown in Figure 5-7, to several droplet radii, as shown in Figure 5-10. The figure shows the tip penetration and shape of the vapour jet emerged from an ED10 fuel droplet during combustion. As shown by the figure, the maximum tip penetration of the vapour jet is more than five times the instantaneous droplet radius prior to puffing. However, this value of the jet penetration is not the average range of the vapour jets emerging from the ED10 droplets; rather it is the maximum value. For

that reason, and for characterizing the puffing intensity of the multicomponent fuel mixtures during droplet combustion, the average penetration distance of the vapour jet emerged by droplet puffing is calculated. Another advantage of the vapour penetration calculation is that it describes more the puffing intensity rather than the number of puffs per droplet lifetime. This is because as mentioned earlier, the difference in droplet lifetime between the blends and emulsions – due to emulsion droplets microexplosion – and the difference in droplet instantaneous diameter will result in a non-realistic description of the puffing rate.
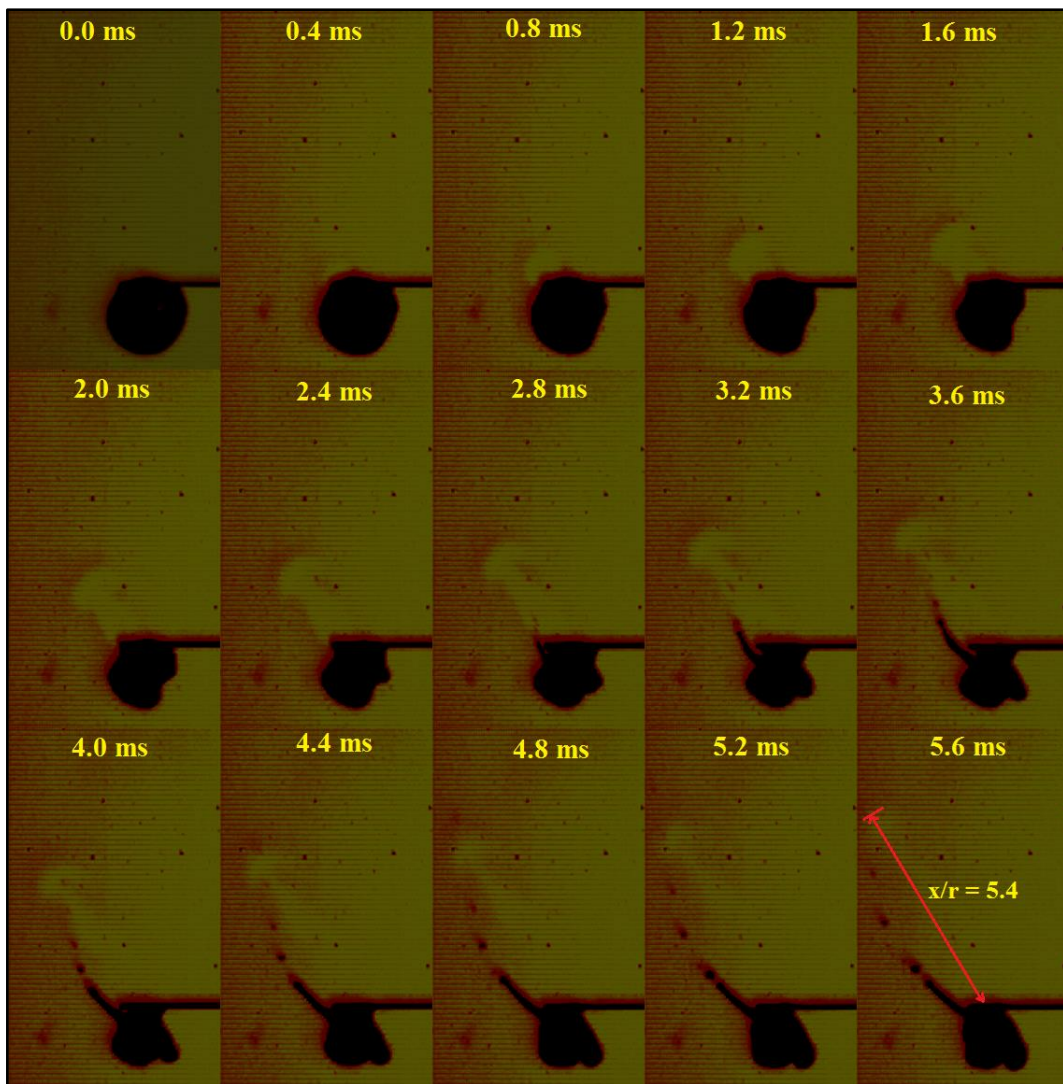
Figure 5-10: Puffing occurrence during the ED10 droplet combustion with an illustration to the shape of the vapour (time is set from the start of puffing).

Additionally, the calculated puffing rate will not be practically worthwhile because, the real droplets in the liquid fuel sprays are order of magnitudes less than the ones studied

135

in the present work, in addition to the lifetime of the real droplet is much less than that of the one studied in-lab. Hence, it is more practically beneficial to evaluate the effect of these puffs firstly, on the neighbouring droplets, and secondly, on the overall spray configuration. Hence the average effective distance – or penetration – of these puffs and the average vapour jet velocity have been evaluated for all the multicomponent fuels and shown in Figure 5-11 against the concentration of the added components (water, biodiesel, and ethanol) to the overall mixture volume. The vapour jet penetration is normalized by the droplet instantaneous radius to give a non-dimensional characterization of the distance. The presented penetration in Figure 5-11 is the average value of all the puffs for each fuel droplet. The average puffing velocity, on the other hand, has been evaluated by dividing the max penetration in millimetre by the total time required in millisecond. The average of all the velocity values calculated from every puffing incident has been evaluated and presented for every multicomponent fuel.
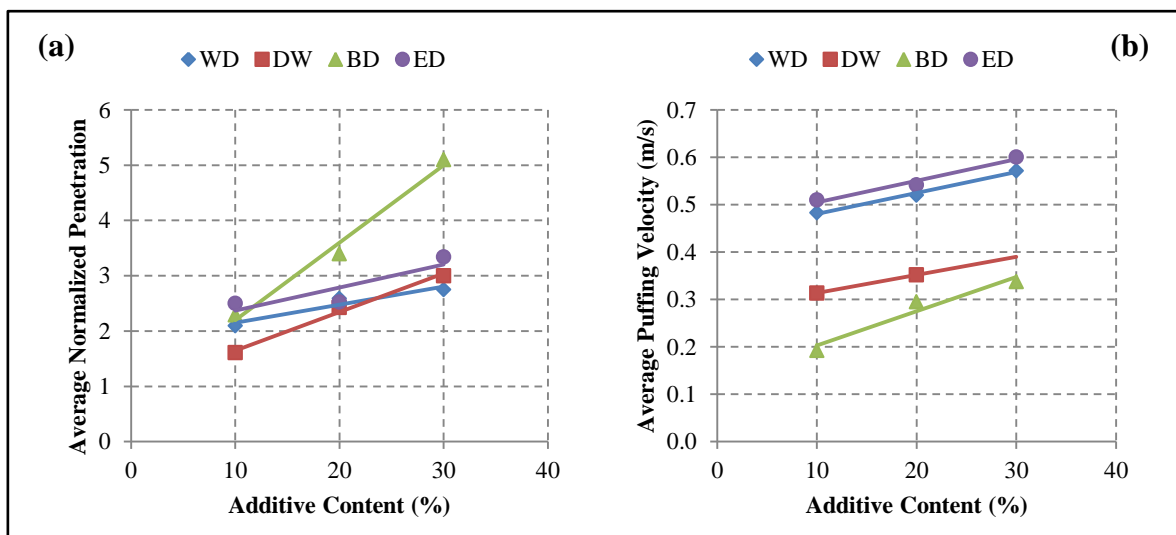
Figure 5-11: The effect of water, biodiesel, and ethanol concentrations on the average vapour (a) normalized vapour penetration, (b) puffing velocity from the burning multicomponent fuel droplets.

As shown in Figure 5-11(a), the average normalized penetration is proportional to the concentration of the added component (whether it is water, biodiesel, or ethanol), so it is increasing by the increase of additive concentration in the fuel mixture for both blends and emulsions. However, this penetration distribution needs to be further comprehended because from the first look it does not interpret the real conditions of the multicomponent fuel droplets. From the figure it may be implied that the BD blend droplets are the ones with the highest penetration and the DW emulsion droplets are the ones with the lowest. In

136

fact, the BD droplets are shown to have the lowest puffing rate among all the multicomponent fuels. But, what is shown by Figure 5-11(a) is the vapour penetration normalized by the droplet instantaneous diameter as mentioned earlier. So, in the case of the BD droplets, firstly the droplet undergoes complete evaporation, and secondly, the puffs take place at the final stages of the droplet lifetime when the droplet diameter is relatively small. Therefore, the resulting penetration to droplet diameter is comparatively high. This is exactly the opposite scenario in the case of the DW droplets. The DW droplet consistently explodes before complete evaporation, and the puffing takes place with the droplet instantaneous diameter is relatively large, so that the resulting normalized penetration is slightly small. The WD emulsions and ED blends on the other hand, have experienced both situations, where complete evaporation takes place in both mixture droplets, and puffing rate is higher and it occurs slightly earlier than that of the BD droplets.

Additionally, it is worthy to mention that the shadowgraph imaging method implemented in the present work provides a 2-D (rather than 3D) visualization of the testing section; and the depth of the testing section is not possible. Therefore, the vapour penetration is only tracked in the xy axes without the z-axis. Hence, any inclination in the direction of the puff cannot be detected. This in turn, may have an effect on the net values of the vapour penetration distance which should be divided by the sine of the inclination angle in the z-direction for obtaining the true value. This inclination angle could be any value from 1º to 89º resulting in a wide range of angle sine values. Thus, the obtained penetration values are more in the qualitative – rather than quantitative – denomination.

Figure 5-11(b) on the other hand, interprets well the real puffing condition, where the WD and ED puffs are faster than those resulting from the DW and BD droplets. As shown by the figure, the average vapour ejection velocity is also increasing with the increase of additive concentration in the multicomponent fuel mixture for all the fuels. As mentioned earlier, this velocity is evaluated according to the total time required by the vapour jet to reach its maximum penetration. However, the initial discharge velocity has also been evaluated and its values are found to be ten times the average velocity shown in Figure 5-11(b). These calculated velocity ranges are in agreement with the 5 m/s discharge velocity reported by Miglani, Basu, and Kumar [153] for water-ethanol mixtures, but less than the predicted values by Shinjo et. al., [158] for the velocity of a vapour emerging from a decane/ethanol droplet. The obtained values for the ethanol/diesel droplets – which are the most comparable mixtures to the decane/ethanol mixture – are in the range of 0.5 to 0.6

m/s whereas the reported value is about 2 m/s and the discharge velocity is 20 m/s. This discrepancy in values between what is predicted and what is calculated experimentally could be attributed to the penetration true value issue raised above, since the evaluated penetration values should be divided by the sine of the inclination angle for obtaining the true values of the puffing penetration distance.

5.3.3 Sub-Droplet Emission by Secondary Atomization

As discussed in the previous section, an intense puffing process is usually followed by sub-droplet ejection from the droplet surface. This sub-droplet ejection – often termed as secondary atomization – takes place either due to the intensive puffing process itself or due the consequent droplet recoiling after puffing. Despite the reason of secondary atomization, its occurrence is beneficial for the overall combustion efficiency of the fuel spray because it enhances liquid fuel evaporation by increasing the surface area and enhances air-fuel mixing as discussed in Chapter Two. Therefore, it is important to examine the tendency of the multicomponent fuel mixture to secondary atomization and evaluate the effect of different proportions of the mixture on that tendency.
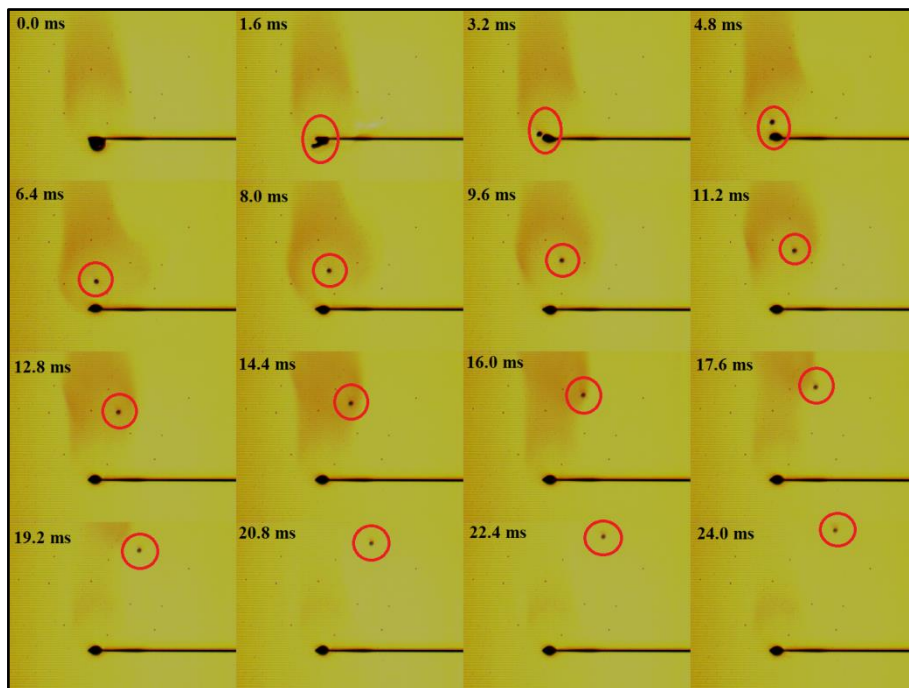
Figure 5-12: Temporal sequence of sub-droplet emission from a burning BD10 droplet.

Figure 5-12 shows the temporal sequence of sub-droplet emission from a BD10 fuel droplet during combustion. This sub-droplet is produced subsequent to droplet recoiling after puffing. The size of the sub-droplet is found to be 0.2 mm whereas the size of the parent droplet prior to secondary atomization is 0.42 mm. The trajectory of the sub-droplet is tracked by the aid of image processing using Matlab. This trajectory is reconstructed and shown in Figure 5-13(a). Using the length of this trajectory and the time required for the sub-droplet to pass it, the flow velocity of the sub-droplet is evaluated and found to be 0.26 m/s which is in the same range with the puffing velocity of the vapour jet shown in Figure 5-11(b) for BD10.
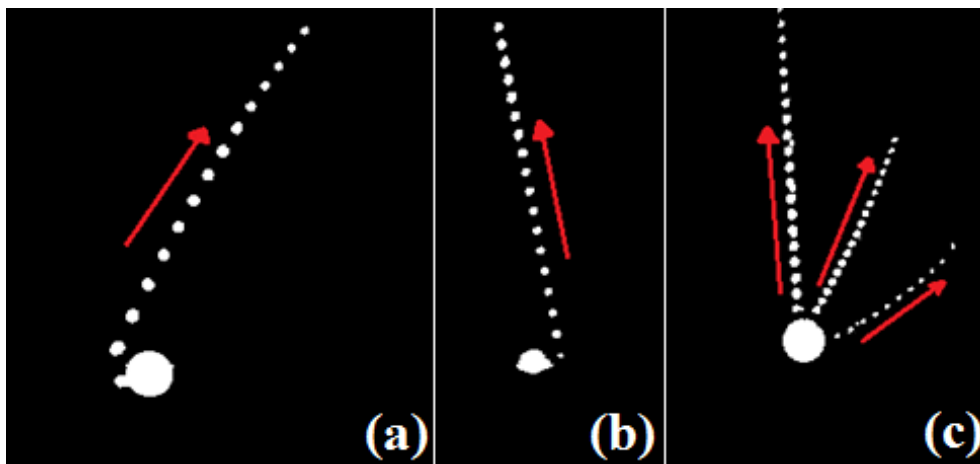
Figure 5-13: Samples of the reconstructed trajectories of single ((a) and (b)) and three (c) sub-droplets ejected from different burning fuel droplets undergoing secondary atomization.

Additionally, as shown in Figure 5-13(c), sometimes multiple sub-droplets are ejected from the droplet surface at the same time. However, the size and velocity of the emerging sub-droplets are not necessarily the same. Sometimes, the emerging sub-droplet is entirely small so that it will evaporate completely once ejected from the droplet surface, such as the sub-droplets emerging from the WD10 fuel droplet shown in Figure 5-7. While, in some instants, the sub-droplet is quite large in size so that it may ignite before undergoing complete evaporation, and in some extreme cases, it may withstand its own surrounding flame for a period of time, such as the sub-droplet shown in Figure 5-14. The sub-droplet shown in Figure 5-14 is initially large in size, and once it left the parent droplet, heating and ignition took place as shown in image 6.9 ms. Due to the motion of the sub-droplet, the flame takes the form of an elongated wake behind the sub-droplet. Another evidence of the sub-droplet large size is its relatively heavy weight that exceeded the buoyancy force

making the sub-droplet to fall by the effect of gravity as shown in images 16.1 ms and the followings.
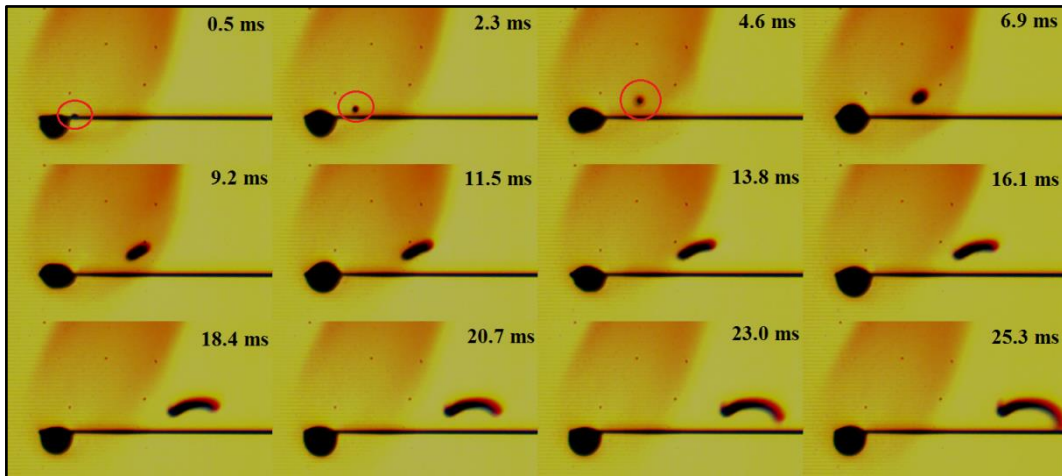
Figure 5-14: Sub-droplet combustion after ejection from a BD10 fuel droplet (time is set from the sub-droplet detachment from the parent droplet).

Likewise the size of the sub-droplets ejected by secondary atomization, the number of these sub-droplets is also important. Despite the fact that the parent droplets under investigation are larger than the real spray droplets. The number of sub-droplets gives an indication of the tendency of the fuel to secondary atomization. Therefore, an algorithm has been developed for counting the number of sub-droplets emitted per incident and the occurrence time, and then the total number of these sub-droplets from the shadowgraph images of the droplets undergoing combustion. The flowchart of this algorithm is sown in Appendix (E), and its execution has been carried out using Matlab.

Figure 5-15 shows the total number of sub-droplets ejected during the overall droplet lifetime for the water-in-diesel and diesel-in-water emulsions, in addition to the biodiesel/diesel and ethanol/diesel blends at all the three proportions 10%, 20%, and 30% additive concentration in the overall mixture volume. As the figure shows, a relatively large variation of the total sub-droplets number is obtained between the four fuel mixtures. Therefore, a logarithmic scale is used for presenting the data in a more comparable configuration. It can be seen from the figure that the number of sub-droplets generated by secondary atomization is proportional to the concentration of both water and biodiesel in the cases of WD emulsions and BD blends, while it is inversely proportional to the water and ethanol concentrations for the DW emulsions and ED blends respectively. This secondary atomization is an indirect consequence of the nucleation inside the droplet

[158]. Bubble nucleation inside the droplet leads to puffing, and puffing is often followed by secondary atomization. Hence, the change in the mixtures trend for secondary atomization may be associated to the bubble nucleation and growth rates within the droplet. It can be noticed also, that despite the difference in values between the mixtures, some similarity in trends is obtained between each two pairs of them. The sub-droplets number in the WD emulsions and the BD blends is shown to increase by increasing the concentrations of both water and biodiesel respectively in the mixture. Exactly the opposite is noticed to occur for the DW emulsions and the ED blends. These different behaviours are sequentially explained.
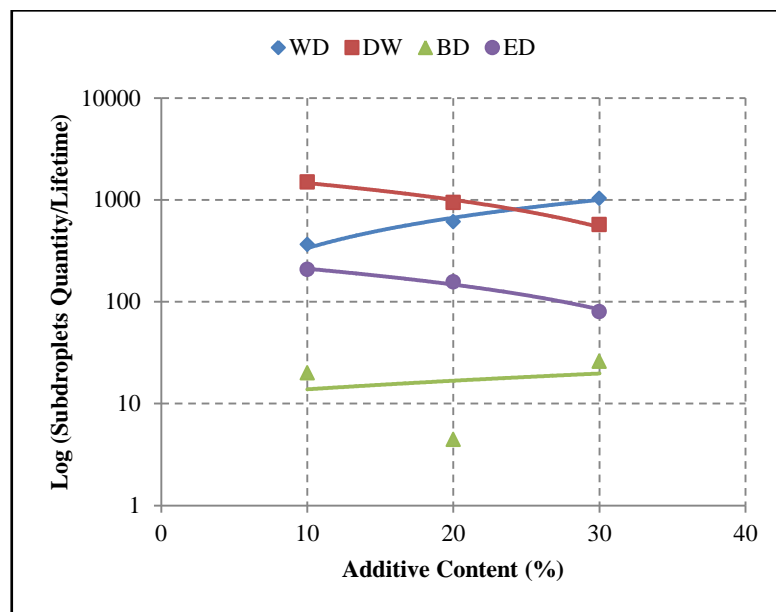
Figure 5-15: The effect of additive (water, biodiesel, and ethanol) concentration on the number of sub-droplets emitted during the overall droplet lifetime of the multicomponent fuel mixtures.

Firstly, regarding the BD blends, both diesel and biodiesel have relatively high boiling points and these boiling points are close to each other despite that of the biodiesel is higher than the boiling point of the diesel as shown in Appendix (B). This low boiling point difference between the BD blend components is not available for the ED, WD, and DW fuel mixtures; therefore, they have experienced higher rates of secondary atomization compared to the BD blends. It is established on the other hand, that the nucleation and bubble growth rate within the liquid-phase of the multicomponent fuel mixture is a function of the boiling point difference between the different components of the mixture [123]. Therefore, this low boiling point difference resulted in lower nucleation rates within the BD fuel droplets and in turn, lower secondary atomization rates. Additionally, the

nucleation rate inside the multicomponent fuel droplet is influenced by the density ratio between the dispersed phase and the continuous phase. The bubble nucleation and growth rate within the droplets of the multicomponent fuel mixtures depends on the densities of the constituents forming the mixture [260]. This is because bubble growth from a higher density liquid to a lower density liquid is certainly different from bubble growth from lower density component to a higher density component. Bubble growth towards the lower density component suggests higher nucleation and growth rates due to the less resistance to the bubble growth, while bubble growth towards the higher density components is suggesting a decrease in the nucleation rate because of the increased resistance to the bubble growth due to the high density of the liquid. Thus for the BD blends, biodiesel is the higher density and higher boiling point component, while diesel is the lower density and lower boiling point component as shown in Appendix (B). Hence, it is expected that the diesel is the constituent undergoing superheated boiling and nucleation, and that bubble growth will take place from diesel to biodiesel. This means bubble growth towards a higher density liquid, suggesting a relatively low rate of nucleation. However, increasing the biodiesel concentration in the blend increased the secondary atomization rate, implying a higher nucleation rate, which is true, but this increased rate of secondary atomization is attributed to increasing the nucleation sites within the droplet by increasing the biodiesel concentration due to the increase in the interference regions between diesel and biodiesel.
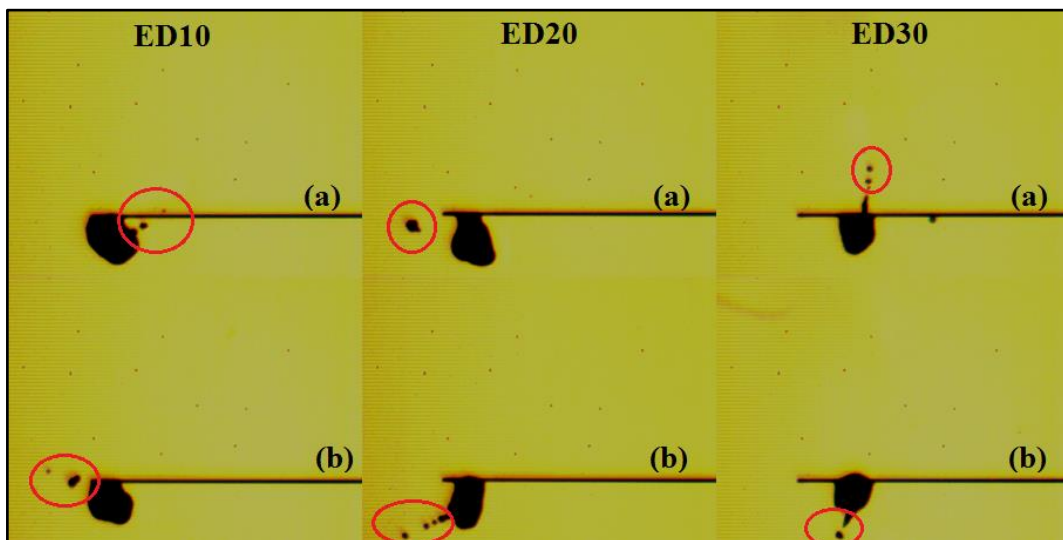
Figure 5-16: Sample images of the large sub-droplets ejected from the ED fuel droplets.

Secondly, regarding the secondary atomization in the ED blends, the scenario is slightly different from that of the BD blends. The boiling point of ethanol is much less than

that of diesel, and the density also is slightly lower. Therefore, in the case of a burning ED fuel droplet, it is expected that ethanol will ignite first due to its higher volatility and lower boiling point, resulting that the diesel will suffer the superheated boiling as in the case of the BD blends. But, the density of ethanol is less than that of the diesel; therefore, nucleation and bubble growth is higher due to the lower resistance of the ethanol to bubble nucleation. This high growth rate within the ED droplets is reflected on the size of the sub-droplets ejected from the parent droplet, the majority of these sub-droplets are of relatively large sizes – in fact they are the largest among the other fuel mixtures – so they are more in the form of large ligaments rather than small sub-droplets as shown in Figure 5-16.

Moreover, it is noticed that increasing the ethanol concentration in the blend resulted in a slight change in the sub-droplet ejection behaviour of the droplet. For the ED10 droplets, multiple sub-droplets are ejected per single incident. The number of these sub-droplets is shown to decrease and their sizes increase when the ethanol concentration is increased. Therefore, in the ED30 case, a single, large sub-droplet is ejected per incident rather than multiple, small sub-droplets. Thus, the number of sub-droplets is shown to be inversely proportional to the ethanol concentration on Figure 5-15.

Thirdly, regarding the WD and DW emulsions, both of the emulsions have experienced a significant increase in the sub-droplet ejection processes. This suggests higher nucleation rates compared to the BD and ED blends. This high nucleation rate of the emulsions compared to the blends has also been described by Lasheras, Fernandez-Pello, and Dryer [123] and is attributed to the large specific volume change of water in the emulsion droplet compared to the components of the blends, in addition to the wide dispersion of water droplets in the emulsion mixture compared to the blends, this in turn, results in higher number of nucleation sites initiation within the emulsion mixture at the same time compared to the blends. These two main parameters led to higher nucleation rates and consequently higher secondary atomization rates from the water-in-diesel and diesel-in-water emulsion droplets compared to the biodiesel/diesel and ethanol/diesel blends. Nevertheless, increasing the water concentration in the emulsions had different effects on the rate of sub-droplet generation from both the WD and DW emulsions as shown in Figure 5-15. The sub-droplet emission rate is shown to increase in the WD emulsions and decrease in the DW emulsions with increasing the water concentration. Sub-droplet generation rate escalation due to increasing the water concentration is expected because of augmenting the nucleation sites by increasing water droplets in the emulsion. But, the decrease in sub-droplet generation shown in the DW emulsions is the unexpected

behaviour. This could be attributed to the effect of surfactant used for emulsion preparation. Because the type of surfactant is the only difference between the WD and DW emulsions, especially with the volume fractions of the constituents are the same. The effect of surfactant weakens with the increase of the emulsion temperature [171]. Therefore, water/diesel separation, and in turn, water coagulation in the centre of the droplet will take place making the droplet to burn in a single-component-like mode rather than multicomponent combustion. This water coagulation is expected to escalate by increasing the water concentration in the emulsions because the same quantity of surfactant is used for all the emulsions, hence, its effect is decreasing with the increase of water volume because of the increased interfacial regions within the emulsion droplet by the increase of water concentration. This water coagulation, then, is the effective parameter in decreasing the number of sub-droplet generation due to nucleation rate decrease [302]. This water coagulation is more revealed during the droplet microexplosion analysis in the next section. However, explosive boiling in the heart of the droplet will continue to occur due to the availability of water.

The same trends of Figure 5-15 are shown in Figure 5-17 which illustrates the effect of added liquid (water, biodiesel, and ethanol) concentrations on the net portion of secondary atomization time compared to the overall droplet lifetime.
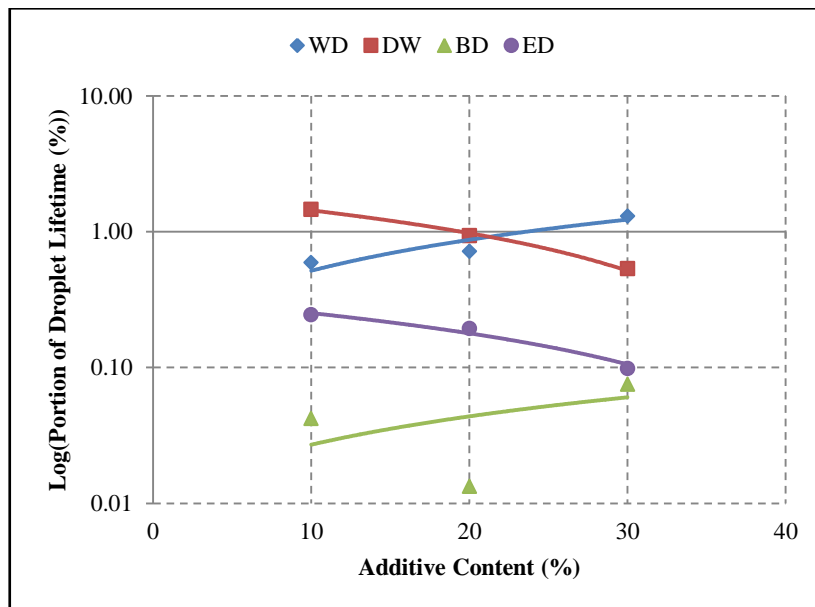
Figure 5-17: The effect of additive (water, biodiesel, and ethanol) concentration on the net portion of the secondary atomization with respect to the overall droplet lifetime.

144

Figure 5-17 represents the ratio of the total period of time (evaluated in µs) where secondary atomization takes place to the total droplet lifetime (also evaluated in µs), to compare the sub-droplet ejection portion with respect to the overall droplet lifetime. The figure has also been presented in the logarithmic form due to the broad difference in magnitudes between the emulsion droplets and those of the blends. As the figure shows, the secondary atomization portion of the droplet lifetime for the BD and ED blends is quite small; in fact it is in the order of $O(10^{-2})$ in the case of the BD blends and $O(10^{-1})$ in the case of the ED blends compared to the overall droplet lifetime. Whereas, it is in the order of $O(1)$ in the cases of WD and DW emulsions. This suggests that the secondary atomization portion of time represents an infinitesimally small percentage of the overall droplet lifetime. However, this small percentage is important for enhancing fuel evaporation and increasing fuel-air mixing. Thus, increasing this portion of time is important as well. Additionally, as it is discussed above, the figure shows that this portion of time is proportional with the volume fractions of both water and biodiesel in the WD emulsions and BD blends respectively, and is inversely proportional to the volume fractions of water and ethanol in the DW emulsions and ED blends respectively.

Furthermore, in spite of its small percentage in the droplet lifetime, secondary atomization of the multicomponent fuel droplet is found to occur at certain intervals of this lifetime. Hence, these intervals may represent the best occurrence probability for droplet secondary atomization of each fuel. Thus, Figure 5-18 shows the secondary atomization occurrence probability with respect to the droplet lifetime for all the multicomponent fuel mixtures under investigation. Generally, the figure shows that each of the four mixtures is following a certain atomization trend that is different from the other mixtures. And that this trend is responsive to the increase of the additive in that mixture.

For the biodiesel/diesel blends shown in the first row of Figure 5-18, it can be seen that the droplet secondary atomization is more likely to start after the first 20% of the droplet lifetime after the heating up period described in Chapter Four. And that its maximum occurrence probability is shifting from the early 30% for BD10 forwards to midterm the droplet lifetime for the BD20 and BD30 blends. This suggests that the peak sub-droplet population is increasing with increasing the biodiesel concentration in the blends. This sub-droplets proportionality with concentration is shown also in the case of the ethanol/diesel blends in the second row of Figure 5-18. For these blends, the secondary atomization is shown to take place after the first 10% of the droplet lifetime, so it is slightly earlier than that of the BD blends.
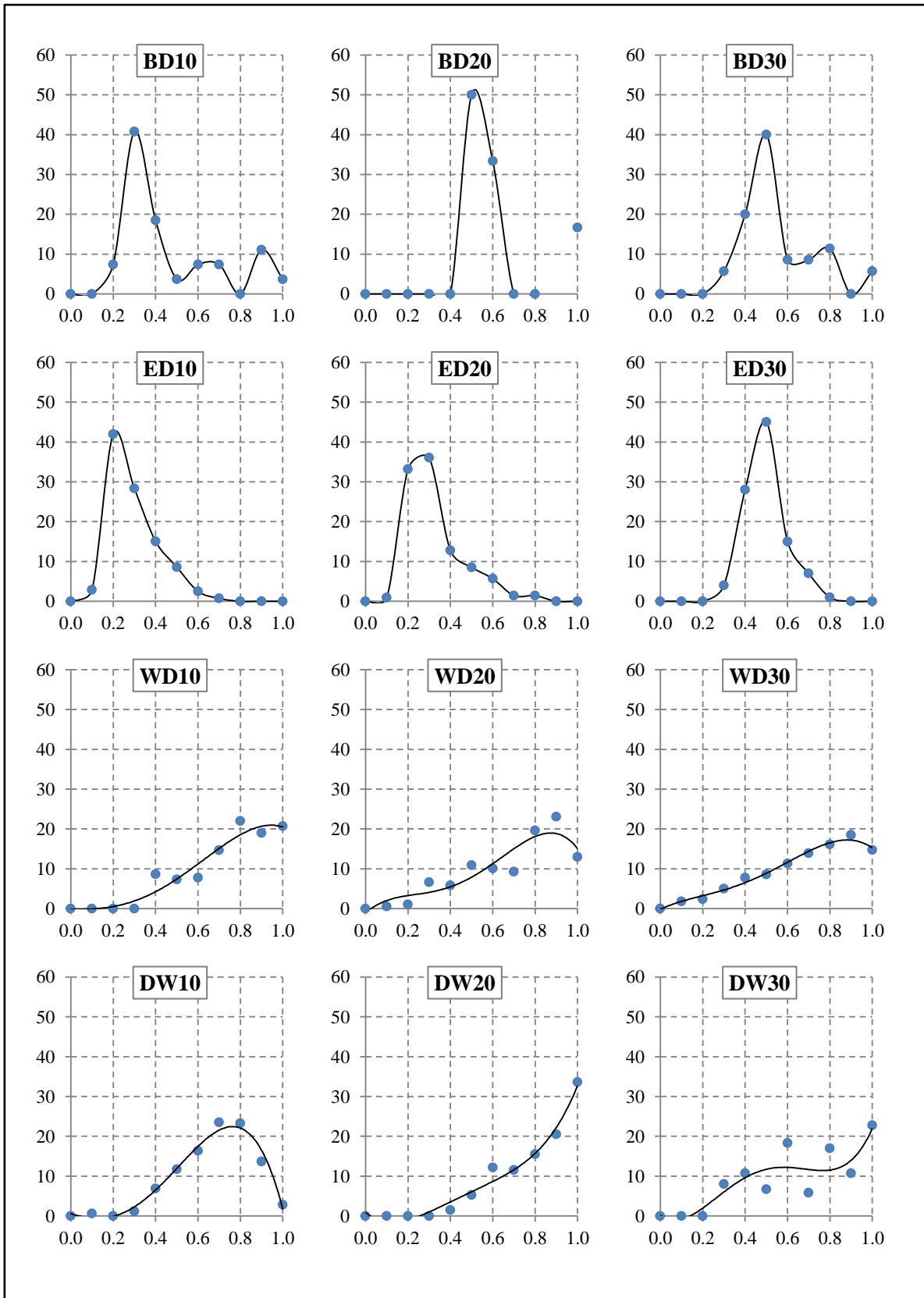
Figure 5-18: Sub-droplet ejection probability (%) – y-axis – with respect to the normalized droplet lifetime – x-axis – for biodiesel/diesel blends (1st row), ethanol/diesel blends (2nd row), water-in-diesel emulsions (3rd row), and diesel-in-water emulsions (4th row).

This trend is in agreement with what is found by Miglani, Basu, and Kumar [153] for bubble generation within the ethanol multicomponent mixtures.

The third row of Figure 5-18 shows the secondary atomization occurrence probability for the water-in-diesel emulsions. Secondary atomization in this mixture is slightly different from those of the BD and ED blends. It starts after the first 10% of the droplet lifetime and continues to increase with time until reaching its peak slightly before the end of the droplet lifetime. This is the same trend as those of the diesel-in-water emulsion droplets shown in the fourth row. This continuous increase in secondary atomization indicates the high degree of nucleation within the liquid-phase of the droplet compared to the blends. Especially, when the droplet diameter decreases with time. This is in agreement with the onset rate distribution of secondary atomization obtained by Tsue et. al., [171] for n-dodecane/water and n-tetradecan/water emulsions.

Figure 5-18 shows also that except the probability shift shown in the blends, the concentration of the additive (water, biodiesel, and ethanol) have no effect on the secondary atomization occurrence probability along the droplet lifetime. However, for the samples analysed, the starting time of secondary atomization is shown to be responsive to the concentrations. This is illustrated clearly in Figure 5-19 which demonstrates the total interval of time between the first and final occurrences of droplet secondary atomization for all the multicomponent fuel mixtures under investigation. This figure gives an overview about the sub-droplet emission trend for every fuel.
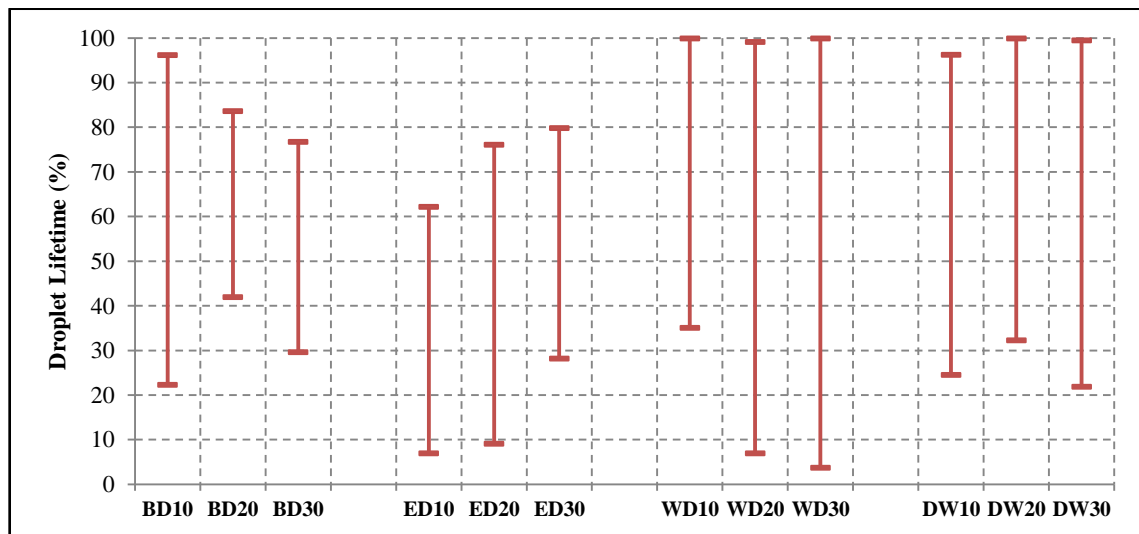
Figure 5-19: The portion of the total secondary atomization period with respect to the overall droplet lifetime for all the multicomponent fuel mixtures under investigation.

From Figure 5-19 it can be seen that the emulsion fuel droplets are experiencing secondary atomization along almost the whole period of their lifetimes, whereas secondary atomization of the blend fuel droplets constitutes half of that period in average. This is attributed to the higher nucleation rate within the liquid-phase of the emulsion droplets compared to that of the blend droplets. Furthermore, it can be noticed from Figure 5-19 that the secondary atomization in the emulsion droplets almost lasts to the end of the droplet lifetime. This is because the emulsion droplets usually do not undergo complete evaporation; instead droplet microexplosion takes place fragmenting the droplet into smaller size sub-droplets. This phenomenon did not occur during the combustion of the biodiesel/diesel and ethanol/diesel blends, so that secondary atomization from the droplets of these mixtures does not last to the end of the droplet lifetime. This emulsion droplet microexplosion has been further investigated in the next section for acquiring more insight information to help comprehending this phenomenon that is associated to the combustion of the emulsion fuel droplets.

5.3.4 Emulsion Droplet Microexplosion

Most of the emulsion droplets prepared and tested in the present work have endured microexplosion before complete evaporation of the liquid-phase. This explosion is attributed to the explosive boiling of the water droplets inside the emulsion droplet [143].

Although, it is reported that the time scale required for this explosion is longer than the time scale available for the real spray combustion [151,161]. But, as shown by Figure 5-20, the ejected sub-droplet have experienced microexplosion causing its fragmentation and evaporation after 4.33 ms of ejection. The sub-droplet initial diameter and explosion diameter are calculated to be 45 μm and 31 μm respectively. These diameters are comparable to the diameter range of the real spray droplets. Thus, comparing the combustion time values evaluated in Table 2-2 in Chapter Two with the time required by the sub-droplet shown in Figure 5-20 it can be inferred that in the real combustion applications – such as the internal combustion engine – there is enough time for the real spray droplets to undergo heating, phase separation, and complete microexplosion, even at low possibilities. Therefore, further investigation of droplet microexplosion is required for comprehending the current understanding of this phenomenon.
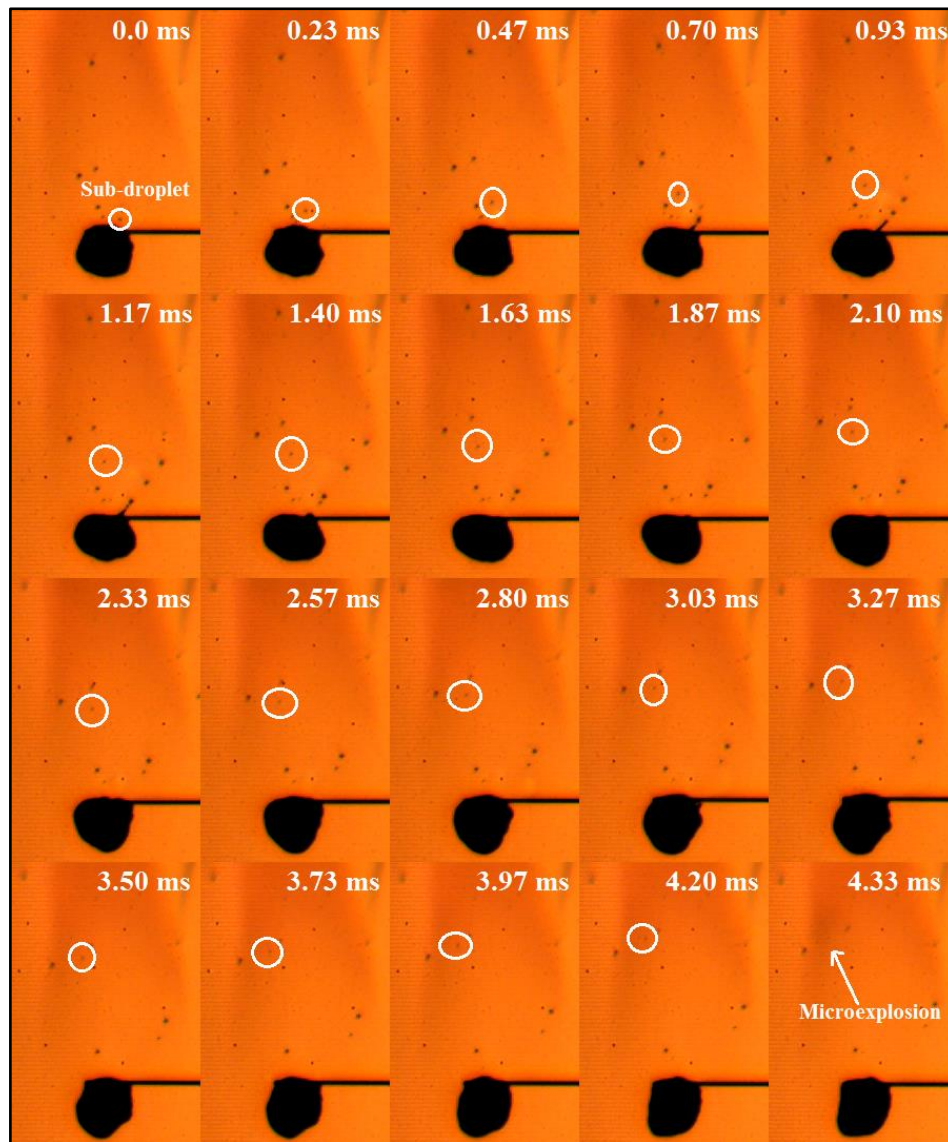
Figure 5-20: The temporal evolution of sub-droplet ejection from a WD10 emulsion droplet illustrating the sub-droplet microexplosion after a period of time (time is set from the sub-droplet detachment).

However, in spite of the enhanced visualization of the droplet surface and the associated processes such as puffing and secondary atomization – as shown in the previous sections – the shadowgraph imaging method implemented in the present investigation did not provide the proper tracking images of the explosion even with the high framing rate used during experimentation. Therefore, the same shadowgraph setup has been modified and turned into Schlieren system by the introduction of a sharp knife edge between the second mirror and the condensing lens as shown in Figure 5-1. Accordingly, a density difference is created across the knife edge increasing the possibility of visualizing the flow of air within the imaging section. This in turn, gave the privilege of tracking the effect of droplet microexplosion on the surrounding air as shown in Figure 5-21.
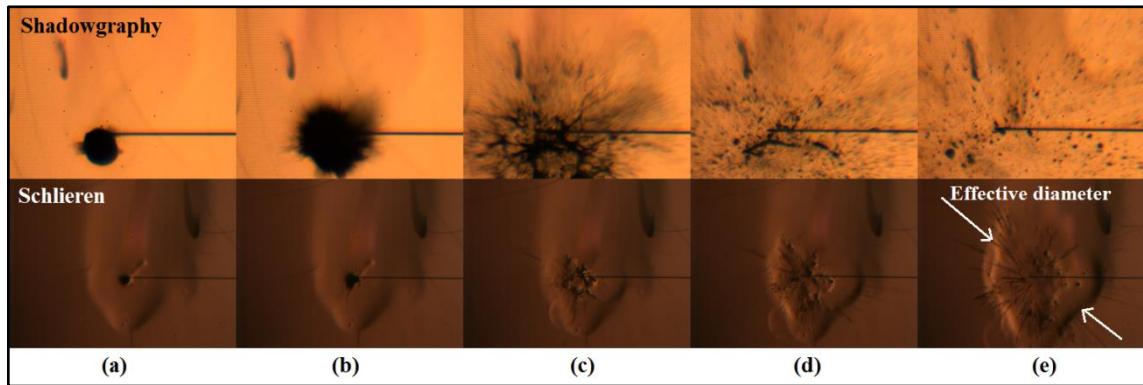
Figure 5-21: Comparison of the WD10 droplet microexplosion images obtained by shadowgraphy and Schlieren methods.

Thus, using this imaging method, the temporal evolution of the explosion wave and its effective diameter in addition to the droplet explosion diameter have all been studied for the water-in-diesel and diesel-in-water emulsion droplets of 10%, 20%, and 30% water concentrations in the emulsion. Every fuel mixture has been tested five times, and the average results of these trials are presented in the current section.
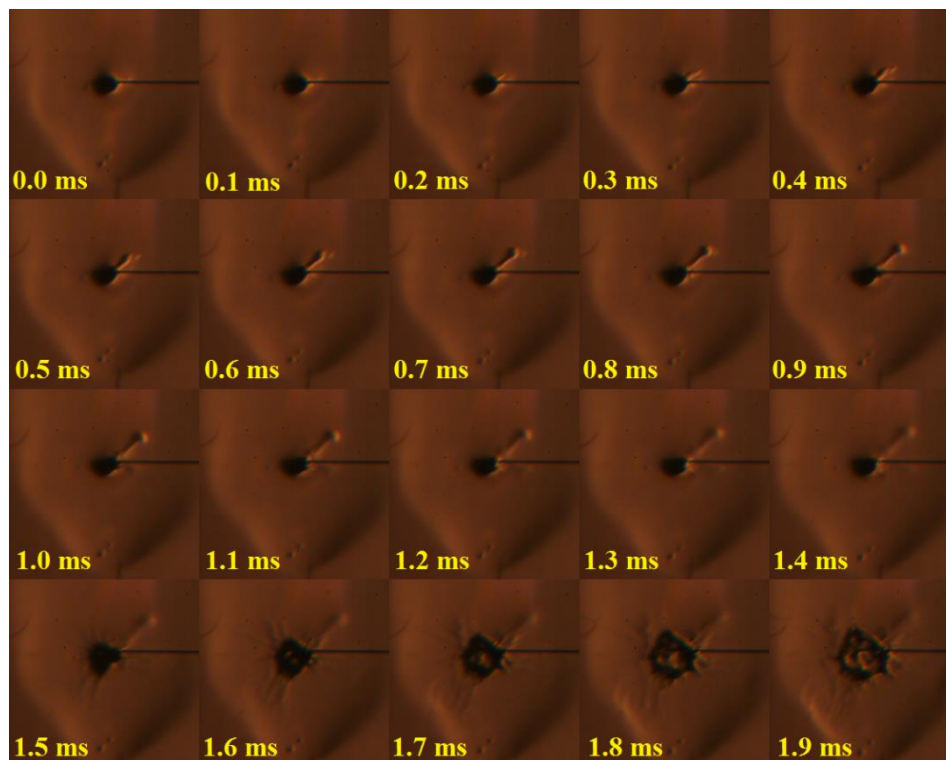
Figure 5-22: Temporal sequence of microexplosion initiation on the surface of a WD10 emulsion droplet (time is set from the start of microexplosion).

Generally, droplet microexplosion is shown to initiate locally in a single site on the droplet surface as shown in Figure 5-22. This has happened for all the tested droplets and for all mixture proportions, proving that droplet microexplosion is basically the result of a catastrophic burst of a single bubble inside the droplet. This bubble pushes the droplet surface outside under the action of the high pressure of the bubble interior causing the droplet to completely disintegrate into smaller size sub-droplets.

Figure 5-23 shows the effect of water concentration in the emulsion on the droplet explosion diameter normalized by the initial droplet diameter for both the water-in-diesel and diesel-in-water emulsion droplets. The explosion diameter is meant to be the droplet diameter at the instant of explosion initiation. First of all, the range of explosion diameter for both emulsions is the same, which is between 0.8 and 1.2 of the droplet initial diameter. Then, this diameter is shown to be susceptible to the variation in water concentration in the emulsion. It is proportional to this concentration in the case of the WD emulsions and inversely proportional in the case of DW emulsions. This proportionality variation between the WD and DW emulsions can be explained in the same way Figure 5-15 and Figure 5-17 were explained. The increased nucleation rate with increasing water concentration in the case of the WD emulsion droplets causes the instantaneous droplet size to increase as a consequent of the bubble growth inside the droplet. While, increasing the water concentration in the DW emulsion droplet increases the water/diesel separation and in turn water coagulation, leading to the decrease in the rate of nucleation within the DW emulsion droplet, and relatively supresses the droplet size increase by nucleation.
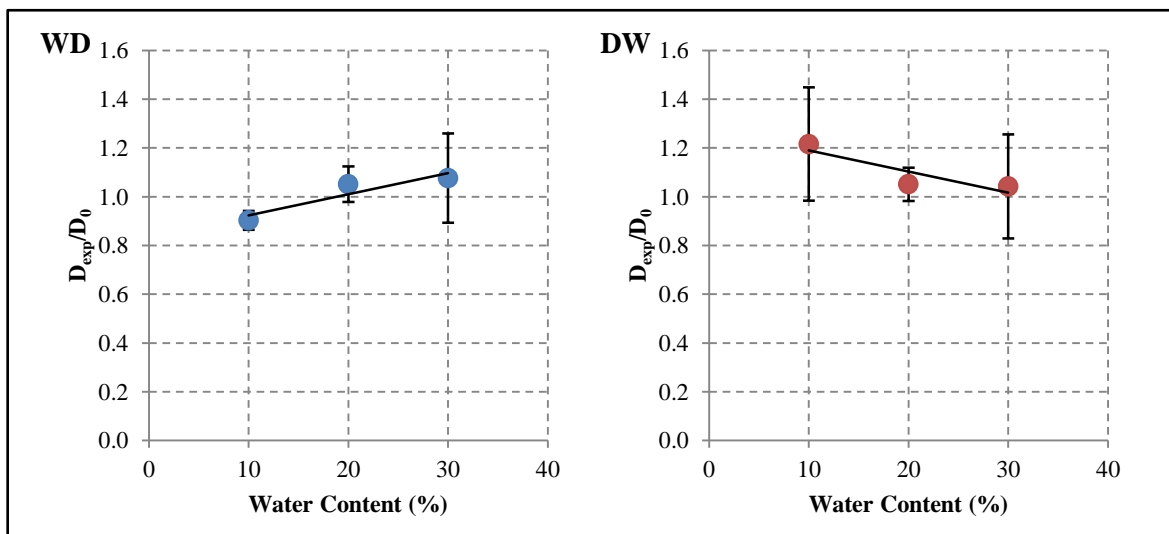
Figure 5-23: The effect of water content on the normalized fragmentation diameter of the water-in-diesel and diesel-in-water emulsion droplets.

Figure 5-24 shows the effect of water concentration on the effective diameter of the explosion wave for the water-in-diesel and diesel-in-water emulsions. The effective diameter has been evaluated as the equivalent diameter of the circle having the same area of the explosion wave. This method of diameter calculation is the same method implemented in the present work for droplet diameter evaluation as discussed in Chapter Four and Appendix (C).
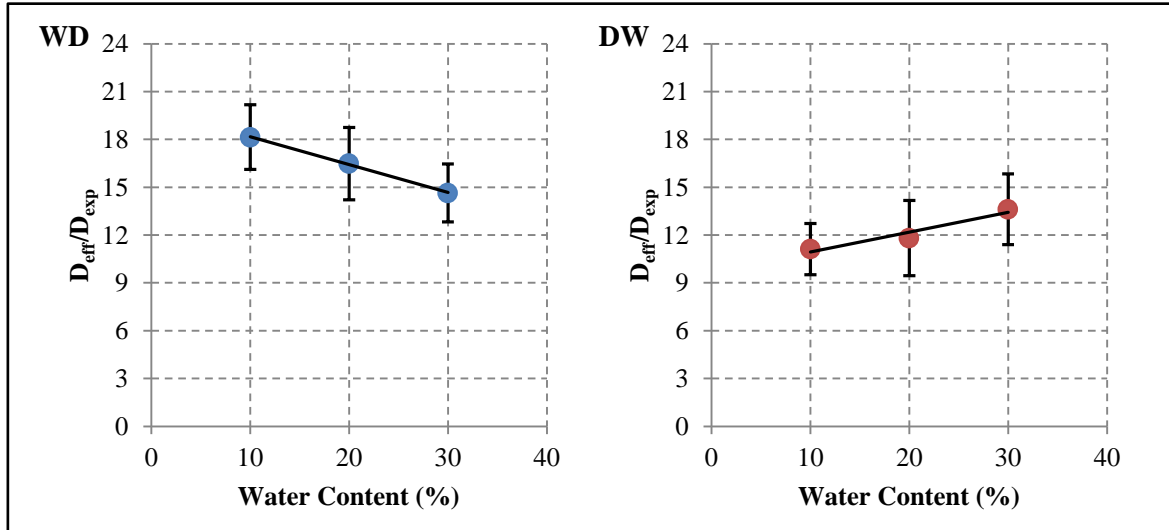
Figure 5-24: The effect of water content on the explosion wave effective diameter normalized with respect to the droplet initial diameter for both the water-in-diesel and diesel-in-water emulsions.

The effective diameter is then normalized by the explosion diameter of the droplet – that is the instantaneous diameter of the droplet at the start of explosion as defined earlier – rather than the droplet initial diameter because of its direct relevance on the explosion wave than the latter diameter. Hence, a more practical, realistic, non-dimensional description of the explosion wave effective diameter is obtained regardless the droplet size variation. As the figure shows, the effective diameter of the explosion wave resulting from the WD emulsion is higher than that of the DW emulsions. The effective diameter of the former is ranging between 18.1 in the case of WD10 and 14.6 for WD30, whereas the effective diameter of the latter ranges between 11.1 for DW10 and 13.6 for DW30. This suggests that higher internal pressure in the bubbles is produced in the case of the WD emulsions compared to the DW emulsions.

Additionally, increasing the water concentration in the emulsions is shown to decrease the effective diameter in the case of WD emulsions, and increases it in the case of DW emulsions. Regarding the WD emulsions, the effective diameter is shown to be almost

constant for all the water-diesel proportions, and that the decrease in diameter is merely because of the increase in explosion diameter shown in Figure 5-23. While, for the DW emulsions, in addition to the decrease in the droplet explosion diameter of Figure 5-23, increasing the water concentration in the emulsion indeed causes a certain increase in the effective diameter of the explosion wave. This could be attributed to the depth of the bursting bubbles inside the droplet, where the intensity of explosion is proportional to the depth of the bubble initiating the explosion [151]. Hence, increasing the water concentration results in increased water coagulation in the DW emulsions as explained earlier in this section. This in turn, causes the water to accumulate in the centre of the droplet, which is the furthest distance from the droplet surface. Then, due to explosive boiling, the water vapour bubbles will burst from the centre of the droplet causing the catastrophic explosion of the droplet. Then, the effective diameter of this explosion is increased by the increase in the quantity of water in the centre of the droplet.

The rate of development of the normalized effective diameter has been used for evaluating the explosion wave spread rate that is shown in Figure 5-25.
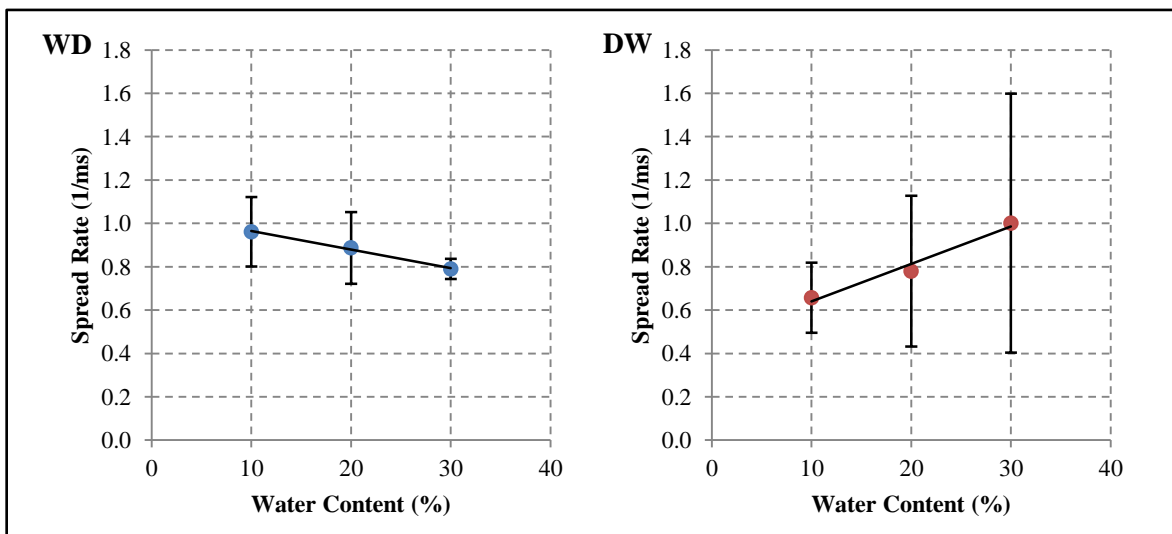
Figure 5-25: The effect of water content on the fragmentation effective diameter spread rate for the water-in-diesel and diesel-in-water emulsion droplets.

As shown in the figure, the explosion wave may spread to up to the diameter of exploding droplet within 1 ms in both emulsions, which means 10 ms for reaching 10 times the droplet diameter. Therefore, with the aid of Table 2-2, it may be inferred that the explosion wave from a single realistic droplet will have the time and strength to affect the surrounding neighbouring droplets in the spray. Additionally, it can be seen from the figure that the standard deviation of the tested samples in the case of the WD emulsions is quite

low suggesting highly repeatable values of the spread rate for that emulsions, whereas the standard deviation for the DW emulsion is relatively high, especially for the DW30.

5.4 Summary

In the present chapter, detailed experimental analyses of the puffing, sub-droplet generation, and microexplosion processes occurring in the burning multicomponent fuel droplets are performed.

Isolated droplet experiments are carried out for investigating the above processes during the combustion of biodiesel/diesel and ethanol/diesel blends, water-in-diesel and diesel-in-water emulsions in addition to the three single-component diesel, biodiesel, and ethanol fuels.

The results have revealed that the droplets of the whole multicomponent fuel mixtures have experienced puffing and secondary atomization with variable intensities, but only the emulsion droplets have undergone microexplosion. The biodiesel/diesel blends have shown the least puffing and secondary atomization tendencies, whereas the other three mixtures have experienced comparable tendencies. The effect of puffing and secondary atomization on both the burning droplet and the surrounding flame has also been revealed. Emulsion droplet microexplosion has been investigated and some quantitative analyses have been carried out.

Furthermore, as it is established, all of the studied processes are driven or triggered by the processes taking place in the liquid-phase of the burning droplet. These processes include nucleation, bubble generation and growth, internal circulation, and bubble burst. Therefore, a localized comprehensive experimental investigation of these processes is demanded. Hence, in the next chapter, the results of a magnified high speed investigation of the droplet liquid-phase during the combustion of multicomponent fuel droplets are presented and discussed.

Chapter 6. Liquid-Phase Monitoring during the Combustion of Multicomponent Fuel Droplet

6.1 Introduction

Nucleation and bubble generation are occurring inside the burning multicomponent fuel droplet in the course of its lifetime. The initiation, development, and effect of these processes on the multicomponent fuel droplet combustion need to be further comprehended. Considering the microscopic size of the fuel droplets in the real spray, studying these processes during the real spray combustion is quite challenging. Accordingly, the investigation of these processes is only affordable during the combustion of an isolated fuel droplet undergoing combustion. However, even with the isolated liquid fuel droplet, obtaining a clear view of the droplet liquid-phase is not easily attainable. Therefore, magnified imaging of the droplet liquid phase during combustion is essential for more in depth investigations of these processes.

Furthermore, as it is shown in Chapter Five, high speed imaging is required for tracking such processes. Consequently, magnified high speed imaging is implemented in the present chapter for investigating the liquid-phase dynamics during the combustion of isolated multicomponent fuel droplets. Backlighting imaging technique has been implemented for studying the liquid-phase dynamics during droplet combustion.

Hence, after describing the experimental work and procedures in section 6.2), the achieved results are presented and discussed in section (6.3). Firstly, the liquid-phase dynamics of the single-component fuel droplets are reviewed, followed by the liquid-phase dynamics of the multicomponent fuel droplets. Then, the nucleation and bubble growth analysis are presented and discussed. The effect of these processes on the puffing, secondary atomization and microexplosion is then covered. And finally, the phase separation and component accumulation in the core of the droplet liquid-phase is discussed. The overall findings of the present chapter are then outlined and summarized in section (6.4).

6.2 Experimental Setup

Generally, the same experimental setup used in Chapter Four has been utilized in this chapter. The schematic drawing of this setup is recalled in Figure 7-1. Some simple but essential changes have been made. The high speed camera is set to 40000 fps framing rate, 25 μs exposure time, and 384x288 pixels image resolution. The IDT 19-LED high intensity illuminator is used in the present test instead of the 72-LED domestic illuminator to provide the adequate lighting for the high imaging rate. The area covered by the camera is 3.84x2.88 mm^2, giving a spatial resolution of 10 μm/pixel for each image. The magnification rate achieved using this setup is thirty times the physical size. Therefore, a detailed investigation of the instantaneous droplet size and shape change during its overall lifetime is performed, in addition to the full tracking of the physical processes occurring in the liquid-phase.
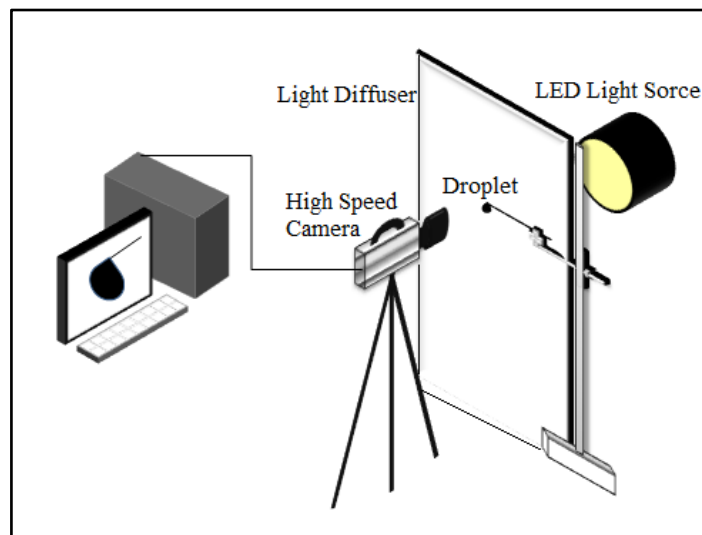
Figure 6-1: Experimental setup of the droplet combustion with backlighting imaging.

The investigated fuels are water-in-diesel and diesel-in-water emulsions, biodiesel/diesel and ethanol/diesel blends, in addition to the neat diesel, biodiesel, and ethanol as single-component base fuels. As it is mentioned in the previous chapters, the biodiesel/diesel blends and diesel-in-water emulsions are characterised by the higher boiling point of the dispersed phase that is biodiesel in the case of the blends and diesel in the case of emulsions compared to the continuous phase which is diesel in the case of the former and water in the case of the latter. In the ethanol/diesel blends and water-in-diesel emulsions on the other hand, the continuous phase – the diesel in both cases – has a higher

boiling point compared to both ethanol and water in both mixtures. Additionally, the miscibility of the constituents is variable for each multicomponent fuel mixture. Biodiesel is completely miscible in diesel, ethanol is partially miscible, and water is immiscible. Therefore, quite variable droplet liquid-phase behaviour is expected for each of these multicomponent fuel mixtures. Three samples have been tested for each of the neat diesel fuel, water-in-diesel, and diesel-in-water emulsions, while two samples have been tested for the rest of the fuels.

The images have been stored in the (TIFF) format and processed according to the procedures described in Chapter Three. Besides, intensity transformation of the grayscale images is performed for image enhancement. This intensity transformation is carried out using the *imadjust* function in the Image Processing Toolbox in Matlab, that maps the intensity values of an image between two certain limits and neglects the values beyond these limits [303]. Accordingly, proper and efficient droplet liquid-phase visualization and tracking is performed as shown in Figure 6-2. In turn, a variety of processes have been tracked and investigated. These processes are presented and discussed in the next section.
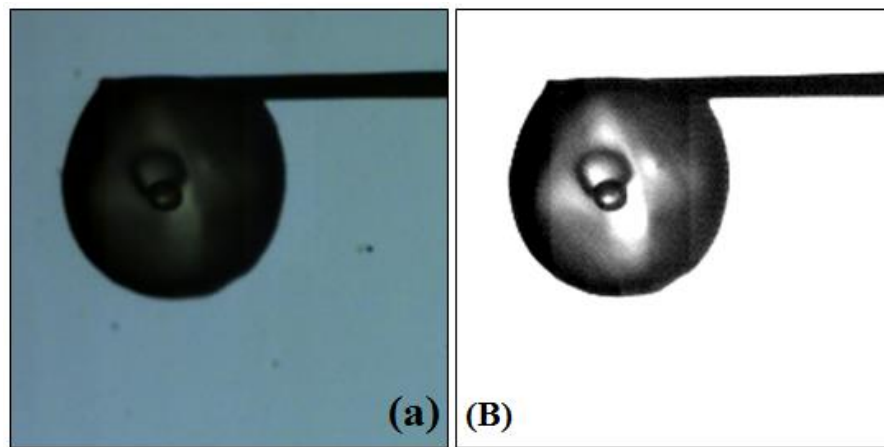
Figure 6-2: The effect of image intensity enhancement on highlighting the bubble growing inside a diesel fuel droplet. (a) the raw image, (b) the intensity enhanced image.

6.3 Results and Discussion

The results section has been arranged according to the sequence of events occurring within the droplet. Therefore, nucleation sites and nucleation rate in the multicomponent fuel droplet are discussed first, and then the dynamics of the growing bubbles are covered. The effect of nucleation and bubble generation on the puffing and secondary atomization

from the multicomponent fuel droplet has also been discussed. Additionally, water and diesel agglomeration has been noticed to occur during the combustion of diesel-in-water emulsions and ethanol/diesel blends. This phenomenon has been discussed at the final part of the present section. These discussions are preceded by general descriptions of the liquid-phase characteristics of both the single-component and multicomponent fuel droplets.

6.3.1 Liquid-Phase of the Single-Component Fuel Droplets

Despite the present work is devoted for studying the liquid-phase dynamics of the multicomponent fuel droplets, the droplet liquid-phase of the single component base fuels has also been investigated. This is for two main reasons; the first is to compare the burning behaviours of these fuels with their multicomponent mixtures, and the second is to estimate the effect of the SiC fibre on the droplet combustion, exploiting the clear structure appearance of these neat fuels compared to the multicomponent mixtures.
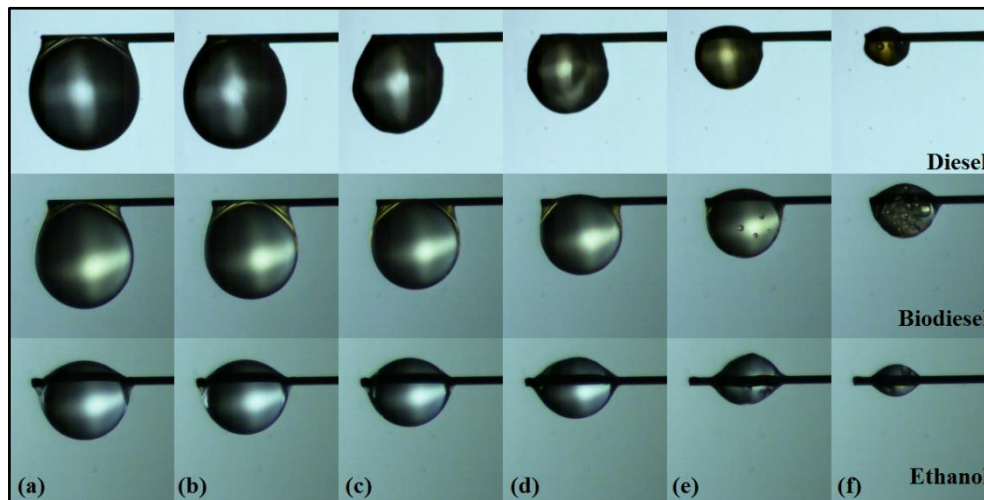
Figure 6-3: Temporal sequence of the droplet combustion of the neat diesel, biodiesel, and ethanol.

Figure 6-3 shows the droplet liquid-phase of the diesel, biodiesel, and ethanol single-component fuels at various periods of the droplet lifetime. Image (a) for each fuel represents the initial droplet diameter, whereas image (f) represents the droplet prior to complete evaporation at the end of its lifetime. Images (b), (c), (d), and (e) are selected so that they represent the droplet after 20%, 40%, 60%, and 80% of its lifetime for each fuel. As the figure shows, the droplets of all the fuels have a transparent structure that is relevant for droplet interior monitoring. Furthermore, the droplet interior remains clear with no

bubble appearance during the majority of the droplet lifetime for all the fuels indicating a steady and undisturbed combustion of the droplets. This clear appearance suggests also that the SiC fibre has no – or negligibly small – effect on the droplet when its size is relatively large. However, the effect of the fibre becomes more obvious when the droplet size is relatively small and is comparable to the fibre size as shown in image (f) for each row. This effect on the liquid-phase takes place in the form of heterogeneous nucleation and bubble generation on the interface between the fibre and the droplet liquid [168]. Hence, bubble generation due to nucleation arises at the final stages of the droplet lifetime for all the single-component fuels. The time of the bubbles early appearance has been evaluated with respect to the droplet lifetime and presented in Figure 6-4. As shown by the figure, bubble generation in the diesel fuel droplet is the latest by an average starting time after the first 79% of the droplet lifetime. And it is preceded by bubble generation in the biodiesel and ethanol by 77% and 69% of the droplet lifetime respectively. The presented values are the average values of three samples for each fuel, with the error bars represent the standard deviation of these values. As shown by the standard deviation, a relatively high repeatability is obtained. This in turn, proves that the effect of the SiC fibre on the combustion of the suspended fuel droplet is only dominant on the final 20-30% stages of the droplet lifetime, and that for the earlier stages, this effect is negligibly small.
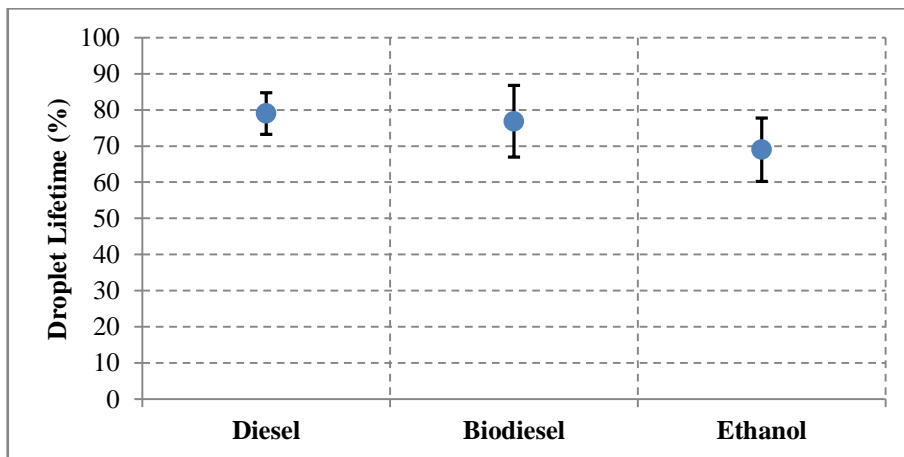
Figure 6-4: Heterogeneous nucleation occurrence time with respect to overall droplet lifetime for the neat diesel, biodiesel, and ethanol fuels.

However, few bubble generation incidents have been noticed within some of the diesel and ethanol droplets far from the fibre such as that shown in Figure 6-5 for a diesel fuel droplet. As shown in the figure, the nucleation site is far away from the fibre thus

eliminating the heterogeneous nucleation probability and implying either the superheat boiling of one of the diesel base constituents or because of some trapped gas pockets in the fuel [123,155]. Additionally, the transparent nature of the diesel fuel droplet made it easy to visualize and track the temporal evolution of the growing bubble. The bubble firstly initiated at the periphery of the droplet interior far from the suspension fibre as shown in the image corresponding to time 0 ms of Figure 6-5. Bubble growth then proceeded in conjunction with circulation around the droplet periphery as shown in images 2.25 ms to 11.25 ms. This circulation is attributed to the temperature gradient between the droplet surface and centre [304]. Then, as the bubble diameter increases, it moves towards the centre of the droplet as shown in images 13.50 ms to 38.25 ms. Then, the bubble bursts causing droplet puffing as shown in image 42.75 ms. The bubble growth rate has been evaluated as the time required by the bubble to reach its maximum volume. This volume is calculated using the maximum bubble diameter that is estimated by means of the equivalent circle diameter of the projected area algorithm that is implemented and described in the previous chapters.
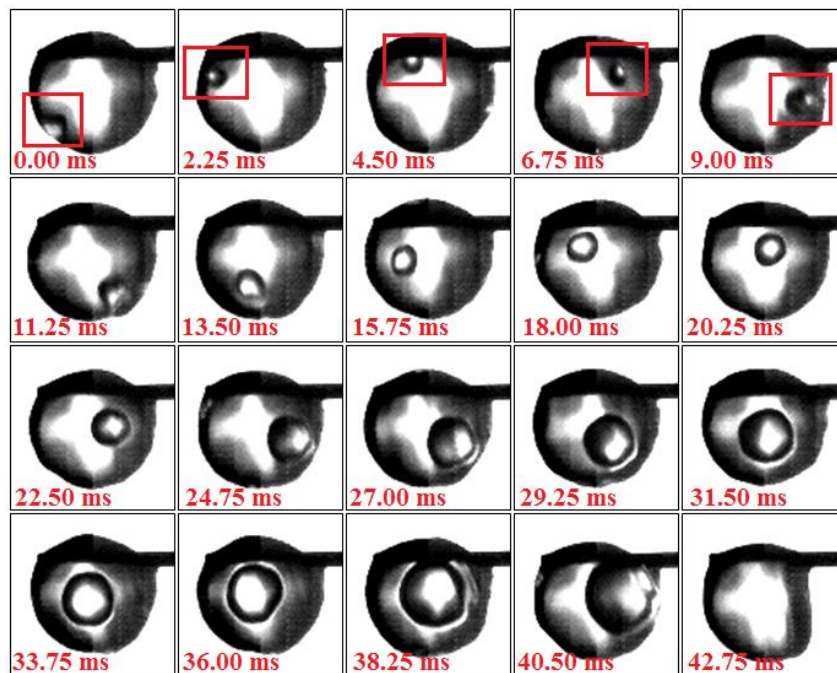
Figure 6-5: Temporal sequence of bubble growth inside a diesel fuel droplet (the time is set from the initiation of the bubble).

Hence, the maximum diameter of the bubble is the one that is in image 40.50 ms in Figure 6-5, and is found to be 0.46 mm. Thus, the bubble growth rate is found to be about

1.28 μm³/μs. This rate will then be compared with the bubble growth rates obtained from the multicomponent fuels. The bubble circulation velocity has also been evaluated as the time required for crossing half the circumference of the droplet. This time is estimated from the images to be 6.8 ms and the droplet diameter is 0.74 mm, therefore, the distance is 0.5*0.74*π and is found to be 1.16 mm, hence, the circulation velocity is about 171 mm/s which is in agreement with the 90-200 mm/s circulation velocity estimated by Miglani, Basu, and Kumar [153]. Eventually, it can be said that the nucleation and bubble generation within the single-component fuel droplets is mostly infrequent, and that the scarce incidents are either because of dissolved gases or low boiling components as in the diesel. However, these rare occurrences were useful in estimating the circulation velocity and bubble growth rate due to the clear and transparent structure of the single-component fuel droplets.

6.3.2 Liquid-Phase of the Multicomponent Fuel Droplets

In contrast to the single-component fuel droplets, the multicomponent fuel droplets have a less transparent structure as shown in Figure 6-6.
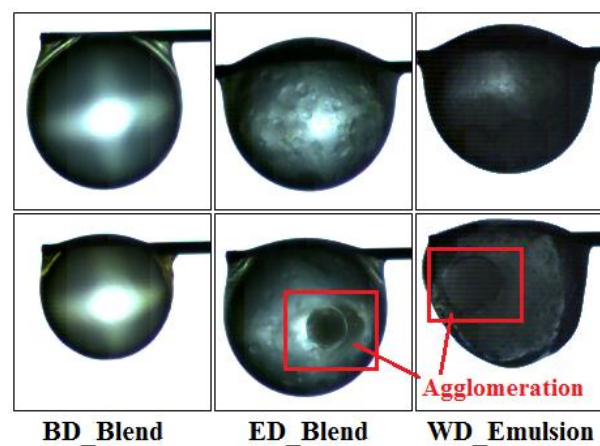
Figure 6-6: Liquid-phase appearance of the biodiesel/diesel and ethanol/diesel blends and the water/diesel emulsions. The upper row represents the initial droplets, and the lower row represents the droplets after a certain time of combustion.

This transparency is variable between the different multicomponent mixtures utilized in the present work. The biodiesel/diesel blends have the highest transparency compared to the other mixtures, then, it comes the ethanol/diesel mixtures, and finally the emulsions of both

161

types the water-in-diesel and diesel-in-water. This is related to the miscibility of biodiesel, ethanol, and water in diesel, where, the biodiesel that is the most miscible liquid in diesel among the three have the most homogeneous – and in turn most transparent – mixture when blended with diesel compared to ethanol and water as shown in the first column of Figure 6-6. Ethanol, on the other hand, is partially miscible as formerly explained. Hence, the resulting ethanol/diesel mixture is less homogeneous and less transparent compared to biodiesel, as shown in the second column of Figure 6-6. While, the water/diesel emulsions shown in the third column of Figure 6-6 have a relatively opaque structure compared to the biodiesel and ethanol blends, that is due to the immiscible nature of water in diesel, even with the use of the emulsifying agent. The second row of Figure 6-6 shows that the ED blend, WD and DW emulsions may experience some sort of agglomeration due to the separation of components. This phenomenon will be discussed at the end of this chapter.

In addition to the difference in transparency, the multicomponent fuel mixtures differ from each other in the nucleation rate and subsequent liquid-phase dynamics. The biodiesel/diesel blend droplets are characterized by steady, undisturbed combustion, with the least nucleation and bubble generation incidents among all the mixtures. Whereas, the other mixtures including ethanol/diesel blends, water-in-diesel-emulsions, and diesel-in-water emulsions are characterized by chaotic combustion behaviours due to the high nucleation and bubble generation incidents leading to increased puffing and sub-droplet generation values as discussed in the previous chapter. These chaotic behaviours are reflected on the shape of the burning droplet as shown in Figure 6-7. The droplet in the figure endures high deformations in shape subsequent to the puffing incident. Additionally, it experiences all the possible processes subsequent to bubble growth and burst, therefore, it serves as an ideal model for describing these processes. The droplet is initially spherical and contains a large bubble with a diameter equals to 90% of the droplet instantaneous diameter so that it is occupying a large space inside the droplet as shown in the image corresponding to time 0.0 ms in Figure 6-7. When the bubble bursts, the droplet starts to flatten on the right side as shown in the images corresponding to times 0.3 ms to 0.9 ms respectively. This flattening is a result of the droplet reaction to the thrust force generated during the water vapour release by puffing. The puffing vapour could not be visualized in the tests corresponding to the present chapter because of the high intensity illumination light used for the backlighting imaging. This illumination light is required to compensate for the high speed imaging, but, unfortunately, the too bright background generated by illumination obscures the visualization of the low intensity vapour emitted by puffing.
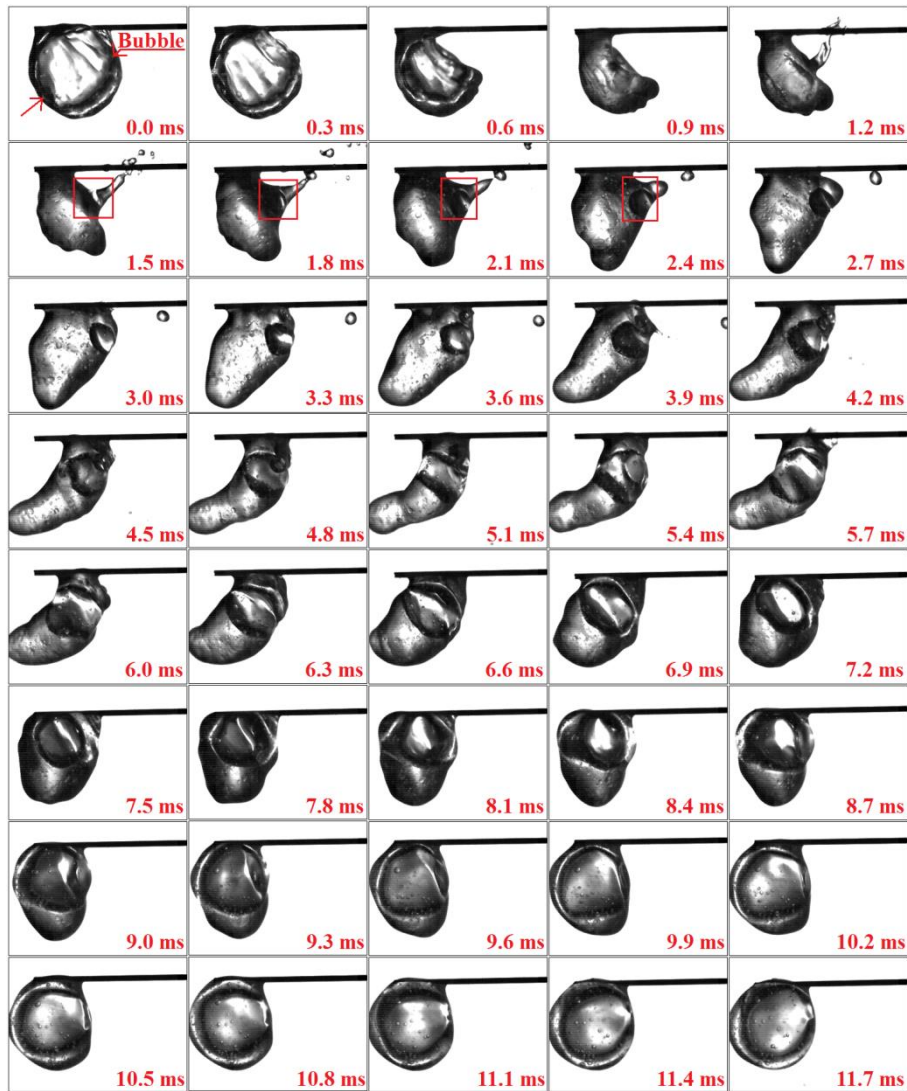
Figure 6-7: Temporal sequence of the droplet shape variation consequent to bubble burst and puffing within a WD20 fuel droplet (the time is set from the start of puff).

Subsequent to puffing, some of the liquid is ejected outside the droplet accompanied by the detachment of different size ligaments in the form of sub-droplets as shown in images 1.2 ms to 2.4 ms respectively. The thrust force resulting from puffing then pushes the droplet to the left side so that it takes a plum shape rather than its original spherical (or semi-spherical) shape, as shown in times 2.7 ms to 3.3 ms in the figure. The droplet then continues to move towards the left side under the puffing thrust force, but, the surface tension of the liquid will resist this movement and keep the droplet suspended in the fibre, causing the droplet to elongate at its far end as shown in times 3.6 ms to 5.7 ms respectively. This droplet elongation continues until the surface tension force exceeds the thrust force and brings the droplet back to its normal position (times 6.0 ms to 7.2 ms respectively) and shape (times 7.5 ms to 11.7 ms).

This sequence of events occurs almost after every bubble growth and burst processes but with varying intensity, because not all bubble burst processes end up with ligament or sub-droplet detachment as it is postulated in Chapter Five.

Furthermore, as shown in image 1.5 ms and the following images, another bubble is generated in the ejection location subsequent to ligament and sub-droplets detachment. Direct connection between the ejection site and the evolution of the new bubble could not be confirmed. Despite the reasons behind this bubble generation, it gives an indication of the nucleation and bubble growth rates in the emulsion droplets. Moreover, Figure 6-7 shows the variety of shapes taken by the droplet during a single occurrence of secondary atomization. Hence, keeping in mind the repeatability of such process, especially for the emulsion droplets, it can be inferred how dominant is the irregular shape of the droplet compared to the regular spherical configuration.

6.3.3 Nucleation Rate

In spite of the size – and the resulting time scale – difference between the tested droplets in the present work and those on the real sprays, the nucleation behaviour of the different multicomponent fuels under investigation could be estimated. Hence, the nucleation rates during the droplet combustion of these fuels have been evaluated and presented in Figure 6-8 with respect to the concentration of the added substance (biodiesel, ethanol, or water). These nucleation rates have been evaluated for the overall droplet lifetime and normalized by 100 ms time interval for procuring more realistic results comparable to the real spray droplet lifetime. Additionally, the nucleation rate has been presented in the logarithmic form due to the large difference in the order of magnitude of the computed values for the different multicomponent fuel mixtures. Bubble nucleation around the fibre region inside the droplet is neglected to eliminate the probability of adding any bubble generated by heterogeneous nucleation due to the presence of the fibre. Hence, the presented results are only for homogeneous nucleation away from the fibre. As shown in the figure, the nucleation rates of all the investigated mixtures are inversely proportional to the concentration of the additive in that mixture. However, the degree of this proportionality is variable among those mixtures. Where, the water-in-diesel emulsions show steep line behaviour with increasing the concentration of the water in the emulsions, whereas this behaviour is less for the other mixtures.
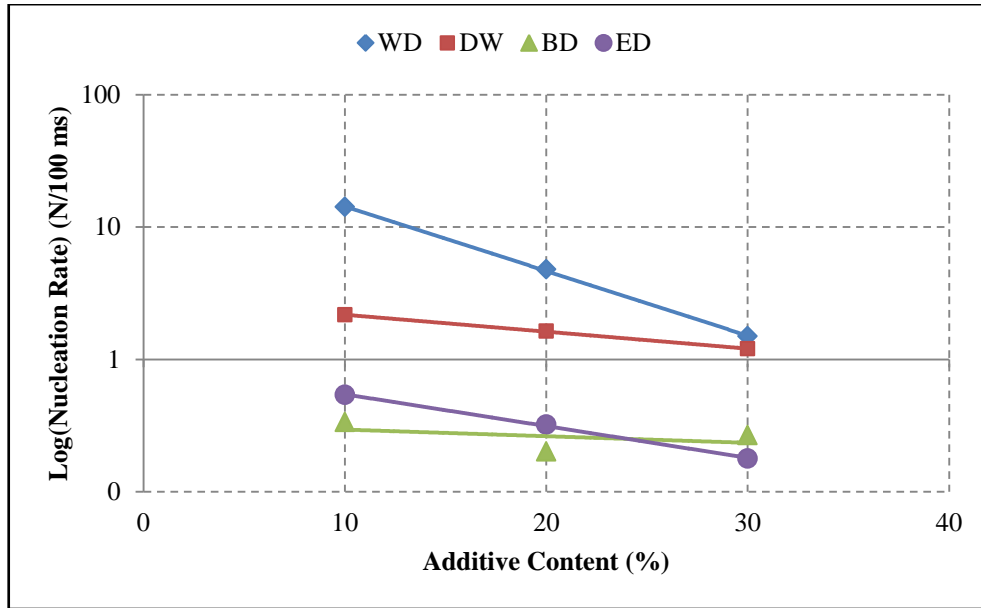
Figure 6-8: Average nucleation rate variation with the content of the substance added to diesel.

Additionally, the nucleation rate in the WD emulsions is the highest among all mixtures, while that of the BD blends is the least, this could be a reflection to the miscibility of these liquids to diesel, where biodiesel is completely miscible and water is completely immiscible.
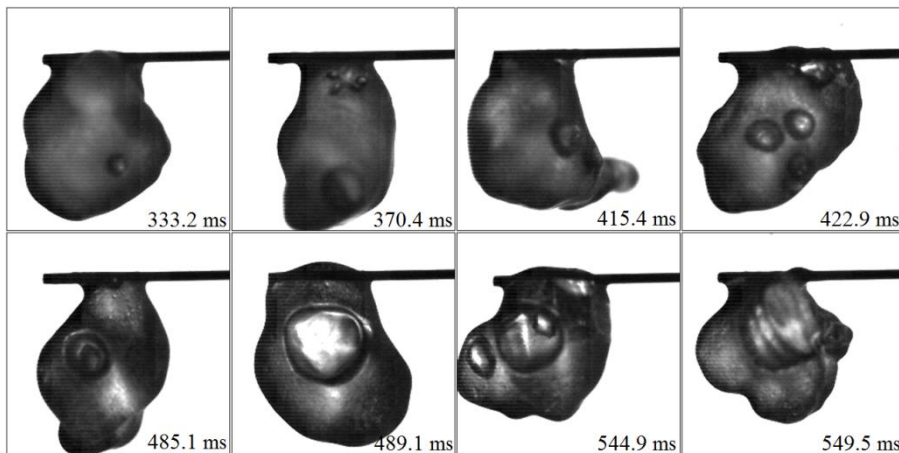
Figure 6-9: Different nucleation sites inside the burning fuel droplet.

Figure 6-9 shows the various nucleation sites inside a WD10 emulsion droplet. The figure shows that the nuclei could initiate at any location inside the droplet, whether this location is the droplet centre as in image 489.1 ms, or any of the peripheries, as it is shown in the other images. All these nucleation sites are away from the suspension fibre, which gives certainty about the occurrence of homogeneous nucleation within the burning

multicomponent fuel droplet. Furthermore, the figure shows that more than one nucleus may develop at the same time, as it is revealed in images 422.9 ms and 544.9 ms.

6.3.4 Bubble Dynamics

Once the nucleation rate has been evaluated, the resulting bubble growth and dynamics are investigated. Figure 6-10 shows the bubble growth rate inside the burning droplets of the multicomponent fuels under investigation presented with respect to the concentration of the substance added to diesel (biodiesel, ethanol, and water). The growth rate is expressed in the logarithmic form due to the big difference between the different mixtures. As Figure 6-10 shows, the bubble growth rate of ethanol/diesel blends is proportional to the increase of ethanol concentration in the blend, while, those growth rates of both biodiesel/diesel blends and water-in-diesel emulsions are inversely proportional to the increase in both biodiesel and water concentrations in the mixture. The bubble growth rate of the diesel-in-water emulsions on the other hand is found to be unaffected by the increase of water concentration in the emulsion.
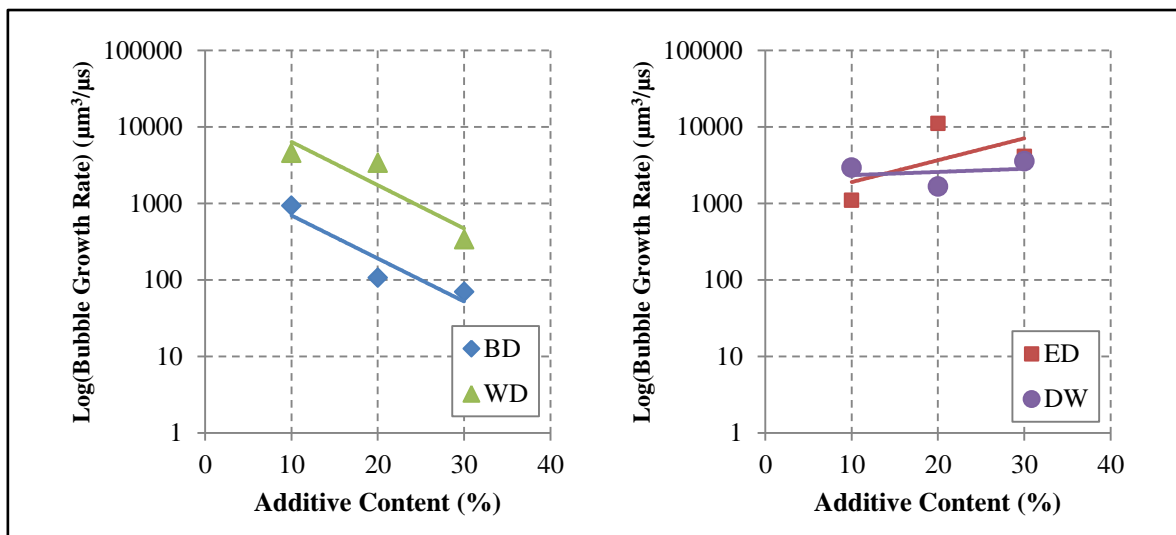
Figure 6-10: The effect of additive content on the average bubble growth rate inside the multicomponent fuel droplet.

Furthermore, as mentioned in section 6.3.3, more than one bubble could be initiated at the same – or relatively close – time. Hence, some of these bubbles are shown to merge into a single large bubble as shown in Figure 6-11. In this figure, two different size bubbles generated during the combustion of ED10 fuel droplet are united in one large bubble

occupying the whole droplet interior. The time periods shown in the figure are set to start from the instant when the two bubbles are attaching each other. However, the first two images in the first row of the figure are before that time, but they have been added to illustrate the change in bubble locations inside the droplet. As the figure shows, the smaller bubble is contained by the larger bubble.
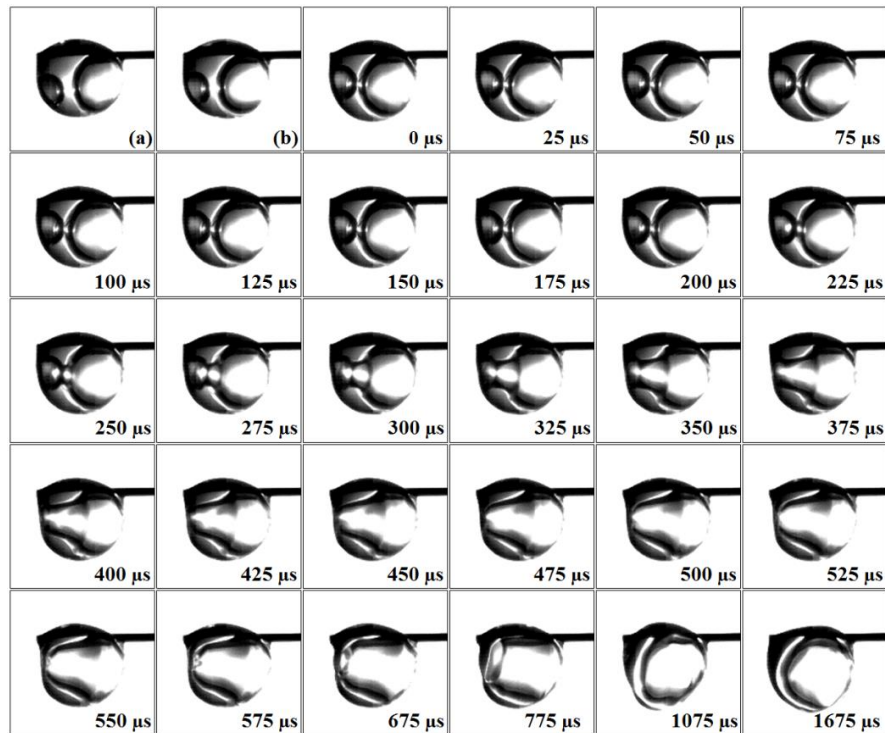
Figure 6-11: The temporal sequence of two bubbles merging occurrence inside an ED10 fuel droplet (time is set from the instant of bubbles attachment).

This bubble merging process has occurred in many occasions and within different fuel droplets including the neat diesel fuel droplet as shown in Figure 6-12. In this figure, both bubbles are circulating inside the droplet and approaching each other in the centre of the droplet. These merging incidents are playing a crucial rule in the dynamics of the droplet surface since these processes unite multiple small bubbles in one large bubble; the explosion of this large bubble is expected to be more effective than the initial smaller ones. However, the larger bubble size will not necessarily generate the sufficient disturbance for disintegrating the droplet. Since the bubble size is not the only effective parameter in droplet disintegration and sub-droplet generation, the other factors are droplet size, bubble location prior to burst, and droplet liquid surface tension.

167
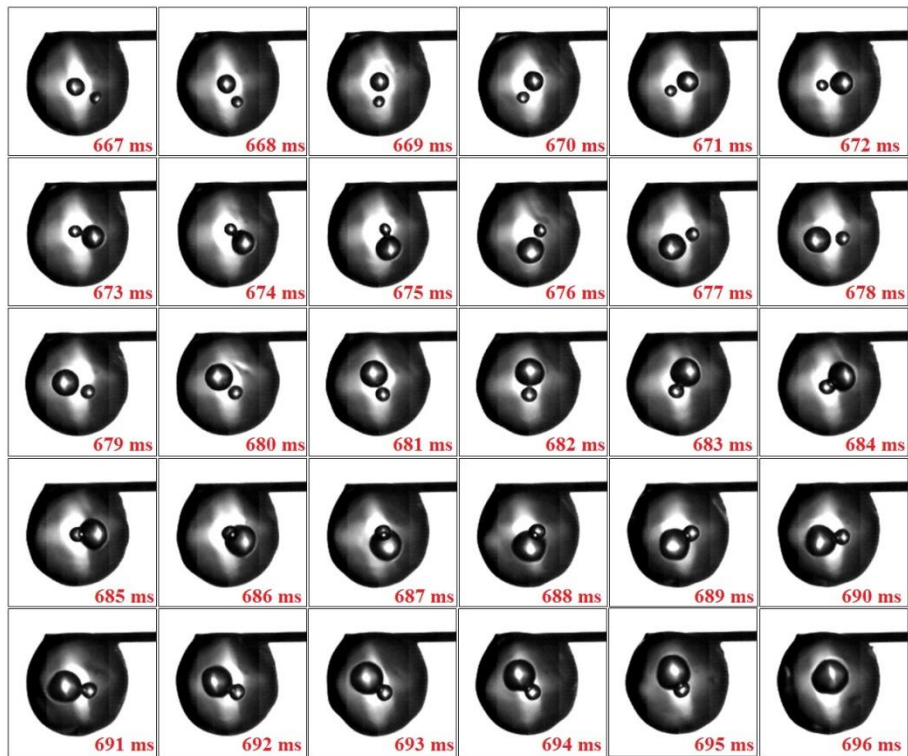
Figure 6-12: Temporal sequence of two bubbles merging process inside a neat diesel fuel droplet.
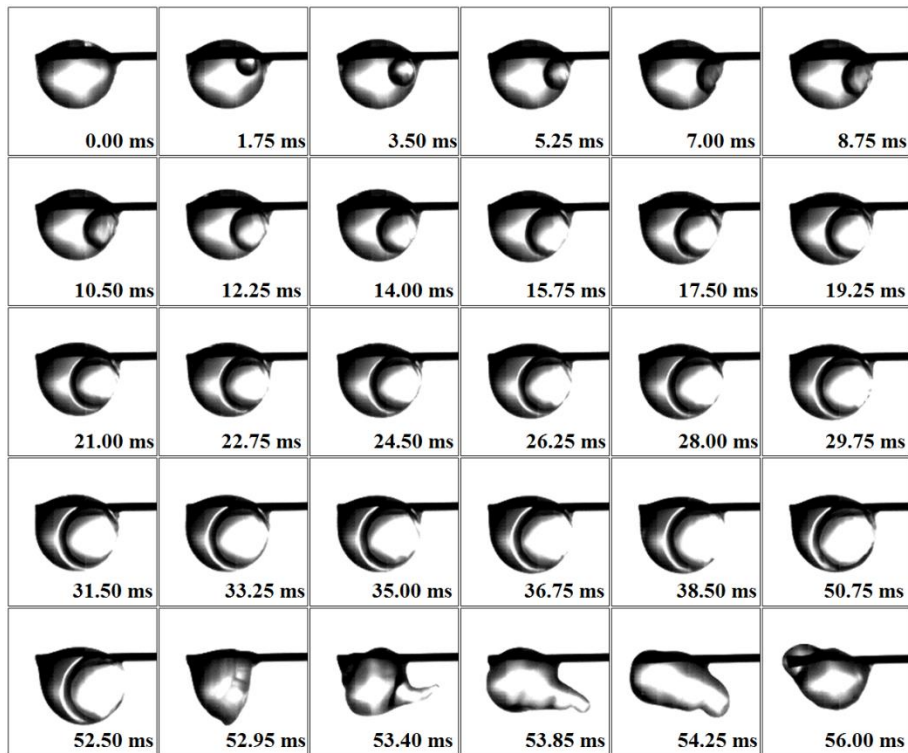
Figure 6-13: Temporal sequence of bubble growth inside a burning BD10 fuel droplet.

Figure 6-13 shows the temporal sequence of bubble growth inside a burning BD10 fuel droplet. The presented bubble has initiated near the droplet surface and developed in

the same location as shown in image 3.50 ms and the followings. Its diameter on image 52.50 ms prior to explosion is measured to be 0.73 of the droplet diameter. However, when exploded, its effect on the droplet is only shown in the form of vapour ejection by puffing without detachment of any portion of the liquid droplet as shown in image 53.40 ms and following images. This suggests that the thrust force resulted from bubble explosion and the subsequent puffing was not sufficiently high to overcome the surface tension of the liquid droplet. Especially, the surface tension of the biodiesel fuels is higher than that of the regular diesel fuels [305]. So that its only effect appeared in the form of droplet shape change followed by restitution to the normal shape.
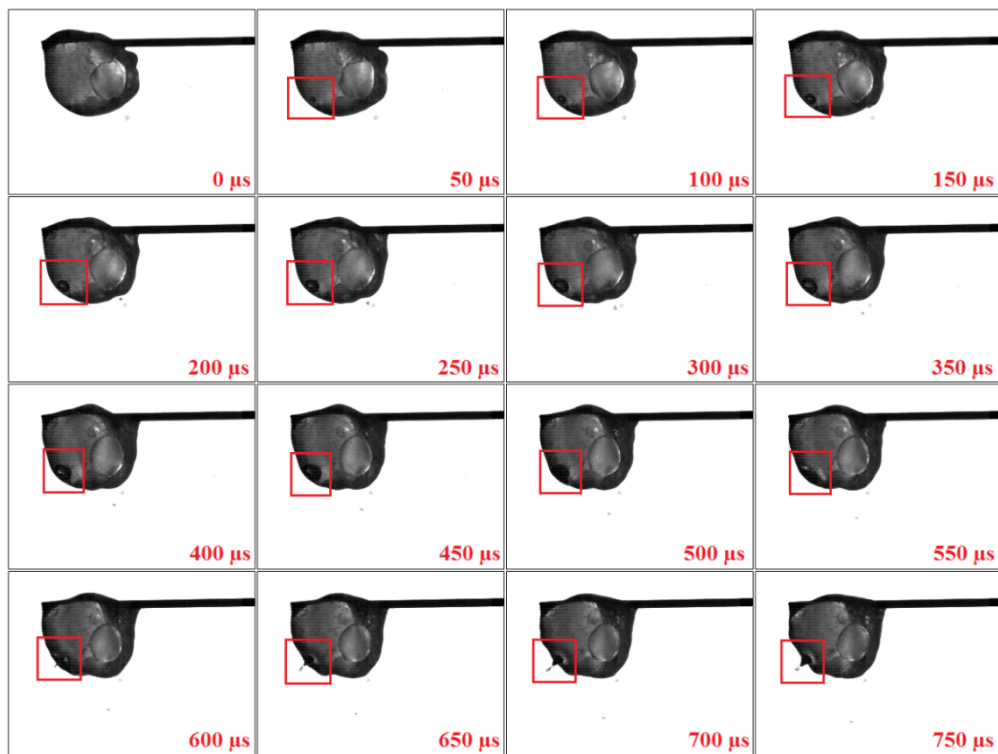
Figure 6-14: Short bubble growth time during the combustion of WD20 fuel droplet.

In contrast, Figure 6-14 shows bubble evolution and explosion inside a WD20 fuel droplet, in which this explosion led to sub-droplet detachment from the parent droplet surface. The bubble is also initiated near the surface of the droplet as shown in image 50 μs, and developed adjacent to the surface as shown in images 100 μs to 550 μs respectively. Its maximum diameter prior to burst is estimated from image 550 μs to be 0.28 of the droplet diameter, and its evolution time is 1/95 of the evolution time for that bubble shown in Figure 6-13. However, its explosion led to the generation of small size

sub-droplet as shown in image 750 µs. Thus, it can be inferred that the size of the bubble is not always the major factor in deciding the occurrence of droplet secondary atomization.

6.3.5 The Effect of Bubbles on Puffing, Secondary Atomization, and Microexplosion

Figure 6-15 shows the effect of bubble burst on the sub-droplet ejection from the surface of an ED20 fuel droplet undergoing combustion.
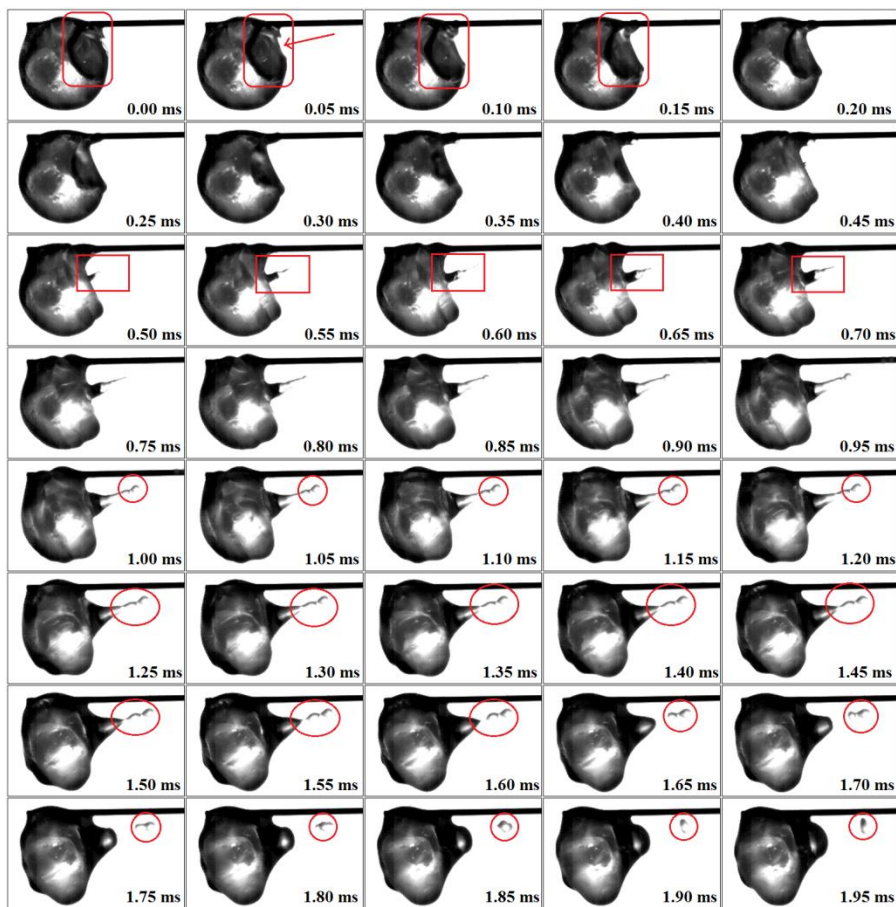
Figure 6-15: Temporal sequence of the effect of a growing bubble on the sub-droplet ejection from a burning ED20 fuel droplet.

Prior to burst, the bubble – bounded by the red box in the first row – is adjacent to the droplet surface. Hence, it is forcing the frontal thin liquid layer of the liquid until it is in contact with the gaseous environment. So, the pressure difference across the bubble causes its rapture releasing all the content vapour outside. The release of this vapour created a low pressure spot on the droplet surface causing the surrounding liquid on the droplet to flow

towards this spot as shown in images 0.05 ms to 0.45 ms in Figure 6-15. These images illustrate the inward movement of the droplet surface subsequent to vapour release by bubble rapture. This inward motion of the liquid edges results in a reflective outward motion of part of the liquid due to the impact of the liquid edges in the low pressure spot as shown in image 0.45 ms and the followings. If the force resulting from this reflective motion is high enough, the moving liquid portion will continue forward with a decrease in the cross-sectional area and flattening in the upstream side as shown in images 0.85 ms to 0.95 ms. With the increase of outward motion of the liquid, the cross-sectional area decrease and upstream face increase will initiate nicking in the liquid portion structure behind the flattened face as shown in the red circles of images 1.00 ms to 1.20 ms. Disintegration of the liquid from this nick then occurs causing a small ligament of liquid to escape in the form of sub-droplet as shown in images 1.25 ms to 1.95 ms respectively. Otherwise, if the force produced by the impact is not sufficiently enough, liquid nicking will not take place, and the resulting effect will be limited to instantaneous deterioration of the droplet surface for a certain time after which the droplet will retain its original shape as it is previously shown in Figure 6-13.

The above described synopsis occurs for all the growing bubbles inside the fuel droplets, but with varying degree. Where, occasionally the impact force is relatively small due to the small size of the exploding bubble and in turn the low pressure difference. Hence, smaller portion of the liquid is forced outside as shown in Figure 6-16. This figure illustrates the temporal sequence of bubble growth inside a WD20 fuel droplet. As it is shown by tracking the bubble bounded by the red box in each image, the bubble is initiated at time 181.1 ms near the droplet surface. Then, it continued to grow up with time until reaching the instant 183.1 ms where it reached its maximum size and attached the droplet surface from inside. Since, the liquid layer at the droplet surface is thin; it did not withstand the force exerted by the bubble. Therefore, droplet surface layer rupture occurred bringing the bubble in contact with the surrounding gaseous environment. This attachment with the environment led to the rapture of the bubble itself due to the pressure difference across the bubble boundaries. Because of this rapture, a small portion of the liquid from the droplet surface is ejected according to the same mechanism described formerly. However, this liquid portion is relatively small as shown in images 183.5 ms to 183.8 ms.
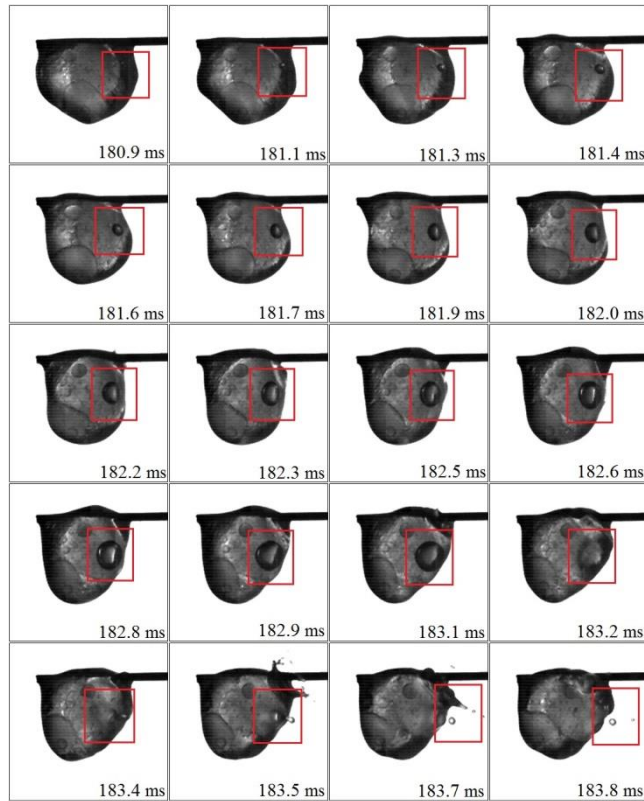
Figure 6-16: Temporal sequence of the effect of a growing bubble on the sub-droplet ejection from a burning WD10 fuel droplet.

Figure 6-17 on the other hand, shows the secondary atomization and sub-droplet emission from a WD20 fuel droplet. The sub-droplet is bounded by the white rectangle for tracking purposes. It is emitted as a result of the parent droplet puffing shown in images at 0 ms and 0.1 ms. Although the exact composition of the sub-droplet is not currently affordable; its burning characteristics are compared to the parent droplet that is WD20. The initial diameter of the sub-droplet is found to be 40 μm. It has experienced explosion at about 1.9 ms after its ejection. Therefore, its burning rate constant is calculated as (0.84 mm^2/s), which is slightly lower than that of the WD20 fuel droplet evaluated in Chapter Four, that is (1.18 mm^2/s). Though, in the case of sub-droplet, this value represents the vaporization rate constant rather than the burning rate constant since the sub-droplet experienced explosion before leaving the vaporization zone of the parent droplet. Since the radial distance of the sub-droplet centre from the parent droplet centre in image 1.8 ms is evaluated to be 1.8 of the parent droplet instantaneous radius. Whereas, the flame stand-off ratio for that droplet is found to be ~ 4. Thus, the sub-droplet is more likely to explode during vaporization rather than combustion. This implies that the actual secondary

atomization from the emulsion droplet is higher than that estimated from the regular droplet and flame observations.
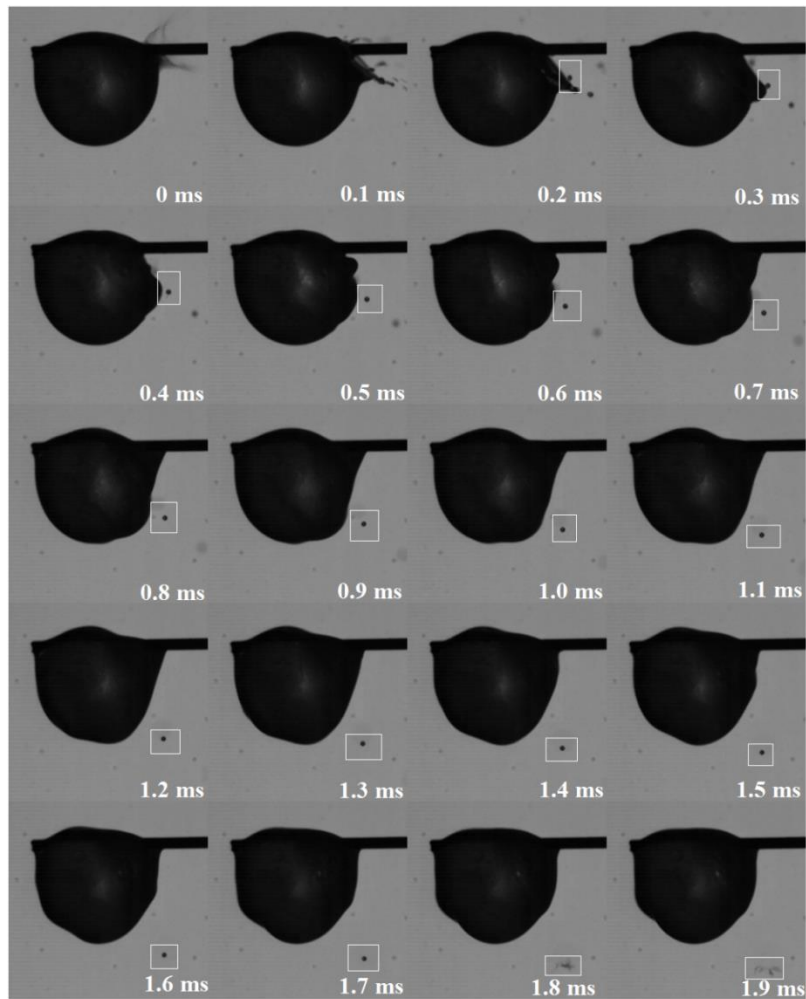
Figure 6-17: Temporal sequence of the ejected sub-droplet lifetime during the combustion of a WD20 fuel droplet.
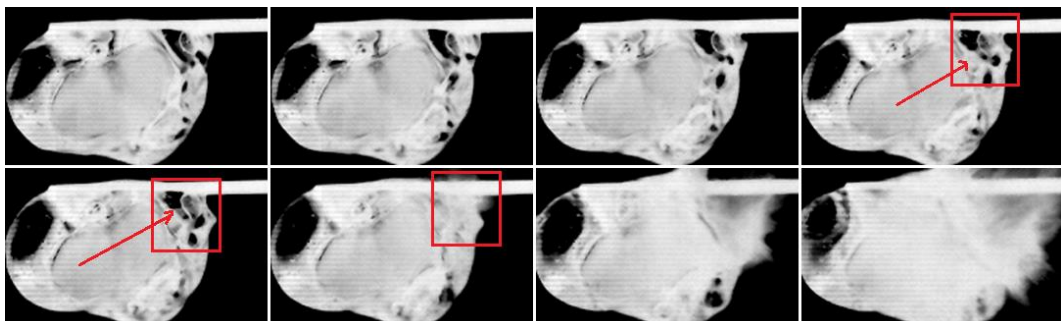
Figure 6-18: WD20 emulsion fuel droplet microexplosion during combustion (the time difference between images is 25µs).

Figure 6-18 shows the temporal sequence of WD20 emulsion fuel droplet microexplosion during combustion. The images have been inverted using Matlab for proper visualization of the explosion initiation point. The use of high intensity backlight during imaging resulted in the tracking of the explosion point inside the droplet is quiet challenging. As the figure reveals, the micro-explosion of the droplet took place due to the explosion of one of the bubbles inside the droplet. This bubble – bounded by the red box – exploded inside the droplet in a point relatively far away from the droplet surface. Hence, due to its location inside the droplet, the effect of this explosion on the droplet was more intensive than the bubble explosions on the droplet surface. This form of microexplosion has been noticed to occur during the combustion of the majority of the water-in-diesel and diesel-in-water emulsion droplets and for some of the ethanol/diesel blends.

6.3.6 Accumulation within the Burning Multicomponent Fuel Droplet

During the liquid-phase magnified monitoring during the combustion of the multicomponent fuel droplets, some of the droplets belonging to the ethanol/diesel blends, water-in-diesel and diesel-in-water emulsions have experienced a kind of component separation. This is followed by accumulation of one of these components in the form of a spherical mass moving in the centre of the droplet as shown in Figure 6-19.
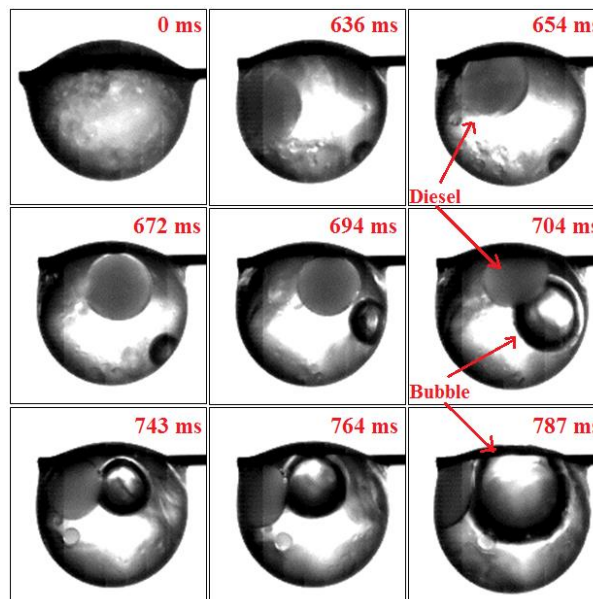
Figure 6-19: The temporal sequence of diesel fuel accumulation during the combustion of ED30 fuel droplet.

As the figure shows, the structure and transparency of this mass are different from those of the bubble. Hence, it implies that the formation of this mass is due to the separation of the components of the fuel mixture and the accumulation of the less volatile component in the centre of the droplet. In the case of the ethanol/diesel blends, the less volatile component in the blend is the diesel, thus, the mass accumulating in the centre of the droplet in Figure 6-19 is expected to be diesel. This is also shown in Figure 6-20 for the combustion of WD20 fuel droplet. For both water-in-diesel and diesel-in-water emulsions water is the less volatile component, hence, the accumulating mass in Figure 6-20 is expected to be water rather than diesel.

This accumulated water is shown to augment the nucleation and bubble generation rates inside the droplet because it serves as a nucleation site. This type of separation and accumulation has not been noticed to occur during the combustion of biodiesel/diesel blends, which may be attributed to the complete miscibility of biodiesel in diesel as explained formerly.
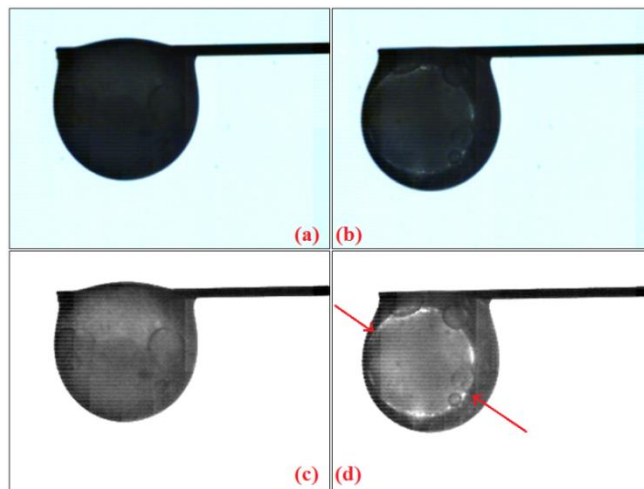
Figure 6-20: Water accumulation during the combustion of WD20 fuel droplet: (a) original image of the droplet at time =0, (b) original image of the droplet with water accumulation appears in the middle, (c) intensity enhanced image of the (a) image, and (d) intensity enhanced image of the (b) image.

6.4 Summary

In the present chapter, a magnified high speed imaging of the liquid-phase during the droplet combustion of the multicomponent fuels in addition to the base single-component fuels have been performed. Several physical processes have been visualized and tracked including nucleation, bubble generation, and fuel component separation and accumulation.

Quantitative analysis has been performed for estimating the nucleation and bubble growth rates.

The high speed images have revealed the occurrence of homogeneous nucleation within the multicomponent fuel droplet during combustion. The subsequent analysis then, have shown that the rate of this nucleation is inversely proportional to the degree of miscibility between the basic constituents of the multicomponent fuel mixture. Thus, the biodiesel/diesel blends – which are the mixtures of the completely miscible components – are characterized with the least nucleation rates, whereas the water/diesel emulsions – which are the mixtures with the least miscibility of components among all the studied mixtures – have had the highest nucleation rates.

The effect of nucleation and bubble generation on the puffing, secondary atomization, and microexplosion of the multicomponent fuel droplet has also been investigated. It is shown that the size of the bubble is not the only factor that determines sub-droplet emission from the droplet surface.

Additionally, some bubble dynamics have also been observed, such as the bubble circulation and the multiple bubble merge. All these processes have an effect on the overall dynamics of the droplet liquid-phase and surface during combustion.

Furthermore, separation and accumulation of diesel in the ethanol/diesel blends, and water in the water-in-diesel and diesel-in-water emulsions has been observed. This accumulation leads to the generation of a relatively large size mass in the centre of the droplet; this mass sometimes serves as a nucleation site resulting in increasing the nucleation rate within the droplet.

To conclude, the magnified high speed imaging of the droplet liquid phase was effective in revealing the different occurring processes during droplet combustion. However, these results are for the combustion of an isolated fuel droplet. Nevertheless, the real burning spray is an integral of a vast number of droplets which are interacting among each other and with the surrounding environment along their own lifetimes. Hence, the effect of droplet-droplet interaction on the liquid-phase dynamics of the burning droplet have been investigated and further discussed in the next chapter.

Chapter 7. Combustion Characteristics of Two-Neighbouring Multicomponent Fuel Droplets

7.1 Introduction

The liquid fuel spray is a group of small size droplets that can interact among each other within the spray volume. This interaction is in turn reflected on the overall characteristics of the spray. During combustion, this interaction could be more effective due to the presence of the flame that is either surrounding a single droplet or multiple droplets. Hence, the combustion characteristics of the isolated fuel droplet are expected to be different from those of the same droplet when surrounded by other droplets. This applies to the droplet liquid-phase dynamics, since the droplet interior is directly affected by the surrounding temperature and species gradients which are influenced by the droplet-droplet interaction. Therefore, in the present chapter a magnified high speed visualization of the interaction between two multicomponent fuel droplets undergoing combustion is carried out. Emphasis is applied to the liquid-phase dynamics including nucleation, bubble generation, and the related droplet surface processes such as puffing and secondary atomization. The effect of droplet fragmentation on the neighbouring droplet has also been investigated.

Biodiesel/diesel blends, ethanol/diesel blends, water-in-diesel emulsions, and diesel-in-water emulsions have been investigated in the present work as the multicomponent fuels, in addition to the neat diesel, biodiesel, and ethanol as the single-component base fuels. The experimental work procedures and setups are explained in section (7.2) of the chapter. After which, the main findings are presented and discussed in section (7.3). The first part of the results section is assigned for discussing the effect of interactive droplet combustion on the droplet combustion characteristics – mainly the burning rate constant and flame shape – compared to those of the corresponding isolated fuel droplet. The liquid-phase dynamics of the interacting fuel droplets are then discussed. Additionally, the effects of droplet puffing and secondary atomization on its neighbour droplet are outlined. The overall findings of the present chapter are then summarized in section (7.4).

7.2 Experimental Setup

The schematic diagram of the two-droplet suspension setup is shown in Figure 7-1. The droplets are suspended opposite to each other with a spacing distance (x). Each of the droplets is suspended on a single monofilament SiC fibre that is attached to the sliding arm of a lab stand for easier control of the droplet position in accordance to the camera. The normalized spacing distance is varied in a range of (1-5) to investigate its effect on the droplet combustion. Backlighting imaging with the optical setup described in section (3.3.2.A) has been used for tracking droplet combustion throughout this experiment. Two camera settings are used in the present work. The first setting is used for tracking the droplet overall combustion and the surrounding flame. For these reasons, the camera is set to 1000 fps framing rate, 1 ms exposure time, and 768x768 pixels image resolution. The area covered by the camera was 7.68x7.68 mm^2, giving a spatial resolution of 30 μm/pixel for each image. The magnification rate achieved using this setup is 30 times the physical size. The second setting on the other hand, is used for tracking the liquid-phase of the interacting fuel droplets. Hence, the camera is set to 40000 fps framing rate, 25 μs exposure time, and 320x240 pixels image resolution. The area covered by the camera was 3.2x2.4 mm^2, giving a spatial resolution of 30 μm/pixel for each image.
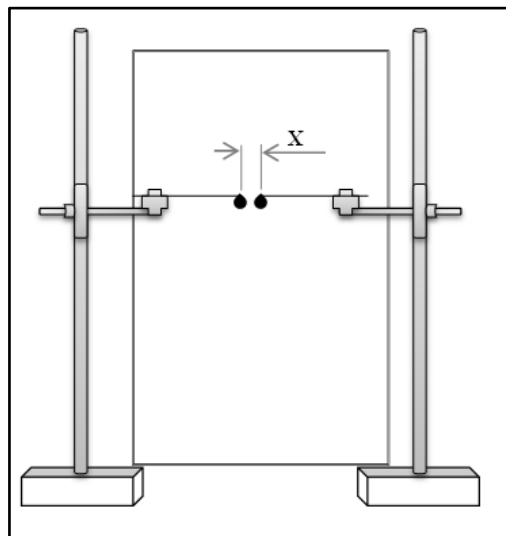
Figure 7-1: Schematic drawing of the two-neighbouring droplets suspension.

The investigated fuels are water-in-diesel and diesel-in-water emulsions, biodiesel/diesel and ethanol/diesel blends all of 10%, 20%, and 30% of the added substance concentration by volume with respect to the overall mixture volume. The neat

diesel, biodiesel, and ethanol have also been investigated as the single-component base fuels. The multicomponent fuel mixtures have been prepared in-lab prior to experiments according to the procedures described in section (3.2). The tests have been carried out many times for each fuel, and three successful tests are selected and saved for processing for each case. The images have been stored in the (TIFF) format and processed according to specifically written Matlab algorithms following the procedures described in Chapter Three.

7.3 Results and Discussion

The first part of the results section has been dedicated for presenting and discussing the variation in burning rate constant between the isolated fuel droplet and the corresponding interactive fuel droplets. Then, the nucleation rates and bubble growth rates in the multicomponent fuel droplet are discussed. The effect of nucleation and bubble generation on the puffing and secondary atomization from the multicomponent fuel droplet has also been discussed. Additionally, the secondary atomization and microexplosion as two forms of physical interaction between the neighbouring droplets has been discussed. Then, some of the processes tracked during the combustion of interacting droplets have been presented and discussed in the final part of the present section.

7.3.1 Flame Shape and Droplet Burning Rate

As mentioned in the experimental work description of the present chapter, the normalized droplet spacing distance has been varied along a span of (1-5). The spacing distance is defined in Chapter Two as the distance between the centres of the adjacent droplets normalized by the initial diameter. The present values of the normalized spacing distance have been selected so that the magnified imaging of the droplet is not affected, since, increasing the spacing distance results in the need to increasing the covered imaging area by increasing the distance between the lens and the droplet. This in turn, results in decreasing the magnification rate. Hence, the above range is selected to compromise for both the spacing distance and droplet image magnification. Additionally, since the distance is normalized by the droplet initial diameter, its values are not exactly the same for all the tested fuel droplets, but all are within the above specified range. This is because the droplet

initial diameter is changing slightly every time within a small range, and due to the delay resulting from suspending each droplet on its own fibre, these values are also slightly different. Hence, the resulting normalized spacing distance is within the range but not exactly the same for all the fuels as it will be shown in the following discussions.
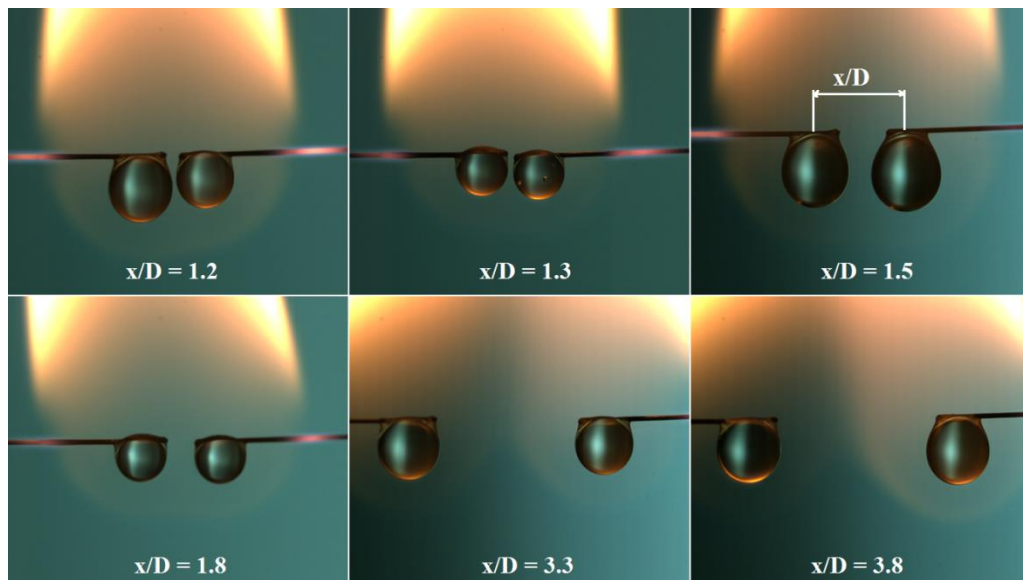
Figure 7-2: The effect of droplet normalized spacing distance on the flame surrounding the burning diesel fuel droplets.

Figure 7-2 shows the effect of changing the normalized spacing distance on the flame surrounding the interacting diesel fuel droplets. The normalized droplet spacing distance is set to 1.2, 1.3, 1.5, 1.8, 3.3, and 3.8 respectively. As the figure shows, for small distance values (<2), one flame is surrounding both droplets, and for higher values of the spacing distance (namely 3.3 and 3.8), each droplet have had its own surrounding luminous flame. Each of the interacting droplets in the cases listed in Figure 7-2 initially had its own flame, and then for small distances, these flames have merged into a single large flame. The same behaviour is shown to occur during the interactive combustion of the biodiesel droplets presented in Figure 7-3. The normalized droplet spacing distance for biodiesel fuel droplets is set to 1.2, 1.5, 2.7, 3, 3.4, and 3.8 respectively. As shown in Figure 7-3, for the first two cases – 1.2 and 1.5 spacing – the adjacent droplets are surrounded by a single flame. The same fuel droplets have had two separated flames for the spacing distances 2.7, 3, and 3.4. It is worthy to emphasize here that the ignition process of the droplets is fixed for all the tests. This process is performed by side heating of the SiC fibre of the droplet on the right

side of the viewing plane. After this droplet is ignited, the droplet to the left is ignited by the heat transferred from the burning droplet.
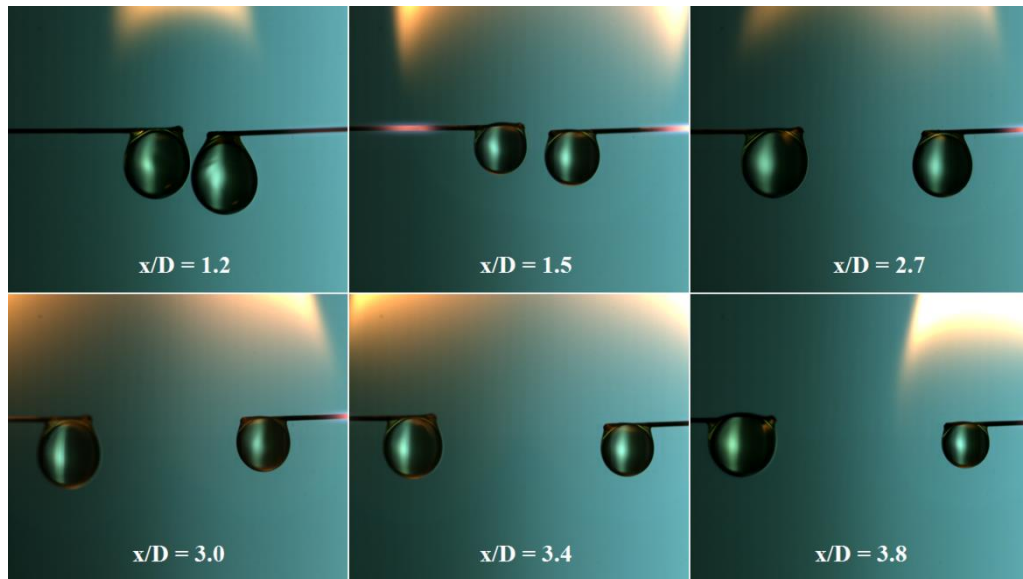
Figure 7-3: The interactive combustion of two-biodiesel fuel droplets at different normalized spacing distance values.

As shown in Figure 7-3 for the 3.8 spacing distance, the droplet to the left did not ignite despite the fact that its neighbouring droplet is already undergoing combustion. This implies that the heat transferred to the left droplet was not sufficient for creating a combustible mixture above the droplet, which in turn suggests that this heat was also not sufficient for raising the surface temperature of the droplet to the boiling point of the biodiesel.

The mechanism of flame propagation from a burning fuel droplet to its neighbouring droplet and the subsequent ignition of the latter droplet are shown in Figure 7-4. As shown in the figure, the droplet on the right side of the viewing plane – perpendicular to the paper – is ignited by the hot wire ignition method described in Chapter Three. The suspension fibre is heated by the butane flame away from the suspension point. Once it reached the ignition point, the fuel vapour/air mixture above the droplet is ignited as shown in the image corresponding to time 63 ms. Flame propagation then takes place as shown in images 71 ms to 119 ms respectively. In the interim, the left side droplet – that did not ignite yet – will start to heat up by the effect of the heat received from the adjacent droplet via convection and radiation. This is illustrated in the liquid phase of the left side droplet in images 87 ms to 143 ms compared to the preceding images. The heating up processes raises the droplet surface temperature, until reaching the boiling point of the diesel. Hence,

181

fuel vapour is emitted from the droplet surface and mixed with the surrounding air forming a combustible mixture that is ready for ignition. Once reached the instantaneous ignition point of the diesel, the combustible mixture is ignited on top of the droplet surface as shown by the red bounding circles in images 143 ms and 151 ms. Flame propagation took place through the combustible mixture until the left side droplet is completely surrounded by its own flame as shown in images 159 ms to 183 ms.
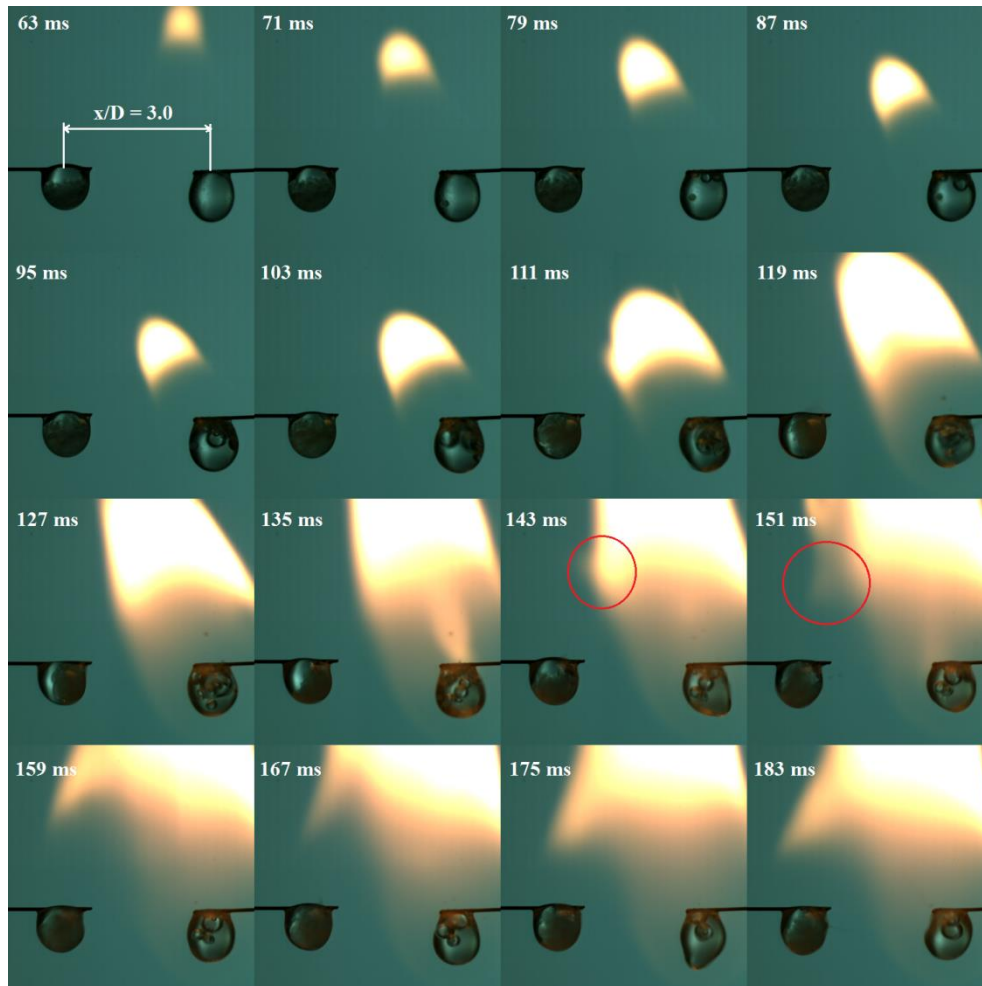
Figure 7-4: Temporal sequence of the flame propagation from a burning DW20 emulsion fuel droplet to its neighbour droplet.

Figure 7-5 shows the interactive combustion of two BD10 fuel droplets at normalized spacing distance values of 1.3, 1.7, 1.9, 2.4, 2.5, and 2.9 respectively. As shown in the figure, a single flame is surrounding the two droplets for the distance values up to 2.5, while for the spacing distance 2.9, each droplet had its own flame surrounding it. This is the same scenario for the BD10 fuel droplets and BD30 fuel droplets. Thus, it can be inferred that in the case of the biodiesel/diesel blends, the critical normalized spacing

distance below which the adjacent droplets will have a single flame surrounding them is about 3.
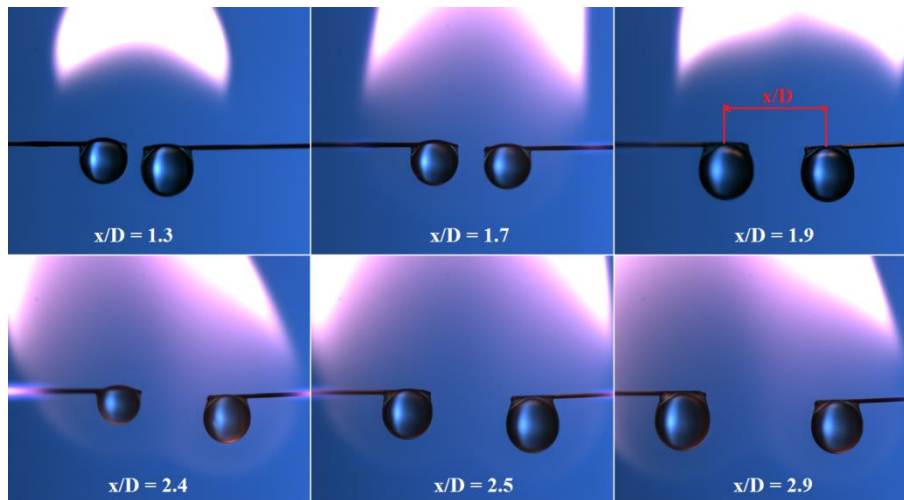
Figure 7-5: The effect of normalized spacing distance on the flame surrounding the interacting BD10 fuel droplets.

This is slightly different from the case of ethanol/diesel blends. In the case of the ED blends a single flame is bounding the two adjacent droplets even at higher distance values, as shown in Figure 7-6. The figure shows an example of the ED blends combustion, where two adjacent ED10 droplets are investigated at different normalized spacing distance values. The two droplets are surrounded by a single flame at distance values up to (2.9), and that the two droplets have had their own separated flames at 3.4 spacing distance.
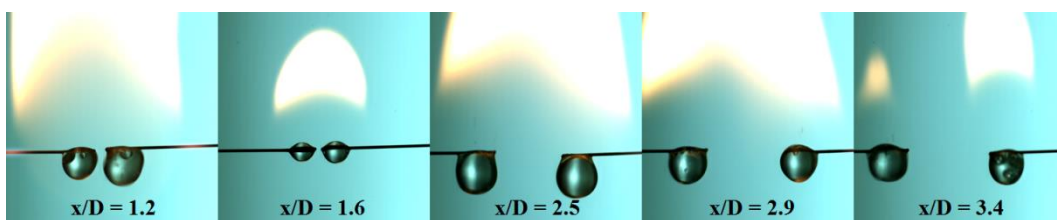
Figure 7-6: The interactive combustion of two-neighbouring ED10 fuel droplets at different normalized spacing distance values.

Therefore, it can be suggested that the critical normalized spacing distance for the ethanol/diesel blends is slightly above those of the biodiesel/diesel blends. This is shown to be somewhat comparable to the critical normalized spacing distance of the emulsion droplets. The latter are shown to have a single flame surrounding the adjacent droplet at a distance of 3 as shown in Figure 7-4, and shown to have two separate flames at 3.4 spacing

distance in the case of DW20. Hence it can be deduced that the critical normalized spacing distance of the emulsion droplets is between these two values.

The average burning rate constant during the combustion of two-neighbouring fuel droplets has also been investigated and evaluated for all the fuels under investigation. These include the single-component diesel, biodiesel, and ethanol, and the multicomponent biodiesel/diesel blends, ethanol/diesel blends, water-in-diesel emulsions, and diesel-in-water emulsions.

Figure 7-7 shows the effect of the normalized droplet spacing distance on the burning rate constant during the interactive droplet combustion of the single-component fuels, biodiesel/diesel blends, ethanol/diesel blends, diesel-in-water emulsions, and water-in-diesel emulsions. The first graph in the figure shows the burning rates of the neat diesel, biodiesel, and ethanol fuels. As shown in the graph, the burning rates of both diesel and biodiesel fuel droplets are proportional to the droplet spacing distance, while those of the ethanol fuel droplets are shown to be irresponsive to the normalized spacing distance. This is attributed to the increase in the projected area of the sooty flame by increasing the distance leading to the increasing the effect of heat transfer by radiation and convection and in turn, rising the temperature of the surrounding environment [107]. Additionally, the concentration gradient in the combustion zone is proportional to the normalized spacing distance [178], hence, increasing the spacing distance causes the increase in the burning rate.

The second graph of Figure 7-7 shows the effect of the normalized spacing distance on the burning rate constants of the biodiesel/diesel blends. The blends are of 10%, 20%, and 30% biodiesel volume concentration with respect to the overall volume of the mixture. The burning rate of the BD blends shows a slight increase with increasing the normalized spacing distance for all the blend proportions. This increase is from 0.96 to 1.01 mm^2/s, 096 to 1.17 mm^2/s, and 0.84 to 1.16 mm^2/s for spacing increase from 1.7 to 2.5, 0.9 to 4, and 1.2 to 3.5 in the cases of BD10, BD20, and BD30 blends respectively. The same trends are shown in the third graph of Figure 7-7 for the ethanol/diesel blends but with higher values of the burning rate constant.

It can be seen from the figure also, that both the BD and ED blends show a uniform distribution of the burning rate with respect to the spacing distance. This uniform distribution is not seen in the cases of the emulsions presented in the fourth and fifth graphs of the figure. The burning rates of the interactive emulsion droplets are more scattered as a response to changing the spacing distance.

184
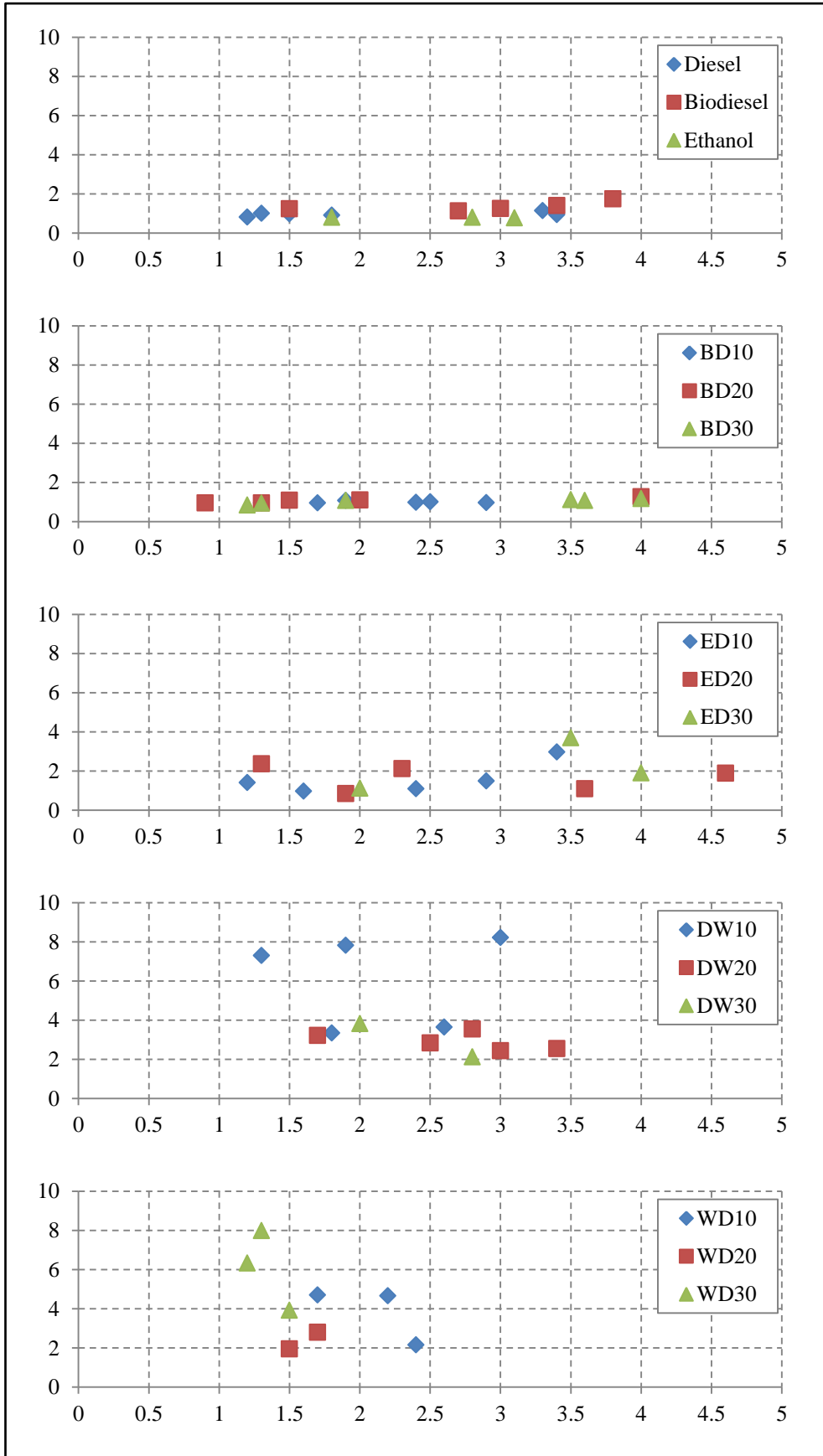
Figure 7-7: The effect of the normalized spacing distance (x-axis) on the average burning rate constant (mm²/s) (y-axis) during the interactive droplet combustion of all the fuels under investigation.

185

This is shown in the case of the DW10 emulsion, where the burning rate constants at 1.8 and 2.6 spacing distance values are less than those at 1.3, 1.9, and 3.8 distance values. This in turn, makes it difficult to decide whether the burning rate is proportional or inversely proportional to the spacing distance. This is because the emulsion droplet did not undergo complete evaporation in all the tested cases, instead, microexplosion and complete rapture of the droplets takes place in all the cases.

Additionally, in all these cases the droplet experiences a slight increase in size rather than the expected decrease due to the generation and growth of bubbles within these droplets. These bubbles are grown to sizes almost comparable to the droplet size; hence the droplet size did not decrease a lot. This resulted that the calculated droplet burning rate constant is not precisely reflecting the burning rate of the droplet because it is simply evaluated as the rate of change of droplet diameter with time, and because the rate of change could not be evaluated exactly, due to the interaction between the effect of fuel evaporation from the droplet surface that leads to droplet size decrease on one side, and the effect of bubble growth inside the droplet that results in droplet size increase on the other. This scenario did not occur for the other multicomponent fuel droplets, thus, the evaluated burning rate constants reflect precisely the burning rate of the droplet for these fuels.

Furthermore, comparing the burning rate values of Figure 7-7 with those evaluated for the isolated fuel droplet combustion described in Chapter Four, it can be inferred that the present burning rate constants of the interactive droplet combustion are higher than those of the corresponding isolated droplet combustion. In order to compare the difference in magnitude between the burning rates of both cases, the ratio of these values has been evaluated according to equation (7-1).

$$\eta = \frac{K_{int}/X_n}{K_{isol}} \qquad \text{.........} \qquad \textbf{(7-1)}$$

Where K_{int} is the burning rate during the interactive droplet combustion, X_n is the corresponding normalized spacing distance, and K_{isol} is the burning rate of the isolated droplet. The burning rate of the interactive droplet combustion has been normalized by the spacing distance to evaluate the net value of the burning rate per unit value of the distance. The average of all the η ratio values and the corresponding standard deviation values have been evaluated and presented in Figure 7-8. As the figure shows, the value of η for the neat diesel and biodiesel are slightly above unity, while that of the neat ethanol is below unity.

The η values of the multicomponent fuel mixtures are all above unity implying higher burning rates of the interactive fuel droplet combustion compared to the corresponding isolated fuel droplet combustion. However, different ratio magnitudes are obtained for each fuel mixture.
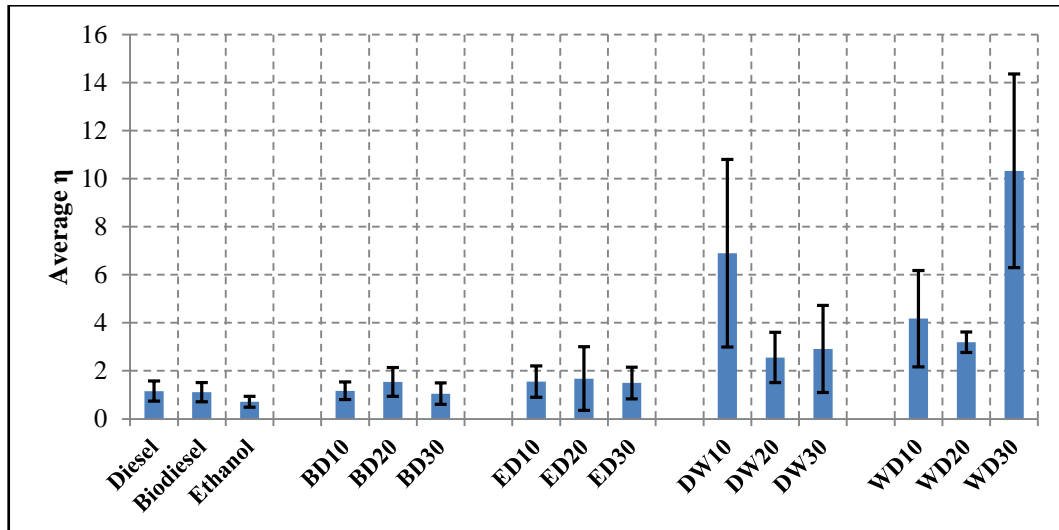
Figure 7-8: The average of η for all the fuels under investigation.

The BD blends have shown the least ratio magnitudes among all the multicomponent fuel mixtures, with values in the range of 1.1-1.5. The ED blends also are showing η values in the range of 1.5-1.7, whereas these values jump to the ranges of 3-7 and 4-10 in the cases of the DW and WD emulsions respectively. Although, the standard deviation of all the emulsion droplets are relatively high, suggesting an uneven repeatability of the calculated ratio compared to those of the BD and ED blends in addition to the single-component fuels.

In conclusions, the burning rate of the multicomponent and even single-component fuel droplets under interactive combustion is almost proportional to the spacing distance separating between the adjacent droplets. And that the critical normalized spacing distance below which the two adjacent droplets will have a single flame surrounding them is about 3 in the case of the biodiesel/diesel blends, and slightly above 3 for each of the ethanol/diesel blends, water-in-diesel emulsions, and diesel-in-water emulsions.

With the flame shape and droplet burning rate constant of the interacting fuel droplets are clarified, it is time now to further investigate the liquid-phase of the interacting fuel droplets. This is carried out in the next section.

7.3.2 Nucleation and Bubble Growth Rates

As mentioned in the experimental work description, for studying the liquid-phase dynamics, the camera is set to 40000 fps framing rate rather that the 1000 fps used for studying flame shape and burning rate. Hence, a magnified high speed tracking of the interiors of the two-interacting fuel droplets is achieved.
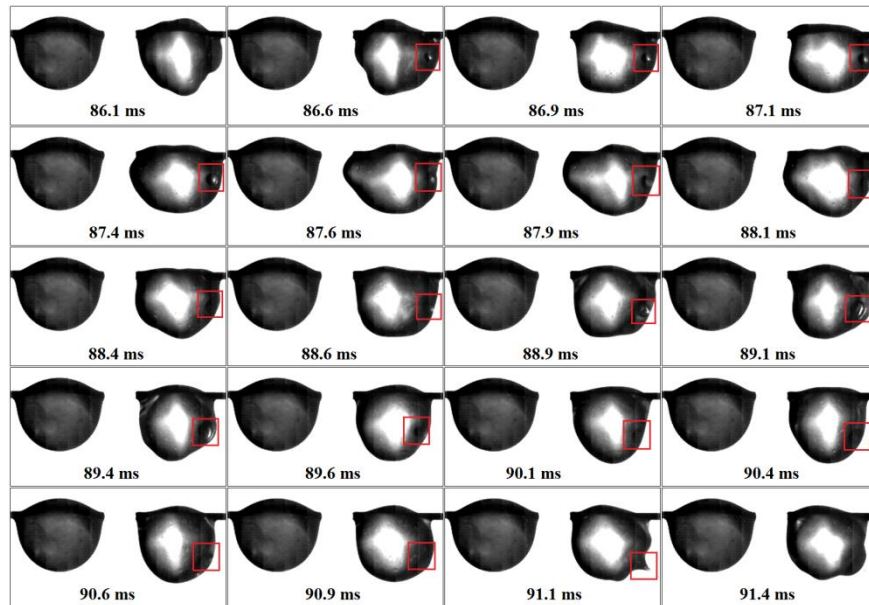
Figure 7-9: Temporal sequence of the bubble growth inside a WD20 droplet during the combustion of two-interactive droplets.

Figure 7-9 shows the temporal sequence of bubble growth inside one of the interactively burning WD20 fuel droplets. The bubble is initiated in one site and travelled due to circulation inside the droplet into another site. The sequence of bubble growth is the same as discussed in Chapter Six, therefore, no further discussions will be performed on this issue. However, the number of bubbles generated is noticed to be higher than that of the isolated fuel droplets. Hence, statistical investigation has been carried out to compare the nucleation rates of the multicomponent fuel droplets during interactive two droplet combustion with those obtained in Chapter Six for the isolated droplets during combustion. Figure 7-10 shows the effect of biodiesel, ethanol, and water concentrations on the average nucleation rate within the biodiesel/diesel blend, ethanol/diesel blend, water-in-diesel emulsion, and diesel-in-water emulsion fuel droplets. The nucleation rate has been presented in the logarithmic form due to the big difference in magnitudes between the different multicomponent fuel mixtures. As shown in the figure, the nucleation rate for all the fuel mixtures is inversely proportional with the concentration of the substance –

biodiesel, ethanol, or water – added to diesel. This is the same trend shown for the nucleation rate inside the isolated fuel droplets of these mixtures in Chapter Six. Additionally, the emulsion droplets of both water-in-diesel and diesel-in-water have had the highest nucleation rates, followed by the ethanol/diesel blends, and the lowest are the biodiesel/diesel blends. Again, this is attributed to the miscibility of the added substances on diesel, where biodiesel is completely miscible in diesel so that the resulting mixture from blending diesel with biodiesel has the most stable structure compared to the others and accordingly the lowest nucleation rate is obtained. This is because nucleation takes place due to the separation of the constituents and superheat boiling of the low boiling point components.
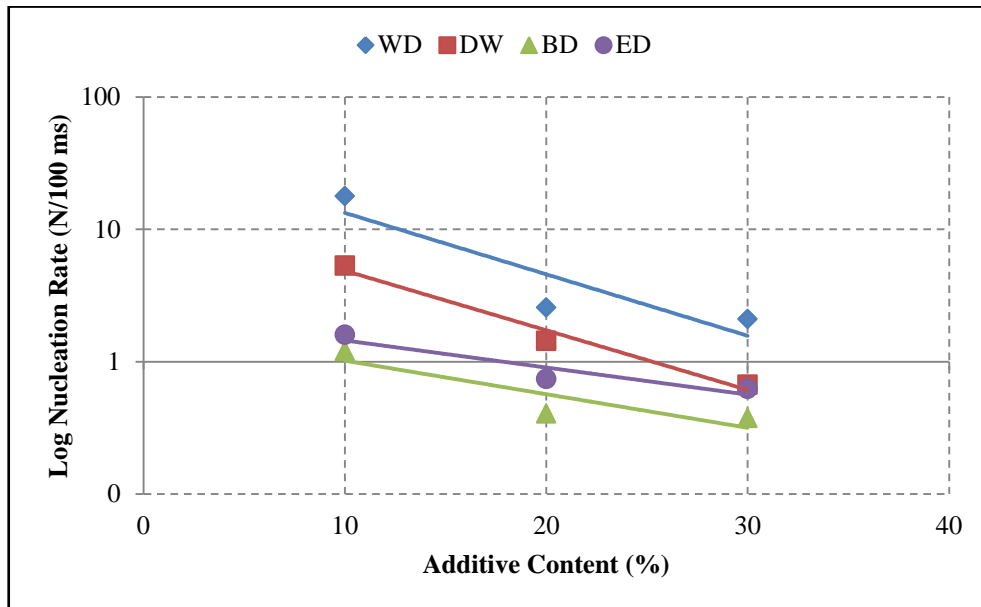
Figure 7-10: Average nucleation rate with respect to the concentration of the substance added to diesel in the multicomponent fuels during the combustion of two interacting fuel droplets.

Ethanol on the other hand, is partially miscible in diesel; therefore, the nucleation rate within the ethanol/diesel blends is higher than that in the corresponding biodiesel/diesel blends of the same concentrations. Whereas, the water is completely immiscible in diesel, therefore, the resulting emulsions – whether WD or DW – are unstable and the separation of the components is potentially high. Thus, the nucleation rate within the emulsion droplets is the highest as shown in Figure 7-10. Furthermore, to compare the nucleation rate within the multicomponent droplets during both isolated combustion and interactive combustion conditions, the ratio of the latter to the former has been evaluated and presented in Figure 7-11 with respect to the concentration of both water and ethanol on the

left side, and water and biodiesel on the right side. In order to illustrate the similarity in behaviours, the water-in-diesel emulsions and ethanol/diesel blends are presented together, while the diesel-in-water emulsions and biodiesel/diesel blends are plot together. As the figure shows, generally, the nucleation rate within the interacting fuel droplets is higher than that within the corresponding isolated fuel droplets. This is imputed to the higher heat transfer rates to the droplet from the neighbouring droplet and its surrounding flame. This in turn increases the temperature of the liquid-phase of the droplet and increases the superheat boiling of the low boiling point components in the mixtures, leading to augmenting the nucleation sites and nucleation rate in the droplet interior.
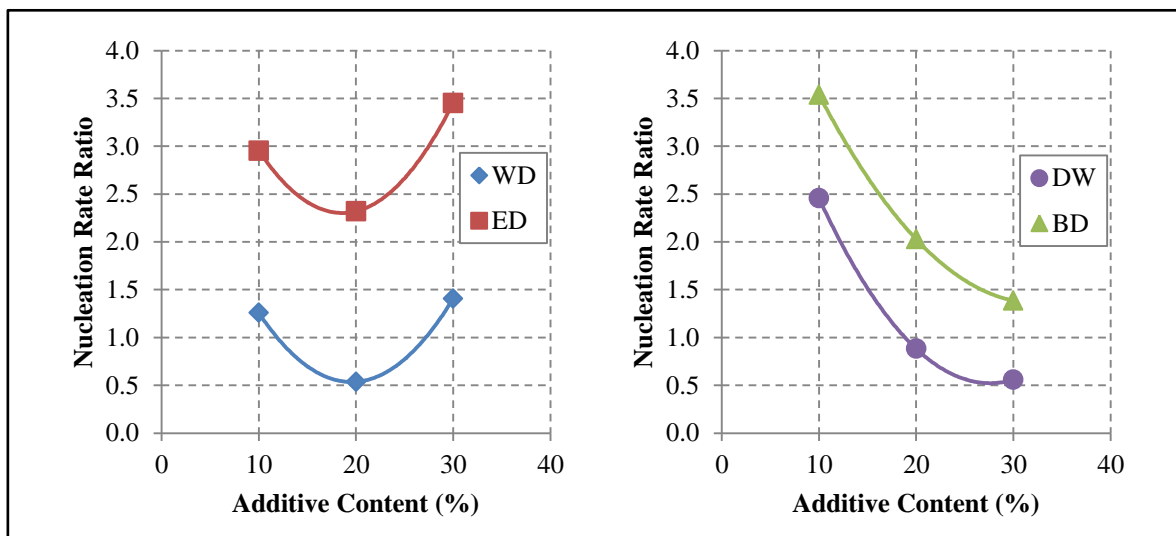
Figure 7-11: The effect of additive concentration on the ratio of the average nucleation rate evaluated to the two-interacting fuel droplets to that evaluated to the single isolated fuel droplet.

Additionally, it can be seen from the figure that even the BD blends which are the least in nucleation rate are experiencing an increase in the nucleation rate during the two-droplet interactive combustion. This increase may reach up to more than three times the rates of the isolated droplet as sown in the case of BD10 fuel blend. These high ratio magnitudes of the BD blends and also the ED blends are due to the lower nucleation rates reported for these fuels in the isolated droplet case, which makes the denominator relatively small, whereas in the case of emulsions, the denominator is relatively large therefore, the ratio of the nucleation rate between the two-droplet and single droplet combustion is slightly above unity in most of the cases except the DW10 case in which the ratio is up to two and a half.

Figure 7-12 shows the effect of additive concentration on the average bubble growth rate within the multicomponent fuel droplets. The bubble growth rate has been presented in

the logarithmic format because of the big value difference between the different fuel mixtures. From the figure it can be seen that except the diesel-in-water emulsion, the bubble growth rate is inversely proportional to the increase in additive concentration. Additionally, it can be seen that the ethanol/diesel blends and water-in-diesel emulsions have had the highest growth rates, while the lowest growth rates are shown in the case of the biodiesel/diesel blends which are preceded by the diesel-in-water emulsions. This is in agreement with the nucleation rate behaviours shown in Figure 7-10.
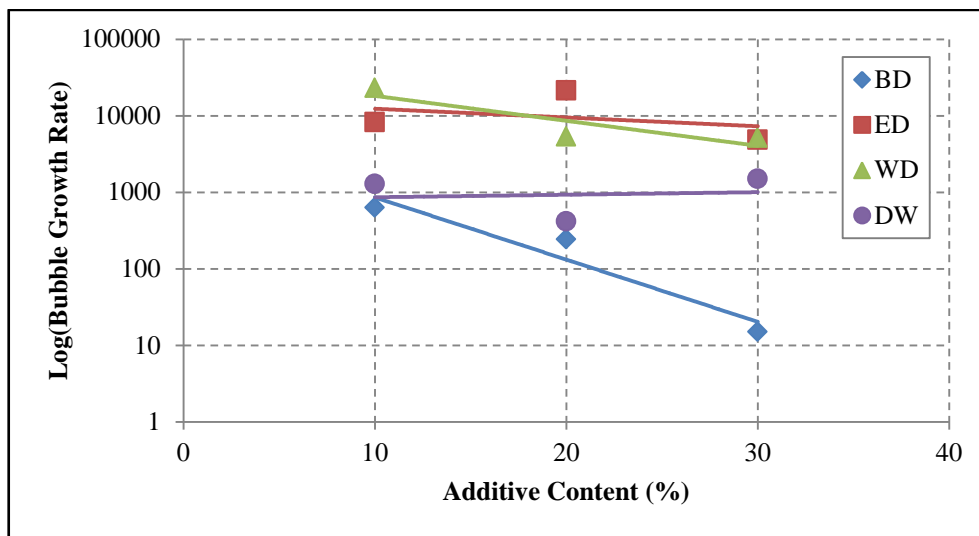
Figure 7-12: The effect of additive concentration on the average bubble growth rate during the combustion of two-interacting fuel droplets.

7.3.3 Secondary Atomization and Micro-Explosion

The interaction between the adjacent droplets may take different forms, such as the thermal interaction shown in the form of increased high transfer rates between the droplets as formerly discussed, sharing the same flame in the case of small size droplets, and the dynamic interaction shown in the collision and coalescence of these droplets. On the other hand, the multicomponent fuel droplet combustion is mostly characterized by the high rates of secondary atomization. Hence, the effect of this process on the neighbouring droplets may be added to the dynamic interaction between the adjacent droplets. Therefore, understanding the effect of secondary atomization on the neighbouring droplets is essential for understanding the overall dynamic behaviour of the real spray during combustion.

Figure 7-13 shows the temporal sequence of the impact and merge of sub-droplet emitted from a burning WD10 fuel droplet with an adjacent droplet. The sub-droplet is

emitted from the droplet on the right side of the viewing plane. It continued moving towards the droplet on the left side as shown in images 187.25 ms to 187.85 ms. The sub-droplet, then touched the droplet as shown by the red bounding box in image 187.90 ms. The collision between the left droplet and moving sub-droplet then occurred in the form of coalescence as shown in image 187.90 ms and the subsequent images. By this coalescence, the sub-droplet is merged with the droplet causing an increase in the size and mass of the latter. The droplet has also experienced a shape change due to the impact of the fast flowing sub-droplet as shown in image 188.20 ms. Hence, it can be deduced that this form of interaction between the neighbouring droplets – that is not available in the case of isolated droplets – is effective in defining the nature of the consequent combustion behaviour of the droplet.
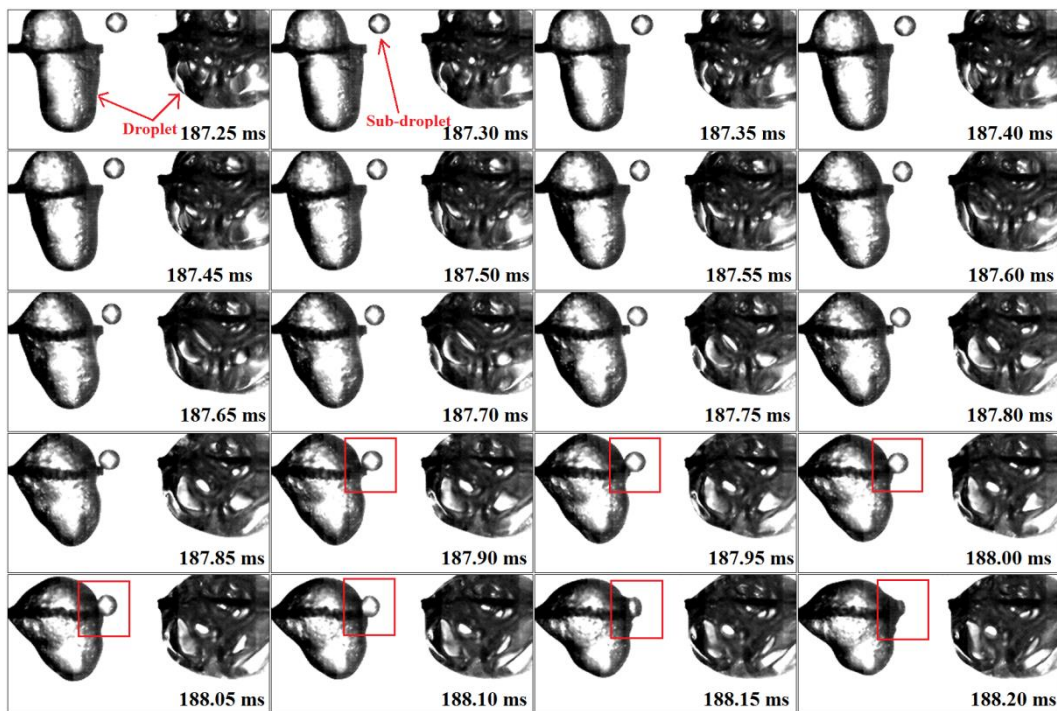
Figure 7-13: Temporal sequence of WD10 droplet merging with a sub-droplet emitted from a neighbouring parent droplet.

Another form of droplet-droplet interaction is revealed in the effect of droplet microexplosion on its neighbour droplet as shown in Figure 7-14. The droplet on the left hand side of the viewing plane is exploded by the high pressure burst of the bubble inside as explained in Chapter Six. The resulting explosion wave has travelled radially as shown in images 0.03 ms and 0.13 ms. This wave then, hit the droplet on the right causing an impact-like disturbance on the droplet side facing the wave as shown in images 0.13 ms to

0.38 ms. Subsequent to the impact, the right side droplet went on partial disintegration leading to secondary atomization and sub-droplet ejection as shown in image 0.50 ms and the consequent images. Hence, the effect of microexplosion is not limited on the droplet suffering the explosion, instead, it exceeds to the adjacent droplets and cause further disintegration of the droplets.
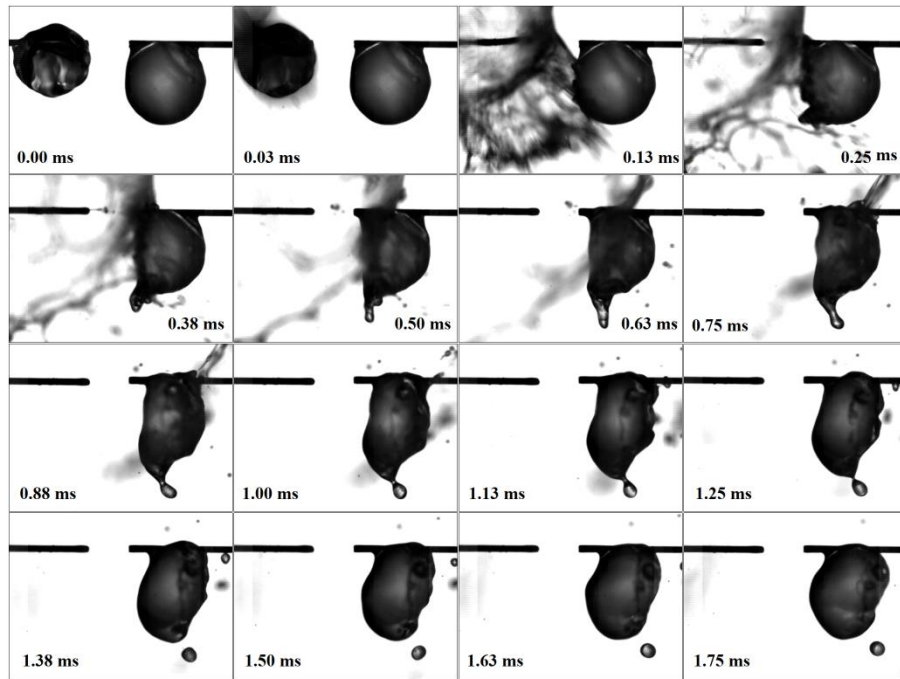
Figure 7-14: Temporal sequence of the effect of WD10 droplet explosion on the droplet neighbouring it (the time is set from the start of explosion).

7.3.4 Other Liquid Phase Dynamics

Figure 7-15 shows the accumulation of water within the two-interacting WD10 fuel droplets. This water is resulting from the emulsion mixture separation, and is acting as a source of heterogeneous nucleation as shown in by the growing bubble in the red bounding boxes. This accumulation occurs almost on the water-in-diesel and diesel-in-water emulsions in addition to the ethanol/diesel blends, and never occurred in the biodiesel/diesel blends. As it is shown in the figure, the grayscale intensity of this object is different from those of the droplet overall liquid phase and the growing bubble, therefore, it is distinguished as water accumulation in the case of the emulsions, and diesel in the case of ethanol/diesel blends, because in both cases, water and diesel represent the low volatility substance in the multicomponent fuel mixture. It can be seen from the figure that the

193

growth time of the bubble generated on the water mass is about 0.95 ms which is relatively short period, this implies that the accumulation of water – or diesel in the ED blend – enhances bubble growth rate, and in turn, the subsequent dynamics such as puffing and secondary atomization.
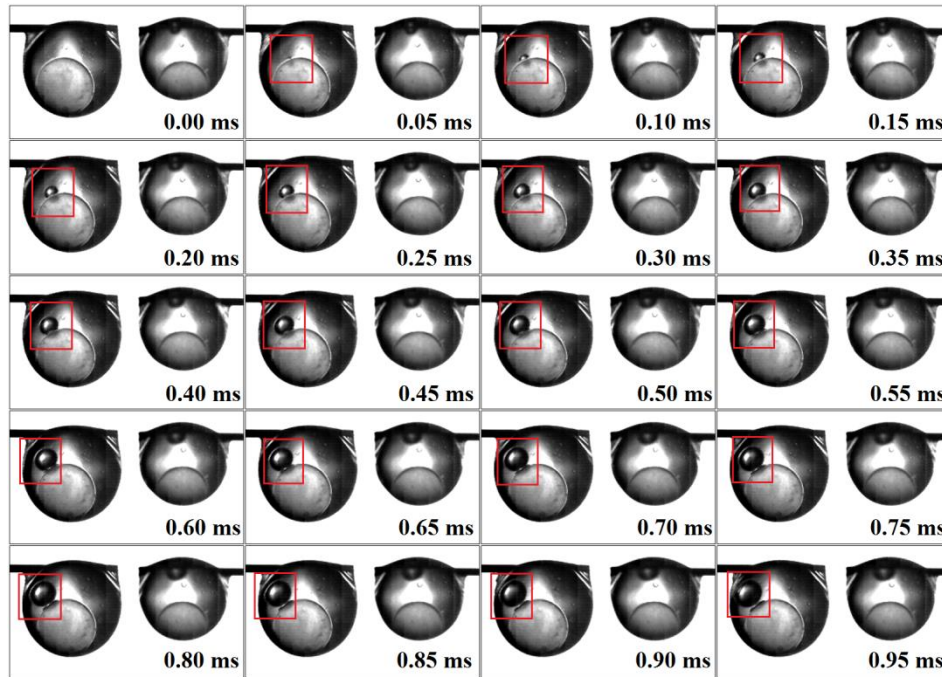
Figure 7-15: Temporal sequence of the effect of water agglomeration on the nucleation and bubble growth within a WD10 droplet.

Another phenomenon that is noticed to occur in the droplet liquid-phase is the internal circulation of the droplet. This phenomenon has already been described by a number of studies. However, in the present work it is noticed that the direction of this circulation is variable between the left and right hand side droplets. Figure 7-16 shows the temporal sequence of bubble circulation inside each of the two-interactive burning BD10 fuel droplets. The motion of the bubble in the left droplet is tracked by the red bounding box, and that of the bubble in the right droplet is tracked by the yellow box. As the figure shows, the bubble in the yellow box is moving clockwise and that in the red box is moving counter-clockwise. This direction has been noticed to occur for all the bubbles inside all the droplets, but, the case in Figure 7-16 is selected to be representative because the bubble motion inside the two droplets is occurring simultaneously. Accordingly, this internal circulation is attributed to the effect of the SiC fibre on the droplet, because the direction of circulation is always starting from the side of the fibre and continuing to the other side.
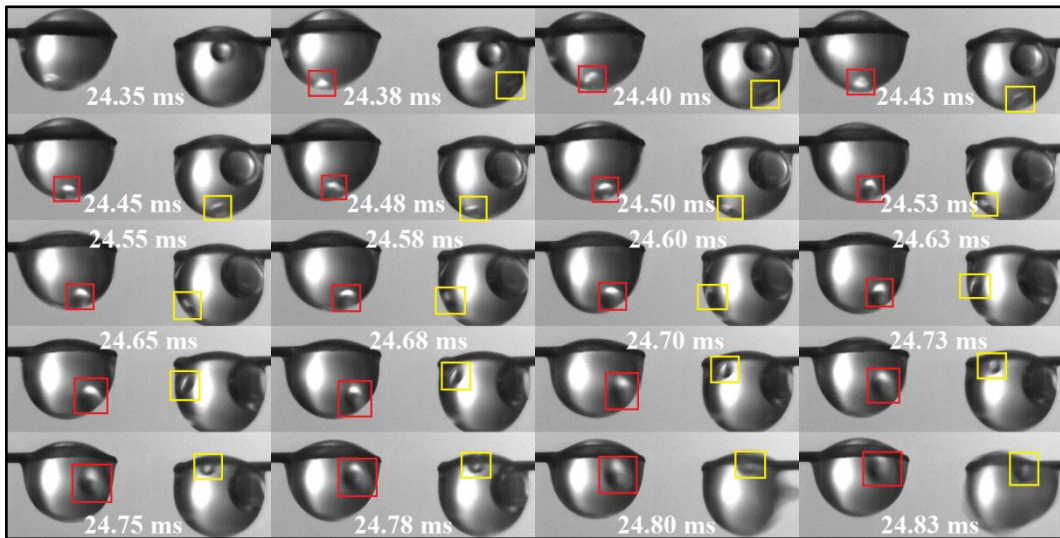
Figure 7-16: Temporal sequence of the effect of the SiC fibre on inducing circulation within the suspended burning droplets.

This in turn, suggests that the suspension fibre has an effect on inducing circulation within the droplet due to the temperature difference between the fibre and the droplet liquid-phase. This is in agreement with the findings of Liu et. al., [281] about the effect of the supporting fibre on inducing gas-phase micro-convection during the combustion of n-octane and n-decane fuel droplets in microgravity.
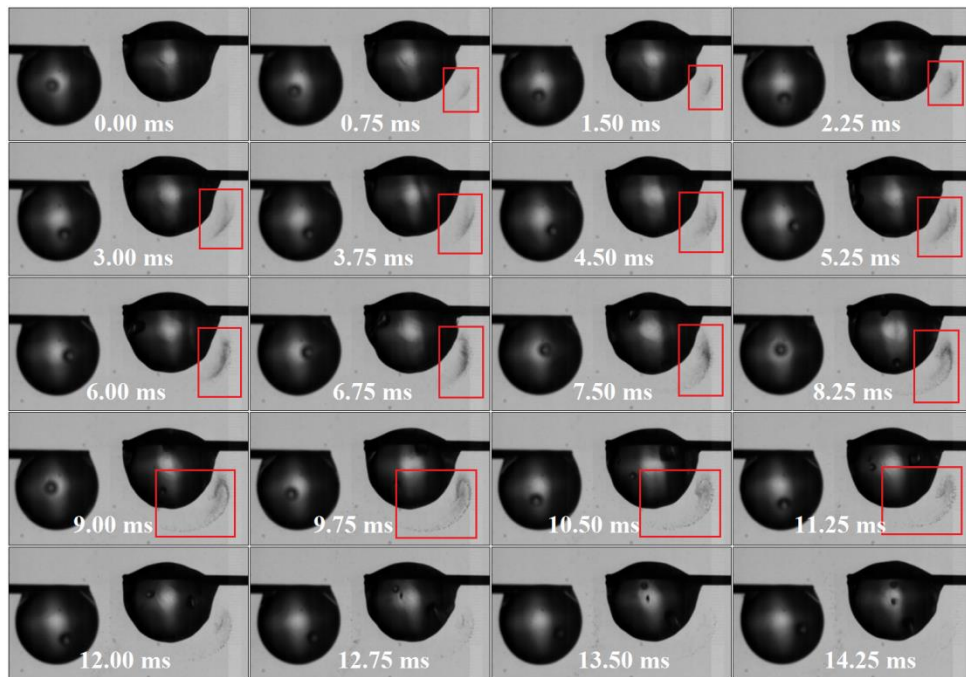
Figure 7-17: Temporal sequence of the soot aggregation around a burning diesel fuel droplet (the time is set from the appearance of the soot).

Moreover, Figure 7-17 shows the local and instantaneous soot aggregation on one side of a burning neat diesel fuel droplet during the interactive combustion of two adjacent fuel droplets. The neat diesel fuel is burning steadily without any chaotic shape variation and sub-droplet emission. Hence, flow visualization within and around the diesel fuel droplet is easier than that during the multicomponent fuel droplet combustion. Once formed, the soot aggregated on the outer side of the right hand side droplet as shown in images 0.75 ms to 11.25 ms. The soot aggregation on this side is because it represents the boundary of the flame surrounding both droplets; therefore, soot aggregation on the middle part between the two droplets was not possible. Thereafter, the soot move upwards due to the buoyancy effect as shown in images 5.25 ms to 11.25 ms. The upward motion of the soot takes the form of a vortex as shown in the figure. This suggests the existence of such vortices around the burning droplet.

7.4 Summary

In the present chapter, a magnified high speed imaging of the liquid-phase during the interactive two droplet combustion of the multicomponent fuels in addition to the base single-component fuels have been implemented. The effect of droplet-droplet interaction on the droplet burning rate constant and the resulting flame shape have been firstly investigated. Then, the effect of the interactive droplet combustion on the nucleation and bubble generation within the droplet has been investigated. Quantitative analysis has then been performed for estimating the nucleation and bubble growth rates. The results have shown that compared to the isolated fuel droplet results, both nucleation and bubble growth rates within the multicomponent fuel droplet are increased with the presence of an adjacent fuel. These rates may reach to up to three times the rates of the corresponding isolated fuel droplet. This is attributed to the increased heat transfer rates to the droplet from the adjacent fuel droplet and its surrounding flame.

The effect of secondary atomization and microexplosion processes of one of the droplets on the other neighbouring droplet has also been investigated. These processes are shown to enhance the secondary atomization and sub-droplet emission propensity of the droplet by causing impact like action that induces droplet disintegration.

Furthermore, separation and accumulation of diesel in the ethanol/diesel blends, and water in the water-in-diesel and diesel-in-water emulsions has also been observed.

Chapter 8. Summary and Future Work

8.1 Summary

In the present work, a high speed backlighting and shadowgraph imaging and subsequent image processing leading to quantitative analysis of the multicomponent fuel droplet combustion including liquid-phase dynamics are performed. Two categories of multicomponent fuels – in which diesel is the base fuel – are prepared and utilized. The first category is the biodiesel/diesel and bioethanol/diesel blends, while the second category is the water-in-diesel and diesel-in-water emulsions.

Specific optical setups are developed in-lab and used for tracking droplet combustion. The first setup is associated with the backlighting imaging with the resulting magnification of the droplet images being 30 times the real size. The second optical setup is used for Schlieren and shadowgraph imaging, with the resulting magnification being 10 times the real size for both techniques. Those magnifications made the high speed visualization and tracking of the droplet interior easily affordable.

Using the aforementioned optical setups, spatial and temporal tracking of nucleation, bubble generation, internal circulation, puffing, microexplosion, and secondary atomization during the combustion of isolated multicomponent fuel droplets are performed. This offered the privilege of full sequential tracking of droplet secondary atomization from initiation to sub-droplet generation.

8.1.1 Shape and Size Characteristics of the Isolated Multicomponent Fuel Droplet

- Both types of emulsions show an increase in the burning rate with increasing water content in the emulsion, with higher rate for the WD emulsion. This is attributed to the increase in puffing and secondary atomization from the emulsion droplets that enhances air fuel mixing and in turn increases burning rate. And it is in agreement with the published results.

- Increasing the concentrations of ethanol and biodiesel in the mixture will lead to a steep – in the ED blends – and slight – in the BD blends – decrease in the droplet

197

burning rate. This is expected in light of the burning rate values of the single-component fuels (diesel, biodiesel, and ethanol) respectively, and is in agreement with the published work on diesel burning rate values when blended with biodiesel and ethanol respectively.

- The BD blends are burning relatively smoothly compared to the other multicomponent fuels as a result of the miscibility of diesel and biodiesel in each other leading to a relatively homogeneous mixture. The early stage constant droplet size shown for the single-component fuels is also occurring with the BD fuel droplets. Moreover, for a short time period within the interval bounded by the 50% and 60% portions of the droplet lifetime, a slightly constant droplet size pattern is noticed for the blends compared to diesel and biodiesel. This is referred to the heating and evaporation of the less volatile component in the multicomponent mixtures.

- The ED blends have shown the most chaotic behaviour among all the studied fuels. This is attributed to the partial miscibility of ethanol in diesel as stated previously. Hence, compared to the mixtures produced by blending diesel with biodiesel – which are completely miscible in each other – and the emulsions generated by mixing water with diesel – with the aid of the emulsifying agents – blending diesel with ethanol results in highly metastable mixtures. This random droplet combustion behaviour of the ED blends is in agreement with the published results.

- The same combustion behaviour of the ED blends is shown to happen during the combustion of the emulsion droplets with less instability. This is due to the effect of the emulsifying agents used for preparing the emulsions. These agents act as mixture stabilizers that prevent phase separation within the emulsified fuel.

- Generally, the multicomponent fuel droplets show a higher droplet size fluctuation compared to the single-component fuel droplets. The intensity of this fluctuation is uneven among the multicomponent fuel droplets because of the effect of components miscibility in each other and the resulting mixture stability as explained above. This intensity is higher at the second half of the droplet lifetime for all the studied fuels. And is occasionally high compared to the droplet initial diameter.

- Increasing the additive concentration in the ED and BD blends decreases the fluctuations in the droplet size. This is exactly the opposite in the case of emulsion

198

droplets, where the fluctuation is increased by increasing the concentration of water in the emulsion. The size increase occurrence time is almost the same and it accounts for about 40-50% of the droplet lifetime. This implies that in a large portion – almost half – of its lifetime, the burning multicomponent fuel droplet experiences size fluctuation leading to an increase in its diameter. This fluctuation is basically attributed to the stability of the multicomponent fuel mixture resulting from the miscibility of its components in each other.

- There are three distinctive stages in the combustion of the fuel droplet. The first stage is shown in the early 20% of the droplet lifetime, where ignition and flame initiation takes place, followed by flame propagation. The second stage is for the next 60% of droplet lifetime, where steady burning of fuel takes place, and flame size is relatively constant. And the third stage is the last 20% of the droplet lifetime, where the flame starts to shrink height wise while its width remains almost the same until the final stages of combustion.

- At the early 10% of the overall droplet combustion time, the diesel droplet experiences dramatic increase in flame height, thereafter, the flame decreases slightly, and grows again. This increase in flame height is attributed to the combustion of the diesel vapour that is generated during droplet heating prior to ignition. After the vapour is consumed by combustion, flame height decreases to a certain level that is defined by the rate of diesel fuel evaporation from the droplet surface and the tendency of this fuel to generate soot during combustion.

- Compared to the flame surrounding the neat diesel fuel droplet, the flames of all the diesel-based multicomponent fuels are lower in height and similar in width. Accordingly, lower sooting tendency of the multicomponent fuels is suggested. This is in agreement with the published data for biodiesel/diesel blends, ethanol/diesel blends, and water/diesel emulsions.

- The three combustion stages shown during the combustion of the single-component fuels are also recognisable for the multicomponent fuels, especially for the BD and ED blends. However, for the WD and DW emulsions, the third stage is shifting to the final 10% of the droplet lifetime.

- The sudden increase in flame height noticed during the combustion of the neat diesel droplet has also been observed during the early stages of droplet combustion of the ethanol/diesel blends and water-in-diesel emulsions. Though, in the case of

199

biodiesel/diesel blends, the sudden increase in flame height is barely recognized to occur during the combustion of the blend.

- The flames surrounding the emulsion droplets have experienced sudden decrease in the size – both height and width – midterm the droplet lifetime. This reduction in the luminous flame size is ascribed to the instantaneous blow-off of the flame due to water vapour emission from the droplet by puffing. This water vapour blows the soot – that gives the flame its luminosity - away from the droplet so that the luminous flame height appears to be reduced. Once the effect of the vapour jet is retracted, soot accumulation upstream resumes, and the flame retrieve its size.

- Since flame width is almost constant and is not affected by buoyancy, it might be considered as the flame diameter. Especially, when compared with flame results under zero gravity conditions, it shows a good similarity in shape and magnitude. Accordingly, with the aid of droplet diameter variation and using the flame width as its diameter, the flame stand-off ratio is evaluated.

8.1.2 Puffing, Sub-droplet Emission, and Microexplosion Characteristics of the Isolated Multicomponent Fuel Droplet

- Shadowgraph imaging is found to be effective in tracking the vapour jets emerging from the droplet in the form of puffs. The boundaries of the jets were clearly distinguishable from other objects in the image including the droplet.

- The single-component droplets did not experience puffing and secondary atomization occurrences during their lifetimes. However, some odd puffing incidents took place at the end of both neat biodiesel and neat diesel droplets. These puffing events are attributed to the heterogeneous nucleation inside the diesel and biodiesel droplets.

- Generally, the droplets of all the multicomponent fuel mixtures studied in the present work have experienced puffing and secondary atomization. The puffing incidents are shown to occur over the entire droplet lifetime. The number and intensity of these puffs are variable for each type of the multicomponent fuel mixtures.

- The biodiesel/diesel blends have shown the least number of puffs compared to the other mixtures that were relatively comparable to each other. Furthermore, some of

the water-in-diesel and diesel-in-water emulsion droplets have suffered microexplosion before undergoing complete evaporation. This in turn, have resulted the emulsion droplets are experiencing high number of puffs along a short period of time, resulting in higher puffing rates compared to the droplet of the biodiesel/diesel and ethanol/diesel blends.

- Despite the type of fuel mixture, almost all the droplets shared the same sequence of events before and during puffing. The first sign of puffing occurrence is the droplet size increase. This increase is attributed to the bubble growth inside the droplet prior to puffing. This bubble continues pushing the thin layer of the droplet surface outwards from inside until the moment when the droplet surface cannot withstand this force, so the droplet raptures locally and the vapour contained in the bubble emerges outside in the form of a jet. The release of the vapour from the droplet causes sudden size reduction and shape deformation of the burning droplet.

- If the puff is weak, the droplet will retain its original shape and size after a short period of recoiling. And, if the puff is strong, ligament detachment from the droplet surface leading to sub-droplet generation will take place.

- Prior to sub-droplet ejection, the parent droplet is found to encounter a certain shape change that may be linked to the strength of the puff and in turn, to the size of the bubble triggering that puff.

- The maximum penetration of the vapour jet is found to range from a fraction of the droplet radius to several droplet radii, and is proportional to the concentration of the added component. The average vapour ejection velocity is also increasing with the increase of additive concentration in the multicomponent fuel mixture for all the fuels.

- The number of sub-droplets generated by secondary atomization is proportional to the concentration of both water and biodiesel in the cases of WD emulsions and BD blends, while it is inversely proportional to the water and ethanol concentrations for the DW emulsions and ED blends respectively.

- Increasing the ethanol concentration in the blend resulted in a slight change in the sub-droplet ejection behaviour of the droplet. For the ED10 droplets, multiple sub-droplets are ejected per single incident. The number of these sub-droplets is shown to decrease and their sizes increase when the ethanol concentration is increased.

- Both of the WD and DW emulsions have experienced a significant increase in the sub-droplet ejection processes. This suggests higher nucleation rates compared to the BD and ED blends. This high nucleation rate is attributed to the large specific volume change of water in the emulsion droplet compared to components of the blends, in addition to the wide dispersion of water droplets in the emulsion mixture compared to the blends, this in turn, results in higher number of nucleation sites initiation within the emulsion mixture at the same time compared to the blends.

- The sub-droplet emission rate is shown to decrease in the DW emulsions with increasing the water concentration due to the effect of surfactant used for emulsion preparation.

- The secondary atomization portion of the droplet lifetime represents an infinitesimally small percentage of the overall droplet lifetime. However, this small percentage is important for enhancing fuel evaporation and increasing fuel-air mixing. Thus, increasing this portion of time is important as well.

- Generally, each of the four mixtures is following a certain secondary atomization trend that is different from the other mixtures. This trend is responsive to the increase of the additive in that mixture. The secondary atomization in the emulsion droplets almost lasts to the end of the droplet lifetime. This is because the emulsion droplets usually do not undergo complete evaporation; instead droplet microexplosion takes place fragmenting the droplet into smaller size sub-droplets. This phenomenon did not occur during the combustion of the biodiesel/diesel and ethanol/diesel blends, so that secondary atomization from the droplets of these mixtures does not last to the end of the droplet lifetime.

- Schlieren imaging is found to be effective in tracking the explosion wave formed due to the microexplosion of the emulsion droplets.

- Droplet microexplosion is shown to initiate locally in a single site on the droplet surface. And is a result of a catastrophic burst of a single bubble inside the droplet. This bubble pushes the droplet surface outside under the action of the high pressure of the bubble interior causing the droplet to completely disintegrate into smaller size sub-droplets.

- The droplet explosion diameter is found to be proportional to the concentration of water in the emulsions in the case of the WD emulsions and inversely proportional

in the case of DW emulsions. This is due to increasing bubble growth in the former and water/diesel separation in the latter.

- The effective diameter of the explosion wave resulting from the WD emulsion is higher than that of the DW emulsions. This suggests that higher internal pressure in the bubbles is produced in the case of the WD emulsions compared to the DW emulsions. Additionally, increasing the water concentration in the emulsions is shown to decrease the effective diameter in the case of WD emulsions, and decreases it in the case of DW emulsions.

8.1.3 Liquid-Phase Dynamics of the Multicomponent Fuel Droplet

- The SiC fibre has no – or negligibly small – effect on the droplet when its size is relatively large. However, the effect of the fibre becomes more obvious when the droplet size is relatively small and is comparable to the fibre size. This effect on the liquid-phase takes place in the form of heterogeneous nucleation and bubble generation on the interface between the fibre and the droplet liquid.

- The nucleation and bubble generation within the single-component fuel droplets is mostly infrequent, and that the scarce incidents are either because of dissolved gases or low boiling components as in the diesel.

- The biodiesel/diesel blend droplets are characterized by the least nucleation and bubble generation incidents among all the mixtures. Whereas, the ethanol/diesel blends, water-in-diesel-emulsions, and diesel-in-water emulsions are all characterized by high nucleation and bubble generation incidents. These chaotic behaviours are reflected on the shape of the burning droplet. The droplets endure high shape deformations subsequent to the puffing incident.

- Subsequent to puffing, some of the liquid is ejected outside the droplet accompanied by the detachment of different size ligaments in the form of sub-droplets.

- The nucleation rates of all the investigated mixtures are inversely proportional to the concentration of the additive in that mixture. However, the degree of this proportionality is variable among those mixtures. The nucleation rate in the WD emulsions is the highest among all mixtures, while that of the BD blends is the

least, this could be a reflection to the miscibility of these liquids to diesel, where biodiesel is completely miscible and water is completely immiscible.

- The nuclei could initiate at any location inside the droplet, whether this location is the droplet centre or any of the peripheries.

- The bubble growth rate of ethanol/diesel blends is proportional to the increase of ethanol concentration in the blend, while, those growth rates of both biodiesel/diesel blends and water-in-diesel emulsions are inversely proportional to the increase in both biodiesel and water concentrations in the mixture. The bubble growth rate of the diesel-in-water emulsions on the other hand is found to be unaffected by the increase of water concentration in the emulsion.

- Some of the bubbles are shown to merge into single large bubble. These merging incidents are playing crucial rules in the dynamics of the droplet surface since these processes unite multiple small bubbles in one large bubble; the explosion of this large bubble is expected to be more effective than the initial smaller ones.

- The effect of bubble burst on the sub-droplet ejection from the surface of the burning fuel droplet is revealed. Prior to burst, the bubble is adjacent to the droplet surface. Hence, it is forcing the frontal thin liquid layer of the liquid until it is in contact with the gaseous environment. So, the pressure difference across the bubble causes its rapture releasing all the content vapour outside. The release of this vapour will create a low pressure spot on the droplet surface causing the surrounding liquid on the droplet to flow towards this spot. This inward motion of the liquid edges results in a reflective outward motion of part of the liquid due to the impact of the liquid edges in the low pressure spot.

- During the magnified monitoring of the droplet liquid-phase throughout the combustion of the multicomponent fuel droplets, some of the droplets belonging to the ethanol/diesel blends, water-in-diesel and diesel-in-water emulsions have experienced a kind of component separation. This is followed by accumulation of one of these components in the form of a spherical object that is moving in the core of the droplet. This type of separation and accumulation has not been noticed to occur during the combustion of biodiesel/diesel blends, which may be attributed to the complete miscibility of biodiesel in diesel.

8.1.4 Two-Neighbouring Droplets Interaction

- The critical normalized spacing distance below which the two adjacent droplets will have a single flame surrounding them is found to be about 3 in the case of the biodiesel/diesel blends and slightly higher for each of the ethanol/diesel blends, water-in-diesel emulsions, and diesel-in-water emulsions.

- The same trends of the burning rate constants evaluated for the isolated droplet combustion are obtained for the interactive two-droplet combustion. However, the ratio of the droplet burning rate constant of the interactive droplet combustion to that of the isolated droplet combustion is higher than unity. This implies that the droplet burning rate constant for all the fuels under investigation is higher than that of the isolated droplet combustion for these fuels. Therefore, the interactive droplet combustion has an effect on the predicted droplet burning rate compared to that of the isolated droplet combustion. This is attributed to the increased heat transfer rate to the droplet by the presence of the neighbouring droplet with its surrounding flame.

- The nucleation rate of all the fuel mixtures is inversely proportional to the concentration of the substance – biodiesel, ethanol, or water – added to diesel. This is the same trend shown for the nucleation rate inside the isolated fuel droplets of these mixtures. Additionally, the emulsion droplets both water-in-diesel and diesel-in-water have had the highest nucleation rates, followed by the ethanol/diesel blends, and the lowest are the biodiesel/diesel blends. This is attributed to the miscibility of the added substances on diesel.

- The nucleation rate within the interacting fuel droplets is higher than that within the corresponding isolated fuel droplets. This is imputed to the higher heat transfer rates to the droplet from the neighbouring droplet and its surrounding flame.

- Except the diesel-in-water emulsion, the bubble growth rate is inversely proportional to the increase in additive concentration. Additionally, the ethanol/diesel blends and water-in-diesel emulsions have the highest growth rates, while the lowest growth rates are shown in the case of the biodiesel/diesel blends which are preceded by the diesel-in-water emulsions.

8.2 Future Work

During the course of this research, there appear some aspects that can be further developed to enhance this work; the following suggestions could serve as further topics of research within the same field of this thesis.

8.2.1 Multi-Component Fuels:

  i. Producing and testing micro- and nano-emulsions (both water-in-diesel and diesel-in-water).
 ii. Trying higher diesel, biodiesel, and ethanol blends.
iii. Trying tri-component diesel mixtures.
 iv. Studying the chemical side of the problem by performing colour image processing.
  v. Studying the effect of nano-particles on the droplet dynamics.
 vi. Studying the effect of blending diesel by Ferro fluids on the droplet dynamics.
vii. Testing the effect of diluting the environment by CO, CO_2, and N_2 respectively.
viii. Investigating the effect of boiling point difference between diesel and its different blending additives on the droplet dynamics.
 ix. Blending diesel by another fuel with a boiling point equal or at least very close to that of water, and then comparing the results. And then emulsifying diesel by another liquid that is immiscible with diesel, and comparing the results. This is for investigating whether the chaos behaviour of water/diesel fuels is because of chemistry or boiling point difference.

8.2.2 Developing the Experimental Techniques:

  i. Using simultaneous high speed imaging for studying different levels of the droplet combustion at the same time. This may be performed using two cameras, one for the flame characteristics and the other for droplet liquid-phase dynamics. This will insure relevant and confirmed matching between the liquid phase dynamics and the flame dynamics.
 ii. Performing three dimensional analyses for the sub-droplets generated by secondary atomization. This can be carried out using magnified stereo imaging for visualizing of the sub-droplet. Alternatively, magnified stereo shadowgraphy can be utilized for the same purposes.

iii. Trying other non-intrusive methods for suspending the droplet, such as ultrasonic suspension or electromagnetic fields.

8.2.3 Droplet Dynamics:

i. Studying the effect of environmental conditions (pressure and/or temperature) on the droplet dynamics if possible.

ii. Studying the effect of forced convection on droplet dynamics.

iii. Performing three dimensional analysis for the sub-droplets generated by secondary atomization.

iv. Trying more than two-adjacent droplets for studying droplet interactions. However, increasing the number of adjacent droplets will affect the image magnification rate.

v. Focusing on droplet dynamics during ignition, but with more precise ignition technique.

Appendices

Appendix (A): Fuels with Types and Abbreviations

Substance	Type	Ratio		Abbreviation
Diesel	Neat	***		D
Biodiesel		***		B
Ethanol		***		E
Water		***		W
Water-in-Diesel	Emulsion	W/D	10/90	WD10
			20/80	WD20
			30/70	WD30
Diesel-in-Water	Emulsion	D/W	90/10	DW10
			80/20	DW20
			70/30	DW30
Biodiesel-Diesel	Blend	B/D	10/90	BD10
			20/80	BD20
			30/70	BD30
Ethanol-Diesel	Blend	E/D	10/90	ED10
			20/80	ED20
			30/70	ED30

Appendix (B): Neat Fuel Properties

Fuel Property	Unit	Diesel	Biodiesel	Ethanol
Kinematic Viscosity @ 40ºC	mm^2/s	3.05[a]	4.363[a]	1.08
Density @ 15.5ºC	kg/m^3	830[a]	877.8[a]	785
Specific Gravity @ 15.5ºC	---	0.83[a]	0.88[a]	0.79
Flash Point	ºC	79[a]	122[a]	16.6
Cloud Point	ºC	3[a]	5[a]	
Boiling Point	ºC	181[b]	302[b]	78
Pour Point	ºC	-35 to -15[b]	-15 to 10[b]	
Surface Tension @ 25ºC	mN/m	28.2[b]	30.7-31.1[b]	22.1
Higher Heating Value	MJ/kg	47.8[b]	41.2[b]	29.7
Lower Heating Value	MJ/kg	43.2[b]	37.1[b]	26.8
Latent Heat of Vaporization	kJ/kg	254[b]	254[b]	873
(a) From the supplier.		(b) From literature.		

Appendix (C): Droplet Diameter Evaluation Method Selection

As it is emphasised in section (3.4.4), different methods are used of calculating droplet diameter from the corresponding images of droplet during combustion. The more frequently used methods are based on evaluating the diameter from:

a) The square root of the droplet projected area as shown in equation (C-1). This method will be entitled here as the projected area method.

$$D = \sqrt{\frac{4}{\pi}(Projected\ Area)} \qquad \text{.........} \qquad \textbf{(C-1)}$$

b) The square root of the product of major and minor diameters of the ellipsoid representing the droplet as shown in equation (C-2). This method will be named as the elliptical area method.

$$D = \sqrt{D_{maj} * D_{min}} \qquad \text{.........} \qquad \textbf{(C-2)}$$

c) The cubic root of the product of minor diameter squared by the major diameter of the ellipsoid representing the droplet as shown in equation (C-3). This method will be named as the elliptical volume method.

$$D = \sqrt[3]{D_{maj} * (D_{min})^2} \qquad \text{.........} \qquad \textbf{(C-3)}$$

To select the most suitable technique for the present work, these three methods have been tested using images of 10 circular shapes of diameters ranging from 0.5 to 5 cm marching 0.5 cm each. The size of each of the shapes has been evaluated using all of these methods by the means of Matlab. The estimated error for all the methods is shown in Figure (C-1). The maximum error of all the methods is below 1%, especially the projected area and elliptical area methods. Thus, the three of them are found to be highly precise in evaluating equivalent droplet diameter from regular shapes.

Nevertheless, in droplet combustion of the multicomponent fuels, sometimes the droplet suffer from certain irregularities during its lifetime due to the physical processes taking place within the droplet. Hence, the droplet is not fully circular or regularly elliptical. Therefore, evaluating the major and minor diameters does not give the exact area

of the projected shape. Accordingly, the projected area method offers the best precision among the three methods. Therefore, it has been implemented for droplet size estimation from droplet images in the present work.
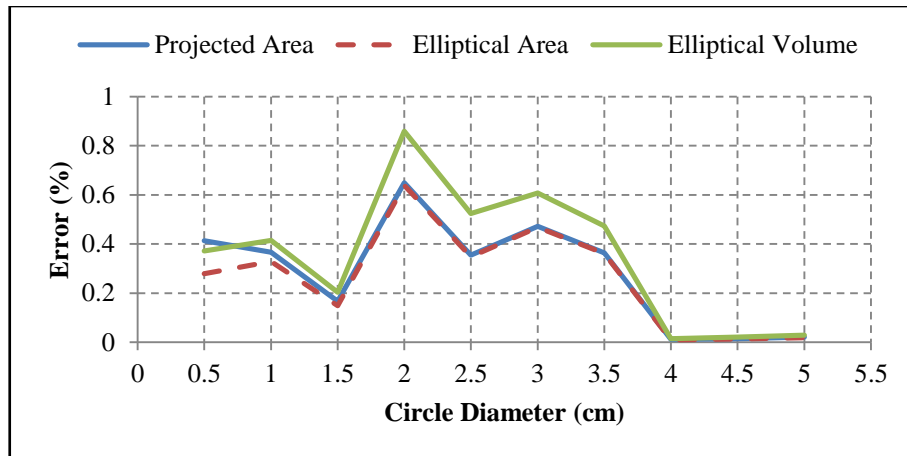
Figure C-1: The estimated error percentage resulting from different methods of droplet equivalent diameter calculation.

Appendix (D): Burning Rate Comparison

Table D-1: Burning rate constants of diesel, biodiesel, and ethanol published in literature.

Fuel	Authors	Test Condition	Burning Rate (mm^2/s)	Present Work
Diesel	Xu et al., 2016 [130]	M.G. (SiC Mesh)	0.46	**0.63±0.04**
	Pan and Chiu 2013 [128]	M.G. (fibre mesh)	0.57	
	Pan et al., 2009 [66]	M.G. (SiC Mesh)	0.6	
	Wang et al., 2013 [129]	F. F.	0.68	
	Ooi et al., 2016 [149]	N.G. (thermocouple)	0.68	
	Pan et al., 2009 [66]	N.G. (SiC Mesh)	0.75	
	Ghamari and Ratner, 2016 [150]	N.G. (SiC Mesh)	0.75	
	Bartle et al., 2011 [291]	N.G. (ceramic rod)	0.79	
	Botero et al., 2012 [122]	F. F.	0.8	
Biodiesel	Xu et al., 2016 [130]	M.G. (SiC Mesh)	0.54	**0.57±0.09**
	Pan et al., 2009 [66]	M.G. (SiC Mesh)	0.65	
	Pan and Chiu 2013 [128]	M.G. (fibre mesh)	0.65	
	Botero et al., 2012 [122]	F. F.	0.7	
	Pan et al., 2009 [66]	N.G. (SiC Mesh)	0.78	
	Bartle et al., 2011 [291]	N.G. (ceramic rod)	1	
Ethanol	Hara and Kumagai, 1990 [70]	M.G. (SiC Mesh)	0.55	**0.53±0.06**
	Ueda et al., 2002 [201]	M.G. (quartz fibre)	0.6	
	Nakaya et al., 2013 [290]	M.G. (quartz fibre)	0.62	
	Okajima and Kumagai, 1975 [69]	M.G. (SiC fibre)	0.65	
	Bartle et al., 2011 [291]	N.G. (ceramic rod)	0.8	
	Imamura et al., 2005 [306]	N.G. (quartz fibre)	0.9	
F.F: Free Fall		**M.G: Microgravity**		**N.G: Normal gravity**

Appendix (E): Flow Charts of the Matlab Codes

E-1: Droplet Size Calculations

The sequence followed for evaluating the droplet size from each image is shown below. From which the droplet real diameter is evaluated and stored. This sequence is repeated for every droplet image.
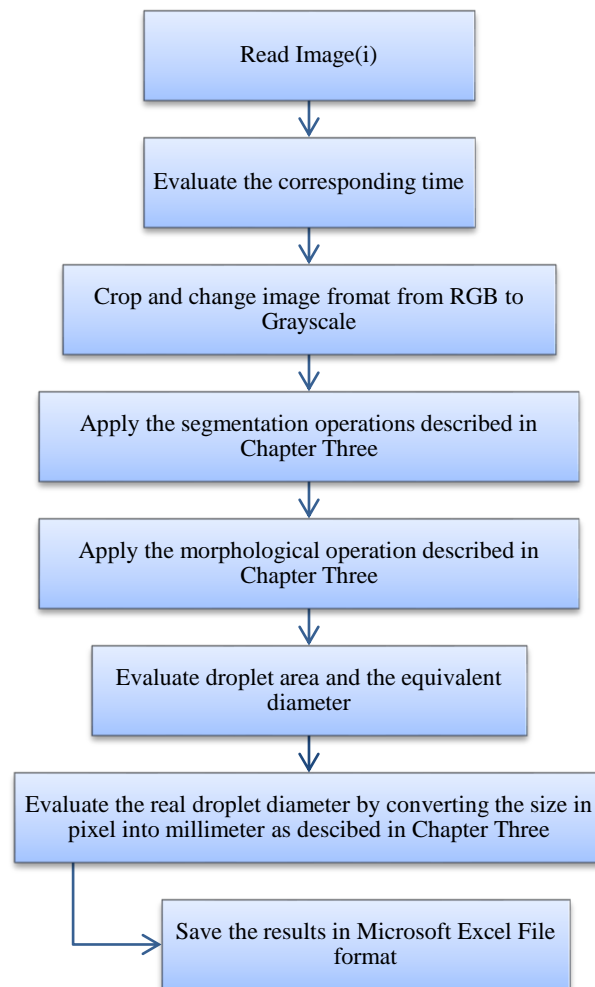
E-2: Flame Size Calculations

The flame size analyses are divided into two parts, the first part is dedicated to evaluate flame dimensions including the height and width, while the second part is set for evaluating the instantaneous size evolution of the droplet corresponding to each image of the flame. The flow chart combining these two parts is shown below. By which the flame dimensions and the corresponding droplet diameter are evaluated and stored. These calculation steps are repeated for every flame image.

```
                           Read Image(i)
                                |
                                v
                    Evaluate the corresponding
                              time
                   /                           \
                  v                             v
    Read the background image          Crop the image for droplet only
                  |                             |
                  v                             v
 Subtract the background from image(i)    Apply the same procedure described in
                  |                        section (E-1) for droplet size calculation
                  v
Apply the segmentation operations described in Chapter Three
                  |
                  v
   Evaluate flame height and with in pixel
                  |
                  v
Normalize flame height and width by initial droplet diameter
                  |
                  v
Evaluate flame stand-off ratio according to equation (2.6)
                  |
                  v
       Save the results in Microsoft Excel File format
```

E-3: Sub-Droplet Counting

The number of sub-droplets emitted by the droplet through secondary atomization is evaluated according to the sequence shown below. This sequence is repeated for every droplet image.

```
┌─────────────────────┐
│   Read Image(i)     │
└─────────────────────┘
          │
          ▼
┌─────────────────────────────┐
│ Evaluate the corresponding time │
└─────────────────────────────┘
          │
          ▼
┌───────────────────────────────────┐
│ Change image fromat from RGB to Grayscale │
└───────────────────────────────────┘
          │
          ▼
┌───────────────────────────────────────┐
│ Take the negative of the image and then threshold │
└───────────────────────────────────────┘
          │
          ▼
┌──────────────────────────────────────────┐
│ Evaluate the max number of objects N(i) within the image │
└──────────────────────────────────────────┘
          │
          ▼
┌──────────────────────────────────────────┐
│ Evaluate the number of sub-droplets emitted from: │
│                N(i) - N(i-1)             │
└──────────────────────────────────────────┘
          │
          └──────────►┌──────────────────────────────────────────┐
                      │ Save the results in Microsoft Excel File format │
                      └──────────────────────────────────────────┘
```
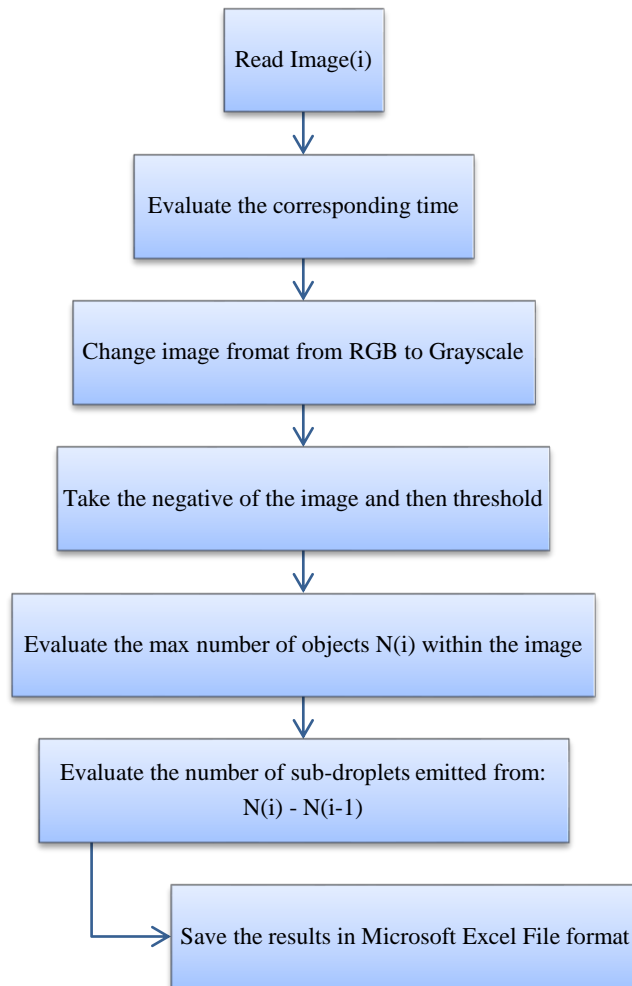
References

[1]   Griffiths, J.F., Barnard, J.A. "*Flame and Combustion.*" 3rd Editio. Springer Science+Business Media Dordrecht; 1995.

[2]   Keating, E.L. "*Applied Combustion.*" 2nd Editio. CRC Press/Taylor and Francis Group; 2007.

[3]   Jarosinski, J., Veyssiere, B. "*Combustion Phenomena, Selected Mechanisms of Flame Formation, Propagation, and Extinction.*" CRC Press/Taylor and Francis Group; 2009.

[4]   Law, C.K. "*Recent Advances in Droplet Vaporization and Combustion.*" Progress in Energy and Combustion Science 1982;8:171–201.

[5]   Sirignano, W.A. "*Advances in Droplet Array Combustion Theory and Modeling.*" Progress in Energy and Combustion Science 2014;42:54–86.

[6]   Wang, Q. Advanced Optical and 3D Reconstruction Diagnostics for Combustion and Fluids Research. The University of Sheffield, 2012.

[7]   El-Mahallawy, F., Habik, S.E. "*Fundamentals and Technology of Combustion.*" Elsevier Science Ltd; 2002.

[8]   Ragland, K. W., Bryden, K.M. "*Combustion Engineering.*" 2nd Editio. CRC Press/Taylor and Francis Group; 2011.

[9]   Chigier, N.A. "*Energy, Combustion, And Environment.*" McGraw-Hill; 1981.

[10] Law, C.K. "*Combustion Physics.*" Cambridge University Press; 2006.

[11] Drysdale, D. "*An Introduction to Fire Dynamics.*" 3rd Editio. John Wiley and Sons Ltd.; 2011.

[12] Kanury, M.A. "*Introduction to Combustion Phenomena.*" Gordon and Breach Publishers; 1975.

[13] Williams, A. "*Combustion of Liquid Fuel Sprays.*" Butterworth and Co Publishers; 1990.

[14] Williams, D. A., Jone, G. "*Liquid Fuels.*" New York: Pergamon Press; 1963.

[15] Warnatz, J., Maas, U., Dibble, R.W. "*Combustion: Physical and Chemical Fundamentals, Modeling and Simulation, Experiments, Pollutant Formation.*" 4th Editio. Springer; 2006.

[16] Baumgarten, C. "*Mixture Formation in Internal Combustion Engines.*" Springer; 2006.

[17] Lefebvre, A.H. "*Atomization and Sprays.*" Hemisphere Publishing Corporation;

1989.

[18] Lefebvre, A. H., Ballal, D.R. *"Gas Turbine Combustion: Alternative Fuels and Emissions."* 3rd Editio. CRC Press/Taylor and Francis Group; 2010.

[19] Beer, J. M., Chigier, N.A. *"Combustion Aerodynamics."* London: Applied Science Publishers; 1972.

[20] Iyer, V. A., Abraham, J., Magi, V. *"Exploring Injected Droplet Size Effects on Steady Liquid Penetration in a Diesel Spray with a Two-Fluid Model."* International Journal of Heat and Mass Transfer 2002;45:519–31.

[21] Komada, K., Sakaguchi, D., Tajima, H., Ueki, H., Ishida, M. *"Relation between Tip Penetration and Droplet Size of Diesel Spray."* SAE Technical Paper 2013;2.

[22] Polymeropoulos, C. E., Das, S. *"The Effect of Droplet Size on the Burning Velocity of Kerosene-Air Sprays."* Combustion and Flame 1975;25:247–57.

[23] Sarv, H., Nizami, A. A., Cernansky, N.P. Droplet Size Effects on NOx Formation in a One-Dimensional Monodisperse Spray Combustion System. 1982 Joint Power Generation Conference: GT Papers, The American Society of Mechanical Engineers (ASME); 1982.

[24] Onuma, Y., Ogasawara, M. *"Studies on the Structure of a Spray Combustion Flame."* Symposium (International) on Combustion / The Combustion Institute 1975;15:453–65.

[25] Sutton, G.P. *"Rocket Propulsion Elements."* John Wiley and Sons Ltd.; 1976.

[26] Ambekar, A., Chowdhury, A., Challa, S., Radhakrishna, D. *"Droplet Combustion Studies of Hydrocarbon-Monopropellant Blends."* Fuel 2014;115:697–705.

[27] Yu, Y., Li, M., Zhou, Y., Lu, X., Pan, Y. *"Study on Electrical Ignition and Micro-Explosion Properties of HAN-Based Monopropellant Droplet."* Frontiers of Energy and Power Engineering in China 2010;4:430–5.

[28] Dakka, S. M., Shaw, B.D. *"Influences of Pressure on Reduced-Gravity Combustion of HAN-Methanol-Water Droplets in Air."* Combustion and Flame 2006;146:484–92.

[29] Tarifa, C. S., Del Notario, P. P., Moreno, F.G. *"Combustion of Liquid Monopropellants and Bipropellants in Droplets."* Symposium (International) on Combustion / The Combustion Institute 1961;8:1035–56.

[30] Fendell, F. *"Near-Equilibrium Decompositional Burning of Monopropellant Droplets in a Stagnant Atmosphere."* International Journal of Heat and Mass Transfer 1969;12:223–31.

[31] Faeth, G.M. "*Monopropellant Droplet Burning at Low Reynolds Numbers.*" Combustion and Flame 1967;11:167–174.

[32] Faeth, G.M. "*Flame Zone Development of Monopropellant Droplets.*" Combustion and Flame 1968;2007:4–4.

[33] Allison, C. B., Faeth, G.M. "*Decomposition and Hybrid Combustion of Hydrazine, MMH and UDMH as Droplets in a Combustion Gas Environment.*" Combustion and Flame 1972;19:213–26.

[34] Godsave, G.A.E. "*Combustion of Droplets in a Fuel Spray.*" Nature 1949;164:708.

[35] Godsave, G.A.E. "*Combustion of Fuel Droplets.*" Nature 1950;166:1111.

[36] Kumagai, S., Isoda, H. "*Combustion of Fuel Droplets.*" Nature 1950;166:1111.

[37] Godsave, G.A.E. "*Studies of the Combustion of Drops in a Fuel Spray-The Burning of Single Drops of Fuel.*" Symposium (International) on Combustion/The Combustion Institute 1953;4:818–30.

[38] Spalding, D.B. "*The Combustion of Liquid Fuels.*" Symposium (International) on Combustion/The Combustion Institute 1953;4:847–64.

[39] Choi, M. Y., Dryer, F.L. Microgravity Droplet Combustion. In: Ross HD, editor. Microgravity Combustion: Fire in Free Fall, Academic Press; 2001, p. 183–297.

[40] Law, C.K. "*Unsteady Droplet Combustion with Droplet Heating.*" Combustion and Flame 1976;26:17–22.

[41] Law, C. K., Sirignano, W.A. "*Unsteady Droplet Combustion with Droplet Heating-II: Conduction Limit.*" Combustion and Flame 1977;28:175–86.

[42] Prakash, S., Sirignano, W.A. "*Liquid Fuel Droplet Heating with Internal Circulation.*" International Journal of Heat and Mass Transfer 1978;21:885–95.

[43] Shaygan, N., Prakash, S. "*Droplet Ignition and Combustion Including Liquid-Phase Heating.*" Combustion and Flame 1995;102:1–10.

[44] Sazhin, S. "*Modelling of Heating, Evaporation and Ignition of Fuel Droplets: Combined Analytical, Asymptotic and Numerical Analysis.*" Journal of Physics: Conference Series 2005;22:174–93.

[45] Sazhin, S. S., Abdelghaffar, W. A., Sazhina, E. M., Heikal, M.R. "*Models for Droplet Transient Heating: Effects on Droplet Evaporation, Ignition, and Break-up.*" International Journal of Thermal Sciences 2005;44:610–22.

[46] Aggarwal, S.K. "*Single Droplet Ignition: Theoretical Analyses and Experimental Findings.*" Progress in Energy and Combustion Science 2014;45:79–107.

[47] Moriue, O., Eigenbrod, C., Rath, H. J., Sato, J., Okai, K., Tsue, M., Kono, M.

"*Effects of Dilution by Aromatic Hydrocarbons on Staged Ignition Behavior of n-Decane Droplets.*" Proceedings of the Combustion Institute 2000;28:969–75.

[48] Moriue, O., Eigenbrod, C., Rath, H., Tsue, M., Kono, M., Sato, J. "*Spontaneous Ignition of n-Alkane Droplets with Various Volatility.*" Transactions of the Japan Society for Aeronautical and Space Sciences 2004;47:189–94.

[49] Marchese, A. J., Vaughn, T. L., Kroenlein, K., Dryer, F.L. "*Ignition Delay of Fatty Acid Methyl Ester Fuel Droplets: Microgravity Experiments and Detailed Numerical Modeling.*" Proceedings of the Combustion Institute 2011;33:2021–30.

[50] Nishiwaki, N. "*Kinetics of Liquid Combustion Processes: Evaporation and Ignition Lag of Fuel Droplets.*" Symposium (International) on Combustion/The Combustion Institute 1955;5:148–58.

[51] Saitoh, T., Ishiguro, S., Niioka, T. "*An Experimental Study of Droplet Ignition Characteristics Near the Ignitable Limit.*" Combustion and Flame 1982;48:27–32.

[52] Nakanishi, R., Kobayashi, H., Kato, S., Niioka, T. "*Ignition Experiment of a Fuel Droplet in High-Pressure High-Temperature Ambient.*" Symposium (International) on Combustion/The Combustion Institute 1994;25:447–53.

[53] Huang, L. W., Chen, C.H. "*Droplet Ignition in a High-Temperature Convective Environment.*" Combustion and Flame 1997;109:145–62.

[54] Kassoy, D. R., Williams, F.A. "*Variable Property Effects on Liquid Droplet Combustion.*" AIAA Journal 1968;6:1961–5.

[55] Puri, I. K., Libby, P.A. "*The Influence of Transport Properties on Droplet Burning.*" Combustion Science and Technology 1991;76:67–80.

[56] LAW, C. K., LAW, H.K. "*Quasi-Steady Diffusion Flame Theory with Variable Specific Heats and Transport Coefficients.*" Combustion Science and Technology 1976;12:207–16.

[57] Law, C. K., Law, H.K. "*Theory of Quasi-Steady One-Dimensional Diffusional Combustion with Variable Properties Including Distinct Binary Diffusion Coefficients.*" Combustion and Flame 1977;29:269–75.

[58] Chung, S. H., Law, C.K. "*Importance of Dissociation Equilibrium and Variable Transport Properties on Estimation of Flame Temperature and Droplet Burning Rate.*" Combustion and Flame 1984;55:225–35.

[59] Jackson, G. S., Avedisian, C. T., Yang, J.C. "*Observations of Soot during Droplet Combustion at Low Gravity: Heptane and Heptane/Monochloroalkane Mixtures.*" International Journal of Heat and Mass Transfer 1992;35:2017–33.

[60] Choi, M. Y., Lee, K.O. "*Investigation of Sooting in Microgravity Droplet Combustion.*" Symposium (International) on Combustion/The Combustion Institute 1996;26:1243–9.

[61] Manzello, S. L., Yozgatligil, A., Choi, M.Y. "*An Experimental Investigation of Sootshell Formation in Microgravity Droplet Combustion.*" International Journal of Heat and Mass Transfer 2004;47:5381–5.

[62] Urban, B. D., Kroenlein, K., Kazakov, A., Dryer, F. L., Yozgatligil, A., Choi, M. Y., Manzello, S. L., Lee, K. O., Dobashi, R. "*Sooting Behavior of Ethanol Droplet Combustion at Elevated Pressures under Microgravity Conditions.*" Microgravity Science and Technology 2004;15:12–8.

[63] Xu, G., Ikegami, M., Honma, S., Ikeda, K., Dietrich, D. L., Struk, P.M. "*Sooting Characteristics of Isolated Droplet Burning in Heated Ambients under Microgravity.*" International Journal of Heat and Mass Transfer 2004;47:5807–21.

[64] Liu, Y. C., Avedisian, C.T. "*A Comparison of the Spherical Flame Characteristics of Sub-Millimeter Droplets of Binary Mixtures of n-Heptane/Iso-Octane and n-Heptane/Toluene with a Commercial Unleaded Gasoline.*" Combustion and Flame 2012;159:770–83.

[65] Kumagai, S., Isoda, H. "*Combustion of Fuel Droplets in a Falling Chamber.*" Symposium (International) on Combustion/The Combustion Institute 1957;6:726–31.

[66] Pan, K. L., Li, J. W., Chen, C. P., Wang, C.H. "*On Droplet Combustion of Biodiesel Fuel Mixed with Diesel/Alkanes in Microgravity Condition.*" Combustion and Flame 2009;156:1926–36.

[67] Isoda, H., Kumagai, S. "*New Aspects of Droplet Combustion.*" Symposium (International) on Combustion / The Combustion Institute 1958;7:523–31.

[68] Kumagai, S., Sakai, T., Okajima, S. "*Combustion of Free Fuel Droplets in a Freely Falling Chamber.*" Symposium (International) on Combustion/The Combustion Institute 1971;13:779–85.

[69] Okajima, S., Kumagai, S. "*Further Investigations of Combustion of Free Droplets in a Freely Falling Chamber Including Moving Droplets.*" Symposium (International) on Combustion/The Combustion Institute 1975;15:401–7.

[70] Hara, H., Kumagai, S. "*Experimental Investigation of Free Droplet Combustion under Microgravity.*" Symposium (International) on Combustion/The Combustion Institute 1990;23:1605–10.

[71] Okajima, S., Kumagai, S. "*Experimental Studies on Combustion of Fuel Droplets in Flowing Air under Zero- and High-Gravity Conditions.*" Symposium (International) on Combustion/The Combustion Institute 1982;19:1021–7.

[72] Hara, H., Kumagai, S. "*The Effect of Initial Diameter on Free Droplet Combustion with Spherical Flame.*" Symposium (International) on Combustion/The Combustion Institute 1994;25:423–30.

[73] Norberg, C. "*Human Spaceflight and Exploration.*" Springer Berlin Heidelberg; 2013.

[74] Marchese, A. J., Dryer, F. L., Colantonio, R. O., Nayagam, V. "*Microgravity Combustion of Methanol and Methanol/Water Droplets: Drop Tower Experiments and Model Predictions.*" Symposium (International) on Combustion/The Combustion Institute 1996;26:1209–17.

[75] Farouk, T. I., Liu, Y. C., Savas, A. J., Avedisian, C. T., Dryer, F.L. "*Sub-Millimeter Sized Methyl Butanoate Droplet Combustion: Microgravity Experiments and Detailed Numerical Modeling.*" Proceedings of the Combustion Institute 2013;34:1609–16.

[76] Dakka, S. M., Shaw, B.D. "*Influences of Pressure on Reduced-Gravity Combustion of 1-Propanol Droplets.*" Microgravity Science and Technology 2006;18:5–13.

[77] Shaw, B. D., Vang, C.L. "*Oxygen Lewis Number Effects on Reduced Gravity Combustion of Methanol and n-Heptane Droplets.*" Combustion Science and Technology 2016;188:1–20.

[78] Kadota, T., Satoh, K., Segawa, D., Sato, J., Marutani, Y. "*Autoignition and Combustion of a Fuel Droplet in Supercritical Gaseous Environments under Microgravity.*" Symposium (International) on Combustion/The Combustion Institute 1998;27:2595–601.

[79] Chauveau, C., Gökalp, I., Segawa, D., Kadota, T., Enomoto, H. "*Effects of Reduced Gravity on Methanol Droplet Combustion at High Pressures.*" Proceedings of the Combustion Institute 2000;28:1071–7.

[80] Segawa, D., Kadota, T., Nakainkyo, A., Hirota, S., Enomoto, H. "*Effects of Ambient Pressure on Autoignition of a Fuel Droplet in Supercritical and Microgravity Environment.*" Proceedings of the Combustion Institute 2000;28:1063–9.

[81] Segawa, D., Yoshida, M., Nakaya, S., Kadota, T. "*Autoignition and Early Flame Behavior of a Spherical Cluster of 49 Monodispersed Droplets.*" Proceedings of the Combustion Institute 2007;31:2149–56.

[82] Tanabe, M., Kono, M., Sato, J, Koenig, J., Eigenbord, C., Rath, H. "*Effects of Natural Convection on Two Stage Ignition of an n-Dodecane Droplet.*" Symposium (International) on Combustion/The Combustion Institute 1994;25:455–61.

[83] Hicks, M. C., Nayagam, V., Williams, F.A. "*Methanol Droplet Extinction in Carbon-Dioxide-Enriched Environments in Microgravity.*" Combustion and Flame 2010;157:1439–45.

[84] Dietrich, D. L., Nayagam, V., Hicks, M. C., Ferkul, P. V., Dryer, F. L., Farouk, T., Shaw, B. D., Suh, H. K., Choi, M. Y., Liu, Y. C., Avedisian, C. T., Williams, F.A. "*Droplet Combustion Experiments Aboard the International Space Station.*" Microgravity Science and Technology 2014;26:65–76.

[85] Nayagam, V., Dietrich, D. L., Hicks, M. C., Williams, F.A. "*Cool-Flame Extinction during n-Alkane Droplet Combustion in Microgravity.*" Combustion and Flame 2015;162:2140–7.

[86] Farouk, T. I., Hicks, M. C., Dryer, F.L. "*Multistage Oscillatory 'Cool Flame' Behavior for Isolated Alkane Droplet Combustion in Elevated Pressure Microgravity Condition.*" Proceedings of the Combustion Institute 2015;35:1701–8.

[87] Vang, C. L., Shaw, B.D. "*Estimates of Liquid Species Diffusivities in N-Propanol/Glycerol Mixture Droplets Burning in Reduced Gravity.*" Microgravity Science and Technology 2015;27:281–95.

[88] Dietrich, D. L., Haggard, J. B., Dryer, F. L., Nayagam, V., Shaw, B. D., Williams, F.A. "*Droplet Combustion Experiments in Spacelab.*" Symposium (International) on Combustion/The Combustion Institute 1996;26:1201–7.

[89] Nayagam, V., Haggard Jr., J. B., Colantonio, R. O., Marchese, A. J., Dryer, F. L., Zhang, B. L., Williams, F.A. "*Microgravity n-Heptane Droplet Combustion in Oxygen-Helium Mixtures at Atmospheric Pressure.*" AIAA Journal 1998;36:1369–78.

[90] Marchese, A. J., Dryer, F. L., Colantonio, R.O. "*Radiative Effects in Space-Based Methanol / Water Droplet Combustion Experiments.*" Symposium (International) on Combustion/The Combustion Institute 1998;27:2627–34.

[91] Manzello, S. L., Choi, M. U., Kazakov, A., Dryer, F. L., Dobashi, R., Hirano, T. "*The Burning of Large n-Heptane Droplets in Microgravity.*" Proceedings of the Combustion Institute 2000;28:1079–86.

[92] Shaw, B. D., Harrison, M.J. "*Influences of Support Fibers on Shapes of Heptane/Hexadecane Droplets in Reduced Gravity.*" Microgravity Science and

Technology 2002;13:30–40.

[93]   Javed, I., Baek, S. W., Waheed, K. "*Autoignition and Combustion Characteristics of Kerosene Droplets with Dilute Concentrations of Aluminum Nanoparticles at Elevated Temperatures.*" Combustion and Flame 2015;162:774–87.

[94]   Sabourin, S. W., Boteler, C. I., Hallett, W.L.H. "*Droplet Ignition of Approximately Continuous Liquid Mixtures of n-Paraffins and n-Alkyl Aromatics.*" Combustion and Flame 2016;163:326–36.

[95]   Choi, M. Y., Dryer, F. L., Haggard, J.B. "*Observations on a Slow Burning Regime for Hydrocarbon Droplets: n-Heptane/Air Results.*" Symposium (International) on Combustion/The Combustion Institute 1990;23:1597–604.

[96]   Xu, G., Ikegami, M., Honma, S., Ikeda, K., Ma, Xi., Nagaishi, H., Dietrich, D. L., Struk, P.M. "*Inverse Influence of Initial Diameter on Droplet Burning Rate in Cold and Hot Ambiences: A Thermal Action of Flame in Balance with Heat Loss.*" International Journal of Heat and Mass Transfer 2003;46:1155–69.

[97]   Xu, G., Ikegami, M., Honma, S., Ikeda, K., Dietrich, D. L., Struk, P.M. "*Interactive Influences of Convective Flow and Initial Droplet Diameter on Isolated Droplet Burning Rate.*" International Journal of Heat and Mass Transfer 2004;47:2029–35.

[98]   Mikami, M., Yagi, T., Kojima, N. "*Occurrence Probability of Microexplosion in Droplet Combustion of Miscible Binary Fuels.*" Symposium (International) on Combustion/The Combustion Institute 1998;27:1933–41.

[99]   Hoxie, A., Schoo, R., Braden, J. "*Microexplosive Combustion Behavior of Blended Soybean Oil and Butanol Droplets.*" Fuel 2014;120:22–9.

[100] Lee, K., Jensen, K. A., Choi, M.Y. "*Investigation of Sooting in Normal-Gravity Droplet Combustion using Light Extinction and Gravimetric Techniques.*" Symposium (International) on Combustion/The Combustion Institute 1996;26:2397–404.

[101] Marsh, N. D., Zhu, D., Wornat, M.J. "*Pyrolysis Product Absorption by Burning Benzene Droplets.*" Symposium (International) on Combustion/The Combustion Institute 1998;27:1897–905.

[102] Xu, G., Ikegami, M., Honma, S., Sasaki, M., Ikeda, K., Nagaishi, H., Takeshita, Y. "*Combustion Characteristics of Droplets Composed of Light Cycle Oil and Diesel Light Oil in a Hot-Air Chamber.*" Fuel 2003;82:319–30.

[103] Wardana, I.N.G. "*Combustion Characteristics of Jatropha Oil Droplet at Various Oil Temperatures.*" Fuel 2010;89:659–64.

[104] Mishra, D. P., Patyal, A., Padhwal, M. "*Effects of Gellant Concentration on the Burning and Flame Structure of Organic Gel Propellant Droplets.*" Fuel 2011;90:1805–10.

[105] Mishra, D. P., Patyal, A. "*Effects of Initial Droplet Diameter and Pressure on Burning of ATF Gel Propellant Droplets.*" Fuel 2012;95:226–33.

[106] Sato, J., Tsue, M., Niwa, M., Kono, M. "*Effects of Natural Convection on High-Pressure Droplet Combustion.*" Combustion and Flame 1990;82:142–50.

[107] Struk, P. M., Dietrich, D. L., Ikegami, M., Xu, G. "*Interacting Droplet Combustion under Conditions of Extinction.*" Proceedings of the Combustion Institute 2002;29:609–15.

[108] Goldsmith, M., Penner, S.S. "*On the Burning of Single Drops of Fuel in an Oxidizing Atmosphere.*" Journal of Jet Propulsion 1954;24:245–51.

[109] Polymeropoulos, C. E., Peskin, R.L. "*Ignition and Extinction of Liquid Fuel Drops—Numerical Computations.*" Combustion and Flame 1969;13:166–72.

[110] Law, C.K. "*Asymptotic Theory for Ignition and Extinction in Droplet Burning.*" Combustion and Flame 1975;24:89–98.

[111] Dash, S. K., Som, S.K. "*Ignition and Combustion of Liquid Fuel Droplet in a Convective Medium.*" Journal of Energy Resources Technology 1991;113:167–70.

[112] Chiu, H. H., Hu, L.H. "*Dynamics of Ignition Transience and Gasification Partition of a Droplet.*" Symposium (International) on Combustion / The Combustion Institute 1998;27:1889–96.

[113] Lacas, F., Calimez, X. "*Numerical Simulation of Simultaneous Breakup and Ignition of Droplets.*" Proceedings of the Combustion Institute 2000;28:943–51.

[114] Pindera, M. Z., Brzustowski, T.A. "*A Model for the Ignition and Extinction of Liquid Fuel Droplets.*" Combustion and Flame 1984;55:79–91.

[115] Pope, D. N., Gogos, G. "*Numerical Simulation of Fuel Droplet Extinction due to Forced Convection.*" Combustion and Flame 2005;142:89–106.

[116] Wang, C. H., Liu, X. Q., Law, C.K. "*Combustion and Microexplosion of Freely Falling Multicomponent Droplets.*" Combustion and Flame 1984;56:175–97.

[117] Siringnano, W.A. "*Fluid Dynamics and Transport of Droplets and Sprays.*" 2nd Editio. Cambridge University Press; 2010.

[118] Wood, B. J., Wise, H., Inami, S.H. "*Heterogeneous Combustion of Multicomponent Fuels.*" Combustion and Flame 1960;4:235–42.

[119] Law, C.K. "*Multicomponent Droplet Combustion with Rapid Internal Mixing.*"

Combustion and Flame 1976;26:219–33.

[120] Niioka, T., Sato, J. "*Combustion and Microexplosion Behavior of Miscible Fuel Droplets under High Pressure.*" Symposium (International) on Combustion/The Combustion Institute 1986;21:625–31.

[121] Takei, M., Tsukamoto, T., Niioka, T. "*Ignition of Blended-Fuel droplet in High-Temperature Atmosphere.*" Combustion and Flame 1993;93:149–56.

[122] Botero, M. L., Huang, Y., Zhu, D. L., Molina, A., Law, C.K. "*Synergistic Combustion of Droplets of Ethanol, Diesel and Biodiesel Mixtures.*" Fuel 2012;94:342–7.

[123] Lasheras, J. C., Fernandez-Pello, A. C., Dryer, F.L. "*Experimental Observations on the Disruptive Combustion of Free Droplets of Multicomponent Fuels.*" Combustion Science and Technology 1980;22:195–209.

[124] Lasheras, J. C., Fernandez-Pello, A. C., Dryer, F.L. "*On the Disruptive Burning of Free Droplets of Alcohol/n-Paraffin Solutions and Emulsions.*" Symposium (International) on Combustion/The Combustion Institute 1981;18:293–305.

[125] Yap, L., Kennedy, I. M., Dryer, F.L. "*Disruptive and Micro-Explosive Combustion of Free Droplets in Highly Convective Environments.*" Combustion Science and Technology 1984;41:291–313.

[126] Yang, J. C., Avedisian, C.T. "*The Combustion of Unsupported Heptane/Hexadecane Mixture Droplets at Low Gravity.*" Symposium (International) on Combustion/The Combustion Institute 1988;22:2037–44.

[127] Mikami, M., Kono, M., Sato, J., Dietrich, D.L. "*Interactive Effects in Two-Droplet Combustion of Miscible Binary Fuels at High Pressure.*" Symposium (International) on Combustion/The Combustion Institute 1998;27:2643–9.

[128] Pan, K. L., Chiu, M.C. "*Droplet Combustion of Blended Fuels with Alcohol and Biodiesel/Diesel in Microgravity Condition.*" Fuel 2013;113:757–65.

[129] Wang, C. H., Pan, K. L., Ueng, G. J., Kung, L. J., Yang, J.Y. "*Burning Behaviors of Collision-Merged Water/Diesel, Methanol/Diesel, and Water+Methanol/Diesel Droplets.*" Fuel 2013;106:204–11.

[130] Xu, Y., Keresztes, I., Condo, A. M., Phillips, D., Pepiot, P., Avedisian, C.T. "*Droplet Combustion Characteristics of Algae-Derived Renewable Diesel, Conventional #2 Diesel, and their Mixtures.*" Fuel 2016;167:295–305.

[131] Avulapati, M. M., Ganippa, L. C., Xia, J., Megaritis, A. "*Puffing and Micro-Explosion of Diesel-Biodiesel-Ethanol Blends.*" Fuel 2016;166:59–66.

[132] Han, K., Chen, H., Yang, B., Ma, X., Song, G., Li, Y. "*Experimental Investigation on Droplet Burning Characteristics of Diesel-Benzyl Azides Blend.*" Fuel 2017;190:32–40.

[133] Yang, J. C., Jackson, G. S., Avedisian, C.T. "*Combustion of Unsupported Methanol/Dodecanol Mixture Droplets at Law Gravity.*" Symposium (International) on Combustion/The Combustion Institute 1990;23:1619–25.

[134] Okai, K., Moriue, O., Araki, M., Tsue, M., Kono, M., Sato, J., Dietrich, D. L., Williams, F.A. "*Pressure Effects on Combustion of Methanol and Methanol/Dodecanol Single Droplets and Droplet Pairs in Microgravity.*" Combustion and Flame 2000;121:501–12.

[135] Avedisian, C. T., Callahan, B.J. "*Experimental Study of Nonane/Hexanol Mixture Droplet Combustion without Natural or Forced Convection.*" Proceedings of the Combustion Institute 2000;28:991–7.

[136] Dee, V., Shaw, B.D. "*Combustion of propanol-glycerol mixture droplets in reduced gravity.*" International Journal of Heat and Mass Transfer 2004;47:4857–67.

[137] Randolph, A. L., Law, C.K. "*Time-Resolved Gasification and Sooting Characteristics of Droplets of Alcohol/Oil Blends and Water/Oil Emulsions.*" Symposium (International) on Combustion/The Combustion Institute 1986;21:1125–31.

[138] Yamasaki, H., Tsue, M., Kadota, T. "*Evaporation and Combustion of Emulsified Fuel: Onset of Microexplosion.*" JSME International Journal Series B 1993;36:677–81.

[139] Tsue, M., Segawa, D., Kadota, T., Yamasaki, H. "*Observation of Sooting Behavior in an Emulsion Droplet Flame by Planar Laser Light Scattering in Microgravity.*" Symposium (International) on Combustion/The Combustion Institute 1996;26:1251–8.

[140] Kadota, T., Tanaka, H., Segawa, D., Nakaya, S., Yamasaki, H. "*Microexplosion of an Emulsion Droplet during Leidenfrost Burning.*" Proceedings of the Combustion Institute 2007;31:2125–31.

[141] Jeong, I. C., Lee, K.H. "*Auto-Ignition and Micro-Explosion Behaviors of Droplet Arrays of Water-in-Fuel Emulsion.*" International Journal of Automotive Technology 2008;9:735–40.

[142] Jeong, I., Lee, K. H., Kim, J. "*Characteristics of Auto-Ignition and Micro-Explosion Behavior of a Single Droplet of Water-in-Fuel.*" Journal of Mechanical Science and

Technology 2008;22:148–56.

[143] Califano, V., Calabria, R., Massoli, P. "*Experimental Evaluation of the Effect of Emulsion Stability on Micro-Explosion Phenomena for Water-in-Oil Emulsions.*" Fuel 2014;117:87–94.

[144] Tsue, M., Kadota, T., Segawa, D., Yamasaki, H. "*Statistical Analysis on Onset of Microexplosion for an Emulsion Droplet.*" Symposium (International) on Combustion/The Combustion Institute 1996;26:1629–35.

[145] Segawa, D., Yamasaki, H., Kadota, T., Tanaka, H., Enomoto, H., Tsue, M. "*Water-Coalescence in an Oil-in-Water Emulsion Droplet Burning under Microgravity.*" Proceedings of the Combustion Institute 2000;28:985–90.

[146] Ocampo-Barrera, R., Villasenor, R., Diego-Marin, A. "*An Experimental Study of the Effect of Water Content on Combustion of Heavy Fuel Oil/Water Emulsion Droplets.*" Combustion and Flame 2001;126:1845–55.

[147] Jackson, G. S., Avedisian, C.T. "*Combustion of Unsupported Water-in-n-Heptane Emulsion Droplets in a Convection-Free Environment.*" International Journal of Heat and Mass Transfer 1998;41:2503–15.

[148] Tanvir, S., Qiao, L. "*Droplet Burning Rate Enhancement of Ethanol with the Addition of Graphite Nanoparticles: Influence of Radiation Absorption.*" Combustion and Flame 2016;166:34–44.

[149] Ooi, J. B., Ismail, H. M., Swamy, V., Wang, X., Swain, A. K., Rajanren, J.R. "*Graphite Oxide Nanoparticle as a Diesel Fuel Additive for Cleaner Emissions and Lower Fuel Consumption.*" Energy and Fuels 2016;30:1341–53.

[150] Ghamari, M., Ratner, A. "*Combustion Characteristics of Diesel and Jet-A Droplets Blended with Polymeric Additive.*" Fuel 2016;178:63–70.

[151] Shinjo, J., Xia, J., Ganippa, L.C., Megaritis, A. "*Physics of Puffing and Microexplosion of Emulsion Fuel Droplets.*" Physics of Fluids 2014;26:103302.

[152] Watanabe, H., Harada, T., Matsushita, Y., Aoki, H., Miura, T. "*The Characteristics of Puffing of the Carbonated Emulsified Fuel.*" International Journal of Heat and Mass Transfer 2009;52:3676–84.

[153] Miglani, A., Basu, S., Kumar, R. "*Insight into Instabilities in Burning Droplets.*" Physics of Fluids 2014;26.

[154] Wang, Z.G. "*Internal Combustion Processes of Liquid Rocket Engines: Modeling and Numerical Simulations.*" John Wiley and Sons Ltd.; 2016.

[155] Lasheras, J. C., Yap, L. T., Dryer, F.L. "*Effect of the Ambient Pressure on the*

Explosive Burning of Emulsified and Multicomponent Fuel Droplets." Symposium (International) on Combustion / The Combustion Institute 1984;20:1761–72.

[156] Zhang, Y., Huang, R., Wang, Z., Xu, S., Huang, S., Ma, Y. "*Experimental Study on Puffing Characteristics of Biodiesel-Butanol Droplet.*" Fuel 2017;191:454–62.

[157] Watanabe, H., Matsushita, Y., Aoki, H., Miura, T. "*Numerical Simulation of Emulsified Fuel Spray Combustion with Puffing and Micro-Explosion.*" Combustion and Flame 2010;157:839–52. doi:10.1016/j.combustflame.2010.01.013.

[158] Shinjo, J., Xia, J., Ganippa, L. C., Megaritis, A. "*Puffing-Enhanced Fuel/Air Mixing of an Evaporating n-Decane/Ethanol Emulsion Droplet and a Droplet Group under convective heating.*" Journal of Fluid Mechanics 2016;793:444–76.

[159] Shinjo, J., Xia, J. "*Combustion Characteristics of a Single Decane/Ethanol Emulsion Droplet and a Droplet Group under Puffing Conditions.*" Proceedings of the Combustion Institute 2017;36:2513–21.

[160] Watanabe, H., Harada, T., Hoshino, K., Matsushita, Y., Aoki, H., Miura, T. "*An Experimental Investigation of the Characteristics of the Secondary Atomization and Spray Combustion for Emulsified Fuel.*" Journal of Chemical Engineering of Japan 2008;41:1110–8.

[161] Watanabe, H., Okazaki, K. "*Visualization Of Secondary Atomization in Emulsified-Fuel Spray Flow by Shadow Imaging.*" Proceedings of the Combustion Institute 2013;34:1651–8.

[162] Watanabe, H., Shoji, Y., Yamagaki, T., Hayashi, J., Akamatsu, F., Okazaki, K. "*Secondary Atomization Behavior and Spray Flame Characteristics of Carbonated W/O Emulsified Fuel.*" Fuel 2016;182:6–7.

[163] Watanabe, H., Suzuki, Y., Harada, T., Matsushita, Y., Aoki, H., Miura, T. "*An Experimental Investigation Of The Breakup Characteristics Of Secondary Atomization Of Emulsified Fuel Droplet.*" Energy 2010;35:806–13.

[164] Suzuki, Y., Harada, T., Watanabe, H., Shoji, M., Matsushita, Y., Aoki, H., Miura, T. "*Visualization of Aggregation Process of Dispersed Water Droplets and the Effect of Aggregation on Secondary Atomization of Emulsified Fuel Droplets.*" Proceedings of the Combustion Institute 2011;33:2063–70.

[165] Pulkrabek, W.W. "*Engineering Fundamentals of the Internal Combustion Engine.*" Prentice Hall; 1997.

[166] Vehkamäki, H. "*Classical Nucleation Theory in Multicomponent Systems.*" Springer Berlin Heidelberg; 2006.

[167] Caupin, F., Herbert, E. "*Cavitation in Water: A Review.*" Comptes Rendus Physique 2006;7:1000–17.

[168] Kadota, T., Yamasaki, H. "*Recent Advances in the Combustion of Water Fuel Emulsion.*" Progress in Energy and Combustion Science 2002;28:385–404.

[169] Avedisian, C.T. "*The Homogeneous Nucleation Limits of Liquids.*" Journal of Physical and Chemical Reference Data 1985;14:695–729.

[170] Chung, S. H., Kim, J.S. "*An Experiment on Vaporization and Microexplosion of Emulsion Fuel Droplets on a Hot Surface.*" Symposium (International) on Combustion / The Combustion Institute 1990;23:1431–5.

[171] Tsue, M., Yamasaki, H., Kadota, T., Segawa, D., Kono, M. "*Effect of Gravity on Onset of Microexplosion for an Oil-in-Water Emulsion Droplet.*" Symposium (International) on Combustion/The Combustion Institute 1998;27:2587–93.

[172] Wang, C. H., Fu, S. Y., Kung, L. J., Law, C.K. "*Combustion and Microexplosion of Collision-Merged Methanol/Alkane Droplets.*" Proceedings of the Combustion Institute 2005;30:1965–72.

[173] Sirignano, W.A. "*Fuel Droplet Vaporization and Spray Combustion Theory.*" Progress in Energy and Combustion Science 1983;9:291–322.

[174] Sangiovanni, J. J., Kesten, A.S. "*Effect of Droplet Interaction on Ignition in Monodispersed Droplet Streams.*" Symposium (International) on Combustion/The Combustion Institute 1977;16:577–92.

[175] Segawa, D., Yoshida, M., Nakaya, S., Kadoka, T. "*Effects of Spacing and Arrangement of Droplet on Combustion Characteristics of Monodispersed Suspended-Droplet Cluster Model under Microgravity.*" Microgravity Science and Technology 2005;17:23–30. doi:10.1007/BF02872084.

[176] Nomura, H., Iwasaki, H., Suganuma, Y., Mikami, M., Kikuchi, M. "*Microgravity Experiments of Flame Spreading Along a Fuel Droplet Array in Fel Vapor-Air Mixture.*" Proceedings of the Combustion Institute 2011;33:2013–20.

[177] Koshland, C. P., Bowman, C.T. "*Combustion of Monodisperse Droplet Clouds in a Reactive Environment.*" Symposium (International) on Combustion/The Combustion Institute 1984;20:1799–807.

[178] Okai, K., Tsue, M., Kono, M., Mikami, M., Sato, J., Dietrich, D. L., Williams, F.A. "*Strongly Interacting Combustion of Two Miscible Binary-Fuel Droplets at High Pressure in Microgravity.*" Symposium (International) on Combustion/The Combustion Institute 1998;27:2651–7.

[179] Okai, K., Moriue, O., Araki, M., Tsue, M., Kono, M., Sato, J., Dietrich, D. L., Williams, F.A. "*Combustion of Single Droplets and Droplet Pairs in a Vibrating Field under Microgravity.*" Proceedings of the Combustion Institute 2000;28:977–83.

[180] Nomura, H., Takahashi, H., Suganuma, Y., Kikuchi, M. "*Droplet Ignition Behavior in the Vicinity of the Leading Edge of a Flame Spreading along a Fuel Droplet Array in Fuel-Vapor/Air Mixture.*" Proceedings of the Combustion Institute 2013;34:1593–600.

[181] Kataoka, H., Yamashita, H., Tada, J., Oka, Y., Morinaga, Y., Itai, M., Segawa, D., Kadota, T. "*Autoignition Behavior of a Spherical Cluster Consisted of a Center Fine Droplet and Surrounding Twelve Fine Droplets.*" Proceedings of the Combustion Institute 2015;35:1629–37.

[182] Queiroz, M., Yao, S.C. "*Experimental Exploration of the Thermal Structure of an Array of Burning Droplet Streams.*" Combustion and Flame 1990;82:346–60.

[183] Mikami, M., Niwa, M., Kato, H., Sato, J., Kono, M. "*Clarification of the Flame Structure of Droplet Burning Based on Temperature Measurement in Microgravity.*" Symposium (International) on Combustion/The Combustion Institute 1994;25:439–46.

[184] Rosebrock, C. D., Shirinzadeh, S., Soeken, M., Riefler, N., Wriedt, T., Drechsler, R., Mädler, L. "*Time-Resolved Detection of Diffusion Limited Temperature Gradients Inside Single Isolated Burning Droplets using Rainbow Refractometry.*" Combustion and Flame 2016;168:255–69.

[185] Merzkirch, W. "*Flow Visualization.*" 2nd Editio. Academic Press; 1987.

[186] Settles, G.S.S. "*Schlieren and Shadowgraph Techniques: Visualizing Phenomena in Transport Media.*" Springer; 2001.

[187] Klein-Douwel, R. J. H., Frijters, P. J. M., Somers, L. M. T., de Boer, W. A., Baert, R.S.G. "*Macroscopic Diesel Fuel Spray Shadowgraphy using High Speed Digital Imaging in a High Pressure Cell.*" Fuel 2007;86:1994–2007.

[188] Klinner, J., Willert, C. "*Tomographic Shadowgraphy for Three-Dimensional Reconstruction of Instantaneous Spray Distributions.*" Experiments in Fluids 2012;53:531–43.

[189] Mauger, C., Méès, L., Michard, M., Lance, M. "*Velocity Measurements Based on Shadowgraph-Like Image Correlations in a Cavitating Micro-Channel Flow.*" International Journal of Multiphase Flow 2014;58:301–12.

[190] Xu, F., Patterson, J. C., Lei, C. "*Shadowgraph Observations of the Transition of the Thermal Boundary Layer in a Side-Heated Cavity.*" Experiments in Fluids 2005;38:770–9.

[191] Vinze, R., Chandel, S., Limaye, M. D., Prabhu, S. V. "*Heat Transfer Distribution and Shadowgraph Study for Impinging Underexpanded Jets.*" Applied Thermal Engineering 2017;115:41–52.

[192] Schöpf, W., Patterson, J. C., Brooker, A.M.H. "*Evaluation of the Shadowgraph Method for the Convective Flow in a Side-Heated Cavity.*" Experiments in Fluids 1996;21:331–40.

[193] Jenkins, D.R. "*Interpretation of Shadowgraph Patterns in Rayleigh-Bénard Convection.*" Journal of Fluid Mechanics 1988;190:451–69.

[194] Ishino, Y., Hasegawa, T., Yamaguchi, S., Ohiwa, N. "*Optical Analysis of Pulse Combustion using Shadowgraph and Planar CH-LIF Imaging Technique.*" Journal of Energy Resources Technology 2001;123:59–63.

[195] Ochoterena, R. "*High Speed Shadowgraph and Diffraction Based Imaging for Spray Characterisation and Combustion Studies.*" SAE Technical Paper 2009.

[196] Ogawa, H., Shibata, G., Noguchi, Y., Numata, M. "*Visualization Analysis of Diesel Combustion with Water and Diesel Fuel Emulsified Blend in a Constant Volume Chamber Vessel.*" SAE International 2014.

[197] Kobayasi, K. "*An Experimental Study on the Combustion of a Fuel Droplet.*" Symposium (International) on Combustion/The Combustion Institute 1955;5:141–8.

[198] Faeth, G. M., Dominicis, D. P., Tulpinsky, J. F., Olson, D.R. "*Supercritical Bipropellant Droplet Combustion.*" Symposium (International) on Combustion / The Combustion Institute 1969;12:9–18.

[199] Tanabe, M., Kuwahara, T., Satoh, K., Fujimori, T., Sato, J., Kono, M. "*Droplet Combustion in Standing Sound Waves.*" Proceedings of the Combustion Institute 2005;30:1957–1964.

[200] Lehmann, S., Lorenz, S., Rivard, E., Brüggemann, D. "*Experimental Analysis and Semicontinuous Simulation of Low-Temperature Droplet Evaporation of Multicomponent Fuels.*" Experiments in Fluids 2015;56:1871.

[201] Ueda, T., Imamura, O., Okai, K., Tsue, M., Kono, M., Sato, J. "*Combustion Behavior of Single Droplets for Sooting and Non-Sooting Fuels in Direct Current Electric Fields under Microgravity.*" Proceedings of the Combustion Institute 2002;29:2595–601.

[202] Bachalo, W.D. Methods for Compressible Flows. In: Smits, A. J., Lim TT, editor. Flow Visualization: Techniques and Examples. 2nd Editio, Imperial College Press; 2012, p. 227–65.

[203] Krier, H., Wronkiewicz, J.A. "*Combustion of Single Drops of Fuel.*" Combustion and Flame 1972;18:159–66.

[204] Ogami, Y., Sakurai, S., Hasegawa, S., Jangi, M., Nakamura, H., Yoshinaga, K., Kobayashi, H. "*Microgravity Experiments of Single Droplet Combustion in Oscillatory Flow at Elevated Pressure.*" Proceedings of the Combustion Institute 2009;32:2171–8.

[205] Reichenbach, R., Squires, D., and Penner, S.S. "*Flame Propagation in Liquid-Fuel Droplet Arrays.*" Symposium (International) on Combustion/The Combustion Institute 1961;8:1068–73.

[206] Miles, R.B. Planar Imaging of Gas Phase Flows. In: Smits, A. J., Lim TT, editor. Flow Visualization: Techniques and Examples. 2nd Editio, Imperial College Press; 2012, p. 107–42.

[207] Andersen, P. Laser Induced Fluorescence. Optical Measurements: Techniques and Applications. 2nd Editio, Springer Berlin Heidelberg; 2001, p. 199–230.

[208] Castanet, G., Lebouché, M., Lemoine, F. "*Heat and Mass Transfer of Combusting Monodisperse Droplets in a Linear Stream.*" International Journal of Heat and Mass Transfer 2005;48:3261–75.

[209] Pfeil, M. A., Groven, L. J., Lucht, R. P., Son, S.F. "*Effects of Ammonia Borane on the Combustion of an Ethanol Droplet at Atmospheric Pressure.*" Combustion and Flame 2013;160:2194–203.

[210] Beck, C. H., Koch, R., Bauer, H.J. "*Identification of Droplet Burning Modes in Lean, Partially Prevaporized Swirl-Stabilized Spray Flames.*" Proceedings of the Combustion Institute 2009;32:2195–203.

[211] Burkert, A., Paa, W., Reimert, M., Klinkov, K., Eigenbrod, C. "*Formaldehyde LIF Detection with Background Subtraction Around Single Igniting GTL Diesel Droplets.*" Fuel 2013;111:384–92.

[212] Castanet, G., Maqua, C., Orain, M., Grisch, F., Lemoine, F. "*Investigation of Heat and Mass Transfer between the Two Phases of an Evaporating Droplet Stream using Laser-Induced Fluorescence Techniques: Comparison with Modeling.*" International Journal of Heat and Mass Transfer 2007;50:3670–83.

[213] Maqua, C., Castanet, G., Lemoine, F. "*Bicomponent Droplets Evaporation:*

Temperature Measurements and Modelling." Fuel 2008;87:2932–42.

[214] Zhang, Y., Zhang, G., Xu, M., Wang, J. "*Droplet Temperature Measurement based on 2-Color Laser-Induced Exciplex Fluorescence.*" Experiments in Fluids 2013;54:1–10.

[215] Albrecht, H. E., Borys, M., Damaschke, N., Tropea, C. "*Laser Doppler and Phase Doppler Measurement Techniques.*" Springer; 2003.

[216] Eder, A., Durst, B., Jordan, M. Laser-Doppler Velocimetry - Principle and Application to Turbulence Measurements. In: Mayinger, F., Feldmann O, editor. Optical Measurements: Techniques and Applications. 2nd Editio, Springer Berlin Heidelberg; 2001, p. 117–38.

[217] Ofner, B. Phase Doppler Anemometry (PDA). In: Mayinger, F., Feldmann O, editor. Optical Measurements: Techniques and Applications. 2nd Editio, Springer Berlin Heidelberg; 2001, p. 139–52.

[218] Kawazoe, H., Ohsawa, K., Fujikake, K. "*LDA Measurement of Fuel Droplet Sizes and Velocities in a Combustion Field.*" Combustion and Flame 1990;82:151–62.

[219] Birouk, M., Chauveau, C., Gökalp, I. "*Turbulence Effects on the Combustion of Single Hydrocarbon Droplets.*" Proceedings of the Combustion Institute 2000;28:1015–21.

[220] Birouk, M., Toth, S.L. "*Hydrocarbon Droplet Turbulent Combustion in an Elevated Pressure Environment.*" Flow, Turbulence and Combustion 2015;94:843–58.

[221] Sankar, S. V., Buermann, D. H., Ibrahim, K. M., Bachalo, W.D. "*Application of an Integrated Phase Doppler Interferometer/Rainbow Thermometer/Point-Diffraction Interferometer for Characterizing Burning Droplets.*" Symposium (International) on Combustion/The Combustion Institute 1994;25:413–21.

[222] Raffel, M., Willert, C., Kompenhams, J. "*Particle Image Velocimetry - A Practical Guide.*" 2nd Editio. Springer; 2007.

[223] Merzkirch, W. Particle Image Velocimetry. In: Mayinger, F., Feldmann O, editor. Optical Measurements: Techniques and Applications. 2nd Editio, Springer Berlin Heidelberg; 2001, p. 340–57.

[224] Riethmuller, M., David, L., Lecordier, B. Particle Image Velocimetry. In: Boutier A, editor. Laser Velocimetry in Fluid Mechanics, John Wiley and Sons Ltd.; 2012, p. 159–282.

[225] Roth, N., Karl, A., Anders, K., Frohn, A. "*Flame Propagation in Planar Droplet Arrays and Interaction Phenomena between Neighboring Droplet Streams.*"

Symposium (International) on Combustion/The Combustion Institute 1996;26:1697–703.

[226] Nomura, H., Takahashi, M., Ujiie, Y., Hara, H. "*Observation of Droplet Motion during Flame Spread on Three-Fuel-Droplet Array with a Pendulum Suspender.*" Proceedings of the Combustion Institute 2005;30:1991–9.

[227] Birouk, M., Fabbro, S.C. "*Droplet Evaporation in a Turbulent Atmosphere at Elevated Pressure - Experimental Data.*" Proceedings of the Combustion Institute 2013;34:1577–84.

[228] He, M., Qiu, H. "*Internal Flow Patterns of an Evaporating Multicomponent Droplet on a Flat Surface.*" International Journal of Thermal Sciences 2016;100:10–9.

[229] Xiao, C., Zhou, L., Sun, Z., Du, X., Yang, Y. "*Near-Wall Fluid Flow Near the Pinned Contact Line during Droplet Evaporation.*" Experimental Thermal and Fluid Science 2016;72:210–7.

[230] Hairharan, P. "*Basics of Interferometry.*" 2nd Editio. Academic Press; 2007.

[231] Mikami, M., Oyagi, H., Kojima, N., Wakashima, Y., Kikuchi, M., Yoda, S. "*Microgravity Experiments on Flame Spread along Fuel-Droplet Arrays using a New Droplet-Generation Technique.*" Combustion and Flame 2005;141:241–52.

[232] Mikami, M., Oyagi, H., Kojima, N., Wakashima, Y., Kikuchi, M., Yoda, S. "*Microgravity Experiments on Flame Spread along Fuel-Droplet Arrays at High Temperatures.*" Combustion and Flame 2006;146:391–406.

[233] Nomura, H., Suganuma, Y., Setani, A., Takahashi, M., Mikami, M., Hara, H. "*Microgravity Experiments on Droplet Motion during Flame Spreading Along Three-Fuel-Droplet Array.*" Proceedings of the Combustion Institute 2009;32:2163–9.

[234] Marchese, A. J., Dryer, F. L., Nayagam, V., Colantonio, R.O. "*Hydroxyl radical chemiluminescence imaging and the structure of microgravity droplet flames.*" Symposium (International) on Combustion/The Combustion Institute 1996;26:1219–26.

[235] Yao, R., Qiu, Z., Li, J., Huang, J., Chen, X., Wang, N. "*Experimental Study on N-heptane Droplet Combustion in a Micro-Tube.*" Energy Procedia 2014;61:2528–31.

[236] Liu, Y. C., Xu, Y., Hicks, M. C., Avedisian, C.T. "*Comprehensive Study of Initial Diameter Effects and Other Observations on Convection-Free Droplet Combustion in the Standard Atmosphere for n-Heptane, n-Octane, and n-dDecane.*" Combustion and Flame 2016;171:27–41.

[237] Wu, M. S., Yang, S.I. "*Combustion Characteristics of Multi-Component Cedar Bio-Oil/Kerosene Droplet.*" Energy 2016;113:788–95.

[238] Ajav, E. A., Singh, B., Bhattacharya, T.K. "*Experimental Study of Some Performance Parameters of a Constant Speed Stationary Diesel Engine Using Ethanol-Diesel Blends as Fuel.*" Biomass and Bioenergy 1999;17:357–65.

[239] Li, D., Huang, Z., Lu, X., Zhang, W., Yang, J. "*Physico-Chemical Properties of Ethanol-Diesel Blend Fuel and its Effect on Performance and Emissions of Diesel Engines.*" Renewable Energy 2005;30:967–76.

[240] Rakopoulos, D. C., Rakopoulos, C. D., Kakaras, E. C., Giakoumis, E.G. "*Effects of Ethanol-Diesel Fuel Blends on the Performance and Exhaust Emissions of Heavy Duty DI Diesel Engine.*" Energy Conversion and Management 2008;49:3155–62.

[241] Kumar, S., Cho, J. H., Park, J. Moon, I. "*Advances in Diesel-Alcohol Blends and Their Effects on the Performance and Emissions of Diesel Engines.*" Renewable and Sustainable Energy Reviews 2013;22:46–72.

[242] Tutak, W., Lukács, K. Szwaja, S., Bereczky, Á. "*Alcohol-Diesel Fuel Combustion in the Compression Ignition Engine.*" Fuel 2015;154:196–206.

[243] Datta, A., Mandal, B.K. "*Impact of Alcohol Addition to Diesel on the Performance Combustion and Emissions of a Compression Ignition Engine.*" Applied Thermal Engineering 2016;98:670–82.

[244] Rajesh Kumar, B., Saravanan, S. "*Use of Higher Alcohol Biofuels in Diesel Engines: A Review.*" Renewable and Sustainable Energy Reviews 2016;60:84–115.

[245] Benjumea, P., Agudelo, J., Agudelo, A. "*Basic Properties of Palm Oil Biodiesel-Diesel Blends.*" Fuel 2008;87:2069–75.

[246] Pucher, G., Allan, W., LaViolette, M., Poitras, P. "*Emissions from a Gas Turbine Sector Rig Operated with Synthetic Aviation and Biodiesel Fuel.*" Journal of Engineering for Gas Turbines and Power 2011;133:111502(8).

[247] Chiaramonti, D., Rizzo, A. M., Spadi, A., Prussi, M., Riccio, G., Martelli, F. "*Exhaust Emissions from Liquid Fuel Micro Gas Turbine Fed with Diesel Oil, Biodiesel and Vegetable Oil.*" Applied Energy 2013;101:349–56.

[248] Kurji, H., Valera-Medina, A., Runyon, J., Giles, A., Pugh, D., Marsh, R., Cerone, N., Zimbardi, F., Valerio, V. "*Combustion Characteristics of Biodiesel Saturated with Pyrolysis Oil for Power Generation in Gas Turbines.*" Renewable Energy 2016;99:443–51.

[249] Habibullah, M., Masjuki, H. H., Kalam, M. A., Rizwanul Fattah, I. M., Ashraful, A.

M., Mobarak, H.M. "*Biodiesel Production and Performance Evaluation of Coconut, Palm and their Combined Blend with Diesel in a Single-Cylinder Diesel Engine.*" Energy Conversion and Management 2014;87:250–7.

[250] Yasin, M. H. M., Paruka, P., Mamat, R., Yusop, A. F., Najafi, G., Alias, A. "*Effect of Low Proportion Palm Biodiesel Blend on Performance, Combustion and Emission Characteristics of a Diesel Engine.*" Energy Procedia 2015;75:92–8.

[251] Ileri, E., Atmanli, A., Yilmaz, N. "*Comparative Analyses of n-Butanole-Rapeseed Oil-Diesel Blend with Biodiesel, Diesel and Biodiesel-Diesel Fuels in a Turbocharged Direct Injection Diesel Engine.*" Journal of the Energy Institute 2016;89:586–93.

[252] Rahman, S. M. A., Masjuki, H. H., Kalam, M. A., Abedin, M. J., Sanjid, A., Sajjad, H. "*Production of Palm and Calophyllum Inophyllum based Biodiesel and Investigation of Blend Performance and Exhaust Emission in an Unmodified Diesel Engine at High Idling Conditions.*" Energy Conversion and Management 2013;76:362–7.

[253] Alahmer, A., Yamin, J., Sakhrieh, A., Hamdan, M.A. "*Engine Performance using Emulsified Diesel Fuel.*" Energy Conversion and Management 2010;51:1708–13.

[254] Maiboom, A., Tauzia, X. "*NOx and PM Emissions Reduction on an Automotive HSDI Diesel Engine with Water-in-Diesel Emulsion and EGR: An Experimental Study.*" Fuel 2011;90:3179–92.

[255] Fahd, M. E. A., Wenming, Y., Lee, P. S., Chou, S. K., Yap, C.R. "*Experimental Investigation of the Performance and Emission Characteristics of Direct Injection Diesel Engine by Water Emulsion Diesel under Varying Engine Load Condition.*" Applied Energy 2013;102:1042–9.

[256] Debnath, B. K., Saha, U. K., Sahoo, N. "*A Comprehensive Review on the Application of Emulsions as an Alternative Fuel for Diesel Engines.*" Renewable and Sustainable Energy Reviews 2015;42:196–211.

[257] Ithnin, A. M., Ahmad, M. A., Bakar, M. A. A., Rajoo, S. Yahya, W.J. "*Combustion Performance and Emission Analysis of Diesel Engine Fuelled with Water-in-Diesel Emulsion Fuel Made from Low-Grade Diesel Fuel.*" Energy Conversion and Management 2015;90:375–82.

[258] Leal-Calderon, F., Schmitt, V., Bibette, J. "*Emulsion Science Basic Principles.*" 2nd Editio. Springer; 2007.

[259] Bakry, A. M., Abbas, S., Ali, B., Majeed, H., Abouelwafa, M. Y., Mousa, A., Liang,

L. "*Microencapsulation of Oils: A Comprehensive Review of Benefits, Techniques, and Applications.*" Comprehensive Reviews in Food Science and Food Safety 2016;15:143–82.

[260] Roesle, M. L., Kulacki, F.A. "*Boiling Heat Transfer in Dilute Emulsions.*" Springer; 2013.

[261] Mollet, H., Grubenmann, A. "*Formulation Technology: Emulsions, Suspensions, Solid Forms.*" Wiley-VCH; 2001.

[262] Tadros, T.F. "*Emulsion Science and Technology.*" Wiley-VCH; 2009.

[263] Griffin, W.C. "*Classification of Surface-Active Agents by HLB.*" Journal of Cosmetic Science 1949;1:311–26.

[264] Babu, M. K. G., Subramanian, K.A. "*Alternative Transportation Fuels: Utilisation in Combustion Engines.*" CRC Press/Taylor and Francis Group; 2013.

[265] Williams, F.A. "*Combustion Theory.*" 2nd Editio. The Benjamin/Cummings Company Incorporation; 1985.

[266] Gollahalli, S. R., Brzustowski, T.A. "*Experimental Studies on the Flame Structure in the Wake of a Burning Droplet.*" Symposium (International) on Combustion/The Combustion Institute 1973;14:1333–44.

[267] Canada, G. S., Faeth, G.M. "*Fuel Droplet Burning Rates at High Pressures.*" Symposium (International) on Combustion/The Combustion Institute 1973;14:1345–54.

[268] Gollahalli, S. R., Brzustowski, T.A. "*The Effect of Pressure on the Flame Structure in the Wake of a Burning Hydrocarbon Droplet.*" Symposium (International) on Combustion/The Combustion Institute 1975;15:409–17.

[269] Sangiovanni, J. J., Dodge, L.G. "*Observations of Flame Structure in the Combustion of Monodispersed Droplet Streams.*" Symposium (International) on Combustion/The Combustion Institute 1979;17:455–65.

[270] Gore, J. P., Meng, W. H., Jang, J.H. "*Droplet Flames in Reactive Environments.*" Combustion and Flame 1990;82:126–41.

[271] Deng, S. Zhou, J. "*An Experimental Study of the Effect of Water Content on Combustion of Coal Tar/Water Emulsion Droplets.*" Energy 2011;36:6130–7.

[272] Feng, S., He, B., He, H., Su, L., Hou, Z., Nie, W., Guo, X. "*Experimental Studies the Burning Process of Gelled Unsymmetrical Dimethylhydrazine Droplets under Oxidant Convective Conditions.*" Fuel 2013;111:367–73.

[273] Hottel, H. C., Williams, G. C., Simpson, H.C. "*Combustion of Droplets of Heavy*

Liquid Fuels." Symposium (International) on Combustion/The Combustion Institute 1955;5:101–29.

[274] Bolt, J. A., Saad, M.A. "*Combustion Rates of Freely Falling Fuel Drops in a Hot Atmosphere.*" Symposium (International) on Combustion/The Combustion Institute 1957;6:717–25.

[275] Teodorczyk, A., Wojcicki, S. "*The Combustion of a Liquid Fuel Droplet during Forced Convection.*" Journal of Fire Sciences 1994;12:44–61.

[276] Wang, C. H., Hung, W. G., Fu, S. Y., Huang, W. C., Law, C.K. "*On the Burning and Microexplosion of Collision-Generated Two-Component Droplets: Miscible Fuels.*" Combustion and Flame 2003;134:289–300.

[277] Dietrich, D. L., Nayagam, V., Williams, F.A. Experimental Observations of Cool-Flame Supported Binary- Droplet Arrays Combustion in Microgravity. 9th US National Combustion Meeting, Cincinnati, Ohio, USA: 2015, p. 1–5.

[278] Farouk, T. I., Dietrich, D., Alam, F. E., Dryer, F.L. "*Isolated n-decane droplet combustion – Dual stage and single stage transition to 'Cool Flame' droplet burning.*" Proceedings of the Combustion Institute 2016;36:2523–30.

[279] Wakashima, Y., Yamamoto, S., Kikuchi, M., Yoda, S., Mikami, M., Umemura, A. "*Numerical and Experimental Study on Flame Propagating Mechanism of a Fuel Droplet Array.*" Microgravity Science and Technology 2005;16:338–41.

[280] Liu, Y. C., Savas, A. J., Avedisian, C.T. "*The Spherically Symmetric Droplet Burning Characteristics of Jet-A and Biofuels Derived from Camelina and Tallow.*" Fuel 2013;108:824–32.

[281] Liu, Y. C., Xu, Y., Avedisian, C. T., Hicks, M.C. "*The Effect of Support Fibers on Micro-Convection in Droplet Combustion Experiments.*" Proceedings of the Combustion Institute 2015;35:1709–16.

[282] Avedisian, C. T., Jackson, G.S. "*Soot Patterns Around Suspended n-Heptane Droplet Flames in a Convection-Free Environment.*" Journal of Propulsion and Power 2000;16:974–9.

[283] Bae, J. H., Avedisian, C.T. "*High-Pressure Combustion of Submillimeter-Sized Nonane Droplets in a Low Convection Eenvironment.*" Combustion and Flame 2006;145:607–20.

[284] Gonzales, R. C., Woods, R.E. "*Digital Image Processing.*" 3rd Editio. Pearson Printice Hall; 2008.

[285] Dougherty, G. "*Digital Image Processing for Medical Applications.*" Cambridge

University Press; 2009.

[286] Taylor, J.R. "*An Introduction to Error Analysis: The Study of Uncertainities in Physical Measurements.*" 2nd Editio. University Science Books; 1997.

[287] Liu, Y. C., Savas, A. J., Avedisian, C.T. "*Spherically Symmetric Droplet Combustion of Three and Four Component Miscible Mixtures as Surrogates for Jet-A.*" Proceedings of the Combustion Institute 2013;34:1569–76.

[288] Villasenor, R., Garcia, F. "*An Experimental Study of the Effects of Asphaltenes on Heavy Fuel Oil Droplet Combustion.*" Fuel 1999;78:933–44.

[289] Mishra, D.P. "*Experimental Combustion - An Introduction.*" CRC Press/Taylor and Francis Group; 2014.

[290] Nakaya, S., Fujishima, K., Tsue, M., Kono, M., Segawa, D. "*Effects of Droplet Diameter on Instantaneous Burning Rate of Isolated Fuel Droplets in Argon-Rich or Carbon Dioxide-Rich Ambiences under Microgravity.*" Proceedings of the Combustion Institute 2013;34:1601–8.

[291] Bartle, K. D., Fitzpatrick, E. M., Jones, J. M., Kubacki, M. L., Plant, R., Pourkashanian, M., Ross, A. B., Williams, A. "*The Combustion of Droplets of Liquid Fuels and Biomass Particles.*" Fuel 2011;90:1113–9.

[292] Kim, H., Baek, S.W. "*Combustion of a Single Emulsion Fuel Droplet in a Rapid Compression Machine.*" Energy 2016;106:422–30.

[293] Gupta, R. B., Demirbas, A. "*Gasoline, Diesel, and Ethanol Biofuels from Grasses and Plants.*" Cambridge University Press; 2010.

[294] Turns, S.R. "*An Introduction To Combustion - Concepts and Applications.*" 3rd Editio. McGraw-Hill; 2012.

[295] Lin, C. Y., Wang, K.H. "*Diesel Engine Performance and Emission Characteristics using Three-Phase Emulsions as Fuel.*" Fuel 2004;83:537–45.

[296] Yang, W. M., An, H., Chou, S. K., Chua, K. J., Mohan, B., Sivasankaralingam, V., Raman, V., Maghbouli, A., Li, J. "*Impact of Emulsion Fuel with Nano-Organic Additives on the Performance of Diesel Engine.*" Applied Energy 2013;112:1206–12.

[297] Sanjid, A., Masjuki, H. H., Kalam, M. A., Ashrafur Rahman, S. M., Abedin, M. J., Palash, S.M. "*Production of Palm and Jatropha Based Biodiesel and Investigation of Palm-Jatropha Combined Blend Properties, Performance, Exhaust Emission and Noise in an Unmodified Diesel Engine.*" Journal of Cleaner Production 2014;65:295–303.

[298] Kalogeras, K., Bezergianni, S., Kazantzi, V., Pilavachi, P.A. "*On the Prediction of Properties for Diesel/Biodiesel Mixtures Featuring New Environmental Considerations.*" Computer Aided Chemical Engineering 2010;28:973–8.

[299] Li, T. X., Zhu, D. L., Akafuah, N. K., Saito, K., Law, C.K. "*Synthesis, Droplet Combustion, and Sooting Characteristics of Biodiesel Produced from Waste Vegetable Oils.*" Proceedings of the Combustion Institute 2011;33:2039–46.

[300] Hansen, A. C., Zhang, Q., Lyne, P.W.L. "*Ethanol-Diesel Fuel Blends - A Review.*" Bioresource Technology 2005;96:277–85.

[301] Liu, Y. C., Farouk, T., Savas, A. J., Dryer, F. L., Avedisian, C.T. "*On the Spherically Symmetrical Combustion of Methyl Decanoate Droplets and Comparisons with Detailed Numerical Modeling.*" Combustion and Flame 2013;160:641–55.

[302] Colbeck, I. Aerosol Formation. In: Wedlock DJ, editor. Controlled Particle, Droplet and Bubble Formation, Butterworth-Heinemann; 2004, p. 137–58.

[303] Gonzales, R. C., Woods, R. E., Eddins, S.L. "*Digital Image Processing Using Matlab.*" 2nd Editio. Tata McGraw-Hill; 2010.

[304] Mandal, D. K., Bakshi, S. "*Internal Circulation in a Single Droplet Evaporating in a Closed Chamber.*" International Journal of Multiphase Flow 2012;42:42–51.

[305] Shehata, M. S., Abdel Razek, S.M. "*Experimental Investigation of Diesel Engine Performance and Emission Characteristics using Jojoba/Diesel Blend and Sunflower Oil.*" Fuel 2011;90:886–97.

[306] Imamura, O., Kubo, Y., Osaka, J., Sato, J., Tsue, M., Kono, M. "*A Study on Single Fuel Droplets Combustion in Vertical Direct Current Electric Fields.*" Proceedings of the Combustion Institute 2005;30:1949–56.